Metal-air Batteries: RRDE and EC-SPM Studies of Electrode Kinetics and Electrode Structure

Dissertation
zur
Erlangung des Doktorgrades (Dr. rer.nat)
der
Mathematisch-Naturwissenschaftlichen Fakultät
der
Rheinische Friedrich-Wilhelms-Universität Bonn

vorgelegt von

Lingxing Zan

aus

Baoji, VR China

Bonn, 2017

Angefertigt mit Genehmigung der Mathematisch-Naturwissenschaftlichen Fakultät der Rheinischen Friedrich-Wilhelms-Universität Bonn

Promotionskommission

Erster Gutachter: Prof. Dr. Helmut Baltruschat
Zweiter Gutachter: Prof. Dr. Thomas Bredow
Fachnaher Gutachter: Prof. Dr. Werner Mader
Fachfremder Gutachter: Prof. Dr. Peter Koepke

Tag der mündlichen Prüfung: 07.09.2017

Erscheinungsjahr: 2017

For my Motherland (P.R. China),

My Parents,

My beloved Wife

Contents

Notations

Q_F	Faradaic charge	C	Concentration
C_0	Initial concentration	J_0	Diffusion flux
σ	Charge density	ε	Energy
m	Mass	C_s	Surface concentration
w	Width	r	Atomic radius
E	Potential	t	Time
e	Elemental charge, 1.602×10^{-19} C	V	Voltage
E_0	Standard potential	z	The number of electrons transferred
l	Length	E_D	Disk electrode potential
E_{onset}	Onset potential	E_R	Ring electrode potential
F	Faraday constant, 96485 C·mol^{-1}	d	Distance
I_F	Faradaic current	f_0	Resonant Frequency
k_i	The rate constant of i-th reaction	θ	Surface coverage
j	Current density	ϑ	Relative coverage
$N_{surf.atoms}$	The number of surface atoms	ν	Potential scan rate
D	Diffusion coefficient	τ	Time constant
A_{real}	Real surface area	A_{Geom}	Geometric surface area
η	Overpotential	Φ	Work function
i_R	Ring current	Ψ	Binding energy
I_t	Tunneling current	i_D	Disk current
i_{lim}	Limiting current	μ	Friction coefficient
ħ	Planck's constant	δ_N	Nernst diffusion layer thickness
α	Chemical activity	T	Temperature in Kelvin
N	Collection efficiency	ω	The angular rotation rate
E_{open}	Open circuit potential	S	Shielding constant
R	The universal gas constant, 8.3144598(48) J K^{-1} mol^{-1}	Γ	The fraction of the number of occupied sites

Abbreviations

AFM	Atomic force microscopy	ML	Monolayer
RHE	Reversible hydrogen electrode	DN	Donor number
UPD	Underpotential deposition	AN	Accept number
OPD	Overpotential deposition	Dc	Dielectric constant
CN	Coordination number	OCP	Open circuit potential
CE	Counter electrode	PZC	Potential of zero charge
WE	Working electrode	RE	Reference electrode
CV	Cyclic voltammetry	UHV	Ultrahigh vacuum
OER	Oxygen evolution reaction	ORR	Oxygen reduction reaction
DFT	Density functional theory	Pt(pc)	Polycrystalline platinum
SCE	Saturated calomel electrode	RRDE	Rotating ring disk electrode
SPM	Scanning probe microscopy	STM	Scanning tunnelling microscope
OHP	Outer Helmholtz plane	IHP	Inner Helmholtz plane
GDL	Gas diffusion layer	XPS	X-ray photoelectron spectroscopy
LEED	Low energy electron diffraction	LFM	Lateral force microscopy
IR	Infrared spectroscopy	2D	Two-dimensional
VW	Volmer-Weber growth mode	3D	Three-dimensional
MFM	Magnetic force microscopy	RDE	Rotating disk electrode
CFM	Chemical force microscopy	IPES	Inverse photoemission spectroscopy
GC	Glassy carbon	FV	Frank-van der Merwe growth mode
R_{RMS}	Root mean square roughness	SK	Stranski-Krasanov growth mode
XRD	X-ray diffraction	SEM	Scanning electron microscope
DM	Dipole moment	KF	Karl-Fischer
DC	Direct current	FM	Frank-van der Merwe growth mode
FC	Fuel cell	AC	Alternating current
fcc	Face centered cubic	bcc	Body catered cubic
hcp	Hexagonal close packed	rds	Rate determining step
eV	Electron volt	ppm	Part per million
EQCM	Electrochemical quartz microbalance	EIS	Electrochemical impedance spectroscopy
HOPG	Highly oriented pyrolytic graphite	FTIR	Fourier transform infrared spectroscopy
EDS	Energy-dispersive X-ray spectroscopy	DEMS	Differential electrochemical mass spectrometry

Chapter 1: Fundamentals

1.1 Metal-air batteries

A metal-air battery is a type of electrochemical battery that consists of a metal anode, an air cathode and an aqueous/nonaqueous electrolyte and uses the electron transfer during the oxidation of a metal with oxygen from atmosphere to produce the electricity.

Since the first description of a Zn-air battery by Vergnes in 1860 [1], metal-air battery has attracted people's attention. In recent years, many other metal-air batteries, such as lithium, sodium, magnesium, and aluminium air batteries have been studied because they have many advantages such as abundant raw materials, safety, environmental friendliness and high theoretical specific energy values ranging from 1000 to 11000 Wh/kg, etc. They are expected to yield electrically rechargeable metal-air batteries for practical application in transportations, communications and other applications requiring high energy capacity and long life of battery discharge, but there are still many challenges to achieve this goal. In order to solve the problems in rechargeable metal air batteries and put them into practical application, the research on the mechanism of oxidation and reduction reactions in these batteries is an essential step. In metal-air batteries, during the discharge, oxygen separated from atmosphere enters the cell from the porous cathode and dissolves in the electrolyte, and then reacts with the metal ions in the electrolyte after electrons transfer from the electrode to form a metal-oxide or metal hydroxide discharge product. In aqueous electrolytes, the discharge products can be dissolved in the electrolyte. But in nonaqueous electrolytes, most of discharge products can not be dissolved in the electrolyte so that they precipitate on the electrode or somewhere else to form a solid phase and grow in size during the discharge process. During the charge process, the discharge products decompose into oxygen and metal ions while losing of electrons. In practice, the performance of these batteries is not as good as people expected because there are still some limitations and shortages, for example, some uncontrollable and irreversible reactions [2], high overpotential in charge and discharge [3], severe ohmic loss [4] and instability of the electrolyte and cathode in charge and discharge cycles [5-7]. So, in order to get a better charge-discharge performance of these batteries, a lot more research on these issues has to be launched.

1.2 Air cathode reactions

Cathode reactions play a very important role in metal air batteries and they largely determines the type of battery such as fuel cell or secondary/rechargeable battery. When the reactions at cathode are reversible, the battery could be rechargeable; otherwise, it is just like fuel cell and can not be recharged again. In metal-air batteries, if the cathode reaction active substance from air is only oxygen (100% O_2), they are also so-called metal-oxygen batteries. Oxygen reduction and evolution reactions are expected to be reversible reactions, which can support charge and discharge in the ideal secondary/rechargeable metal-air batteries.

1.2.1 Oxygen reduction reaction (ORR)

Oxygen reduction reactions are series of complex electrochemical reactions, which are considered to involve one-step or multi-step electron-transfer processes and complicated conversion processes of oxygen species to O_2^-, O_2^{2-} and O^{2-}. Most studies of ORR in aqueous electrolytes are focused on the selection of the cathode material [8-12] (such as Pt, Au, Ag, C, etc) and the catalysts [13-19] (such as metal, metal oxide, bimetallic and multimetallic compound, etc.), which dictate the mechanisms/pathways of ORR.

In aqueous electrolytes, ORR occurs through two pathways: the direct pathway, via 4-electron reduction from O_2 to H_2O, and an indirect pathway, via 2-electron reduction from O_2 to hydrogen peroxide (H_2O_2) and then to H_2O [20, 21].
In alkaline electrolytes, the ORR can be briefly given as:

$$\begin{aligned} Alkaline\ \ media: \quad & O_2 + 2H_2O + 4e^- \rightarrow 4OH^- \cdots\cdots\cdots\cdots (4e^-\ \ process) \quad direct\ \ pathway \\ & \left.\begin{aligned} O_2 + H_2O + 2e^- &\rightarrow HO_2^- + OH^- \cdots\cdots (2e^-\ \ process) \\ H_2O + HO_2^- + 2e^- &\rightarrow 3OH^- \cdots\cdots\cdots\cdots (2e^-\ \ process) \end{aligned}\right\} indirect\ \ pathway \end{aligned}$$

In acid electrolytes, the ORR can be briefly given as:

$$\begin{aligned} Acid\ \ media: \quad & O_2 + 4H^+ + 4e^- \rightarrow 2H_2O \cdots\cdots\cdots\cdots\cdots (4e^-\ \ process) \quad direct\ \ pathway \\ & \left.\begin{aligned} O_2 + 2H^+ + 2e^- &\rightarrow H_2O_2 \cdots\cdots\cdots\cdots\cdots (2e^-\ \ process) \\ H_2O_2 + 2H^+ + 2e^- &\rightarrow 2H_2O \cdots\cdots\cdots\cdots (2e^-\ \ process) \end{aligned}\right\} indirect\ \ pathway \end{aligned}$$

Studies reveal that the direct 4-electron transfer pathway is more efficient than 2-electron transfer pathway. The general schematic of ORR pathways were represented by Wroblowa et al. [22] as shown in Fig. 1.1.

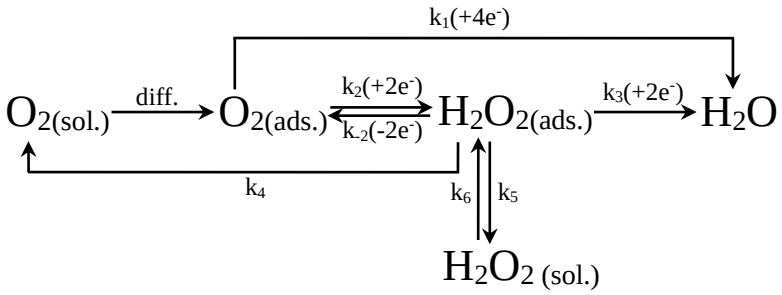

Fig. 1.1 General schematic of ORR pathways in acidic electrolytes

Where, k_i is the rate constant of i-th reaction (i=1, 2, 3, 4, 5 and 6). However, HO_2^- instead of H_2O_2 and OH^- instead of H_2O are produced in alkaline electrolytes during ORR. As described by Singh [23], the ORR is dominated by the direct 4-electron transfer pathway at the high overpotential, where the ratio of k_1/k_2 is constant and $k_1>k_2$; the 2-electron transfer pathway to produce peroxide most commonly appears at the intermediate overpotential, where the ratio of k_1/k_2 decreases; the ratio of k_1/k_2 becomes lower than 1 and k_3 increases at low overpotential, leading to a further reduction of H_2O_2/HO_2^- to H_2O/OH^-, respectively.

Theoretical studies show that the oxygen adsorption configurations and the interactions of adsorbed oxygen molecule at the electrode surface also dictates the ORR pathways [24-26] and final products. In the field of electrocatalysis of oxygen reduction at the electrode surface, according to the molecular orbital theory, the oxygen-oxygen bond is weakened by overlapping of π-electron orbital of oxygen and the unoccupied orbital of catalytic active sites, which could stretch the O-O bond to achieve activation effect and make further dissociation of O-O easy during the oxygen reduction reaction. Meantime, the occupied orbital of catalytic active sites gives feedback to the π* orbital of oxygen leading to oxygen being adsorbed at the catalytic active sites. Three manners of adsorption models for oxygen reduction on the catalytic active site were proposed by Yeager and others [27, 28], including the Pauling model (end-on), the Griffiths model (side-on), and Yeager model (bridge) as shown in Fig. 1.2.

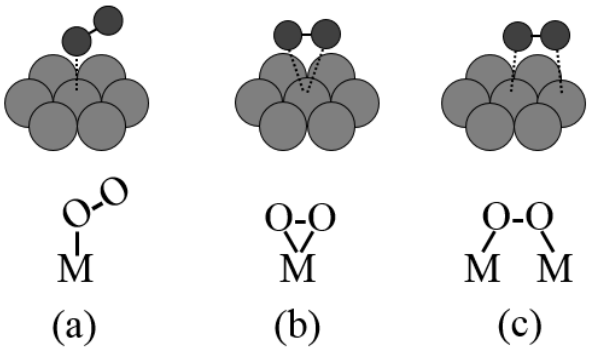

Fig. 1.2 Oxygen adsorption models: (a) the Pauling model, (b) the Griffiths model, (c) the Yeager model.

For the end-on adsorption model, only one oxygen atom in each of oxygen molecules is adsorbed on the surface so that the O-O bond can not be stretched effectively, resulting in that ORR via two-electron pathway to form peroxide is favored and terminated. In contrast, for both side-on and bridge adsorption model, the parallel adsorption of two O atoms will lead to weaken and further break the O-O bond. Therefore, ORR via a direct four-electron pathway without peroxide formation is favored. However, the 2×2 electron pathway could be attributed to the further reaction of peroxide via either two-electron reduction or chemical disproportionation process.

As well known, since ORR via 2-electron transfer pathway will produce the peroxide species, which are considered to be corrosive and lead to the denaturation of catalyst, resulting in a premature degradation phenomenon of cell system, 2-electron transfer pathway is unfavorable [29-32]. Nevertheless, ORR via the direct 4-electron transfer pathway is desirable because it generates high energy efficiency without premature degradation phenomenon. Now, it has been generally recognized through extensive research that the direct 4-electron ORR reduction prefers to occur on noble metals whereas the 2-electron ORR reduction appears primarily on carbonaceous materials [13, 33-35]. For transition metal-oxides and metal macrocycles the ORR pathways are various and dependent on their structure, composition and experiment conditions [33, 36, 37]. Moreover, Pt and its alloys are still considered to be the best catalysts for ORR until now [38-40].

However, in nonaqueous electrolytes most studies of ORR are focused on the selection a suitable solvent [2, 41-45], electrode [46-48], catalyst [49-54], cation [55-58] and anion [59, 60] for achieving high stability of electrolyte/electrode and reversibility of

ORR and OER, and their effects on the mechanisms/pathways of ORR.

In non-aqueous electrolytes, it is a widely accepted notion that oxygen was reduced to peroxide through two pathways: the direct pathway, via 2-electron reduction from O_2 to peroxide (O_2^{2-}) electrochemically, and an indirect pathway, via 1-electron reduction from O_2 to superoxide (O_2^-) electrochemically and then undergoing an induced chemical disproportionation process or a second electron transfer reaction to form O_2^{2-} afterwards [2, 46, 61].

In non-aqueous electrolytes, the ORR can be briefly given as:

$$\text{Nonaqueous media}: \quad O_2 + 2e^- \rightarrow O_2^{2-} \cdots\cdots\cdots (2e^- \ process) \qquad direct \ \ pathway$$

$$\left.\begin{array}{c} O_2 + e^- \rightarrow O_2^- \cdots\cdots\cdots\cdots (1e^- \ process) \\ 2O_2^- \rightarrow O_2^{2-} + O_2 \cdots\cdots\cdots (chemically) \\ or \\ O_2^- + e^- \rightarrow O_2^{2-} \cdots\cdots\cdots\cdots (1e^- \ process) \end{array}\right\} \quad indirect \ \ pathway$$

The general schematic of ORR pathways in non-aqueous electrolytes were represented by combining the ORR paths suggested by Bruce [62], Kwabi [63] and Reinsberg [64] as shown in Fig. 1.3.

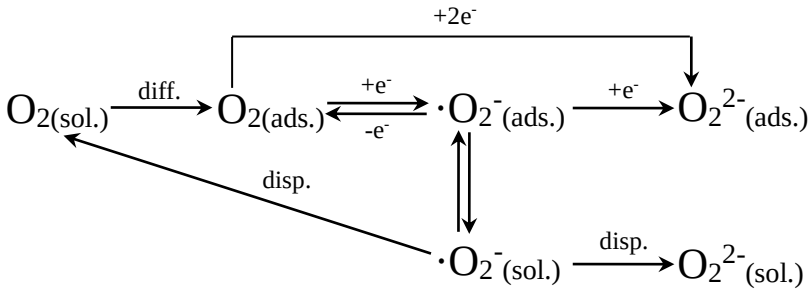

Fig. 1.3 General schematic of ORR pathways in non-aqueous electrolytes

At low overpotential, the ORR pathway via superoxide (O_2^-) formation is predominant because the large amounts of superoxide existing in electrolyte were detected, indicating that the indirect pathway is favored in this case. Moreover, the disproportionation pathway is also dominated because the driving force for electron transfer is small at low overpotential. However, at the high overpotential, probably because the O_2^- species are reduced rapidly or ORR occurs via the direct 2-electron pathway to form O_2^{2-} species, only trace amounts of superoxide were detected [62, 63]. The direct 2-electron pathway to form O_2^{2-} species in Li^+ containing electrolyte has been suggested in the literature [46, 63, 65]. Probably, it also provides direct evidence for the different ORR pathways

(direct and indirect) that in Li^+ containing electrolyte the different morphology of Li_2O_2, particle like and toroidal-like were observed at high and low overpotential, respectively.

Actually, the ORR process is very complicated in non-aqueous electrolytes, as mentioned before, the complex dependencies of ORR mechanisms/pathways on some factors such as solvent, electrode material, cation, anion, etc. are widely exist in the ORR process. A number of studies have found that the solvents with high donor number, strongly coordinating anions, or protic additives (such as water, methanol and perchloric acid) can solvate and stabilize the superoxide species, facilitating Li_2O_2 formation via disproportionation pathway rather than 2-electron direct pathway in Li^+ containing electrolyte. Moreover, it was also found that the cation with larger charge density may support a more effective coordination to the adsorbed superoxide so that it promotes the second electron transfer pathway at low overpotential [46]. Although people have done a lot of effort, there are still many arguments and the ORR mechanisms remain poorly understood [66]. In addition, many problems such as irreversible or quasi-reversible ORR/OER, the produced poor conductivity and solubility of Li_2O_2 and poor tolerance of solvent against the attack of superoxide species and also probably peroxide species, arised during ORR [5]. Therefore, the situation becomes more complicated and extensive efforts have to be reinforced in this area.

1.2.2 Oxygen evolution reaction (OER)

The oxygen evolution reaction (OER) is a reverse reaction of ORR that is essential energy conversion reaction during the charging process of the rechargeable metal-air batteries. Because it is also a thermodynamically unfavorable and sluggish kinetic reaction during the charging process, which needs high energy to drive [67], how to achieve a high efficiency OER becomes a very thorny problem in the development of rechargeable metal-air batteries.

In aqueous electrolytes, OER is the reaction of generating molecular oxygen through oxidation of either H_2O or OH^- by the pathway of 4-electron transfer in acid or alkaline electrolyte, respectively. However, the OER mechanism is largely dependent on the property of the catalyst. The total equations [68] and one of the mechanisms are depicted in Fig. 1.4.

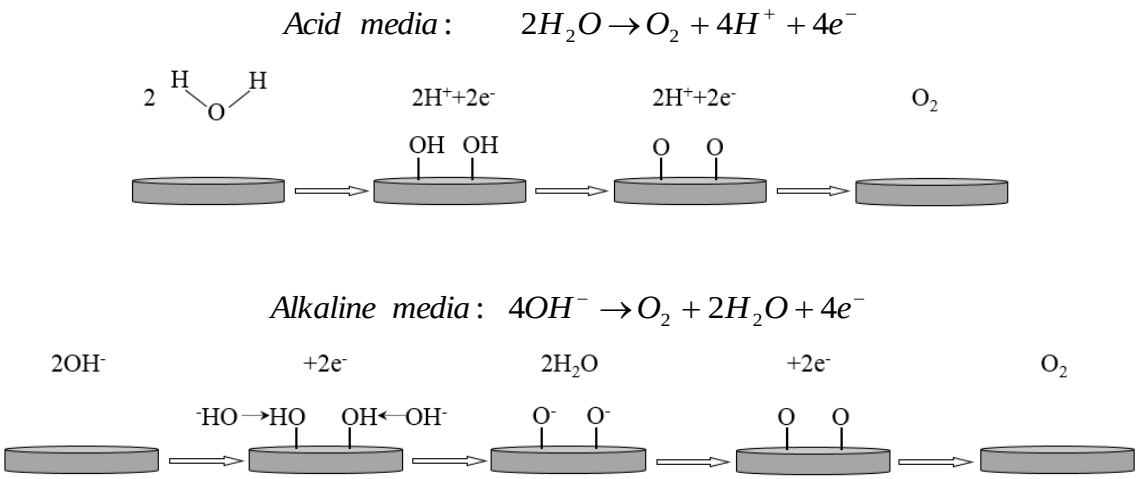

Fig. 1.4 The schematic representations of the mechanisms of OER on metal surface in acid media (up) and alkaline media (down).

The Sabatier principle describes the understanding of the fundamental limitations for heterogeneous OER activity of catalysts and it is generally accepted [68]. For OER, most active sites on the electrode surface are considered to be surface metal cations (M), which the polarized oxygen prefers to adsorb on, and the reaction proceeds via a series of intermediates (such as M-OH, M-O, M-O^-), all these species bound only by the M-O bond. The electrocatalytic activities of catalysts for OER were evaluated by the "volcano" plot of the M-O bond strength against OER activity [69], suggesting that the catalysts with optimal M-O bond strength occupying the top of the "volcano" possess higher catalytic activity for OER, whereas the catalysts with too strong or too weak M-O bond are less active for OER. It provides a basic idea as to how to select out the optimized and robust catalysts, which is one of the important challenges to improve the activity and efficiency of OER.

Over the past decades, a considerable amount of catalysts based on metal (such as Co, Ni, Fe, Mn, etc. and their alloys), metal/transition metal oxide (including Rutile-, Spinel-, Perovskite- and other- types) and metal free catalysts (such as carbon material with nanostructures, doped carbon materials, etc.) have been widely investigated. It has been found that metal oxides can increase the number of the decomposition sites of peroxide [70], but their electrical conductivities are poor. It is generally known that Iridium and Ruthenium oxide-based (IrO_2 and RuO_2) possess the highest catalytic activity for OER in acid media [71] and the bimetal catalysts such as Ni-Fe and Co-Fe exhibit the highest activity for (oxy)hydroxide OER in alkaline media [68]. However,

the kinetics and thermodynamics of OER are dependent not only on the material and composition but also on the electrode surface structure, morphology and effect etc. Namely, the performance of OER is very complicated and it is seriously limited by these several extrinsic factors. Consequently, to achieve the targeted efficiency and comprehend complexity of OER is still key challenge in the development of rechargeable metal-air batteries. In this field, our interest is to develop better cathode materials, which could address the sluggish kinetics of oxygen reactions and improve the efficiency of OER.

In nonaqueous electrolytes, oxygen evolution is one of the most difficult issues in the study field of rechargeable metal-air batteries because it requires overcoming a higher energetic barrier than that of ORR, resulting in more sluggish kinetics (larger overpotential) and subsequently poor reversibility of ORR and OER (discharge and charge cycles). In addition, the OER process is very complicate process in nonaqueous electrolytes. The ambiguities in the reaction mechanisms, the discharge products and their structure and the effect factors on this process still exist, and its controllability is still poor. Therefore, understanding the mechanisms of OER and improving the OER efficiency are most tough tasks in the current study.

So far, OER has been widely investigated and achieved only in Li-air battery system. Based on recent research progress, it is generally believed that the oxygen evolution on the electrode surface is via a direct 2-electrons oxidation of Li_2O_2.

$Li_2O_2 \rightarrow 2Li^+ + O_2 + 2e^-$ $(O_2^{2-} \rightarrow O_2 + 2e^-)$

Recent surface-enhanced Raman spectroscopy (SERS) study suggested that Li_2O_2 decomposed directly to evolve O_2 during OER [72]. However, Lu [73] found that oxygen is evolved chemically from $Li_{2-x}O_2$, which was formed by the delithiation of the Li_2O_2 at lower potential (< 400 mV), whereas the bulk Li_2O_2 oxidation takes place at higher potentials(400-1200 mV) by the galvanostatic intermittent titration technique (GITT) and potentiostatic intermittent titration technique (PITT) and Black [74] also suggested that OER is probably through a two-step oxidation.

$Li_2O_2 \rightarrow LiO_2 + Li^+ + e^-$ (or $O_2^{2-} \rightarrow O_2^- + e^-$)

$2LiO_2 \rightarrow Li_2O_2 + O_2$ (or $2O_2^- \rightarrow O_2^{2-} + O_2$)

or $LiO_2 \rightarrow Li^+ + O_2 + e^-$ (or $O_2^- \rightarrow O_2 + e^-$)

The overall OER process is via $2e^-/O_2$, the same as the direct oxidation of Li_2O_2. Although some disagreements on the OER mechanism arose, they could give us the inspiration to understand the fundamental knowledge and address the sluggish kinetics and poor efficiency of OER.

An effective method in improving the kinetics and efficiency of OER is catalysis by an efficient catalyst. Currently, various catalysts including metal oxide (MnO_2, Co_3O_4, RuO_2, etc.), noble metals (Pt, Au, Ru, Pd), and their alloys (PtNi, PtCo, PtAu, etc.) have been employed for catalysis OER [75]. However, the OER in nonaqueous electrolytes is not obviously promoted and even not fully clarified until now. Furthermore, researches have shown that other side reactions may occur simultaneously during OER and make the OER process more complicate in practice.

1.3 Fundamentals of electrochemical reactions at model surface

In the electrochemical cell an overall electrochemical reaction is separated into two half reactions occurring at the separated two electrodes. Each of the half reactions that convert oxidant (Ox) to reductant (Red) and vice versa can be described as follow:

$$Ox + ne^- \leftrightarrow \mathrm{Re}\,d$$

These reactions are typical electrolysis reactions, which occur at the electrode surface via the transfer of electrons between an electrode and a reactant species at the interface, so the whole process typically involves a series of steps consisting of the reactant reaching at the electrode surface, the heterogeneous electron transfer from the electrode to the reactant species and the product leaving the electrode surface. The schematic representation of this process is shown in Fig. 1.5.

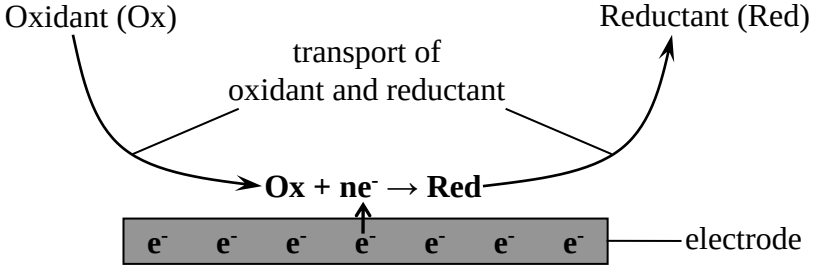

Fig. 1.5 The schematic representation of the electrode surface reaction process

The reaction rate is dominated by the slowest step, mass transport of reactant and product or electron transfer. Specifically, if the electron transfer is too slow to make all of the reactants adsorbed on the electrode surface being converted into products, the rate

of this reaction will be controlled by the rate of the electron transfer. Conversely, if the electron transfer is very fast so that all of the reactants in the vicinity of or adsorbed on the electrode surface can be converted into products immediately, this reaction rate will be controlled by the mass transportation rate. In this case, the limiting current can be estimated by the movement rate of reactants in bulk solution.

1.3.1 Mass transport in electrochemical cell

Three forms of mass transport, including diffusion, convection and migration are existing in an electrochemical process.

Diffusion occurs in all solutions and describes a phenomenon of a random movement of the species (such as molecules, ions, reagents, etc.) from a region of high concentration to one of lower concentration (or from high to lower chemical potential) driven by the entropic force. In an electrochemical measurement, diffusion is a significant transport phenomenon because the reaction only takes place at the electrode surface resulting in a lower concentration of reactant existing close to electrode than in bulk solution and the other way around for product. The diffusion rate of chemical species is not only dependent on the difference of their concentration between two positions in solution, so called the concentration gradient, but also on the diffusion coefficient (D), a characteristic value for a specific chemical species in a specific solution under a certain pressure and temperature. This movement of chemical species in solution by diffusion was studied in detail and the rate of movement was predicted mathematically by Fick [76], who proposed two laws to quantify this process. The first law was described by the following equation:

$$J_0 = -D_0\left(\frac{\partial C_0}{\partial x}\right)$$

Where, J_0 is the diffusion flux, $\partial C_0/\partial x$ is the concentration gradient and D_0 is the diffusion coefficient. The negative sign implies that chemical species move down the concentration gradient (i.e. from regions of high to low concentration).

The second law describes that the rate of change of the concentration (C_0) as a function of time (t) could be related to the change in the concentration gradient as following:

$$\frac{\partial C_0}{\partial t} = D_0\left(\frac{\partial^2 C_0}{\partial x^2}\right)$$

So the steeper concentration gradient signifies the faster rate of diffusion. For most of

electrochemical reactions, diffusion is considered as the most significant transport process in practice and Fick's second law became an important since it can predict the change of the concentration of the species as a function of time in the solution.

Convection is the movement of the species in solution caused by the force action. It contains two forms, natural convection and forced convection. The natural convection is caused by density differences or small thermal differences or vibrations etc. of the surroundings and exists in any solution. It can be not predicted because the solution species move randomly under this condition. The forced convection is generated by mechanical stirring or other ways. In electrochemical measurements, the forced convection is intentionally introduced in a well-defined and quantitative manner (such as rotating disk and wall jet electrodes, flow cell and flow through cell) to eliminate the effects from the random aspect generated by the natural convection because it is typically several orders of magnitude greater than any natural convection [77]. In practice, by introducing the forced convection, the property and form of mass transport and reaction kinetics can be approximately defined and the current flowing under forced convection condition can be predicted.

Migration is the movement of charged species in an electric field. The migration flux is related to the property of the species (such as the charge, concentration and diffusion coefficient) and the magnitude of the electric filed gradient. In an electrochemical measurement, the electrostatic effect is generated by an applied voltage between two electrodes. The migration rate can be calculated accurately in principle, but in practice the calculation becomes difficult because it depends on the properties of the ion and solvent and interactions between diffusion layers in practical solutions. In order to remove the migration effects, supporting electrolyte (strong electrolyte) which does not take part in the reaction but can help the reactants suffering from migratory effects is widely used in the electrochemical measurement in solutions.

In practice, the mass transport in the electrochemical cells is very complicated and of all these forms of mass transport coexist. The Nernst-Plank equation [78] described the contributions from these three coexisting forms of mass transport including diffusion (concentration gradient), migration (electric field) and convection (hydrodynamic velocity), so it has been widely used to describe the total mass transport of species

accurately in one dimension as follows:

$$J_{(x,t)} = -\left[D\frac{\partial C_{(x,t)}}{\partial x} \right] - \left[\left(\frac{zF}{RT} \right) DC_{(x,t)} \right] \left(\frac{\partial \varphi_{(x,t)}}{\partial x} \right) + C_{(x,t)} \nu_{x(x,t)}$$

Where J represents the flux (mol cm^{-2} s^{-1}), D is the diffusion coefficient of the species (cm^2 s^{-1}), C is the concentration of the species (mol cm^{-3}), φ is the electric potential, ν_x is the hydrodynamic velocity, and F, R and T have the usual meaning. It shows that the flux of the species flowing towards the electrode is proportional to either of the concentration gradient, electric potential, or hydrodynamic velocity, all these related to the distance and time.

For an electrochemical reaction, if the reaction rate is determined by the rate of mass transport, the reaction can be classified as a mass-transfer controlled reaction. If the diffusion is considered as the only form of mass transport after eliminating the contributions of other factors (such as electrostatic potential, hydrodynamic velocity, temperature, etc.) to the total flux of mass transport, the reaction can be classified as a diffusion controlled reaction. The measured current during the reaction could be estimated by the flux of the electroactive species. As is shown in the equation $i_t = nFAD(\partial C_i / \partial x) \mid x = 0$ (where, A is the electrode surface area (cm^2) and the meanings of other symbols have been shown before), the current is related to the flux of the electroactive species.

1.3.2 Electrode/electrolyte interface

In electrochemistry, the electrode/electrolyte interface is the interface or transition region between electronic conductor and ionic conductor. Specifically, it is the interface between electrode and electrolyte when they are in contact with each other. This interface region is the place where the electrode reaction takes place, because when the electron flowing through this interface will lead to the occurrence of some components oxidation or reduction reaction (losing or gaining electron) in this area. The nature of the interface has a great influence on the mechanistic and dynamics aspects of the electrode reactions.

It is clear that two different phases contacted with each other will generate the difference of the electrical potential (Galvani potential) between two phases, which can lead to the appearance of excess charge on two phases. For the electrode which is under

potentiostatic control will have an additional excess charge appearing at the surface. These excess charges will result in strong adsorption of opposite-charged ions on electrode surface. This will give rise to the region called the electrical double layer. Many models [79] have been put forward to explain the electrode/electrolyte interface phenomenon. Here, we just demonstrate one of the models which offer a detailed description of the interface between electrode and electrolyte and it is most commonly used now as depicted in Fig. 1.6.

It is generally considered that some solvent molecules and ions (anions, in this model) could penetrate the Stern layer and directly contact with the electrode surface to constitute the inner Helmholtz plane (IHP). These ions are defined as specifically adsorbed ions. These solvent molecules display a certain orientation to the electric field. The solvated ions (cations, in this model), which are out of the IHP and in the region of their closest approach to the electrode surface, are indirectly adsorbed on the electrode surface via electrostatic interaction to constitute the out Helmholtz plane (OHP). Consequently, the so-called double layer is formed and it possesses high electrostatic field strength up to 10^9 V/m [80]. Beyond OHP, there is the diffuse layer.

The potential drop appears across the interface as demonstrated in Fig. 1.6. The potential drop from electrode to bulk electrolyte is called total Galvani potential difference ($\Delta\varphi$), which consists of two potential drops in Helmholtz layer and diffuse layer ($\Delta\varphi_H$ and $\Delta\varphi_{diff}$). In Helmholtz layer the potential drop occurs in a linear manner because it is absolutely analogous to an electrical capacitor in this region. Whereas the potential drop from the Helmholtz plane to bulk electrolyte occurs in exponential manner and its strength in potential drop is largely depending on the electrolyte concentration. This is general distribution form of potential at the interface of the electrode and electrolyte.

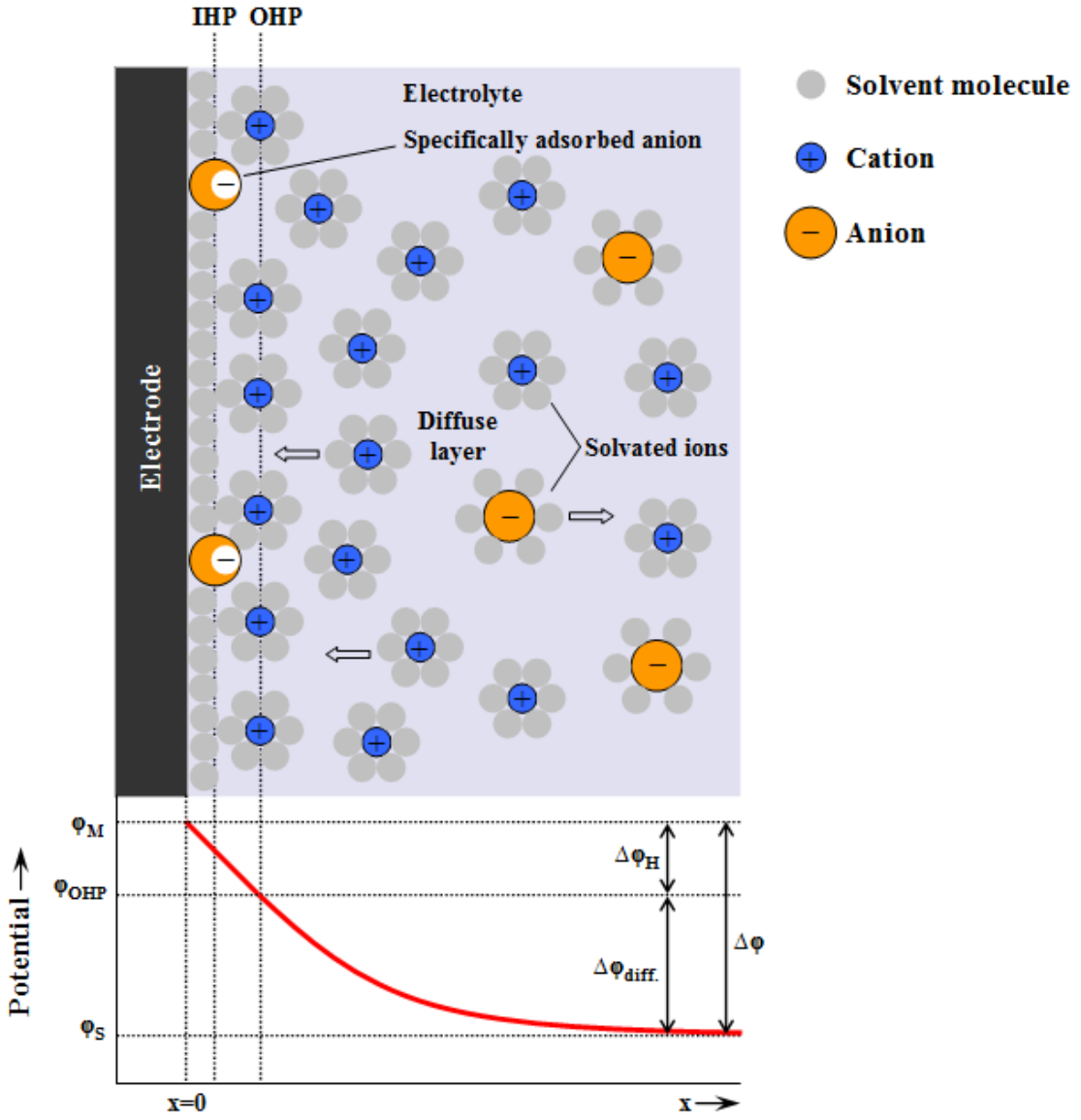

Fig. 1.6 Schematic representation of the electrochemical interface at contact with a negatively-charged electrode

1.3.3 Surface structure of metals

In most materials, metals are used in polycrystalline form, including a massive form such as electrodes and a finely divided form such as supported metal catalysts. At the atomic level, all metal surfaces are irregular and atomically rough and possess defects (such as steps, kinks and terrace vacancies) as shown in Fig. 1.7. The atoms on the surface at these different locations are named as adatom, step adatom, kink atom, etc. These differences on the surface atoms are mainly represented in their different coordination number. For these different type atoms, their chemical behaviour, adsorption heat and catalytic activity are different and these differences are large. Moreover, unlike the electronic states in the material, the distribution of the surface state

energy level is not uniform. The related studies demonstrate that the adsorptions/reactions prefer to occur on the low-coordinated atoms presented at steps and kinks [81-84]. In short, the surface structure and composition determines the physical and chemical properties, usability, adsorption behaviour and catalytic ability, so the studies of the metal surface property are significant for surface reactions.

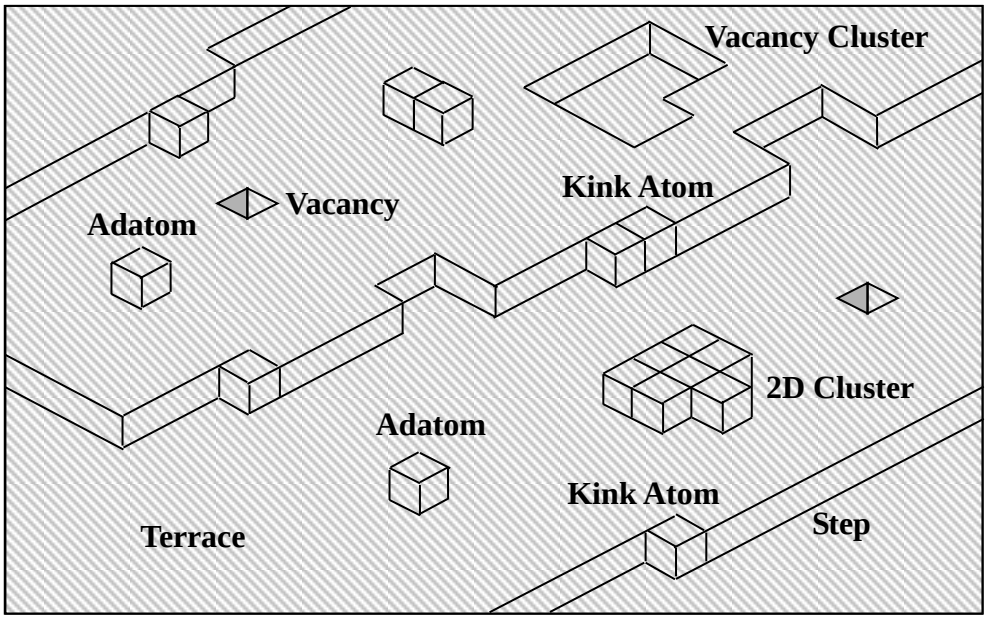

Fig. 1.7 Typical surface sites and defects on a simple cubic (100) surface

At a micro level, most materials can be regarded as an aggregate of single-crystalline crystallites. The surface chemical properties of the material are crucially dependent on the nature and type of these single crystal surfaces or the sum of the individual properties of the contained single crystal surfaces on the polycrystalline surface. In principle, the surface properties of any material could be understood when the surface has been well defined and its properties are well known. In addition, a well-defined surface is vitally important to study and understand the mechanism of the surface reaction. Most metallic crystals exist in the form of body centred cubic (bcc, such as Fe, Cr, etc.), face centred cubic (fcc, such as Cu, Al, Ni, Pb, Ag, Au, Pt, Pd, Rh, etc.) and hexagonal close packed (hcp, such as Cd, Mg, Ti, Zn, etc.). The catalytic activity of metal is closely related to its structure. Most of the transition metals with fcc (or A1) structure are usually used as catalysts in the field of electrochemistry. Nowadays, crystals are made artificially to meet the needs of science, technology, and so on.

1.3.4 Single crystal surfaces

A single crystal surface can be prepared by precise cutting the three-dimensional (3-D)

bulk structure of a solid along a particular crystallographic plane and is usually defined by using Miller indices (hkl), which are identified by the reciprocal of the intercepts of the plane at three x-, y-, z-axes [85]. Because the closely packed face is thermodynamically favorable, the atoms exposed on the surface usually tend to form low indices of crystal plane. The three common low-index (111), (110) and (100) planes formed by cutting a simple fcc lattice are sketched below, and these planes are atomically flat with hexagonal, rectangular and square arrangement of the surface atoms, respectively (see. Fig. 1.8). Of the three planes, the most closely packed fcc (111) plane would be expected to possess the lowest surface energy and highest stability based on the considering of the high surface atom density and high coordination number of the surface atoms.

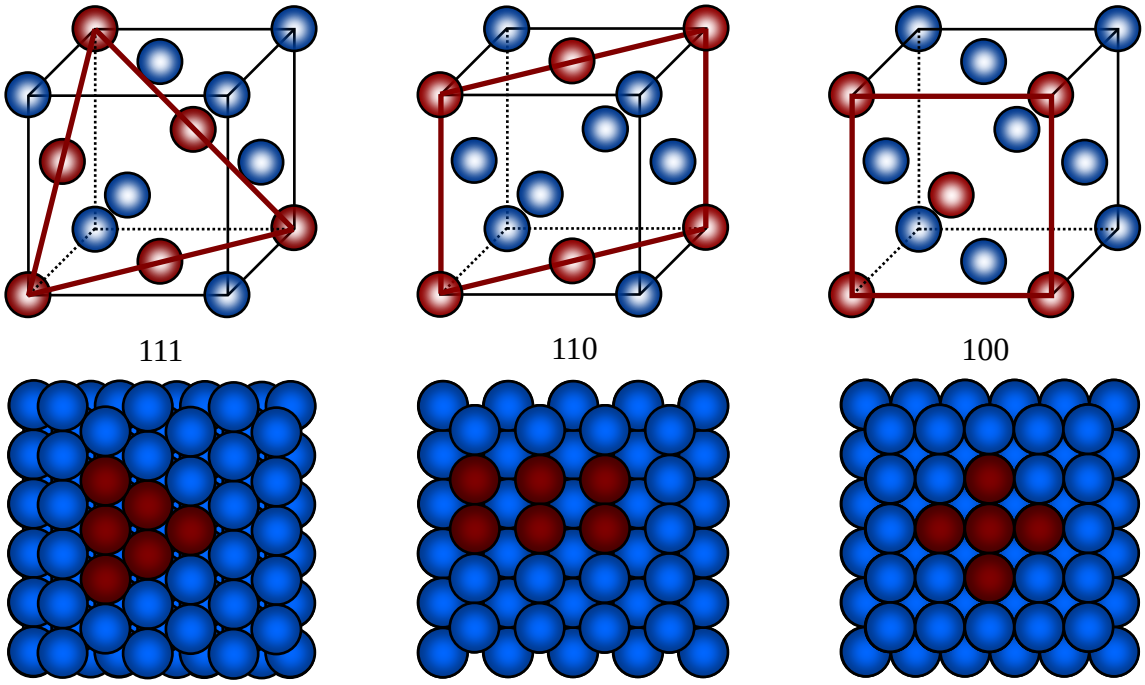

Fig. 1.8 The schematic of the unit cells of a face centred cubic structure (up) and atomic structures of the corresponding (111) (110) (100) surfaces with position of (111) (110) (100) plane (down).

1.4 Adsorption

For a solid electrode, due to the existence of the surface tension and surface energy caused by the unbalanced force-field of metal atoms on the surface, atoms, ions and molecules (adsorbate) can adhere to the surface (adsorbate surface). This process is so called adsorption. From the thermodynamic point of view, this process will lead to the reduction of the surface tension, which can also lower the surface energy. Therefore, it is nearly always an exothermic process. The inverse process of adsorption is desorption,

the removal of the adsorbate from the absorbent surface. Because the adsorption/desorption is an interface phenomenon, it is considered as a significant step toward the reactions taking place at the interface of electrode and electrolyte. Furthermore, for the surface catalysis, the moderate interaction between the catalyst and the substrate is considered as an optimum condition that the catalyst possesses high catalytic activity as described in the Sabatier principle [86]. Based on the Sabatier principle, the famous volcano plot was found and used widely to evaluate the catalytic activity of catalysts for certain reactions (e.g. decomposition of formic acid and hydrogen evolution on transition metals). For a surface reaction, in addition to the reaction rates at different reaction steps, the adsorption rate and desorption rate are also the important kinetic parameters of the reaction; that means, the reaction rate could be determined by the adsorption rate, desorption rate, or both.

The adsorption is generally classified into physical adsorption (physisorption) and chemical adsorption (chemisorption) according to the type of forces existing between the adsorbate molecule and adsorbent surface. The differences between physical adsorption and chemisorption are shown as following:

Physisorption	**Chemisorption**
Weak interaction (Van der Waals' force)	Strong interaction (chemical bond force)
Low enthalpy of adsorption (20-40 kJ mol^{-1})	High enthalpy of adsorption (40-400 kJ mol^{-1})
Reversible process (desorption occurs easily by heating or by decreasing the pressure)	Irreversible process (Efforts to free the adsorbed gas give some definite compound)
Related to the ease of liquefaction of the gas	No such correlation
It is not specific (no compound formation)	It is highly specific (There is some possibility of surface compounds formation)
It does not require any activation energy	It requires activation energy (activated adsorption)
It usually occurs at low temperature and decreases with increase of temperature	It occurs at high temperature and initially increases with increase of temperature

Multilayer adsorption (BET Isotherm)	Monolayer adsorption (Langmuir Isotherm)
It can be used for determining the surface area and pore size	It can be used for determining the surface concentrations, the kinetics and rates of adsorption and desorption, and active centres
e.g. N_2, NH_3, HCl/solid	e.g. C_6H_6/Pd; CO/Pt; H_2/transition metals

1.4.1 Adsorption sites on single crystal surfaces

Fig. 1.9 depicts the four possibilities of the adsorption sites on the fcc-(111) surface in higher symmetry positions: top site, bridge site and two hollow/interstitial sites (octahedral site and tetrahedral site). Certainly, there are also some different types of the bridge sites and hollow sites in the different metal lattice structures, such as long/short bridge site existing on (110) surface, fourfold hollow existing on (100) surface, etc. In addition, Marcus [87] calculated that there are one octahedral site and two tetrahedral sites per metal atom in fcc and hcp metals, whereas three octahedral and six tetrahedral sites per metal atom in bcc metals. On these different adsorption sites, the binding energies, equilibrium bond distances, vibrational frequencies and co-ordination number for adsorbates are different [88]. Consequently, these could probably lead to the appearance of different reaction pathways. Most of molecules are prefer to adsorb at the highest available co-ordination sites where possess highest binding energies and stabilities for molecules adsorption.

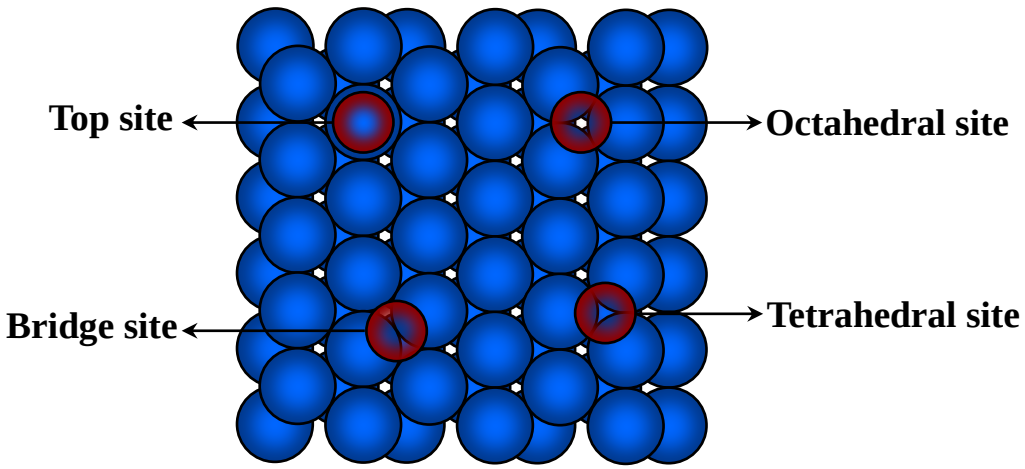

Fig. 1.9 Top view of the different adsorption sites on a fcc-(111) surface

For hydrogen chemisorption, hydrogen atoms are considered as the adsorbed species because the dissociation of hydrogen molecules takes place on metals during the adsorption process. It is generally known that the hydrogen atoms are tending to occupy the octahedral sites for the fcc metals, whereas they are tending to occupy the tetrahedral sites for the bcc and hcp metals [87]. Furthermore, under control of temperature and pressure, the adsorbed hydrogen atoms can even migrate easily from the interface into sub-surface layers of the substrates because of their small size. Halogen chemisorption is also occurring via a dissociative process to give adsorbed halogen atoms. Halogen atoms also prefer to occupy the high co-ordination sites on the surface (e.g. the fourfold hollow sites on fcc(100) surfaces and the threefold hollow sites on fcc(111) surfaces). However, the exception is that a molecule such as carbon monoxide may prefer to bind at a terminal or twofold bridge site rather than the highest available co-ordination site. In addition, undergoing either a dissociative adsorption or molecular adsorption is largely dependent upon the metal surface. The detailed discussion about the nature of adsorbates on surfaces are available in the book of Viswanathan [89].

1.4.2 Chemisorption of oxygen

Clarifying the oxygen chemisorption is crucial for understanding the mechanism of oxygen reduction reaction. Based on the related studies, it has been found that usually oxygen molecules not only undergo a dissociative adsorption on metals, but also undergo a molecular adsorption on some metals, such as Ag and Pt, at low temperature [90].

The models of molecular oxygen adsorption on metal surfaces have been demonstrated before. For those three manners of adsorption, the oxygen molecules adsorbed on the surfaces either via an σ-donor interaction or a π-acceptor interaction, these interactions are relatively weak. These adsorbed oxygen molecules could be reversibly desorbed or irreversibly dissociated once the O=O bond is broken by supplying heat/energy or decreasing the activation energy (e.g. by employing the catalysts). The formed oxygen atoms also prefer to occupy the highest available co-ordination site and they are bonded strongly with the surface metal atoms. This strong interaction between adsorbate and adsorbent may induce the distortion of the metal atoms arrangement on the surface by a series of displacement processes or surface reconstruction. As mentioned before, the

dissociative oxygen adsorption is generally irreversible, so heating the adsorbed oxygen usually results in either the gradual diffusion of oxygen species from the surface into the bulk substrate or the formation of the surface oxide compounds, rather than desorption of oxygen. Even at room temperatures for the active metals, it is obvious that the formation of surface oxide starts immediately once the surface is exposed to oxygen. The oxidation process in the bulk substrate will be hindered by the surface oxide layers (passivation layer) and eventually it may be terminated once the thickness of surface oxide layer reaches the specified value. However, it is not the case for the noble metals.

Most investigations of oxygen adsorption focus on adsorption structure, coverage, types and enthalpy of the adsorbed oxygen on the solid surface and these involve several experimental techniques. It is generally considered that low-energy electron diffraction (LEED) and scanning tunneling microscopy (STM) are the most appropriate techniques to determine the surface structure and coverage of adsorbates. X-ray photoelectron spectroscopy (XPS) could also give a quantitative estimate of the surface coverage of the adsorbate. Infrared spectroscopy (IR) provides some information about the type of adsorption and the adsorbed species. And some other techniques, such as inverse photoemission spectroscopy (IPES), in situ Fourier transform spectroscopy (FTIR), etc. are also valuable for the study of oxygen adsorption.

1.4.3 Definition of the surface coverage

The amount of adsorbate on a substrate surface can be introduced as the surface coverage (θ) and it is can be stated:

a), the fraction of the number of occupied sites (Γ) / the number of available sites (Γ_{max})

$$\theta = \frac{Number\ of\ adsorption\ sites\ occupied\ by\ adsorbate}{Total\ number\ of\ available\ adsorption\ sites\ on\ the\ surface\ of\ the\ substrate} = \frac{\Gamma}{\Gamma_{max}}$$

When θ = 1, it indicates that the adsorbates achieve the saturation.

b), the fraction of the number of occupied sites/the number of surface atoms ($N_{surf.atoms}$)

$$\vartheta = \frac{\Gamma}{N_{surf.atoms}}$$

When ϑ = 1, it indicates all the substrate atom sites are occupied by the adsorbate atoms with the ratio of 1:1. When the well-defined arrangement of atoms/molecules is 1×1, both coverage values are same.

1.5 Electrochemical deposition of metals

Electrochemical deposition, also called electrocrystallization, is a phenomenon of nucleation and crystal growth under the control of externally applied potential in an electrochemical cell. Electrochemical deposition of metals is an ancient surface decoration technique. Early on, the development and application of this technique is just based upon the experiences. Later, in 1878, Gibbs [91] established the concepts and basic principles of the nucleation and crystal growth after his studies on phase equilibrium in different systems. At the beginning of the 20th century, Volmer [92], Kossel [93], Stranski [94], etc. they used the simulation of statistics and molecular motion to improve the concepts and principles. Hereafter, Avrami [95] made a contribution to the kinetic of crystallization, Cabrera and Frank [96] improved the mechanism of spiral nucleating of metals, Kaischew [97] made a significant improvement on the theory of crystallization. In the 70's of the 20th century, Lorenz [98] firstly conducted the UPD of metals on single crystal surface and explained the two-dimensional super crystal structures. Subsequently, Lorenz [99] found the different growth mode of metals, such as layer by layer growth, multilayer growth, spiral growth, etc. In recent decades, with the development of the surface characterization techniques and theoretical chemistry, the cognition of metal electrochemical deposition can reach the atomic level and the knowledge can be further improved.

1.5.1 The mechanism of electrochemical deposition of metals

Electrochemical deposition of metals occurs at the interface of an ionic conducting electrolyte and electronic conducting electrode. It is a complex process, involving the charge transfer process, adsorption process and phase transitions process such as nucleation, growth, etc. at the interface and the ions transportation process under electric field. In general, it involves three stages:

1) Transportation of metal ions to the interface and adsorption on the substrates (native metal substrates or foreign substrates),

2) Phase transitions (nucleation) and cluster growth to form two-dimensional (2D) and three-dimensional (3D) phase formation, and

3) Bulk phase formation and 3D crystal growth.

Specially, the metal ions move from bulk electrolyte to the reaction zone (substrate/electrolyte interface), adsorbing on the electrode surface, exactly in the inner

Helmholtz plane of double layer. Afterwards, the electrons are transferred from the substrate to the adsorbed metal ions leading to the reduction of these metal ions (or the formation of S-M bond) on the electrode surface to form 2D metal phase. 3D phase formation is via bulk deposition based on 2D phase. The detailed descriptions on the mechanism, thermodynamic and kinetic of this process can be found in the literatures [99-101].

1.5.2 Surface modification and catalysis

To study the structure and the chemical composition of the surface is important to understand the mechanism of catalysis, because the change in surface properties (such as surface geometric feature, the electronic structure of surface atoms, etc.) will lead to the change in the catalytic activity of electrode surface. Surface modification is to change the surface chemical compositions and surface structures of materials by physical and chemical methods to improve the physical and chemical properties of materials. In the field of electrocatalysis, the studies found that in most cases the catalyst consisting of two or more metals exhibit better catalytic performance than that of single metal catalysts, which gives a basic idea that the surface modification could be one of the ways to enhance the catalytic activity of the electrode material. At present, chemical modification methods of metal electrode surface decorated by one or more different metals, such as electrochemical deposition (underpotential deposition and overpotential deposition), chemisorptions, etc. are widely adopted to prepare the high efficient and stable catalysts.

1.5.3 Insertion reaction

An insertion reaction is a chemical reaction process in which one chemical substance (a molecule or ion) is interposed into an existing bond of another chemical substance. It is widely involved in organic synthesis (for example, CO insertion into the metal-carbon (M-C) bond to form an acyl group, many electrophilic oxides (e.g. SO_2, CO_2 and NO) insertion into the metal-carbon bond, alkenes insertion into the metal–hydrogen (M-H) bond and carbine insertion into the carbon–hydrogen (C-H) bond to form the corresponding complexes, Mg insertion into the organic group-halide (R-X) bond to form Grignard reagents, etc.).

Some reactions in electrochemistry also involve insertion of alkali metal ions (e.g. Li^+,

Na^+, Mg^{2+}, etc.) into a solid phase, which usually consists of metal, metal oxide or chalcogenides. This kind of reaction is a topochemical reaction accompanying electron-transfer and some changes in the phase and structure of host material.

In the case of metals (such as Sb, Bi, Sn, etc.) as host materials, the reaction can be represented as follows:

$$xA^{z+} + yM + (x \cdot z)e^- \rightarrow A_xM_y$$

It is essentially an alloy formation process. The formation of the A_xM_y alloyed phase may occur through two pathways, a displacement process of the host atoms by the guest atoms in the lattice and directly inserting into the empty sites in the lattice. It involves a series of complex movements of two different atoms in the host material to form a stable structure. And also it could cause the lattice transformation and expansion of the host material. Interestingly, the diffusion limitation current can be also detected during the insertion process in this case. In principle, the diffusion coefficient of guest species in the host material could be calculated by the Cottrell equation or probably some other equations. However, in the case of using the Cottrell equation, the precondition is that the saturated concentration (C_0) of the guest species in the first layer/several layers of host material close to the interface of two phases should be found out. As for the more detailed understanding of the insertion mechanism and the structures of the alloyed phases, it needs to make further study.

Similar insertion reactions were also found in the case of metal oxides (such as Mn_3O_4, MoO_3, Ti_2O, etc.) and chalcogenides (such as TiS_2, MoS_2, etc.) as host materials. The reaction can be described as follows:

$$xA^{z+} + MY_n + (x \cdot z)e^- \rightarrow A_xMY_n$$

However, due to the presence of anion array such as O^{2-} and S^{2-}, the insertion process becomes more complicate. It is considered that the anion array undergoes a diffusionless transformation process to stabilize the new metastable phases in many cases [102]. The detailed descriptions are available in the literatures [102-104].

Here, it is worth to mention that the occurrence of reversible reaction is required for building a rechargeable battery. The reverse reaction of insertion is de-insertion or extraction. It is found that alkali metals insertion and de-insertion in some metal materials are reversible, so it may provide new routes to select anode material for

rechargeable metal-ion batteries and synthesize some novel materials exhibiting unusual structure and properties for other purposes.

1.5.4 Underpotential deposition (UPD) and overpotential deposition (OPD)

For an electrochemical deposition of metal on a native metal electrode, the equation can be usually represented by:

$$Me_{sol.}^{z+} + ze^{-} \Leftrightarrow Me$$

Where $Me_{sol.}^{z+}$ are the metal ions in the electrolyte. The Nernst equilibrium potential is defined as:

$$E_{Me/Me^{z+}} = E^{0}_{Me/Me^{z+}} + \frac{RT}{zF}\ln\frac{\alpha_{Me^{z+}}}{\alpha_{Me}}$$

$E_{Me/Me^{z+}}$ is the Nernst equilibrium potential, $E^{0}_{Me/Me^{z+}}$ is the standard potential, and the $\alpha_{Me^{z+}}$ is the activity of $Me_{sol.}^{z+}$ ions in the electrolyte.

Underpotential and overpotential are defined by convention as:

$$E - E_{Me/Me^{z+}} = \begin{cases} \Delta E\,(underpotential) > 0 \ for\ E > E_{Me/Me^{z+}} \\ \eta\ \ (overpotential)\ \ < 0 \ for\ E < E_{Me/Me^{z+}} \end{cases}$$

Where E is the applied potential. Therefore, underpotential deposition (UPD) is the metal deposition phenomenon in the potential range more positive than the Nernst equilibrium potential, whereas overpotential deposition (OPD) occurs in the potential range more negative than the Nernst equilibrium potential. It is generally believed that the UPD occurs in the case of the interaction between the substrate S and the depositing metal M, S-M is stronger than that between depositing metals, M-M (that is, the formation of S-M is more energetically favoured than the formation of M-M). From the work function point of view, UPD probably occurs when the metal with small work function deposits on the metal with large work function. For example, it is found that the work function of copper is smaller than that of gold, so UPD of copper on gold could be taking place, not vice versa. Typically, the UPD takes place only up to monolayer formation, whereas the OPD occurrence is unlimited. Consequently, UPD and OPD of metal on substrate are related to the formation of monolayer and bulk/multi-layer formation (2D and 3D phases), respectively.

1.5.5 Film growth modes on single crystal surface

Based on extensive experimental and theoretical studies, three classical growth modes of film formation were found and described: Frank-van der Merwe; Stranski-Krastanov and Volmer-Weber [105], which are illustrated schematically in Fig. 1.10. Generally, it is considered that the growth mode is determined mainly by the binding energy of S-Me and the crystallographic misfit [100].

I). Frank-van der Merwe (FV) or layer-by-layer growth is based on that the deposited film atoms are more strongly bound to the substrate than to each other, in other word, the binding energy of Me-S, $\Psi_{Me\text{-}S}$, is larger than that of Me-Me, $\Psi_{Me\text{-}Me}$, ($\Psi_{Me\text{-}S} >> \Psi_{Me\text{-}Me}$), and no crystallographic misfit appears.

II). Stranski-Krastanov (SK) growth is a mixed growth mode. In this case, the binding energy of Me-S, $\Psi_{Me\text{-}S}$, is still larger than that of Me-Me, $\Psi_{Me\text{-}Me}$, ($\Psi_{Me\text{-}S} >> \Psi_{Me\text{-}Me}$), but crystallographic misfit appears, which causes a monolayer or a few monolayers formation first then 3D island formation on the top.

III). Volmer-Weber (VW) or 3D island growth mode means that 3D islands were formed initially, no completely monolayer formation. It is generally considered that the 3D island growth occurs when the binding energy of Me-S, $\Psi_{Me\text{-}S}$, is lower than that of Me-Me, $\Psi_{Me\text{-}Me}$, ($\Psi_{Me\text{-}S} << \Psi_{Me\text{-}Me}$), and it is independent of crystallographic misfit.

In practice, the mechanism of film growth is a very complex process. It is determined not only by the binding energy and crystallographic misfit but also by the property and the structure of substrate surface, temperature, solvation properties of the solvent, etc. Research shows there are five distinct growth modes, including columnar growth mode, step flow mode, step bunching mode, screw-island or spiral-island growth mode and growth on kinked/rough surfaces, in addition to the three classical growth modes depicted above [106].

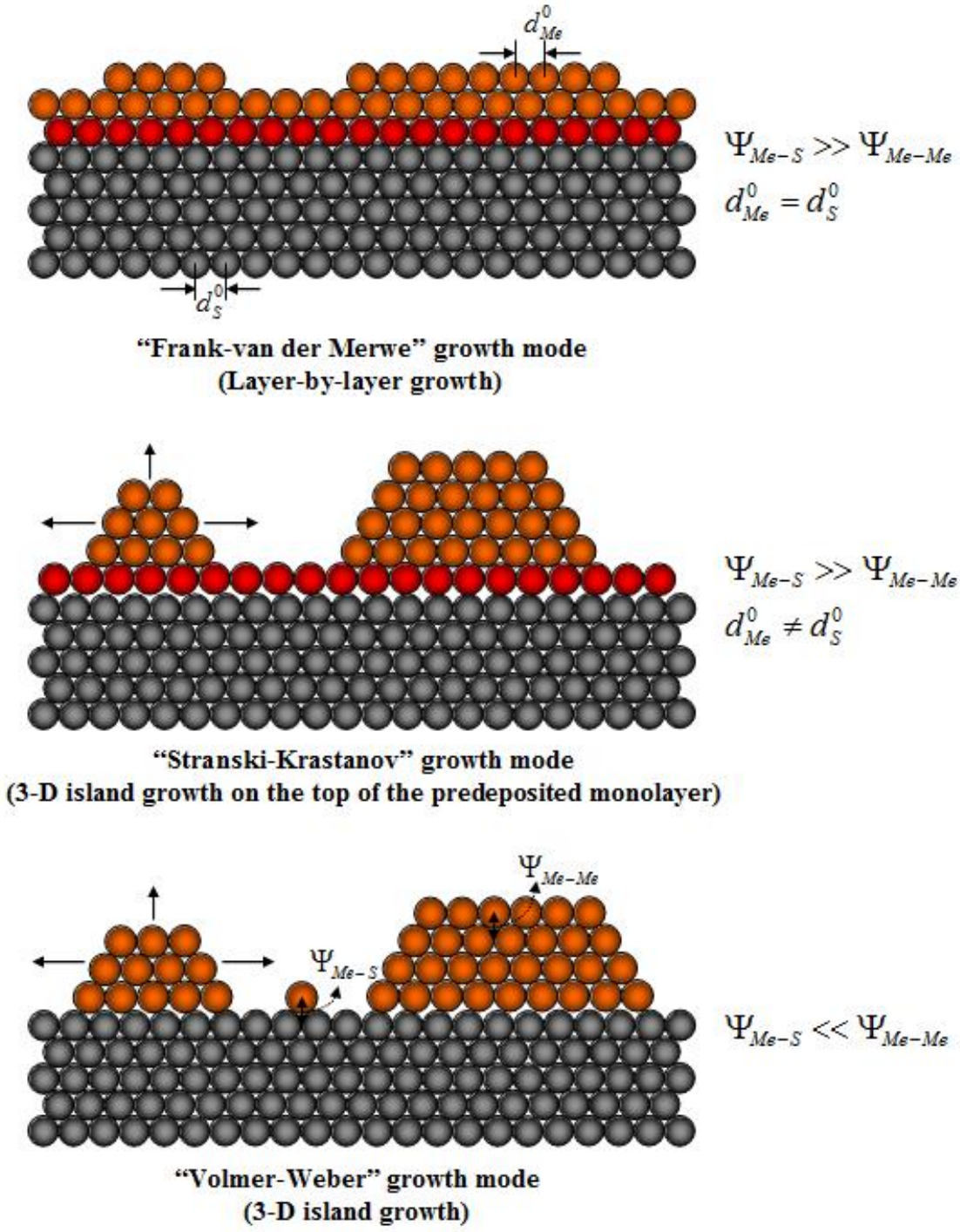

Fig. 1.10 Schematic representation of three different growth modes of metal (Me) deposition on foreign substrate (S) depending on the binding energy of Me on S, $\Psi_{Me\text{-}S}$, compared to that of Me on native substrate Me, $\Psi_{Me\text{-}Me}$, and on the crystallographic misfit characterized by the interatomic distances d^0_{Me} and d^0_S of 3D Me and S bulk phases, respectively. Cross-section views of (a) "Frank-van der Merwe" growth mode, (b) "Stranski-Krastanov" growth mode, (c) "Volmer-Weber" growth mode. The graphics reproduced based on ref. [100].

References

[1] M. Vergnes, US Patent 28317 A (1860).
[2] C. O. Laoire, S. Mukerjee, K. M. Abraham, E. J. Plichta, and M. A. Hendrickson, Journal of Physical Chemistry C 114:9178 (2010).
[3] L. Cecchetto, M. Salomon, B. Scrosati, and F. Croce, Journal of Power Sources 213:233 (2012).
[4] X. B. Zhu, T. S. Zhao, Z. H. Wei, P. Tan, and L. An, Energy & Environmental Science 8:3745 (2015).
[5] D. G. Kwabi, T. P. Batcho, C. V. Amanchukwu, N. Ortiz-Vitoriano, P. Hammond, C. V. Thompson, and Y. Shao-Horn, The Journal of Physical Chemistry Letters 5:2850 (2014).
[6] D. Sharon, M. Afri, M. Noked, A. Garsuch, A. A. Frimer, and D. Aurbach, The Journal of Physical Chemistry Letters 4:3115 (2013).
[7] S. A. Freunberger, Y. Chen, N. E. Drewett, L. J. Hardwick, F. Barde, and P. G. Bruce, Angewandte Chemie-International Edition 50:8609 (2011).
[8] N. M. Markovic, H. A. Gasteiger, and P. N. Ross, The Journal of Physical Chemistry 100:6715 (1996).
[9] T. J. Schmidt, V. Stamenkovic, M. Arenz, N. M. Markovic, and P. N. Ross, Electrochimica Acta 47:3765 (2002).
[10] J. Perez, H. M. Villullas, and E. R. Gonzalez, Journal of Electroanalytical Chemistry 435:179 (1997).
[11] F. Elkadiri, R. Faure, and R. Durand, Journal of Electroanalytical Chemistry 301:177 (1991).
[12] B. B. Blizanac, P. N. Ross, and N. M. Markovic, Journal of Physical Chemistry B 110:4735 (2006).
[13] V. Neburchilov, H. J. Wang, J. J. Martin, and W. Qu, Journal of Power Sources 195:1271 (2010).
[14] E. R. Vago and E. J. Calvo, Journal of Electroanalytical Chemistry 339:41 (1992).
[15] L. Wang, X. Zhao, Y. Lu, M. Xu, D. Zhang, R. S. Ruoff, K. J. Stevenson, and J. B. Goodenough, Journal of The Electrochemical Society 158:A1379 (2011).
[16] A. Sarkar, A. V. Murugan, and A. Manthiram, Langmuir 26:2894 (2010).
[17] H. Zhu, S. Zhang, Y.-X. Huang, L. Wu, and S. Sun, Nano Letters 13:2947 (2013).
[18] L. Dai, Y. Xue, L. Qu, H.-J. Choi, and J.-B. Baek, Chemical Reviews 115:4823 (2015).
[19] M. Bursell, M. Pirjamali, and Y. Kiros, Electrochimica Acta 47:1651 (2002).
[20] S. R. S. Prabaharan and M. S. Michael, Nanotechnology in Advanced Electrochemical Power Sources, Pan Stanford, 2014.
[21] F. Cheng and J. Chen, Chemical Society Reviews 41:2172 (2012).
[22] H. S. Wroblowa, Y. C. Pan, and G. Razumney, Journal of Electroanalytical Chemistry 69:195 (1976).
[23] R. N. Singh, R. Awasthi, and C. S. Sharma, International Journal of Electrochemical Science 9:5607 (2014).
[24] P. A. Christensen, A. Hamnett, and D. Linares-Moya, Physical Chemistry Chemical Physics 13:5206 (2011).
[25] C. F. Zinola, A. J. Arvia, G. L. Estiu, and E. A. Castro, Journal of Physical Chemistry 98:7566 (1994).
[26] Z. Duan and G. Wang, Physical Chemistry Chemical Physics 13:20178 (2011).
[27] Z. Chen, J.-P. Dodelet, and J. Zhang, Non-Noble Metal Fuel Cell Catalysts, Wiley, 2014.
[28] J. Zhang, PEM Fuel Cell Electrocatalysts and Catalyst Layers: Fundamentals and Applications, Springer, London, 2008.

[29] K. Teranishi, K. Kawata, S. Tsushima, and S. Hirai, Electrochemical and Solid State Letters 9:A475 (2006).
[30] Y. Y. Shao, G. P. Yin, and Y. Z. Gao, Journal of Power Sources 171:558 (2007).
[31] K. Kinoshita, Electrochemical Oxygen Technology, Wiley, New York, 1992.
[32] W. Vielstich, A. Lamm, and H. A. Gasteiger, Handbook of Fuel Cells-Fundamentals, Technology and Applications, Wiley, Chichester, 2003.
[33] A. Morozan, B. Jousselme, and S. Palacin, Energy & Environmental Science 4:1238 (2011).
[34] M. Gara and R. G. Compton, New Journal of Chemistry 35:2647 (2011).
[35] E. Yeager, Electrochimica Acta 29:1527 (1984).
[36] Y. J. Feng and N. Alonso-Vante, Physica Status Solidi B-Basic Solid State Physics 245:1792 (2008).
[37] H. J. Choi, N. A. Kumar, and J. B. Baek, Nanoscale 7:6991 (2015).
[38] N. M. Markovic, T. J. Schmidt, V. Stamenkovic, and P. N. Ross, Fuel Cells - From Fundamentals to Systems 1:105 (2001).
[39] A. K. Shukla and R. K. Raman, Annual Review of Materials Research 33:155 (2003).
[40] H. A. Gasteiger, S. S. Kocha, B. Sompalli, and F. T. Wagner, Applied Catalysis B-Environmental 56:9 (2005).
[41] D. Vasudevan and H. Wendt, Journal of Electroanalytical Chemistry 392:69 (1995).
[42] M. J. Trahan, I. Gunasekara, S. Mukerjee, E. J. Plichta, M. A. Hendrickson, and K. M. Abraham, Journal of the Electrochemical Society 161:A1706 (2014).
[43] H. Wang, K. Xie, L. Wang, and Y. Han, Journal of Power Sources 219:263 (2012).
[44] V. S. Bryantsev, V. Giordani, W. Walker, M. Blanco, S. Zecevic, K. Sasaki, J. Uddin, D. Addison, and G. V. Chase, Journal of Physical Chemistry A 115:12399 (2011).
[45] F. Marchini, S. Herrera, W. Torres, A. Y. Tesio, F. J. Williams, and E. J. Calvo, Langmuir 31:9236 (2015).
[46] C. Bondue, P. Reinsberg, A.-E.-A. A. Abd-El-Latif, and H. Baltruschat, Physical Chemistry Chemical Physics (2015).
[47] C. Tran, X. Q. Yang, and D. Y. Qu, Journal of Power Sources 195:2057 (2010).
[48] C. J. Allen, S. Mukerjee, E. J. Plichta, M. A. Hendrickson, and K. M. Abraham, Journal of Physical Chemistry Letters 2:2420 (2011).
[49] X. M. Ren, S. S. Zhang, D. T. Tran, and J. Read, Journal of Materials Chemistry 21:10118 (2011).
[50] T. Shiga, Y. Hase, Y. Kato, M. Inoue, and K. Takechi, Chemical Communications 49:9152 (2013).
[51] R. S. Kalubarme, G.-E. Park, K.-N. Jung, K.-H. Shin, W.-H. Ryu, and C.-J. Park, Journal of the Electrochemical Society 161:A880 (2014).
[52] F. Li, R. Ohnishi, Y. Yamada, J. Kubota, K. Domen, A. Yamada, and H. Zhou, Chemical Communications 49:1175 (2013).
[53] Z.-L. Wang, D. Xu, J.-J. Xu, and X.-B. Zhang, Chemical Society Reviews 43:7746 (2014).
[54] F. S. Gittleson, R. C. Sekol, G. Doubek, M. Linardi, and A. D. Taylor, Physical Chemistry Chemical Physics 16:3230 (2014).
[55] C. J. Allen, J. Hwang, R. Kautz, S. Mukerjee, E. J. Plichta, M. A. Hendrickson, and K. M. Abraham, Journal of Physical Chemistry C 116:20755 (2012).
[56] E. J. Calvo and N. Mozhzhukhina, Electrochemistry Communications 31:56 (2013).
[57] Q. Yu and S. Ye, The Journal of Physical Chemistry C 119:12236 (2015).

[58] C. O. Laoire, S. Mukerjee, K. M. Abraham, E. J. Plichta, and M. A. Hendrickson, Journal of Physical Chemistry C 113 20127 (2009).
[59] I. Gunasekara, S. Mukerjee, E. J. Plichta, M. A. Hendrickson, and K. M. Abraham, Journal of the Electrochemical Society 162:A1055 (2015).
[60] C. M. Burke, V. Pande, A. Khetan, V. Viswanathan, and B. D. McCloskey, Proceedings of the National Academy of Sciences of the United States of America 112:9293 (2015).
[61] D. G. Kwabi, N. Ortiz-Vitoriano, S. A. Freunberger, Y. Chen, N. Imanishi, P. G. Bruce, and Y. Shao-Horn, Mrs Bulletin 39:443 (2014).
[62] L. Johnson, C. M. Li, Z. Liu, Y. H. Chen, S. A. Freunberger, P. C. Ashok, B. B. Praveen, K. Dholakia, J. M. Tarascon, and P. G. Bruce, Nature Chemistry 6:1091 (2014).
[63] D. G. Kwabi, M. Tulodziecki, N. Pour, D. M. Itkis, C. V. Thompson, and Y. Shao-Horn, Journal of Physical Chemistry Letters 7:1204 (2016).
[64] P. Reinsberg, C. Bondue, and H. Baltruschat, Electrochimica Acta 200:214 (2016).
[65] Y.-C. Lu, H. A. Gasteiger, M. C. Parent, V. Chiloyan, and Y. Shao-Horn, Electrochemical and Solid-State Letters 13:A69 (2010).
[66] N. B. Aetukuri, B. D. McCloskey, J. M. García, L. E. Krupp, V. Viswanathan, and A. C. Luntz, Nat Chem 7:50 (2015).
[67] Y. Cheng and S. P. Jiang, Progress in Natural Science-Materials International 25:545 (2015).
[68] M. S. Burke, L. J. Enman, A. S. Batchellor, S. H. Zou, and S. W. Boettcher, Chemistry of Materials 27:7549 (2015).
[69] I. C. Man, H.-Y. Su, F. Calle-Vallejo, H. A. Hansen, J. I. Martínez, N. G. Inoglu, J. Kitchin, T. F. Jaramillo, J. K. Nørskov, and J. Rossmeisl, ChemCatChem 3:1159 (2011).
[70] T. S. Olson, S. Pylypenko, J. E. Fulghum, and P. Atanassov, Journal of the Electrochemical Society 157:B54 (2010).
[71] T. Audichon, T. W. Napporn, C. Canaff, C. Morais, C. Comminges, and K. B. Kokoh, Journal of Physical Chemistry C 120:2562 (2016).
[72] Z. Peng, S. A. Freunberger, L. J. Hardwick, Y. Chen, V. Giordani, F. Bardé, P. Novák, D. Graham, J.-M. Tarascon, and P. G. Bruce, Angewandte Chemie International Edition 50:6351 (2011).
[73] Y. C. Lu and Y. Shao-Horn, Journal of Physical Chemistry Letters 4:93 (2013).
[74] R. Black, J. H. Lee, B. Adams, C. A. Mims, and L. F. Nazar, Angewandte Chemie-International Edition 52:392 (2013).
[75] B. G. Kim, H. J. Kim, S. Back, K. W. Nam, Y. Jung, Y. K. Han, and J. W. Choi, Scientific Reports 4 (2014).
[76] A. Fick, Ann. Phys. 170:59 (1855).
[77] L. Moretto and K. Kalcher, Environmental Analysis by Electrochemical Sensors and Biosensors: Fundamentals, Springer-Verlag New York, New York, 2014.
[78] R. F. Probstein, Physicochemical Hydrodynamics: An Introduction, Butterworth, Stoneham, 1994.
[79] S. Srinivasan, Fuel Cells: From Fundamentals to Applications, Springer Science & Business Media, New York, 2006.
[80] W. Schmickler and E. Santos, Interfacial Electrochemistry, Springer-Verlag Berlin Heidelberg, Berlin, Heidelberg, 2010.
[81] J. Sanabria-Chinchilla, M. P. Soriaga, R. Bussar, and H. Baltruschat, Journal of Applied Electrochemistry 36:1253 (2006).
[82] L. P. Ford, P. Blowers, and R. I. Masel, Journal of Vacuum Science & Technology a-Vacuum Surfaces and Films 17:1705 (1999).

[83] S. A. C. Carabineiro and B. E. Nieuwenhuys, Gold Bulletin 42:288 (2009).
[84] Q. Guo, A. Paulheim, M. Sokolowski, H. Aldahhak, E. Rauls, and W. G. Schmidt, Journal of Physical Chemistry C 118:29911 (2014).
[85] L. A. Kibler, Preparation and Characterization of Noble Metals Single Crystal Electrodes, University of Ulm, 2003.
[86] A. B. Laursen, A. S. Varela, F. Dionigi, H. Fanchiu, C. Miller, O. L. Trinhammer, J. Rossmeisl, and S. Dahl, Journal of Chemical Education 89:1595 (2012).
[87] P. Marcus, Corrosion Mechanisms in Theory and Practice, Third Edition CRC Press, London, 2011.
[88] F. Ruette, Quantum Chemistry Approaches to Chemisorption and Heterogeneous Catalysis, Springer Netherlands, Caracas, 1992.
[89] B. Viswanathan, S. Sivasanker, and A. V. Ramaswamy, Catalysis: Principles and Applications, CRC Press, New Delhi, 2002.
[90] P. V. Kamath, D. D. Sarma, and C. N. R. Rao, Proceedings of the Indian Academy of Sciences-Chemical Sciences 93:335 (1984).
[91] W. Gibbs, On the Equilibrium of Heterogeneous Substances, Published by the Academy, New Haven, 1878.
[92] M. Volmer and A. Weber, Z. Phys. Chem. 119:277 (1926).
[93] W. Kossel, Nachr. Ges. Wiss. Göttingen, Math.-physik. Klasse:135 (1927).
[94] I. N. Stranski, Ann. Sofia Univ. 24:297 (1927).
[95] M. Avrami, J. Chem. Phys. 7:1103 (1939).
[96] W. K. Burton, N. Cabrera, and F. C. Frank, Phil. Trans. Roy. Soc. A. 243:299 (1951).
[97] R. Kaischew, Acta Phys. Acad. Sci. Hung. 8:75 (1957).
[98] F. Hilbert, C. Mayer, and W. J. Lorenz, J. Electroanal. Chem. 47:167 (1973).
[99] W. J. Lorenz and G. Staikov, Surface Science 335:32 (1995).
[100] E. B. Budevski, G. T. Staikov, and W. J. Lorenz, Electrochemical Phase Fomation and Growth: An Introduction to the Initial Stages of Metal Deposition, Wiley-VCH, Weinheim, 1996.
[101] M. Paunovic and M. Schlesinger, Fundamentals of Electrochemical Deposition, 2nd Edition, John Wiley & Sons, Inc.,, Hoboken, 2006.
[102] J. Gopalakrishnan, Bulletin of Materials Science 7:201 (1985).
[103] C. V. Ramana, U. Becker, V. Shutthanandan, and C. M. Julien, Geochemical Transactions 9 (2008).
[104] P. Novak and J. Desilvestro, Journal of the Electrochemical Society 140:140 (1993).
[105] E. Bauer and H. Poppa, Thin Solid Films 12:167 (1972).
[106] D. Elwell and H. J. Scheel, Crystal growth from high-temperature solutions, Academic Press London, 2011.

Chapter 2: Experimental setup and methodology

This chapter describes the experimental setups and methods used in the present work, which involves cyclic voltammetry (CV) technique, scanning probe microscopy (SPM) including scanning tunneling microscopy (STM) and atomic force microscopy (AFM), and rotating ring-disk electrode (RRDE) technique. In addition, the preparation works before an experiment such as cleaning experimental materials, the preparation of STM tip and single crystal surface, etc. are described in detail.

2.1 Cyclic voltammetry

Cyclic voltammetry (CV) is one of the most important and popular methods in the field of electrochemical analysis. It is used primarily for investigating the mechanism of electrochemical reactions and quantitative analysis. The reversibility of the reaction, the possibility of the intermediate formation, the properties of the interface adsorption and coupled chemical reactions, the kinetics parameters of electrode reaction, the mechanism of the reaction and its rate-determining step, etc. can be estimated according to the cyclic voltammogram. In 1938, Matheson and Nichols first successfully developed the cyclic voltammetry. Subsequently, Kemula and kubli improved it and employed it to study the electrode reaction process of organic compounds in 1958. Currently, it is widely used in electrochemistry, such as for research on electrochemical sensors, batteries, capacitors, corrosion, etc. It has been become the most basic method.

Cyclic voltammetry is carried out by a potentiostat. The working principle of cyclic voltammetry is applying a potential which circularly changes between a working electrode and a reference electrode, recording the correlation of the current through the working electrode and the counter electrode and the applied potential. The applied potential is rising (positive scan) and decreasing (negative scan) linearly versus time in cyclic phases between the known upper and lower potential limit to constitute a triangular potential wave, as shown in Fig. 2.1a.

The oxidation process ($R - ne^- \rightarrow Ox$) occurs during the positive scan, whereas the reduction process ($Ox + ne^- \rightarrow R$) occurs during the negative scan. It is well known that the electrode potential governs the reaction current and its rate. The data are plotted as the current versus the applied potential (so called cyclic voltammogram), which can

give the values of the redox potential, the electrochemical reaction rate and other parameters, as seen in Fig. 2.1b.

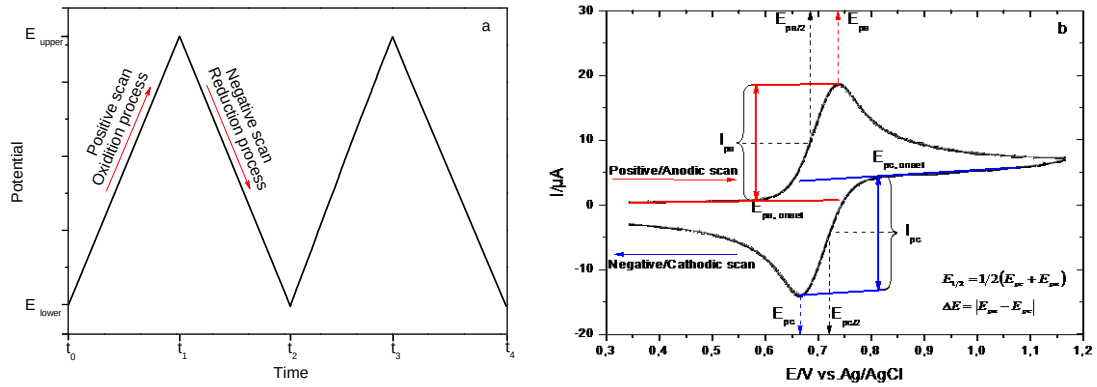

Fig. 2.1 Cyclic voltammetry triangular potential waveform (a) and typical cyclic voltammagram for a reversible reaction (b)

Cyclic voltammograms are usually characterized by the peak location (E_{pc}, E_{pa} and ΔE), the peak current ratio (I_{pc}/I_{pa}) and the dependence of peak currents on the scan rate (I_p vs. $v^{1/2}$). For a reversible reaction (reversible couples) process, it is characterized by: a) the potential difference between two peaks (ΔE) is determined to be 59 mV/n (n, the evolved electron number) which is independent of scan rate for fast electron transfer process; b) the peak current ratio should be 1; c) the peak current increases linearly with the square root of the scan rate, in addition, the diffusion coefficient can be determined by the slope of the linear relationship of I_p vs. $v^{1/2}$ obtained by using the Randles-Sevcik equation [1]. However, there are some deviations in the experimental data in practice, because the waveform of the peak in cyclic voltammagram of even reversible couples is complex due to the combined effects of polarization (the electron transfer rate/activation barrier for electron transfer) and mass transport. Specifically, at low overpotential, the shape of the polarization curve is mainly dominated by the activation polarization process, in which the electron transfer starts to occur across interfaces and the magnitude of the activation energy can be determined when the electrochemical reaction propagates at the rate under control of the electric current as described by Arrhenius equation [2]. A theoretical description on the dependence of the electric current on the overpotential is described by the famous Butler-Volmer equation [3, 4], as follow:

$$j = j_a - j_c = j_0\left(e^{\alpha_a zF\eta/RT} - e^{-\alpha_c zF\eta/RT}\right)$$

Where j, j_a, j_c and j_0 are the electrode current density, anodic current density, cathodic current density and exchange current density (A/m^2), respectively. α_a and α_c are the anodic and cathodic charge transfer coefficient (α_a=1-α_a), respectively. z is the number

of electrons transferred in the reaction, F is the Faraday constant, R is the universal gas constant and T is absolute temperature (K), η is the overpotential (E-Eeq, V).

As the potential is swept to high overpotential, the peak appears since the flux of the reactant to the electrode surface is not fast enough to meet that required by the flux of electron transfer. In this case, the current is dominated by the diffusion rate and it begins to decrease as predicted by the Cottrell equation [5], as follow:

$$i = \frac{zFAD^{1/2}C_{x=\infty}}{\sqrt{\Pi t}}$$

Where i is the current, $C_{x=\infty}$ is the initial concentration of the electroactive species, D is the diffusion coefficient for the species, and other symbols have the same meaning as described before.

Certainly, the electrochemical reaction is complicate and some other effect factors such as some other surface reactions, solvent, containminations, etc. can not be eliminated in experimental investigation. Therefore, it shows that many redox processes are also quasi-reversible and non-reversible in the cyclic voltammogram.

2.2 Rotating ring disk electrode (RRDE)

The rotating ring disk electrode (RRDE) is the technique, which can be used not only to investigate the mechanism and kinetics of the reaction similar to the rotating disk electrode (RDE), but also to detect the intermediates formation during the reaction.

2.2.1 RRDE tip

RRDE tip consists of a disk electrode and a ring electrode surrounding the disk electrode. These two electrodes are separated by an inert Teflon U-cup for keeping them electrically isolated and encased in a cylindrical insulating shroud (non-conducting, solvent-resistant, etc.) which is typically made by Teflon, PEEK or KEL-F, and can be rotated at different frequencies ω (see. Fig. 2.2). The surfaces of the disk, U-cup, ring and shroud are all ideally polished and coplanar.

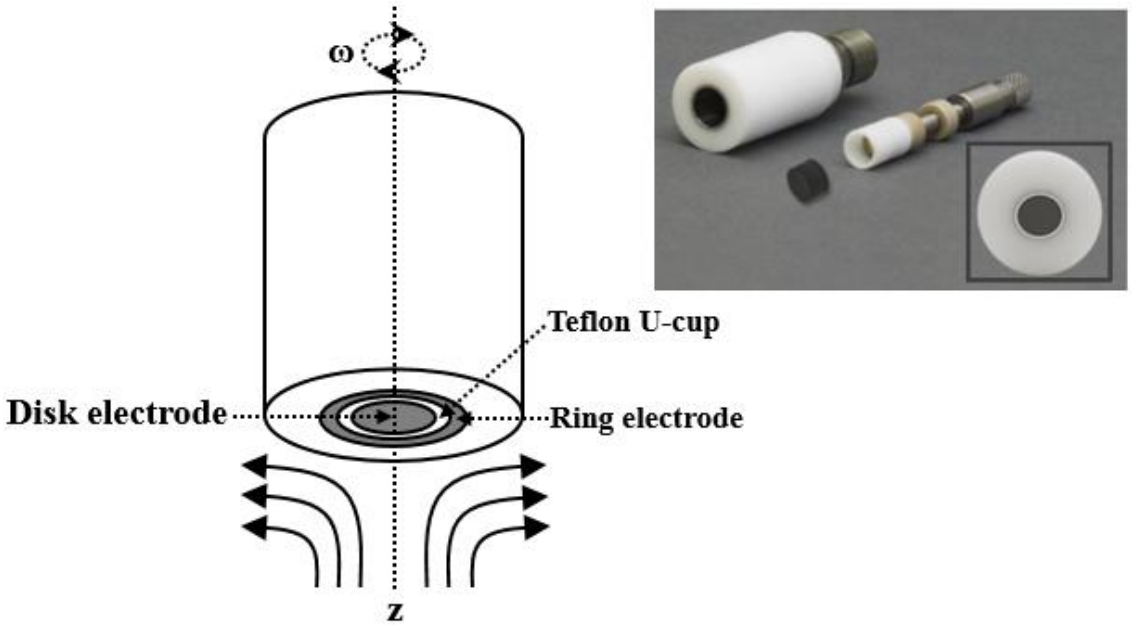

Fig. 2.2 Rotating ring-disk electrode

2.2.2 Surface coating and modification of disk electrode

In the research field of ORR/OER catalysts, coating is the most common way to immobilize the catalysts on the electrode surface, which uses Nafion as binder to stick the catalyst particles to the disk electrode. In order to ensure the accurate quantization and good dispersion of catalysts on the electrode surface, a suspension of catalysts is prepared quantitatively in a suitable solvent, and then a portion of this suspension is transferred exactly by a micropipette and drop coated on the disk electrode surface. The solvent can be easily evaporated. Afterwards, the Nafion solution (5%, by mass, in the mixture of water and ethanol) is employed to bind the catalyst layer on the electrode surface. The quantitative preparation of the suspension of catalysts is through a known amount of catalyst dispersed in a known volume of solvent in a common small disposable vial. Because of the insolubility of the catalysts in most solvents, ultrasonication is required to ensure that the catalysts are uniformly dispersed in the solvent before transfer to the electrode surface. To accelerate the drying process, the electrode can also be placed in an oven.

In addition, electrochemical modification of the electrode could be also a way to develop the catalysts with higher activity. In our work, we used the electrochemical deposition of foreign metal on a metal electrode to prepare the bimetallic catalyst for ORR and OER. The electrochemical deposition could be easily done by applying a

potential where the foreign metal deposition occurs in a suitable solution similar to the chronoamperometry. The amount of the deposits can be controlled by the deposition time and it can be calculated by the charge, which could be calculated by integrating the current-time (i-t) curve. However, in this case if the electron transfer is faster, the change in the current with respect to time should follow the Cottrell equation. Furthermore, the advantages of this method are that there is no catalysts loss and no Nafion effect during the measurements.

2.2.3 Forced convection

As mentioned in chapter 1, the forced convection could eliminate the effects from the random aspect generated by the natural convection, making better understanding of the property of electrolyte and mechanism of the surface reaction, so it is widely used in the research field of ORR. The diffusion/mass transport property of electroactive species towards to electrode surface also determines the cyclic voltammetry. Theoretically, the relationship between diffusion flux and concentration and distance is described in Fick's first law of diffusion.

However, once the convection is applied by a rotating disk system, the diffusion limiting current can be evaluated by Levich equation.

$$i_{\lim} = 0.62 \cdot zFAD^{2/3}\nu^{-1/6}\omega^{1/2}C_{x=\infty}$$

Where ν is the sweep rate, ω is the angular rotation rate, and other symbols have the same meaning as described before.

As illustrated in Fig. 2.3, the reaction rate is controlled by the rate of electron transfer and mass transfer in the lower and higher overpotential, respectively. In the case of the existing of convection, a limiting current plateau instead of a peak (without convection) appears in the diffusion-controlled region.

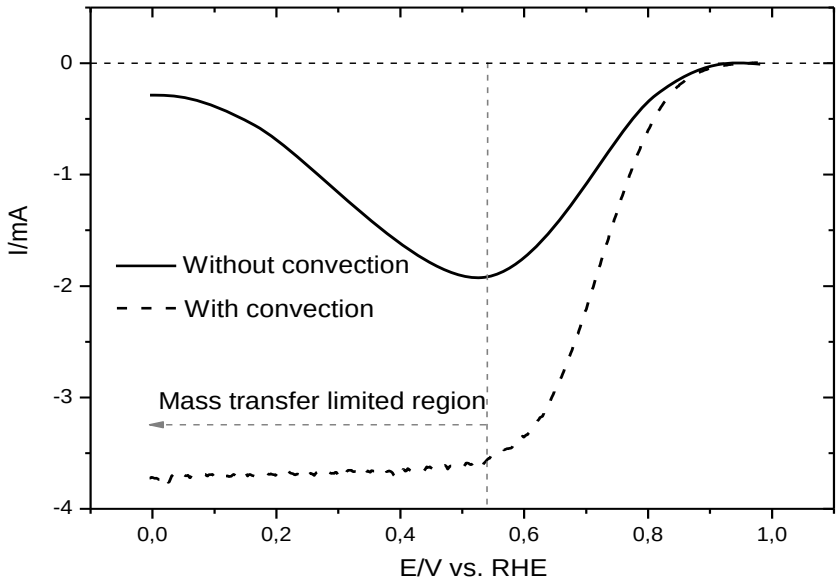

Fig. 2.3 Typical ORR cyclic voltammagrams under condition of forced convection (dash curve) or convection free (solid curve)

2.2.4 Collection efficiency

In an RRDE measurement, not all the intermediates/products generated at the disk electrode can be collected/detected at the ring electrode. The percentage of intermediates which are collected at the ring electrode is called the collection efficiency (N). For a specific RRDE, the collection efficiency can be directly calculated in terms of the disk radius (r_1) and the inner (r_2) and outer (r_3) radii of the ring [6], as follow:

$$N = 1 - G\left(\frac{\alpha}{\beta}\right) + \beta^{2/3}\left[1 - G(\alpha)\right] - \gamma^{2/3} + \gamma^{2/3} G\left(\frac{\alpha\gamma}{\beta}\right)$$

where

$$\alpha = \left(\frac{r_2}{r_1}\right)^3 - 1 \text{ and } \beta = \left(\frac{r_3}{r_1}\right)^3 - \left(\frac{r_2}{r_1}\right)^3 \text{ and } \gamma = 1 + \alpha + \beta$$

and the function G is defined as

$$G(x) = \frac{\sqrt{3}}{4\pi} \ln\left[\frac{\left(x^{1/3} + 1\right)^3}{x + 1}\right] + \frac{3}{2\pi} \tan^{-1}\left(\frac{2x^{1/3} - 1}{\sqrt{3}}\right) + \frac{1}{4}$$

where, x is a function of α, β and γ.

However, the best way to determine the collection efficiency by an empirically measurement in a well-behaved electrochemical system such as the ferricyanide-ferrocyanide redox couple, before employing it for any quantitative work. It is typically

in the range of 20% to 30% and can be determined by the following equation,

$$N = -\frac{n \cdot i_R}{m \cdot i_D}$$

Where i_D and i_R is the disk electrode current and ring electrode current, respectively, and n and m is the electron transfer number involved at disk electrode and ring electrode, respectively.

When both electron numbers involved at disk and ring electrodes are one, the equation can be simplified as [7]

$$N = -\frac{i_R}{i_D}$$

In addition, the collection efficiency can be also determined by measuring the difference of the two ring currents, i_R (E_R=E_D) and i_R (E_R, E_D open), which are obtained in the case of E_R=E_D (both disk and ring potentials are scanning) and absence of disk electrode (only the ring potential is scanning and the disk electrode is disconnected), respectively, by using the equation as follow:

$$N = \frac{i_R(E_R = E_D) - i_R(E_R, E_D open)}{i_D}$$

The ratio of the i_R (E_R=E_D) to i_R (E_R, E_D open) is defined as shielding constant (S),

$$S = \frac{i_R(E_R = E_D)}{i_R(E_R, E_D open)}$$

And theoretically, the relationship between the collection efficiency and shielding constant is given by the equation

$$S = 1 - \frac{N}{b^{2/3}} \text{ with } b = (\frac{r_3}{r_1})^3 - (\frac{r_2}{r_1})^3$$

Where r_1, r_2, r_3 are the disk radius, inner radius of the ring and the outer radius of the ring, respectively.

2.2.5 Detection of peroxide and electron transfer number

In aqueous electrolyte, oxygen molecules can be reduced at the disk electrode via four-electron transfer to produce H_2O and OH^- or via two-electron transfer to produce H_2O_2 and HO_2^- in acidic solution and alkaline solution, respectively. It is well known that H_2O_2 and HO_2^- can be oxidized sufficiently at +1.2 V (vs. RHE) to H_2O and OH^- respectively, so the potential of ring electrode is fixed at +1.2 V for capturing them.

Considering not all oxygen molecules can be reduced at the disk electrode via four-electron transfer, in other words, some part (or few part) of oxygen molecules are reduced via two-electron transfer, so the current flowing at disk electrode (i_D) is the sum of the current of oxygen reduction via four-electron transfer to H_2O/OH^- ($i_{O_2(4e^-)}$) and the current of oxygen reduction to H_2O_2/HO_2^- ($i_{O_2(2e^-)}$).

$$i_D = i_{O_2(4e^-)} + i_{O_2(2e^-)}$$

The current at the ring electrode (i_R) can be defined by using the collection efficiency (N) as following:

$$i_R = N \cdot i_{O_2(2e^-)}$$

The fraction of H_2O_2/HO_2^- formation ($X_{H_2O_2/HO_2^-}$) can be determined by the molar flux rates of oxygen ($\dot{n}_{O_2(4e^-)}$) and H_2O_2/HO_2^- ($\dot{n}_{O_2(2e^-)}$) according to the following equations:

$$\dot{n}_{O_2(4e^-)} = i_{O_2(4e^-)} / 4F \text{ and } \dot{n}_{O_2(2e^-)} = i_{O_2(2e^-)} / 2F$$

$$X_{H_2O_2/HO_2^-} = \frac{\dot{n}_{O_2(2e^-)}}{\dot{n}_{O_2(4e^-)} + \dot{n}_{O_2(2e^-)}} = \frac{2i_R}{Ni_D + i_R}$$

and the number of electron transfer (n) can be determined by

$$n = \frac{4i_D}{i_D + i_R / N}$$

For metal-air batteries it is considered that the smaller the fraction of peroxide formation is, the better is the performance of the battery, meaning that four-electron transfer process is preferred: a smaller number of electrons transferred would reduce the current efficiency and the formed intermediate H_2O_2/HO_2^- may lead to side reactions, damaging the components and shortening the life time of the battery.

2.2.6 Determination of kinetic parameters of ORR by RRDE

For an electrochemical reaction, the current flowing at the electrode can be obtained by

$$i = zFDA\frac{(c_0 - c_S)}{\delta_N}$$

In the case of RRDE (Nernst diffusion layer thickness, $\delta_N = 1.61D^{-1/3}\nu^{1/6}\omega^{-1/2}$), the current flowing at disk electrode can be obtained by

$$i_D = 0.62zFD^{2/3}\nu^{-1/6}\pi r_1^2\omega^{1/2}(c_0 - c_S)$$

As described before, when the concentration of the reactants at the electrode surface has not yet dropped to zero, the reaction rate is determined by both the mass transport and kinetics. In the case of neglecting the reverse reaction, the measured current (i) can be determined by the kinetic current (i_K) and diffusion current ($i_{Diff.}$) as described by the following equation:

$$\frac{1}{i} = \frac{1}{zFAk_f C_0} + \frac{1}{0.62 \cdot zFAC_0 D_0^{2/3} \nu^{-1/6} \omega^{1/2}} = \frac{1}{i_K} + \frac{1}{i_{Diff.}}$$

When we plot i^{-1} vs. $\omega^{-1/2}$ so called Koutecky-Levich plot, the constant of reaction rate (k_f) can be obtained by the intercept and the diffusion constant (D_0) can be obtained by the slope.

For Tafel plot (η vs. $\lg i_K$), i_K can be also obtained by the intercept of Koutecky-Levich plot and also by the following equation.

$$i_k = \frac{i}{1 - \frac{i}{i_{\lim}}} = \frac{i \cdot i_{\lim}}{i_{\lim} - i}$$

Where i_{lim} is the diffusion limiting current.

2.3 Determination of electrochemically active surface area

Adsorption is the most widely used approach to determine the electrochemically active surface area. Hydrogen and carbon monoxide (CO) adsorption can be used for determining the Pt surface area. However, for metals onto which there cannot adsorb, the adsorption of anions such as iodide adsorption, sulfate adsorption, etc. or cations (underpotential deposition) can also be used for determining the active surface area. In these methods the amount of adsorbate is usually determined by the amount of charge transfer during the adsorption and it is related to the corresponding active surface area. In this work, we employed the underpotential deposition of Pb to determine the ratio of Ag active surface area exposed to the electrolyte. It was carried out in argon saturated 0.1 M LiOH + 125 µM $Pb(NO_3)_2$ electrolyte by holding potential at 0.23 V versus RHE for 5 min and then sweeping in the UPD potential range. The Pb stripping charge was used for calculating the Ag active surface area exposed to the electrolyte by assuming a one to one ratio of Pb to Ag atoms.

2.4 Experimental materials and cleaning

2.4.1 Chemicals

All the chemicals and gases used in this work are summarized and listed in the table 2.1. All aqueous solutions were prepared with Milli-Q water (18.2 MΩ cm, TOC of 5 ppm, MILLIPORE, Schwalbach, Germany) and all nonaqueous solutions were prepared in a MBraun glovebox filled with Ar (H_2O < 5 ppm and O_2 < 5 ppm). The water content was determined by a coulometric Karl-Fischer titrator (C20, Metler Toledo), and then de-aerated with analytical grade argon (Ar) and oxygen (O_2) for investigating ORR.

Table 2-1: List of chemicals and gases.

Name	Formula	Company	Purity (degree)
Ethylene glycol	$(CH_2OH)_2$	KMF laborchemie	99.5%
Cobalt(II) chloride	$CoCl_2$	Merck	98%
Lead(II) nitrate	$Pb(NO_3)_2$	Aldrich-Chemie	98%
Boric acid	$B(OH)_3$	Sigma	99%
Potassium sulfate	K_2SO_4	Grüssing	99%
Silver oxide	Ag_2O	Aldrich	99.99%
Lead(II) perchlorate	$Pb(ClO_4)_2$	Santa Cruz	98%
Silver perchlorate	$AgClO_4$	Chempur	99%
Lithium perchlorate	$LiClO_4$	Alfa Aesar	95%
Lithium perchlorate	$LiClO_4$	Sigma-Aldrich	Battery grade
Tetraglyme	$C_{10}H_{22}O_5$	Acros organics	99%
Acetonitrile	CH_3CN	Acros organics	99.9%
Tetrahydrofuran	C_4H_8O	Sigma-Aldrich	≥ 99.9%
Acetone	C_3H_6O	Sigma-Aldrich	99.5%
Dimethyl sulfoxide	C_2H_6OS	Acros Organics	99.7%
Antimony(III) oxide	Sb_2O_3	Aldrich	99.999%
Magnesium chloride	$MgCl_2$	Sigma	98%
Aluminium chloride	$AlCl_3$	Fluka	99%
Sulphuric acid	H_2SO_4	Merck	95-97%, Suprapure
Oxygen	O_2	Air Liquide	99.999%
Argon	Ar	Air Liquide	99.999%
Lithium hydroxide monohydrate	$LiOH·H_2O$	Sigma-Aldrich	99%
Cobalt(II) sulfate	$CoSO_4·7H_2O$	Riedel-de Haën	99%

hexahydrate			
Copper(II) perchlorate	$Cu(ClO_4)_2$	Acros organics	99.8%
Propylene Carbonate	$C_4H_6O_3$	Sigma-Aldrich	99.7%
Magnesium perchlorate	$Mg(ClO_4)_2$	Sigma-Aldrich	≥ 99%
Potassium hydroxide	KOH	Sigma Aldrich	85%
Spinel cobalt oxide nanoparticles (< 50nm)	Co_3O_4	Sigma-Aldrich	99.5%

2.4.2 Electrochemical cells

Conventional electrochemical glass cell 'H-cell'

A conventional electrochemical glass cell, also called 'H-cell', was designed and used for electrochemical cleaning, preparation and electrochemical modification of single crystal electrode under controlled atmosphere in this work. The schematic representation of a typical glass H-cell is shown in Fig. 2.4. It contains three compartments, which are used for placing working electrode, reference electrode and counter electrode, respectively. The working electrode is placed in the central compartment and contacted with solution in a hanging meniscus configuration. The central compartment also contains some inlets and outlets for solution and gas. The reference electrode is placed in the compartment (left compartment), where is connected to the central compartment with a Luggin capillary. The role of the Luggin capillary and the stop cock is to minimize the ohmic losses and restrict the diffusion of metal ions from the central compartment to the left compartment, respectively. The counter electrode is placed in the compartment (right compartment), where it is separated from the central compartment by a glass frit, preventing any byproducts produced at the counter electrode from contaminating the working solution in the central compartment. The counter electrode we used in this work is Pt sheet (as shown in Fig. 2.4) or Au wire.

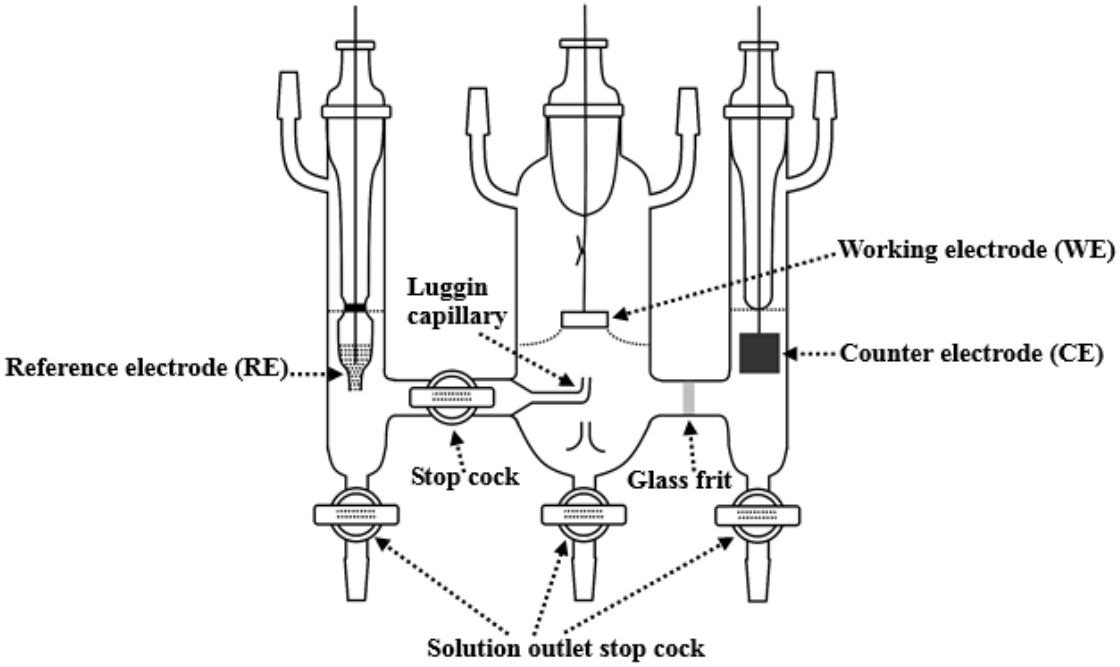

Fig. 2.4 Schematic representation of an H-cell for the electrochemical experiments.

STM/AFM cell

STM/AFM cell (see. Fig. 2.5), a special three-electrode cell was designed and made for EC-STM/AFM measurements. It was made by Kel-F material which is chemically inert to most strong acids, alkalis and organic solvent. A main chamber was made for containing electrolyte solution. The contact of working electrode and electrolyte was through a hole with the diameter of 0.8/0.6 mm made at the bottom of the main chamber. An additional small chamber was made for placing the reference electrode, which can be connected to the main chamber via a small hole. This can avoid the diffusion of metal ion from the main chamber to reference electrode chamber during the metal deposition. The counter electrode was placed around the inner main chamber. Two small through-holes at both sides of the cell were made for clamping the cell and electrode on the sample plate tightly.

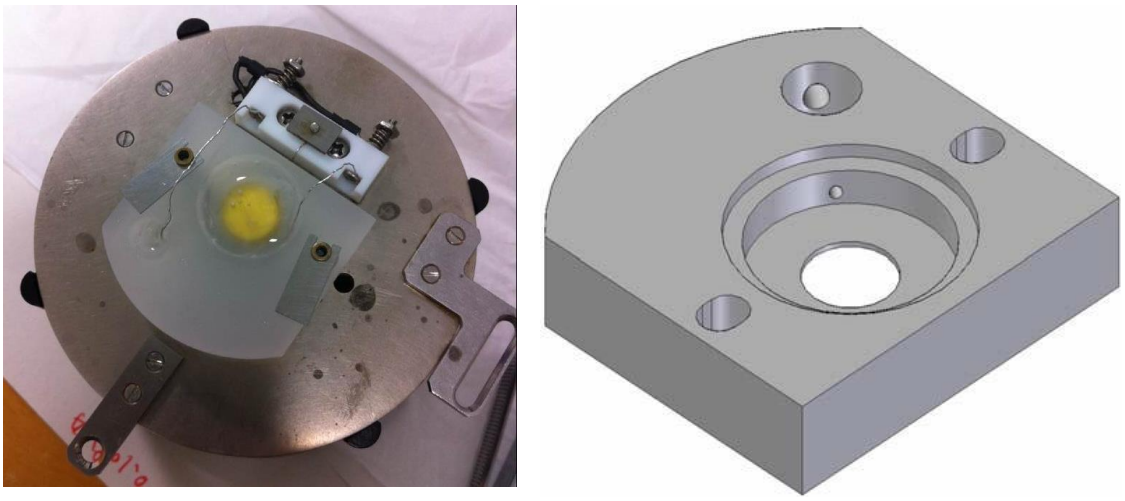

Fig. 2.5 Actual photo STM/AFM cell (left) and schematic view of STM/AFM cell (right).

2.4.3 Three-electrode setup

Three-electrode setup, it is an electrochemical setup consisting of working electrode, reference electrode and counter electrode.

Working electrodes

The working electrodes used in this work are summarized and listed in the table 2.2. The electrodes with a diameter of 0.5 cm were used for RRDE measurement and with a diameter of 1 cm were used for EC-STM/AFM measurement.

Table 2-2: List of disk working electrodes.

Crystal type	Company	Diameter
Glassy carbon	Pine	0.5 cm
Ag(pc)	Pine	0.5 cm
Pt(pc)	Pine	0.5 cm
Pt(111)	MaTeck	1 cm
Au(111)	MaTeck	1 cm
Au(pc)	MaTeck	1 cm

Counter electrodes

In glass H cell, the platinum foil (~1×1 cm) and the gold wire were employed as the counter electrode in the case of Pt working electrode and Au working electrode, respectively. However, the corresponding metal wire was used as the counter electrode

in each case in STM cell.

Reference electrodes

Reversible hydrogen electrode (RHE)

A home-made reversible hydrogen electrode (RHE) based on Will's design [8] was employed in electrochemical glass cell in this work. The schematic representation of RHE is shown in Fig. 2.6. The RHE contains two portions, upper portion and lower portion separated by a seal. The upper portion consists of a glass holder and a Cu wire and the lower portion consists of a glass bulb and Pt wire (inside of the glass bulb). The Pt wire was connected to the Cu wire through the seal. It also briefly illustrates the preparation process of a RHE in Fig. 2.6. Initially, the RHE was rinsed with Milli-Q water and then fully-filled with the supporting electrolyte (0.1 M H_2SO_4) by a vacuum suction system. Then a potential difference of 1.6 V between the Cu wire and Pt wire was applied by a power supply to electrolysis water to produce hydrogen (H_2) and oxygen (O_2), which was collected in the glass bulb and released from the gas outlet to atmosphere, respectively. Finally, the applied potential was disconnected once the collected hydrogen covered about half of the Pt wire.

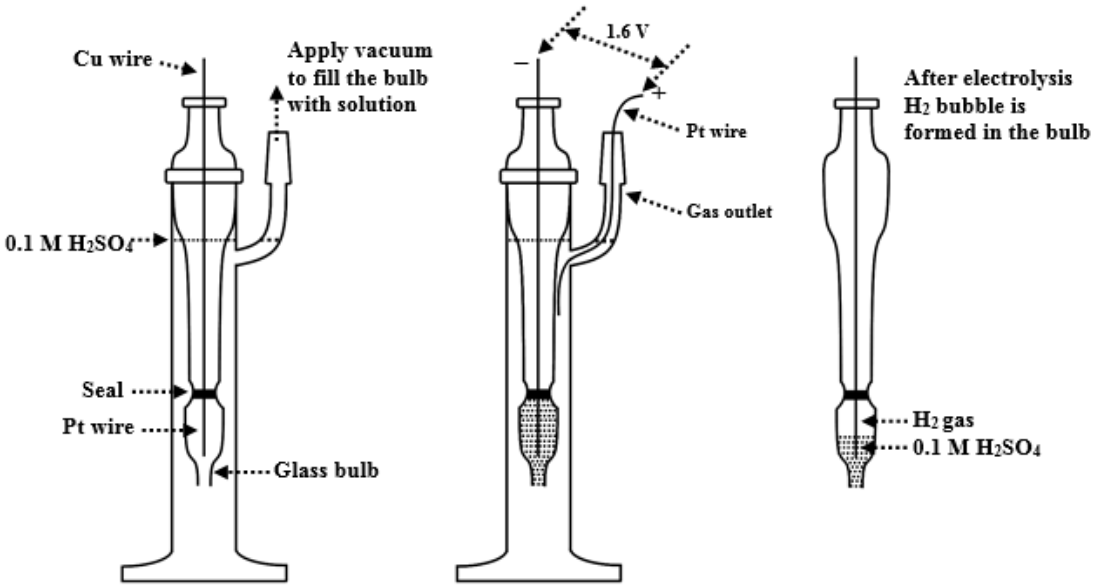

Fig. 2.6 Schematic representation of the reversible hydrogen electrode and its preparation process.

Pt/PtO quasi reversible electrode

The Pt wire was first thoroughly cleaned in the concentrated sulphuric acid (H_2SO_4) solution. Afterwards, it was cleaned by immersing it in boiling dilute sulfuric acid

solution followed by boiling Milli-Q water before each measurement. The well-cleaned Pt wire was employed as the quasi-reference electrode in EC-STM/AFM measurement.

2.4.4 Cleaning of labware

Cleaning labwares before and after each experiment is very essential. Glass and plastic labwares were cleaned manually. In this work, a well prepared chromic acid bath consisting of 21.4 g CrO_3, 640 ml of concentrated H_2SO_4 and 360 ml H_2O was used for laboratory glasswares to remove organics and metal contaminants. All laboratory glasswares were soaked in chromic acid bath all night. The dichromate has to be handled with extreme caution because it is a powerful corrosive, toxicant and carcinogen. Instead of chromic acid bath, an alternative chemical free water steam system was also used for cleaning. Similarly, to remove the residues anions and organic contaminations from the cleaned glasswares by chromic acid bath and the plastic labwares (such as plastic stopcock, taper joint stopper, etc.), the concentrated potassium hydroxide (5 M KOH) bath was prepared and used. Afterward, all the cleaned labwares were rinsed with Milli-Q water.

2.4.5 Cleaning and preparation of single crystal electrodes

The impurities may be introduced into the electrode after each experiment, so the electrode, especially a single crystal electrode, should be cleaned as soon as possible after use. Normally, the used electrode was cleaned electrochemically in the supporting electrolyte (0.1/0.5 M perchloric/sulfuric acid) under potential control, because most of the active metals can be dissolved in this case. However, for those impurities which are hard to be removed, the chemical treatment should be considered.

Chemical treatment

The single crystal electrode was exposed to a cleaning sequence containing a concentrated nitric acid (HNO_3) prior to an ammonia hydrogen peroxide mixture (NH_3/H_2O_2, 1:1) solution for 5 min to remove the most active metal impurities. In addition, hydrofluoric acid (HF) was used to remove the silica impurities because of its strong ability to dissolve almost all of the oxides and silicates. The reactions of HF with SiO_2 are shown as following:

$$SiO_{2(s)} + 4HF_{(aq)} = SiF_{4(g)} + 2H_2O_{(l)} \text{ or } SiO_{2(s)} + 6HF_{(aq)} = H_2SiF_{6(l)} + 2H_2O_{(l)}$$

However, it is also one of the most dangerous acids known, so it needs to be much more

careful when people work on it. After each chemical treatment, the electrode was rinsed with Milli-Q water, following by the electrochemical cleaning as described before and annealing. Sometime, it needs to repeat this cleaning process several times to get rid of all the impurities from the single crystal electrode. The cleanliness of the single crystal surface can be reflected by cyclic voltammetry.

Preparation of single crystal surface

The preparation method we employed is flame annealing method as described by Clavilier [9]. The well-cleaned single crystal electrodes in Ar saturated 0.1 M H_2SO_4 were rinsed with Milli-Q water and then annealed by a butane flame carefully. The crystal electrodes were kept in the flame while cherry red-hot for 60 s. Then the crystal electrodes were rapidly transferred into a glass cell, which was only filled with Milli-Q water saturated by Ar or Ar/H_2 mixture, for around 5 min cooling at room temperature [10].

The Au electrode has to be prepared with extreme care because its melting point is lower. The annealing process should be different from that of high-melting point metals. Consequently, in order to control the temperature at the suitable low temperature carefully (keep it light pink and do not heat it cherry red), an intermittent heating process sustained over long periods of time (~4 min) was used for preparing Au single crystal surface. The cooling process is the same as described before.

Afterwards, the electrode was transferred to the glass H-cell containing the supporting electrolyte deaerated with argon to identify qualitatively the quality of preparation under the protection of deaerated water on the top. It was kept in touch with the electrolyte in a hanging meniscus configuration (see. Fig. 2.4) and the quality of the prepared single crystal electrode surface was identified by comparing the observed CV to its characteristic CV. Notice that the potential range is from 0.05 to 1.2 V (vs. RHE) for Au(111) electrode and from 0.05 to 0.85/0.9 V (vs. RHE) for Pt(111) electrode and the potential should not exceed the upper limiting potential because the surface will be oxidized and roughed at more positive potential. Finally, the well-prepared single crystal electrode was transferred quickly to the destination (in glass H-cell or STM cell filled with working electrolyte). The electrode surface was protected by a droplet of the water or electrolyte during all the transportation processes and all the solutions were

deaerated.

However, if the electrode was prepared for working on non-aqueous electrolyte, the slightly longer cooling process was carried out in a very dry and clean glass cell fully filled with Ar. The electrode was protected under argon atmosphere during the transportation process. In this case, the quality of the prepared crystal surface was identified by the microscope with atomic level resolution such as STM and AFM.

The cyclic voltammograms of Pt(111) and Au(111) in 0.1 M H_2SO_4 electrolyte being obtained in our case are shown in Fig. 2.7. For the CV of Pt(111), some peaks appeared in the hydrogen adsorption region are due to the unavoidable defect of the single crystal itself, which was introduced over time. The better characteristic CVs of noble metal single crystals are available in the booklet [11].

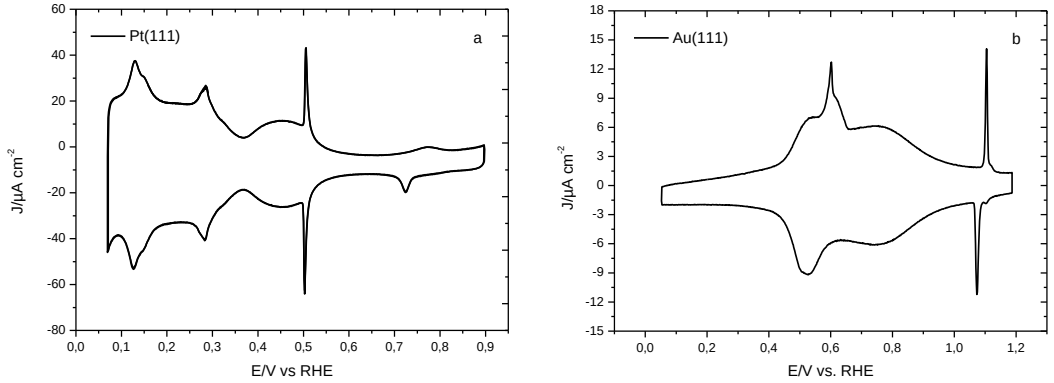

Fig. 2.7 Cyclic voltammograms of Pt(111) (a) and Au(111) (b) in argon saturated 0.1 M H_2SO_4 solution at 50 mV s^{-1} in H-cell.

2.5 Scanning tunneling microscope (STM)

Scanning tunneling microscope (STM) is a type of microscope, of which the working principle is based on the quantum mechanical effects, so called quantum tunneling (or tunneling) [12], in which the electrons could escape from the solid surface into free space through the "tunnel" based on its wave and particle-like properties in quantum mechanics. By applying a bias voltage between two materials which are very close to each other, the tunneling current can be generated and it decreases exponentially with the increase in the distance between them. The first STM was created by Gerd Binnig and Heinrich Rohrer in 1981 at IBM in Zürich [13]. It is the most powerful technique to observe the material surface at the atomic level.

2.5.1 STM working principle

In STM, when the distance between tip and sample is small enough and a small bias voltage (E_{sample} - E_{tip}) is applied between tip and sample, the electrons can tunnel through the vacuum barrier from the tip into the sample (or vice versa), generating the tunneling current. The quantum tunneling through a barrier between tip and sample is depicted schematically in Fig. 2.8. It explains the mechanism of the tunneling process based on quantum mechanical principles.

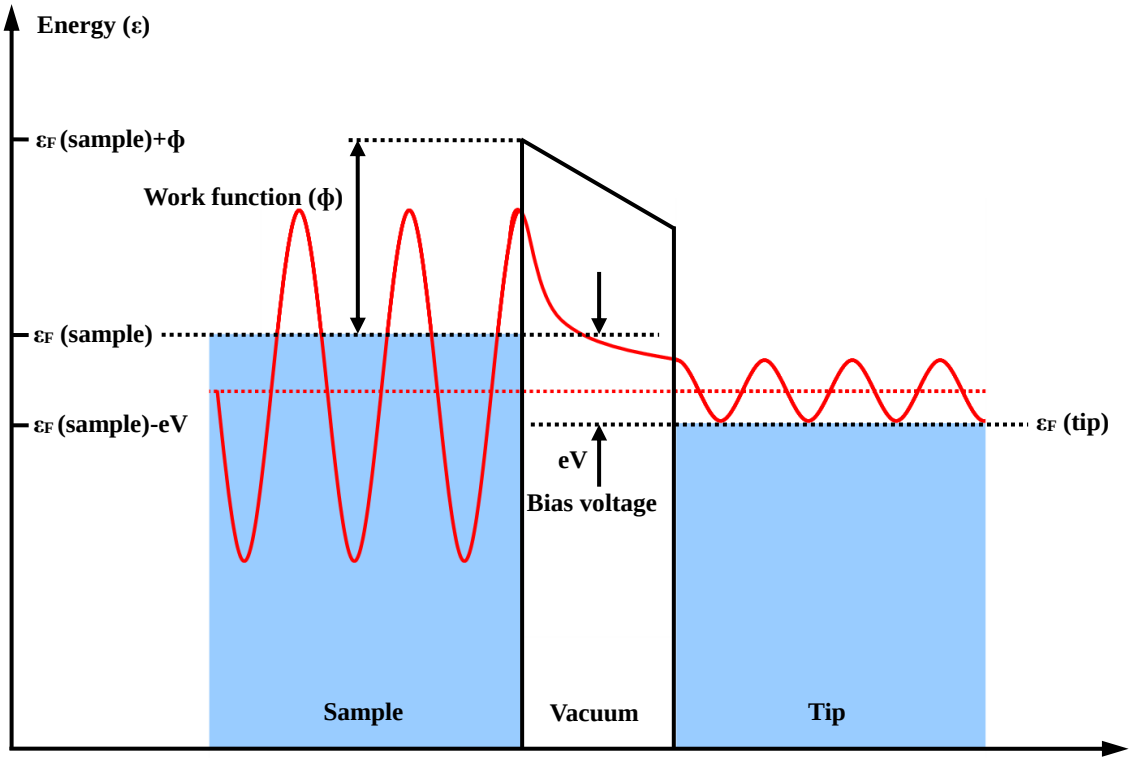

Fig. 2.8 Schematic energy diagram of quantum tunneling through a barrier between tip and sample.

It is found that the tunneling current forms when the overlap of electron wavefunctions at the tip and sample is large enough as the result of that the tip is very close to the sample (only a few angstroms, Å) and a voltage difference or called bias voltage (typically in the range of 0.05-0.20 V) is applied between the tip and sample. The tunneling current depends on the distance between the tip and sample (d), on the bias voltage (V), and on the work function (Φ):

$$I_t = I_0 \cdot e^{(-2k_t d)} \quad (k_t = \frac{\sqrt{2m\Phi}}{\hbar})$$

Where I_0 is the function of the bias voltage and density of states in both tip and sample, **m** is the mass of the electron and ħ is the Planck's constant [14]. When the bias voltage

becomes larger, the effective barrier height Φ-e**V** will become smaller, meaning that the possibility of electron transfer is higher so that the tunneling current become larger. In addition, the tunneling current is strongly/exponentially dependent on the distance d, that it is exactly the distance between the nearest two atoms on the tip and sample, respectively. For metals, the typical value of work function of ~4 eV leads to the k_t value of ~1 $Å^{-1}$, indicating that the tunneling current increases by an order of magnitude for every one angstrom decrease in d value. This means that when the tip is scanned over a typical atomic height of ~3 Å, the tunneling current changes by three orders of magnitude (by a factor of 1000). This supports the STM so sensitive that it can enable people to observe the material surface with high resolution, 0.1 nm lateral resolution and 0.01 nm depth resolution.

2.5.2 STM setup

A STM setup contains five basic components, a sharp metal tip, piezoelectric scanner, tunneling current amplifier, bipotentiostat (bias) and a feedback loop (current), as shown schematically in Fig. 2.9.

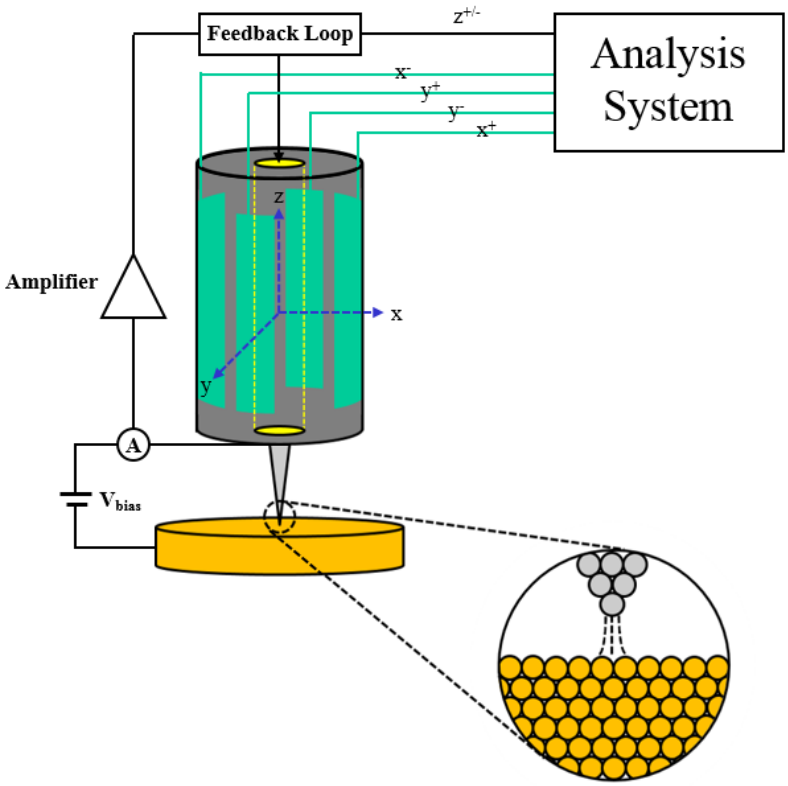

Fig. 2.9 Schematic representation of STM setup

In the STM the sample is scanned by a well prepared metallic tip. The surface

morphology can be imaged in three-dimensional by a piezoelectric scanner. The tip can image the sample surface in either constant current or constant height mode, as shown in Fig. 2.10. It is determined by a feedback loop, which is generally based on a constant current.

2.5.3 STM operation modes

In the constant current mode, the STM tip maintains a constant tunneling current (at the setpoint value) by a feedback controller to adjust the height with a piezoelectric crystal. The height of the tip follows a contour of a constant local density of electronic states and maps the surface topography. Specifically, if the tip is scanned over up or down a step while the tunneling current exceeds or falls below the preset value suddenly, the corresponding feedback increases or decreases the distance in order to keep the tunneling current constant. Normally, this mode is used to image the relative uneven/rough surface.

In the constant height mode, the feedback is very slow and the tip is kept at constant height so that the tunneling current varies during the tip scanning over the sample surface. The tunneling current at each location is recorded to constitute the image. Because the feedback response requires time, the scan rate in the constant height mode is typically faster than in the constant current mode in order to avoid an unnecessary height adjustment of the tip. This mode is usually used to probe the relative smooth and flat surfaces and able to get the images of the atom arrangement.

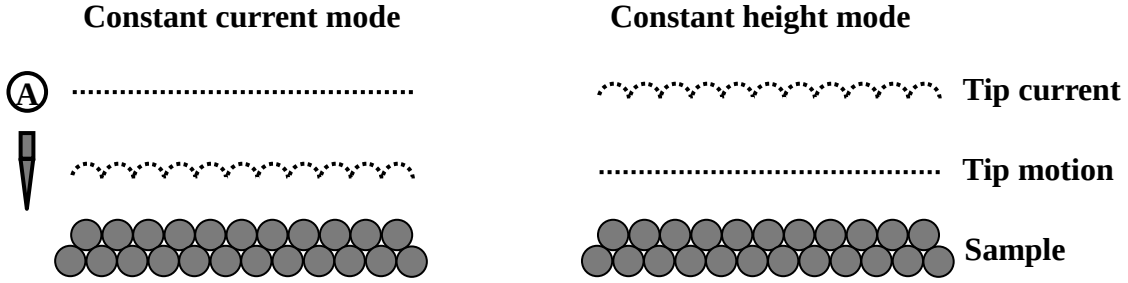

Fig. 2.10 Probing at constant current (left) and constant height (right).

It is worth to point out that the STM image is related to tunneling current, and reflects directly the electronic density of states rather than the nuclear position of surface atoms. Therefore, one of the significant limitations of STM is that both the tip and sample have to be conductive or semi-conductive. To solve this limitation of STM, atomic force microscopy (AFM) was invented, developed and widely used.

2.5.4 STM tip preparation and isolation

All STM tips were prepared by electrochemical etching [15] of Pt/Ir (90:10) wire with a diameter of 0.25 mm in 2 M KOH + 4 M KSCN solution, and further coated with hot-melt glue containing different types of polymer (provided by Steinel Vertrieb GmbH in Herzebrock-Clarholz) to minimize the Faradic current. The electrochemical etching process was carried out by a two electrodes system, consisting of a small well cleaned beaker as a cell, an annular Pt wire as anode and Pt/Ir (90:10) wire as cathode to prepare the tips, as shown in Fig. 2.11. Before inserting the Pt/Ir wire into etching solution, the lower part of it was covered with a Teflon tube in order to better control the wire is in contact with solution in a hanging meniscus configuration (see. Fig. 2.11). Then, a DC signal of 1.5V with a superimposed AC square wave signal of 6.5 V at 1 kHz was applied between two electrodes for electrochemical etching of the wire. The etching occurs around the meniscus to yield an atomically sharp tip. After etching, the lower part of the wire with the Teflon tube would fall into the solution as a discard and the sharp tip would be prepared and remained on the wire, cutting it down with the length of 10-15 mm, rinsing with Milli-Q water and then drying it for following isolation.

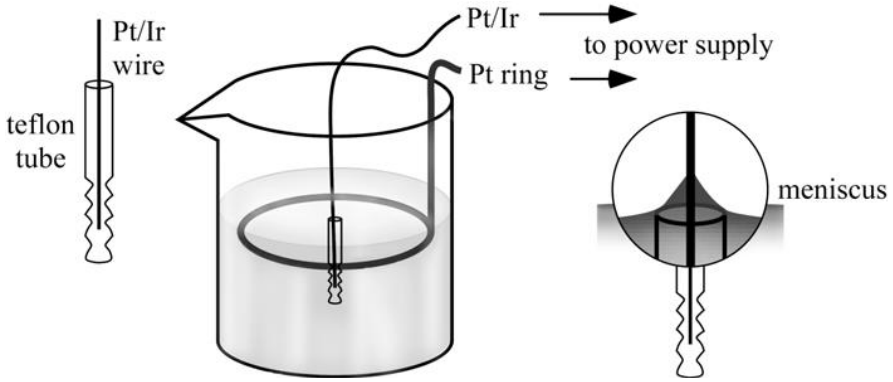

Fig. 2.11 Schematic representation of two electrodes system for preparing the tips [16].

In order to avoid the Faradic current flowing through the tip during the EC-STM measurements, the part of the tip which will be inserted in the working electrolyte except the foremost part of the tip which will be connected to the scanner has to be coated by a chemically inert material such as hot-melt glue containing different types of polymer. The simplest way we employed is using a hot melt glue gun to melt the glue stick (provided by Steinel), inserting the tip into the muzzle for short time and then retracting it quickly. The coated tips should be heat cured by using a simple hair dryer in order to make the coating firmly and examined under an optical microscope. An alternative method of isolating the tips is the electrophoretic paint [16].

2.6 Atomic force microscopy

Atomic force microscopy (AFM) was developed rapidly since 1986, when Binnig and Quate firstly demonstrated the ideas of AFM, which combined with an STM feedback system on the top of an ultra-small AFM diamond tip at the end of the cantilever [17]. One year later, Wickramsinghe et al. developed an AFM setup, which was based on the principle of optical lever, employing a vibrating cantilever technique to probe the sample surface [18].

2.6.1 AFM setup and working principle

Nowadays, AFM has got much better development and become one of the most common surface analysis techniques. In AFM, the image is related to the deflection degree of the cantilever-type spring, also called cantilever, caused by the forces between the tip at the end of the cantilever and the sample surface described by Hooke's Law [19], when the tip scans over the sample surface. The deflection degree is monitored by a photodiode detector, which records the z-movement of the piezo as a function of the lateral x-y position to generate the AFM image with 3-dimensional. A schematic view of basic AFM principles is shown in Fig. 2.12.

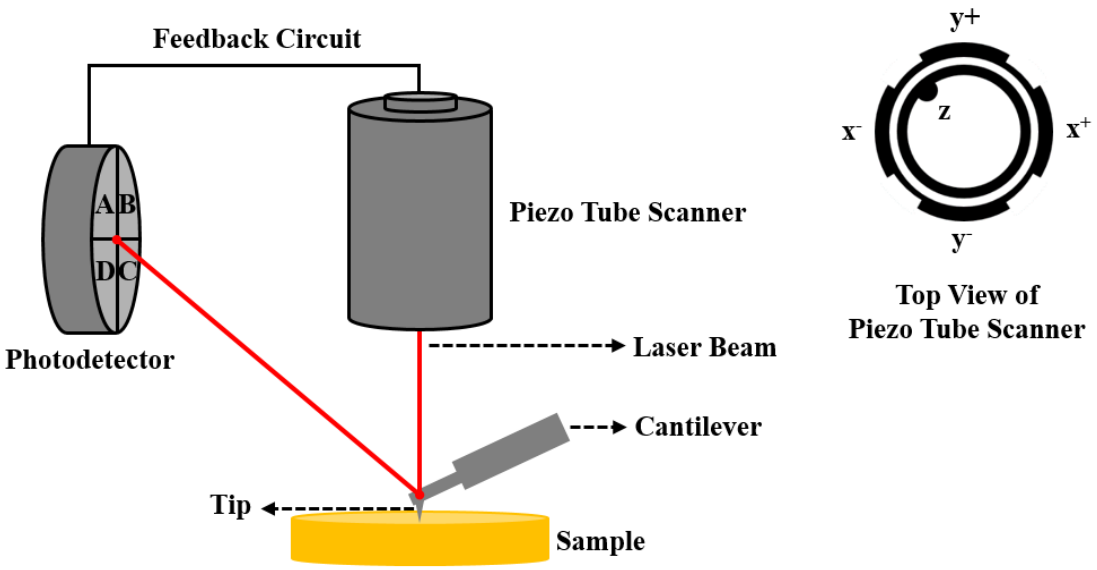

Fig. 2.12 Schematic view of the basic AFM principles.

In AFM, the forces between the tip and sample, including Van der Waals forces, capillary forces, electrostatic forces, magnetic forces, etc. can be measured. However, the dominant interaction forces between the tip and sample surface measured in a small distance is van der Waals forces. As the tip is very close to the sample surface (a few

angstroms), the tip will experience a strong repulsive force due to the overlap of the electronic orbitals at atomic distances. Once the repulsive force is dominant, the tip is considered to be in contact with sample (contact mode). As the tip is retracted away from the sample surface, the attractive force appears due to a polarization effect and it is dominant (non-contact mode). The schematic of the interaction versus tip-sample distance curve is shown in Fig. 2.13.

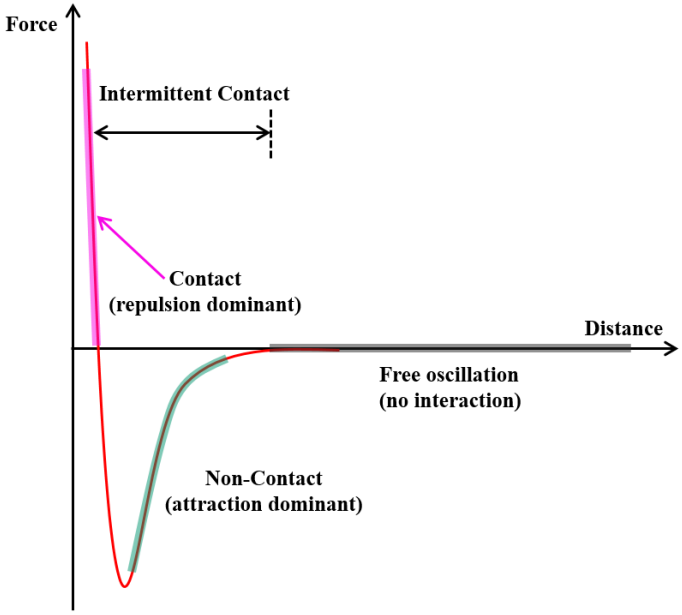

Fig. 2.13 Schematic of the interaction versus tip-sample distance curve

The AFM can provide many different scanning modes, which can be generally classified into static modes and dynamic modes, depending on the application. The static modes are also called contact modes where the tip is in a static state, while the dynamic modes are including the non-contact mode and intermittent contact mode (or tapping mode) where the tip is vibrating at a pre-set frequency by an actuator [17]. Well-defined these three common scanning modes, contact mode, tapping mode and non-contact mode, according to the nature of the tip motion, will be described in detail below.

2.6.2 AFM operation modes

Contact mode

When the spring constant (typically 0.001-5 nN/nm) of cantilever is lower than that of surface and the distance between the tip and sample surface is very small (< 0.5 nm), the cantilever is bended and the repulsive forces (0.1-1000 nN) are dominant, meaning that the tip is in contact with the sample surface. The strength of these repulsive forces are

determined by the setpoint, which is related to the deflection degree of cantilever and controlled by the feedback signal to the piezoelectric positioning element. This contact status at the setpoint (~1 nN) should be maintained during the tip scanning in the contact mode as shown in Fig. 2.14. Generally, the reason for selecting low stiffness cantilevers is to get highly efficient deflection.

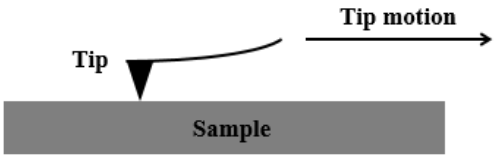

Fig. 2.14 Schematic view of contact mode

In contact mode, the sample surface can be imaged in a constant height mode and constant force mode. In the constant height mode, the height of the tip is constant during scanning and the image is generated by the deflection signal directly. The constant height mode is usually used to get the atomic-resolution images on the atomically flat surfaces. In the constant force mode, the constant force is kept by using the feedback system to control the z-height piezo actuator and the image is generated by the feedback signal. The constant force mode is more commonly used to image the surface in a large scale, but the resolution is relative lower.

The contact mode possess some advantages, such as, it can scan fast, achieve a higher resolution for rough surfaces and be used in friction analysis. However, the disadvantages are that the tip may be damaged and the soft sample may be deformed easily.

Intermittent contact or tapping mode

The tapping mode is one of the dynamic modes, in which the cantilever is mechanically oscillated at its resonant frequency by a small piezo. The amplitude of free oscillation is typically greater than 20 nm when the tip is away from the sample surface. During scanning, the tip taps the sample surface gently and frequently (generally 50 to 500 kHz) and the oscillation amplitude of the cantilever can be kept constant by a feedback system as seen in Fig. 2.15. When the tip is in contact with the sample surface, the oscillation amplitude of the cantilever is necessarily decreased due to the repulsive interaction, which is smaller as compared to that of contact mode. The decrease in the oscillation amplitude is used to reflect the surface features. In tapping mode, the tip can

be operated either in a constant amplitude or in a constant force on the sample surface, which can be adjusted by the feedback loop. Here, it is worth to point out that the spring constant of the cantilever is typically in the range of 1-100 N/m and a sufficient oscillation amplitude should be applied because the tip has to overcome the adhesion forces during the scanning. One of the most important advantages of the tapping mode is that the sample surface cannot be deformed or damaged by the shear forces because the applied force is always keep vertical.

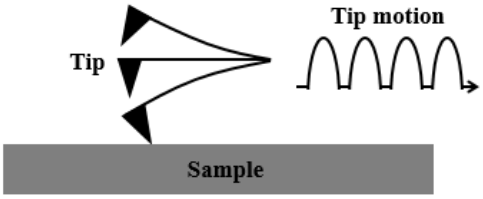

Fig. 2.15 Schematic view of tapping mode

Non-contact mode

In non-contact mode, the cantilever is oscillating freely above the sample surface 5~10 nm and the tip would never contact with the sample surface during the whole scanning process as shown in Fig. 2.16. In this case, the forces between the tip and sample is relatively small (generally 10^{-12} N), which are mostly Van der Waals forces. These forces can be detected by monitoring the change in the oscillation amplitude, phase, or frequency in response to the force gradients between the tip and sample surface, and the images are generated by the tip scanning above the sample surface. In this mode, the soft sample surfaces can be imaged and the tip can not be damaged easily, but the resolution is lower because of the lower interactions between the tip and sample. Generally, under this mode, the resolution is lower and the contaminant on surface can interfere with oscillation so that ultra-high vacuum (UHV) is needed for getting better imaging.

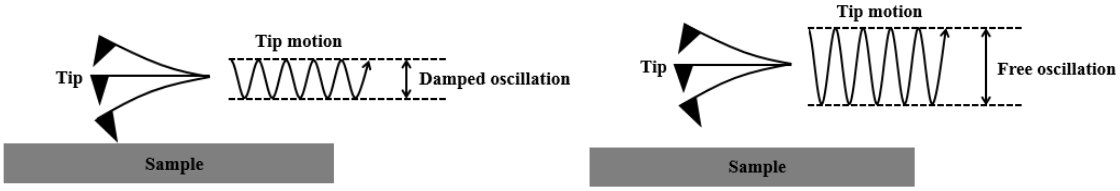

Fig. 2.16 Schematic view of non-contact mode

2.6.3 AFM probes

The AFM probe consists of a cantilever holder, a cantilever and a tip attached to the end

of a cantilever as shown in Fig. 2.17. The AFM probes are typically made from silicon or silicon nitride. Different probes are provided for different propose. The spring constant and resonant frequency can be determined by the cantilever size, material property and the mass as described in following equations.

$$f_0 = \frac{1}{2\pi}\left(\frac{k}{m_0}\right)^{0.5} \quad k = \frac{Ewt^3}{4l^3}$$

Where k is the spring constant, E is Young module, t is the thickness, l is the length, w is the width and m_0 is the effective mass of the cantilever. The spring constant of the cantilevers should be smaller than that of samples (typically ~10 N m^{-1} in a crystalline solid). In commercial probes, the length, thickness and width of cantilevers are in the range of 50-500 μm, 0.5-0.75 μm and 20-80 μm, respectively, which give the spring constant in the range of 0.01-100 N m^{-1}. Furthermore, the tip has a radius of curvature on the order of nanometers, typically from 5 nm to 50 nm depending on the type. The probes can be coated with other function materials to extend some new SPM techniques such as magnetic force microscopy (MFM) and chemical force microscopy (CFM).

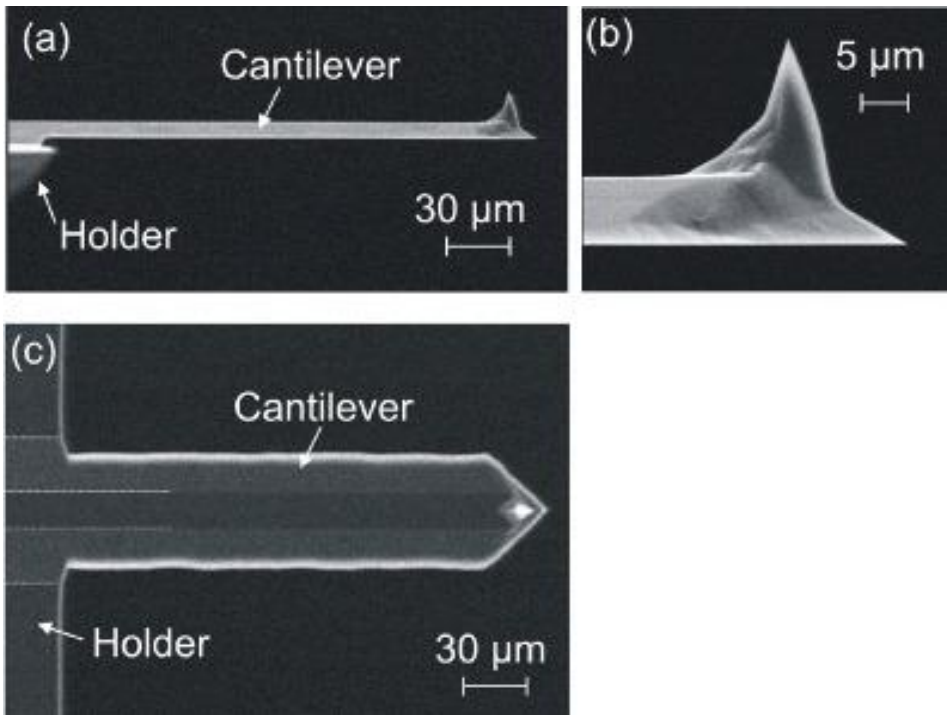

Fig. 2.17 SEM images of AFM probe (a) the side view of a cantilever, (b) an enlarged side view of the sharp tip on the end of cantilever and (c) a bottom view of a cantilever [16].

All the AFM probe employed in this work are provide by Nanosensors and the specifications are shown in table 2.3.

Table 2.3: Probe specifications PPP-CONTSC-20

Type	Material	Coating	Spring constant (N/m)	Length (μm)	Width (μm)	Thickness (μm)	Frequency (kHz)	Lateral force constant (N/m)
PPP-CONTSC	Silicon	Non-coated	0.01~0.3	225	44	1.2~1.4	31~42	50

2.6.4 Vertical force and lateral friction force

The vertical force is an applied force between the tip and sample surface, which can be calculated by the force-distance curve according to Hook's law.

$$F = k \cdot d_c$$

Where k and d_c is the spring constant and deflection of the cantilever, respectively. This force is dependent on the value of setpoint because the setpoint determines the deflection of cantilever. Normally, the plot of the vertical force versus setpoint demonstrates a linear relationship.

The lateral friction force is generated when the tip is mechanically contacted with the sample surface and it moves horizontally across the surface. Theoretically, this force is not dependent on the contact area and the rate of tip movement, but on the applied vertical force (F) and the surface friction coefficient of sample (μ).

$$F_L = \mu \cdot F$$

The friction reflects the surface property of the materials and it currently can be measured by the lateral force microscopy (LFM) [20]. It is worth to mention that the friction at atomic scale is demonstrated by the Tomlinson model, and further modified by Prandtl [21, 22], and the true friction is obtained by subtracting the friction obtained in the retrace direction from the friction obtained in the trace direction because the deflection direction of cantilever at the same position is opposite (positive value in trace direction and negative value in retrace direction) in the trace and retrace directions and the friction is different at the same position when tip is scanning over a step in both directions. The more detailed information is available in the literature [23].

2.7 EC-AFM/STM

2.7.1 EC-AFM/STM setups

In this work, we employed an Agilent Technologies 5500 Scanning Probe Microscope (SPM) combined with the built in bipotentiostat or a Nanoscope III E controller (Digital

Instruments, Santa Barbara, CA) connected with a separate potentiostat and a commercially available STM and AFM scanner (Molecular Imaging/Agilent Technologies) fitted with a homemade electrochemical cell so called AFM/STM cell as described before. The electrochemical measurements were conducted with a three electrodes system consisting of a reference electrode (Pt/PtO), a working electrode (Au(111)/Pt(111)) and a corresponding counter electrode (Pt/Au wire) to working electrode. The schematic view of EC-STM is shown in Fig. 2.18, and the EC-AFM is similar to this setup except no bias voltage applied between the tip and sample.

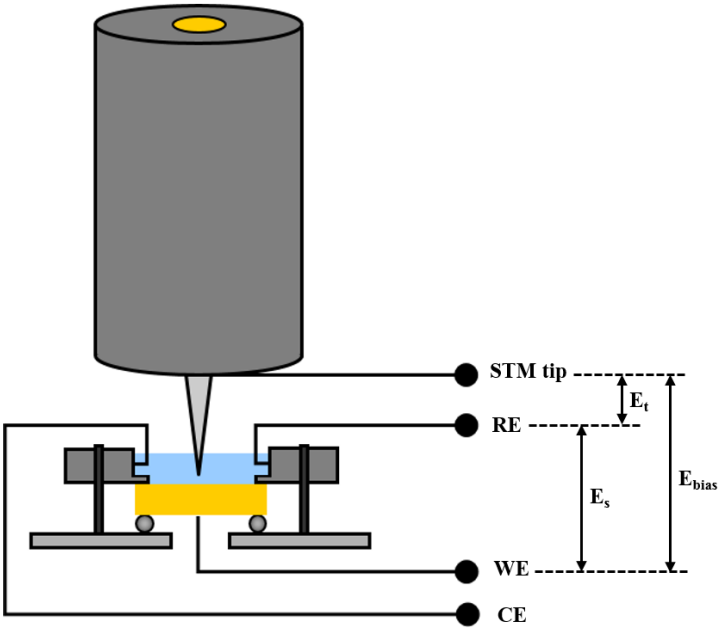

Fig. 2.18 Schematic view of the EC-STM setup.

In EC-STM, there are two operating modes, fixing bias voltage between the tip and sample and fixing tip potential. When the bias voltage (typically 0.05-0.2 V) is fixed, the tip potential (vs. Pt/PtO) is also scanned parallelly to the potential at working electrode during electrochemical scanning, and this probably leads to some reactions taking place at the tip, producing faradic current flowing through the tip and making it unstable. However, for fixing tip potential, the tip potential should be fixed at a potential where no reactions occur. It is worth to note that the bias voltage is constantly changing during electrochemical scanning. Each of these modes has its own advantages and disadvantages, and both modes should be operated carefully.

2.7.2 Cleaning of the STM/AFM cell

The STM/AFM cell and their ancillaries such as reference and counter electrode wires,

plastic tweezer and small glass pipette, etc. were cleaned in boiling dilute sulfuric acid and then in boiling in Milli-Q water before use. Afterward, washed them carefully and dried it when the organic electrolyte was involved. In addition, these stuffs were kept in a 5 M KOH bath after the measurements on organic electrolyte for overnight to decompose the organics before the cleaning process described above. The AFM-nose and the probes were scrubbed by a clean tissue paper with a few drops of ethanol followed by rinsing with Milli-Q water.

2.8 STM/AFM images analysis

First, it is worth to point out that SPM raster scan the tip over the electrode surface to form images and it is typically composed of 512×512 pixels, which forms an array of 512 lines. In this work, the WSxM 5.0 D7 program was used for images analysis, which is the freely available, powerful and user-friendly software for data acquisition and processing in SPM or spectroscopy techniques. It has many analysis functions. Here, some functions we used will be briefly described below. It is necessary to optimize the image quality before analyzing the images because the surface features are sometimes not visible before some adequate treatments due to the distortions of images caused by noise (especially at low frequency), tilt samples and nonlinear scanner behavior such as bow (see. Fig. 2.19), which have to be eliminated and corrected.

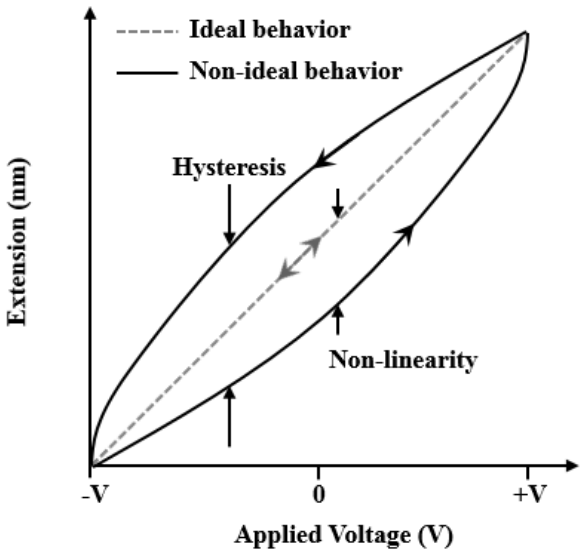

Fig. 2.19 Ideal and non-ideal behaviors of a piezoelectric scanner in one dimension (either x, y, or z). Hysteresis where the sensitivity varies depending on the direction of the applied voltage and non-linear extension in response to linear applied voltage [24, 25].

The most common way is called line by line leveling (also called flattening which generally works line-by-line in the software). It works by subtracting a polynomial function from each line in the unprocessed image [26]. The simplest function is a constant function, the average of each line. However, the linear function (straight line) or quadratic function (parabola) was also often used for line leveling, depending on the surface feature. It should be noted that an artifact may be introduced because the polynomial function probably includes the feature, giving rise to some streak marks in the image, and an appropriate polynomial function should be used to avoid it. Flattening is useful prior to analysis of depth, roughness, section, etc. when the tilt, bow or low frequency noise appearing as stripes or horizontal shifts were displayed in the image.

However, when the tip is never perpendicular to the surface of sample during its scanning, it gives the final image slope. This generally has to be corrected by subtracting a plane, which is well-defined plane by using a single polynomial of a selectable order. It is the most common method that the correcting can be done by defining a plane, which named three selected points that are not on the same line, and then subtracting it from the unprocessed image. The plane leveling/fitting includes options for a global plane leveling and a local plane leveling, which is specially used in the case of the appearance of some slopes on the terraces or the terrace where the background associated with the scanner is much lower than the terraces heights because the global plane leveling can not flatten them when the terraces are at different heights.

In practice, to obtain an accurate image, leveling is not always sufficient. It is necessary eliminate noise in the image by using filters in some cases because the noise is often present in images and it can be easily aroused by surface irregularities, impurities, humidity, vibration, and so on. Generally, two types of filtering, the matrix filtering and Fourier transform, are used for eliminating the noise in images. The detailed description of these filtering methods is available in the software user manual and in the book [26].

References

[1] N. G. Tsierkezos, Journal of Solution Chemistry 36:289 (2007).
[2] K. A. Connors, Chemical Kinetics: The Study of Reaction Rates in Solution, VCH, Madison, 1999.
[3] J. A. V. Butler, Transactions of the Faraday Society 19:729 (1924).
[4] S. Fletcher, Journal of Solid State Electrochemistry 13:537 (2009).
[5] A. J. Bard and L. R. Faulkner, Electrochemical Methods: Fundamentals and Applications, 2nd Edition, Wiley, New York, 2001.
[6] F. Dalton, Electrochem. Soc. Interface Fall 25:50 (2016).
[7] U. A. Paulus, T. J. Schmidt, H. A. Gasteiger, and R. J. Behm, Journal of Electroanalytical Chemistry 495:134 (2001).
[8] F. G. Will, Journal of the Electrochemical Society 133:454 (1986).
[9] J. Clavilier, R. Faure, G. Guinet, and R. Durand, Journal of Electroanalytical Chemistry and Interfacial Electrochemistry 107:205 (1979).
[10] J. Clavilier, K. Elachi, M. Petit, A. Rodes, and M. A. Zamakhchari, Journal of Electroanalytical Chemistry 295:333 (1990).
[11] L. A. Kibler, Preparation and Characterization of Noble Metal Single Crystal Electrode Surfaces, International Society of Electrochemistry, Ulm, 2003.
[12] R. H. Fowler and L. Nordheim, Physical and Engineering Sciences 119:173 (1928).
[13] G. Binnig, H. Rohrer, C. Gerber, and E. Weibel, Physical Review Letters 49:57 (1982).
[14] F. J. Giessibl, Reviews of Modern Physics 75:949 (2003).
[15] J. Lindahl, T. Takanen, and L. Montelius, Journal of Vacuum Science & Technology B 16:3077 (1998).
[16] S. Iqbal, in Mathematisch-Naturwissenschaftlichen Fakultät, Vol. PhD, Rheinischen Friedrich-Wilhelms-Universität Bonn, Bonn, 2015, p. 214.
[17] G. Binnig, C. F. Quate, and C. Gerber, Physical Review Letters 56:930 (1986).
[18] Y. Martin, C. C. Williams, and H. K. Wickramasinghe, Journal of Applied Physics 61:4723 (1987).
[19] B. Cappella and G. Dietler, Surface Science Reports 34:1 (1999).
[20] C. T. Gibson, G. S. Watson, and S. Myhra, Wear 213:72 (1997).
[21] L. Prandtl, ZAMM - Journal of Applied Mathematics and Mechanics / Zeitschrift für Angewandte Mathematik und Mechanik 8:85 (1928).
[22] H. Hölscher, D. Ebeling, and U. D. Schwarz, Physical Review Letters 101:246105 (2008).
[23] B. Bhushan and T. Kasai, Nanotechnology 15:923 (2004).
[24] A. Committee, Guide to Scanner and Tip Related Artifacts in Scanning Tunneling Microscopy and Atomic Force Microscopy, ASTM International, West Conshohocken, 2004.
[25] S. M. Hues, C. F. Draper, K. P. Lee, and R. J. Colton, Rev. Sci. Instrum. 65:1561 (1994).
[26] A. Méndez-Vilas and J. Díaz, Modern Research and Educational Topics in Microscopy, Formatex, Badajoz 2007.

Chapter 3: ORR and OER on Co_3O_4 (nanoparticles)/Ag electrode

This chapter will focus on the fundamental study of ORR and OER on Co_3O_4 (nanoparticles)/Ag electrode prepared by physical deposition of Co_3O_4 on Ag disk electrode. Its catalytic activity and stability for both reactions will be determined by RRDE technique and surface characterization techniques.

3.1 Introduction:

Ag is considered as an alternative catalyst to platinum for ORR in alkaline electrolyte to reduce the high cost of the electrode [1-3] in lithium air batteries [4-6], even metal-air batteries [7, 8]. To improve the catalytic activity of Ag for ORR, single crystal Ag [9], different size, shape and morphology of silver nanostructures [10, 11], and also Ag modified and combined with another metal [12, 13] or metal oxide [14-16] were studied. Ag is not suited as a bifunctional catalyst for reversible oxygen reaction because it is not active for OER. Metal oxides, such as Co_3O_4 [17], MnO_2 [18], the transition metal-doped RuO_2 and IrO_2 [19], and their mixture [20] have a good performance for catalyzing OER because they can increase the number of sites for peroxide decomposition [21, 22]; it was found that Co_3O_4 is one of most active catalysts for OER [23].

Recently, it was found that mixing the ORR and OER catalysts is an approach to achieve a bifunctional catalyst with synergistic effect in alkaline media. Slanac [24] achieved synergy between Ag and MnO_x nanoparticles. In our group, Amin [23] also found that the mixture of spinel Co_3O_4 nanoparticles and Ag particles also showed a synergistic effect. To continue study on this synergistic effect of Co_3O_4/Ag, the fundamental study of ORR and OER on spinel Co_3O_4 nanoparticles modified Ag electrode was done in this work, which has never been done before. The mechanisms of ORR and OER have been investigated by RRDE technique. The surface morphologies before and after potential cycling in Ar saturated electrolyte have been examined by SEM. The number of the accessible sites of Ag surface was determined by Pb-UPD measurements [25].

3.2 Experimental

3.2.1 Preparation of disk electrodes

A glassy carbon (GC) and silver polycrystalline rotating disk electrodes both with the

same diameter of 0.5 cm were employed. A suspension containing Spinel Co_3O_4 nanoparticles (< 50 nm, Sigma-Aldrich) with a concentration of ~0.4 g/L in ethylene glycol was prepared for physical deposition of Co_3O_4 catalyst on Ag and GC disk electrode. A simple way was used, first using a pipette to transfer a certain amount of Co_3O_4 solution onto the disk electrode surface, then the electrode was placed in a common oven at the temperature of 160 °C for 10 min to evaporate ethylene glycol, finally using 20 µL Nafion®117 solution [26] (~5% in a mixture of lower aliphatic alcohols and water) to bind Co_3O_4 nanoparticles on disk electrode surface.

3.2.2 Electrochemical characterization

All electrochemical experiments have been done by a three-electrode system, consisting of a working electrode (glassy carbon or silver polycrystalline rotating disk electrode, both with the area of 0.196 cm^2), a platinum foil counter electrode, and reversible hydrogen reference electrode (RHE) at room temperature. 0.1 M LiOH (lithium hydroxide monohydrate were purchased from Sigma-Aldrich) and 0.1 M LiOH + 125 µM $Pb(NO_3)_2$ (lead nitrate were purchased from Aldrich-chemie) were prepared with Milli-Q water (18.2 MΩ cm, TOC of 5 ppm, MILLIPORE, Schwalbach, Germany) as electrolyte and purged with ultra-high pure argon (99.999%, Air Liquide) and oxygen (99.9995%, Air Liquide) for at least 40 minutes before use for ORR and OER test. Spinel Co_3O_4 nanoparticles (< 50 nm, Aldrich) was used as catalyst and Nafion®117 solution (~5% in a mixture of lower aliphatic alcohols and water) of 20 µL was used as adhesive [26].

Electrochemical measurements were recorded by LabVIEW software (National Instruments GmbH, Munich, Germany) combined with a homebuilt rotating ring disk electrode (RRDE) setup. The RRDE tip was provided by the company (Pine Research Instrumentation, Pennsylvania, USA), consisting of a disk electrode with a diameter of 5 mm, a platinum ring electrode with the internal and outer diameter of 6.5 and 7.5 mm respectively and a Teflon U-cup for keeping two electrodes electrically isolated. For determining the ORR and OER activities of the catalysts, a linear sweep voltammetry from 0 to 1.8 V at the disk electrode with a scan rate of 5 or 10 mV/s and a varying rotation speed of 10-40 Hz and holding the ring electrode at 1.2 V (vs. RHE) where the formed peroxide at the disk electrode can be oxidized in O_2 saturated in 0.1 M LiOH was carried out by RRDE.

3.2.3 Surface characterization

The surface morphology of the catalysts was examined by SEM (Zeiss dual-beam NVISION 40 with an operating voltage of 5-30 kV) by Jörg Bernhard in university of Ulm. Pb-UPD measurements for determining the accessible sites of Ag surface were executed in 0.1 M LiOH + 125 µM $Pb(NO_3)_2$ by holding potential at 0.23 V (vs. RHE) for 5 min and then scanning to anodic direction to 0.58 V at 10 mV/s.

3.3 Results and discussion

3.3.1 ORR and OER on Co_3O_4/Ag electrode surface

Catalytic activity estimation

The electrocatalytic activity of different electrode surfaces such as $Ag_{(pc)}$, Co_3O_4/GC and $Co_3O_4/Ag_{(pc)}$ towards ORR has been examined by recording the corresponding cyclic voltammograms in O_2-saturated 0.1 M LiOH as shown in Fig. 3.1. For examining the catalytic activity of the electrode surfaces for ORR, the ORR curve in the anodic direction is used because it is freed of oxides (such as Ag_2O) at the negative potential limit. On the contrary, oxidation of the metals takes place in the OER region in the anodic sweep, giving rise to an additional current, and therefore the OER curve in cathodic direction should be used for examining the catalytic activity of the electrode surfaces. In the case of 800 µg cm^{-2} Co_3O_4/Ag, the diffusion limiting current decreased obviously compared to pure Ag electrode. This is probably due to the Co_3O_4 nanoparticles hindering oxygen to diffuse to the Ag surface [27], where the ORR prefers to occur. However, the onset of ORR is approximately 50 mV earlier than that of pure Ag electrode and the onset of OER is around 40 mV negative shifted and the current at 1.8 V increased by 22% compared to that of Co_3O_4/GC electrode. All these results indicate that the Co_3O_4/Ag catalyst possesses an excellent catalytic activity to both ORR and OER. However, the theoretical diffusion limiting current was calculated to be 5.08 mA cm^{-2}, which is lower than that obtained at silver electrode, but is almost consistent with that obtained at 800 µg cm^{-2} Co_3O_4/Ag electrode.

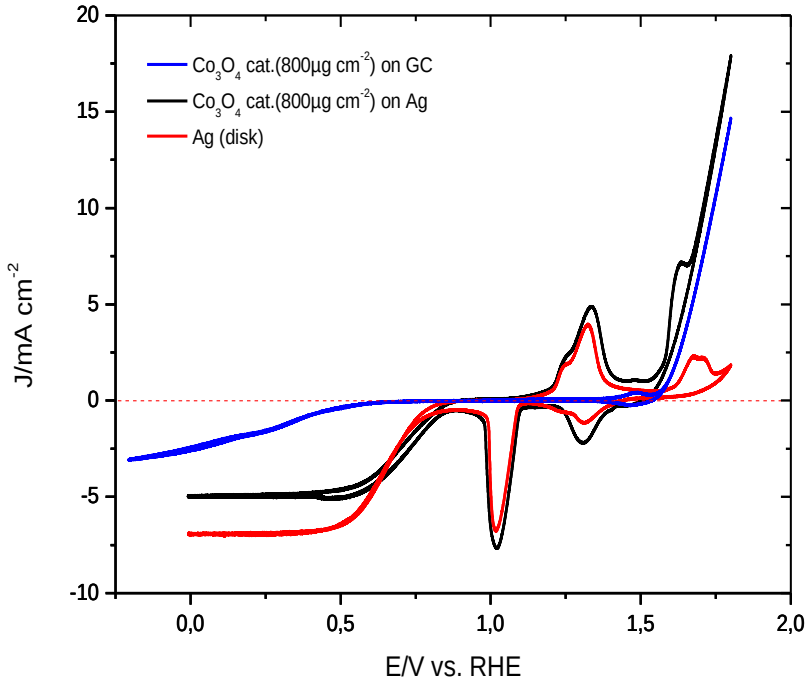

Fig. 3.1 Cyclic voltammograms of ORR and OER on different electrode surfaces in O_2-saturated 0.1 M LiOH solution at a scan rate of 5 mV s^{-1} and a rotation speed of 40 Hz.

Different coverage of Co_3O_4 on Ag electrode

In order to investigate the dependence of the catalytic activity on the coverage of Co_3O_4, a series of comparative RRDE voltammograms were obtained on pure Ag, 200/400/800 µg cm^{-2} Co_3O_4/Ag and 800 µg cm^{-2} Co_3O_4/C electrodes in O_2 saturated 0.1 M LiOH at the rotation rate of 40 Hz as shown in Fig. 3.2. It is interesting that the Ag oxidation peaks and reduction peak become larger with the increase of the coverage of Co_3O_4 on Ag, indicating that Co_3O_4 may promote Ag oxidation and reduction. In order to see the CVs more clearly, ORR and OER curves are selected and shown in Fig. 3.3 and Fig. 3.4, respectively. For ORR curves (see. Fig. 3.3), it is obvious that the diffusion limiting currents decrease with increase in the amount of Co_3O_4 on Ag, but the onset potentials are positive shifted gradually. The pure Ag electrode demonstrates the highest diffusion limiting current. As discussed before, the decrease in the diffusion limiting current is probably due to the Co_3O_4 layer hindering the diffusion of oxygen to the ORR active sites, which are mostly located on Ag surface and at the interface of Co_3O_4 and Ag. It is well known that Co_3O_4 possesses less catalytic activity for ORR. However, the onset (E_{onset}) and half wave ($E_{1/2}$) potentials for ORR are shifted from 0.83 V and 0.63 V at pure Ag to 0.88 and 0.7 V at 800 µg cm^{-2} Co_3O_4/Ag, respectively, meaning that the catalytic activity of Ag for ORR can be improved by modifying it with Co_3O_4. This

phenomenon was also observed on bimetallic alloys: the catalytic activity of a metal for ORR can be enhanced by the presence of the heterogenous transition metal or metal oxide because the d-band center can be shifted by changing the electronic structure of the metal in this case [28-32]. The For OER curves (see. Fig. 3.4), the E_{onset} is shifted from 1.56 V at 800 µg cm^{-2} Co_3O_4/GC to 1.52 V at 800 µg cm^{-2} Co_3O_4/Ag and the current of OER is increased significantly. According to synthetically evaluation, the 800 µg cm^{-2} Co_3O_4/Ag has a higher catalytic activity for both ORR and OER in this work.

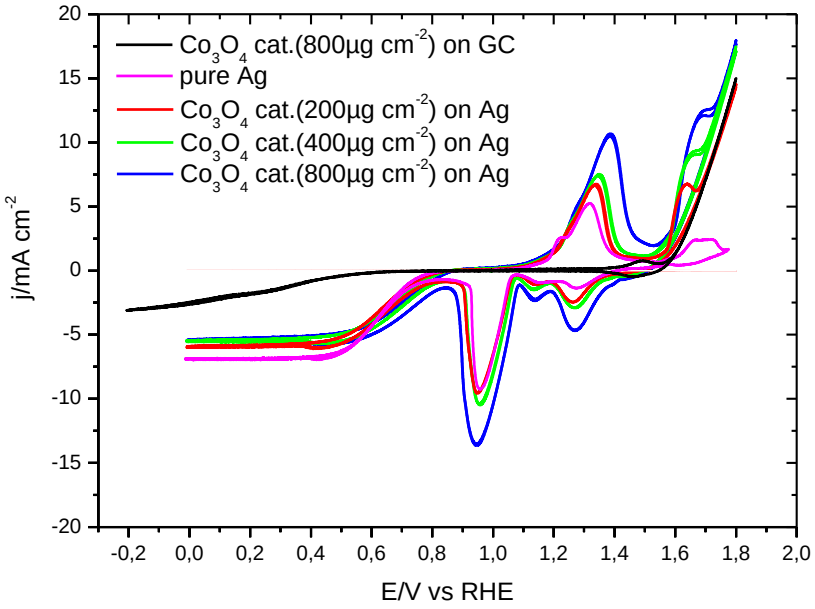

Fig. 3.2 Cyclic voltammograms of ORR and OER on the pure Ag, 200/400/800 µg cm^{-2} Co_3O_4/Ag, 800 µg cm^{-2} Co_3O_4/C electrode in O_2-saturated 0.1 M LiOH solution at a scan rate of 10 mV s^{-1} and a rotation rate of 40 Hz.

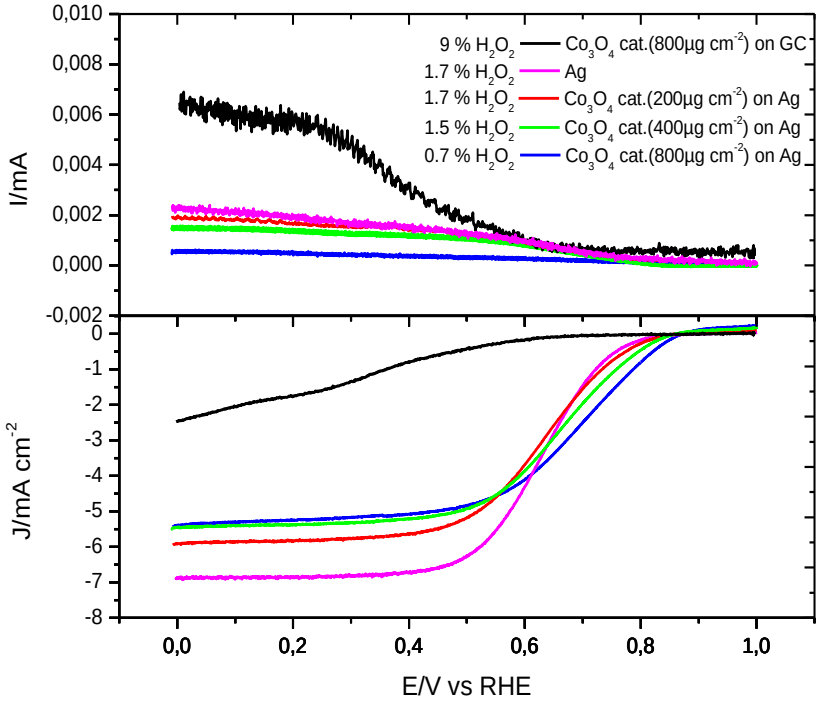

Fig. 3.3 RRDE voltammograms of ORR on the pure Ag, 200/400/800 µg cm^{-2} Co_3O_4/Ag, 800 µg cm^{-2} Co_3O_4/C electrode in 0.1 M LiOH at a scan rate of 10 mV s^{-1} and a rotation rate of 40 Hz. Disk current density (down) and ring current/H_2O_2 yield (up).

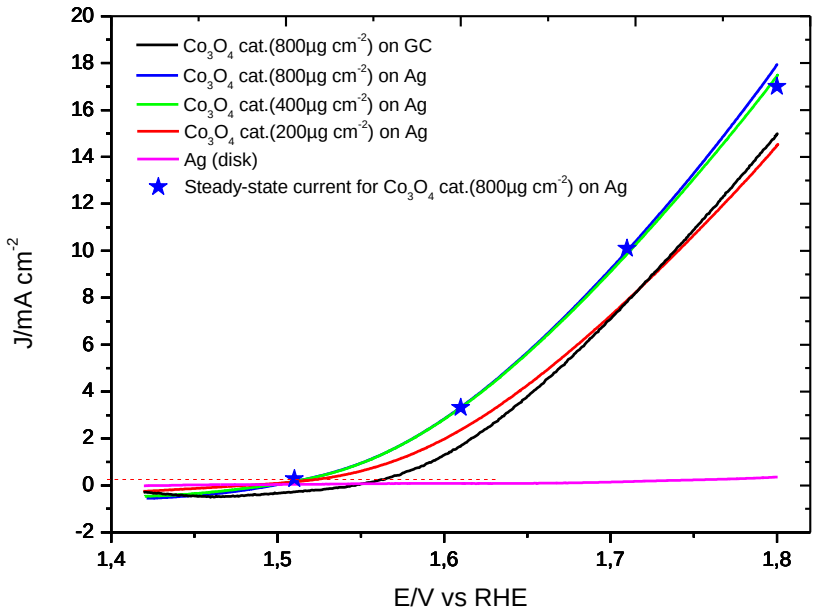

Fig. 3.4 RRDE voltammograms of OER on Ag, 200/400/800 µg cm^{-2} Co_3O_4/Ag and 800 µg cm^{-2} Co_3O_4/C electrode in 0.1 M LiOH at a scan rate of 10 mV s^{-1} and a rotation rate of 40 Hz.

Determination of the H_2O_2 yield and electron transfer number

Fig. 3.3 shows the disk current and ring current recorded at the constant potential of 1.2 V (vs. RHE) where the peroxide species can be oxidized, while the potential of disk electrode was scanned in the range of 0 to 1.8 V with a scan rate of 10 mV s^{-1} and with a rotation speed of 40 Hz. The percentage of peroxide species and the electron transfer number (n) were determined according to the following equations:

$$H_2O_2\% = \frac{2i_R}{Ni_D + i_R}$$

$$n = \frac{4i_D}{i_D + i_R / N}$$

Where i_D is disk electrode current, i_R is ring electrode current, and N=0.256 is the collection efficiency. The yield of peroxide species (H_2O_2%) was calculated and is shown in Fig. 3.3. The highest yield of H_2O_2 (9%) was obtained at 800 µg cm^{-2} Co_3O_4/GC. It is essentially in agreement with the values reported in the literature that the yield of are below ~12% and ~6% for Co_3O_4/rmGO and Co_3O_4/N-rmGO, respectively [33]. Less than 2% yield of H_2O_2 was obtained at the Co_3O_4/Ag electrode surface and the yield decreased with the increasing in the amount of Co_3O_4. Finally, only 0.7% was obtained at the 800 µg cm^{-2} Co_3O_4/Ag. These are consistent with our previous results, which were obtained from the bimetallic catalyst of Ag311 (microparticles)/Co_3O_4 (nanoparticles) [23]. The electron transfer number (n) was calculated to be 4 by the equation (see. above), suggesting that at Co_3O_4/Ag electrode surface of a $4e^-$ ORR process is favoured, which is similar to ORR catalyzed by a commercial Pt/C catalyst.

Mechanism investigation of the reactions

For further analyzing the kinetic parameters and mechanism of ORR at Co_3O_4/Ag electrode surface in 0.1 M LiOH, it is essential to get the Koutecky-Levich plot, which was described by the Koutecky-Levich equation [34] (below), and Tafel slope [35].

$$1/j = 1/j_L + 1/j_K = 1/B\omega^{0.5} + 1/j_K$$

$$B = 0.62nFC_oD_o^{2/3}\nu^{-1/6}$$

$$j_K = nFkC_o$$

Where, j ($mA \cdot cm^{-2}$) is the measured current density, j_K ($mA \cdot cm^{-2}$) is kinetic current density, j_L ($mA \cdot cm^{-2}$) is the limiting current density, ω (s^{-1}) is the rotation rate ($\omega = 2\pi f$, f is frequency in Hz), n is the electrons transfer number, F (A·s) is the Faraday constant,

C_0 (mol·cm^{-3}) is the concentration of oxygen in bulk solution, D_0 (cm^2·s^{-1}) is diffusion coefficient of oxygen, ν (cm^2·s^{-1}) is the kinematic viscosity of the electrolyte and k (mol^{-1}·cm^3·s^{-1}) is the rate constant of electron transfer.

Koutecky-Levich plots were constructed by using the RRDE voltammograms of 800 µg cm^{-2} Co_3O_4/Ag in 0.1 M LiOH in Fig. 3.5a. The linear Koutecky-Levich plots and parallel fitting lines at various potentials, and a zero intercept at 0.2 V, are obtained and shown in Fig. 3.5b. This suggests a first order reaction with respect to the concentration of dissolved oxygen and that the ORR process is not limited by a chemical reaction step, but by the diffusion of oxygen. The electron transfer number calculated by using the Koutecky-Levich slope of 3.2×10^3 cm^2 A^{-1}s$^{1/2}$ (average value at 0.2-0.8 V) is in good agreement with the value calculated by using the ring current. It is around 4e$^-$ in both cases. RRDE voltammograms and the corresponding Koutecky-Levich plots of different amount of Co_3O_4/Ag are shown in Fig. 3.6. In addition, Koutecky-Levich plots at 0.2 V (diffusion control range) for different coverages of Co_3O_4 (0, 200, 400, 800 µg cm^{-2}) on Ag electrode are shown in Fig. 3.5f. The slope of these plots is different but the intercept of these plots is almost zero, suggesting that ORR reactions on these electrode surfaces are diffusion controlled reactions. The decrease of diffusion limiting current decreases with the increase of the Co_3O_4 coverage are probably due to the agglomeration of Co_3O_4 particles on Ag electrode surface, blocking active Ag surface (see SEM images in Fig. 3.9).

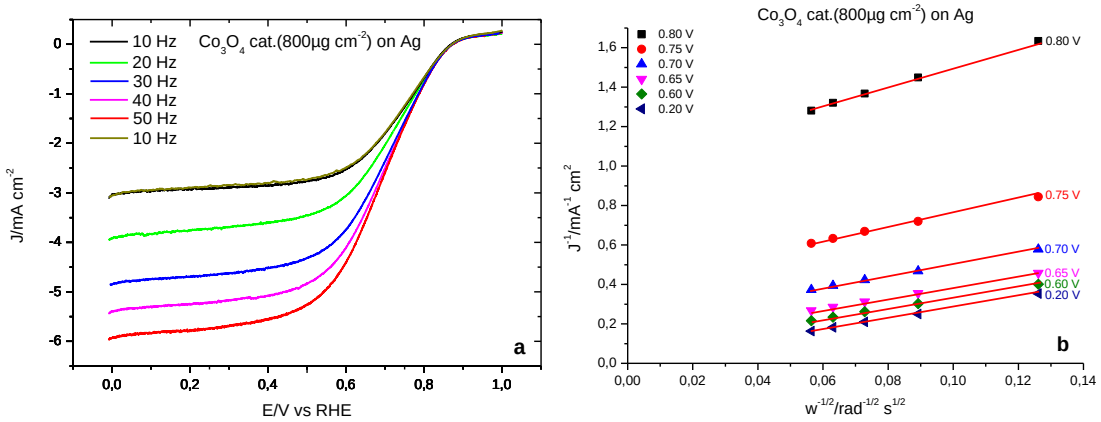

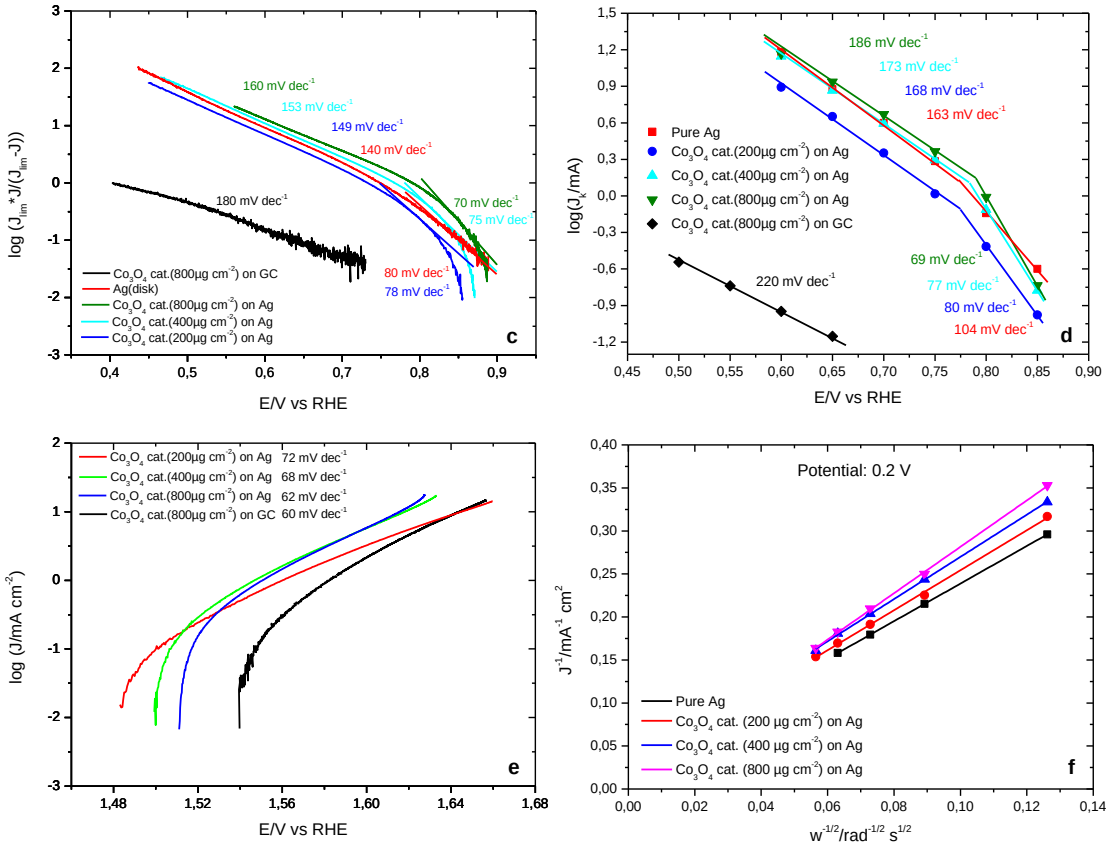

Fig. 3.5 a) RRDE voltammograms of 800 µg cm^{-2} Co_3O_4/Ag in O_2-saturated 0.1 M LiOH at a sweep rate of 10 mV s^{-1} and at different rotation speed (10, 20, 30, 40 and 50 Hz). b) The corresponding Koutecky–Levich plots (J^{-1} vs. $\omega^{-1/2}$) at different potentials (E/V vs. RHE). c), iR-corrected Tafel plots of ORR for 200 µg cm^{-2} Co_3O_4/Ag, 400 µg cm^{-2} Co_3O_4/Ag, 800 µg cm^{-2} Co_3O_4/Ag, 800 µg cm^{-2} Co_3O_4/GC and pure Ag derived by the mass-transport correction of corresponding RRDE data in Fig. 3.3. d) non-iR-corrected Tafel plots in which the kinetic currents were obtained from the intercepts of corresponding K-L plots showed in Fig. 3.5b and Fig. 3.6. e) iR-corrected Tafel plots of OER for 800 µg cm^{-2} Co_3O_4/Ag and 800 µg cm^{-2} Co_3O_4/GC electrodes obtained from the corresponding CV in Fig. 3.4. f), the K-L plots at 0.2 V for different coverage of Co_3O_4 on Ag electrode.

Usually, the reverse reaction rate of ORR at overpotentials higher than 60 mV is negligible [36]. So, the kinetic current density (j_K) can be determined by the measured current density (j) and experimental limiting current density (j_L) from the equation as following:

$$j = \frac{j_K}{1 + \frac{j_K}{j_L}}$$

After rearrangement

$$j_K = \frac{j}{1 - \frac{j}{j_L}} = \frac{j \cdot j_L}{j_L - j}$$

The Tafel slopes for ORR were obtained by plotting the potential (E) against the logarithm of kinetic current density (log j_K) and shown in Fig. 3.5c. Only one Tafel slope (~180 mV dec^{-1}) was observed on 800 μg cm^{-2} Co_3O_4/GC electrode. However, two Tafel slopes appeared separately at low and high overpotentials on Co_3O_4/Ag and pure Ag electrodes. Specifically, on pure Ag electrode surface, the obtained Tafel slopes for ORR are 80 mV dec^{-1} and 140 mV dec^{-1} at low overpotentials and high overpotentials (< 0.8 V), respectively, close to the values in the literature [37], in which the Tafel slopes were found to be 70 mV dec^{-1} at a low overpotentials and 140 mV dec^{-1} at a high overpotentials, suggesting that ORR probably proceeds by different mechanisms. On Co_3O_4/Ag electrode, with the increase of the coverage of Co_3O_4 on Ag, the Tafel slope at low overpotential declined slightly from 78 to 70 mV dec^{-1}, while the Tafel slope at high overpotential increased from 149 to 160 mV dec^{-1}. The Tafel slopes appeared at low overpotential are related to the pre-adsorption process. These Tafel slopes at high overpotential are close to 120 mV dec^{-1}, which is typical for one-electron transfer. The increase/transition in Tafel slope at high overpotential may be correlated to the change of adsorption model of intermediates from Temkin to Langmuirian condition [38, 39] or the effect of the competitive adsorption of OH^- and other special anions, which determine the effective adsorption of oxygen molecules at the electrode surface at high overpotential [40]. The similar transition in Tafel slope at low and high overpotentials is observed when the Tafel slopes are obtained from the intercepts of corresponding K-L plots, as shown in Fig. 3.5d, however, these values are slightly larger than that obtained from the measured current and limiting current.

Only one Tafel slope was obtained for OER to be in the range of 60~72 mV dec^{-1} in all these cases (Fig. 3.5e). It indicates that there is no change in the mechanism of OER catalyzed by Co_3O_4/Ag comparing to Co_3O_4. These Tafel slope values are close to the values in the literatures. Iwakura [41] observed the Tafel slopes of 45 and 55 mV dec^{-1} in the case of using Co_3O_4/Fe and Co_3O_4/Pt as catalyst, respectively. Singh [42] obtained the Tafel slope in the range of 58~64 mV dec^{-1} for the catalysts of Co_3O_4/Ti, Co_3O_4/Co, Co_3O_4/ Ni, Co_3O_4/Nb, Co_3O_4/Ta and Rasiyah [43] found that the Tafel slope

of OER is around 60 mV dec^{-1} on Co_3O_4 and 64 mV dec^{-1} on Li-doped Co_3O_4. For the mechanism of OER it was suggested that the first step is the fast electrosorption of OH^- as OH radical on the electrode surface, followed by the slow conversion process of OH into H_2O_2 as rate limiting step, and chemical decomposition of H_2O_2 into O_2 via two fast chemical steps finally [44], as following:

$$s^* + OH^- = s^*{-}OH + e^- \text{ (fast)}$$

$$s^*{-}OH + OH^- \rightarrow s^*{-}H_2O_2 + e^- \text{ (slow)}$$

$$s^*{-}H_2O_2 + OH^- \rightarrow s^*{-}HO_2^- + H_2O \text{ (fast)}$$

$$2s^*{-}HO_2^- \rightarrow 2s^* + OH^- + O_2 \text{ (fast)}$$

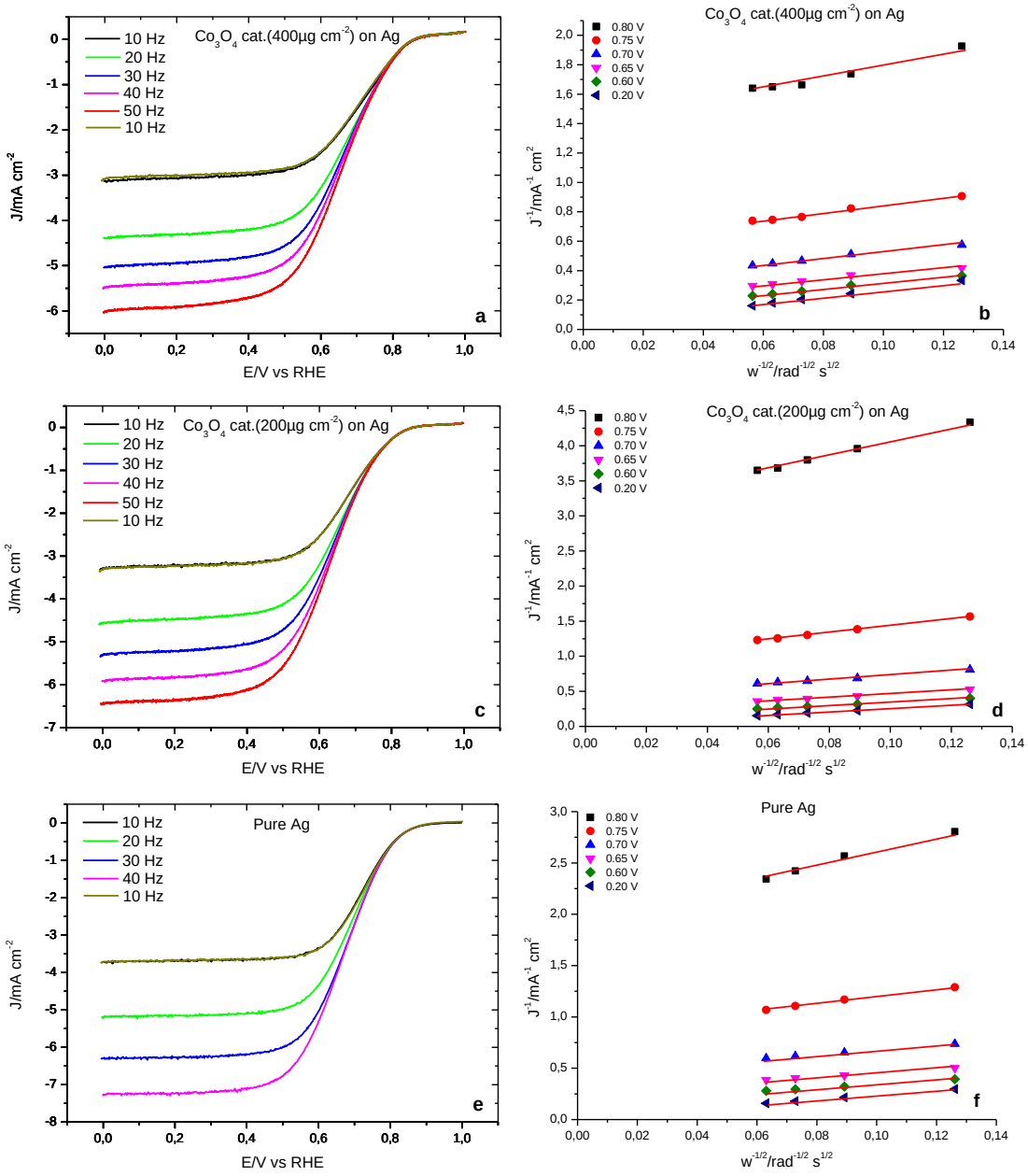

Fig. 3.6 RRDE voltammograms of ORR on 0/200/400 µg cm^{-2} Co_3O_4/Ag electrodes in O_2-saturated 0.1 M LiOH with a sweep rate of 10 mV s^{-1} at the different rotation rates

indicated, and corresponding Koutecky–Levich plots (J^{-1} vs. $w^{-1/2}$) at different potentials (E/V vs. RHE).

Determination of the steady state activity of Co_3O_4/Ag for OER

The steady state activity of 800 µg cm^{-2} Co_3O_4/Ag for OER was tested by the chronoamperometry. The electrode potential was held at the constant value of 1.51, 1.61, 1.71, 1.8 V in 0.1 M LiOH solution saturated with O_2, as shown in Fig. 3.7. The steady state current values are shown together with the corresponding CVs and in Fig. 3.4. This demonstrates that the negative-going scan really reflects the oxygen evolution because the steady state currents at rotation rate of 40 Hz are as the same values as those in the negative-going sweep. It is worth noting that in the potential range below 1.61 V the curves of current vs. time for both rotation speeds (10 Hz and 40 Hz) overlap and the current drops rapidly; but they differ above 1.71 V. In the potential range below 1.61 V, the continuous oxidations of Ag and Co species are the dominant reactions, which cause the rapid decrease of the current since they are surface limited reactions. With the increase in the potential to 1.71 V, oxygen evolution reaction starts to dominate and the current transient curves start to deviate from each other. The degree of the deviation becomes larger with further increase in the potential to 1.8 V. This is mainly because the current decreases more rapidly at 1.8 V, when the rotation rate was set at 10 Hz rather than 40 Hz. This decrease in the current is due to the formation of blocking layer consisting of oxygen bubbles, which are attached at the electrode surface as shown in Fig. 3.8. When the rotation rate was set at 40 Hz, small undulations appeared on the current response curve because the produced oxygen molecules are detached easily once they gathered a certain amount, and finally there is almost no change in the current. Fig. 3.7a and b also show the CVs before/during/after the measurement of the catalyst stability for OER. It is found that the ORR limiting current increases slightly after holding the potentials during OER in subsequent one potential cycle, and then becomes constant as before. All these results suggest that ORR and OER on Co_3O_4/Ag electrode possesses higher catalytic activity and stability and the hybrid bimetallic catalyst Co_3O_4/Ag could be an eligible candidate catalyst for rechargeable metal-air batteries.

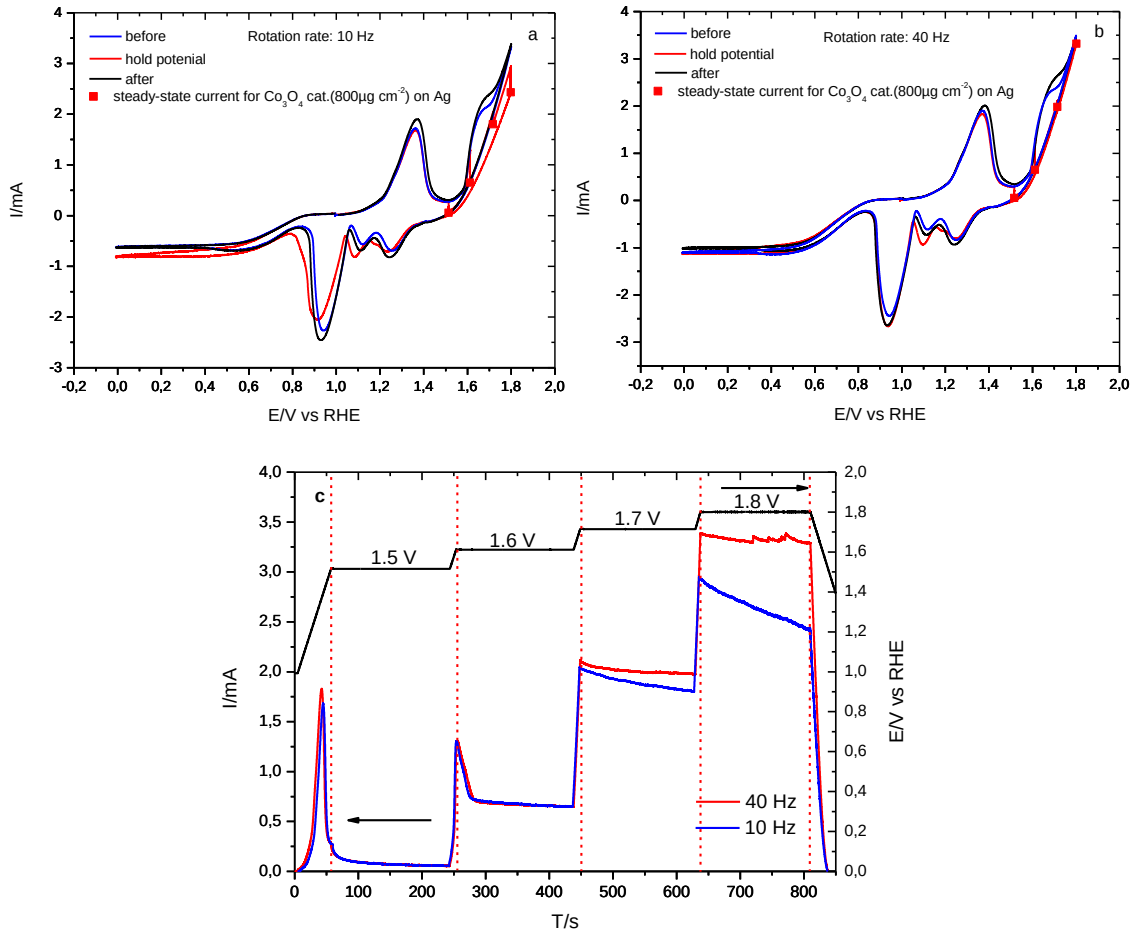

Fig. 3.7 Cyclic voltammograms of ORR and OER on 800 µg cm^{-2} Co_3O_4/Ag electrode in O_2-saturated 0.1 M LiOH solution at a scan rate of 10 mV s^{-1} and a rotation speed of 10 Hz (a) and 40 Hz (b). (c) Chronoamperometric response of the 800 µg cm^{-2} Co_3O_4/Ag electrode at 1.51, 1.61, 1.71, 1.8 V for 3 min in O_2-saturated 0.1 M LiOH.

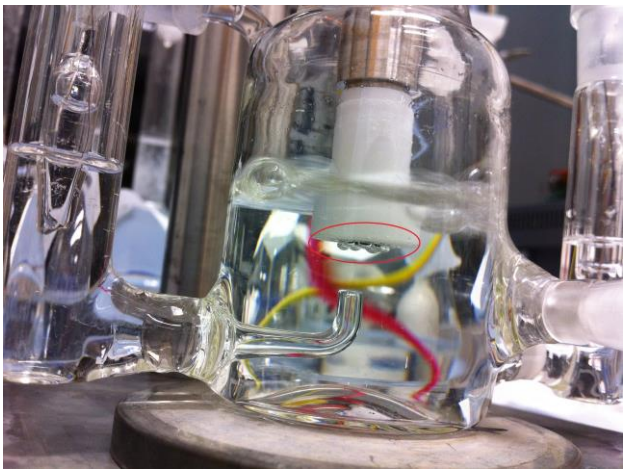

Fig. 3.8 Image of the formation of oxygen bubbles on 800 µg cm^{-2} Co_3O_4/Ag electrode in the case of holding the potential at 1.8 V for 3 min in O_2-saturated 0.1 M LiOH solution with a rotation rate of 10 Hz.

3.3.2 Surface characterization

In order to get insight into the properties and surface distributions of the Co_3O_4 particles, it is necessary to characterize the electrode surface by the surface characterization techniques such as scanning probe microscopy (SPM), X-ray diffraction (XRD) spectra, X-ray Photoelectron Spectroscopy (XPS), etc. In this work, the scanning electron microscope (SEM) and the determination technique of surface active site (Pb-UPD) were employed.

Observation of surface morphology by SEM

The surface morphologies of the electrodes before and after potential cycling in Ar saturated electrolyte were imaged by scanning electron microscope (SEM) as shown in Fig. 3.9 and Fig. 3.10, respectively. Before ORR and OER, it is clear that a part of the Ag disk electrode surface (~40%) was covered by Co_3O_4 nanoparticles (< 50 nm), but part of its surface is still exposed, and the boundary of Co_3O_4 nanoparticles and Ag disk electrode is very clear. In addition, some large particles with a certain shape are observed, which are probably larger Co_3O_4-spinel particles. After 6 potential cycles in the potential range of ORR and OER (see. inset of Fig. 3.10a), the substrate surface becomes rough and the boundary of Co_3O_4 nanoparticles and Ag disappeared (compared Fig. 3.9b with Fig. 3.10b). Nevertheless, the large particles with a certain shape are still observed obviously and they are intact. The changes in surface morphology could be contributed to a series of the oxidation and reduction reactions of Co and Ag species, leading to the surface rough and the slight migrations of surface atoms and molecules. It is found that Ag can be oxidized into Ag_2O or $AgIAgIIIO_2$ during OER [23]. This may cause the change in surface morphology. The charge of the peak at 1.38 V in the first potential cycle (see. inset of Fig. 3.10a) is calculated to be ~6×10^4 μC cm^{-2}, which means that ~279 Ag layers are oxidized by assuming that a monolayer of Ag requires 215 μC cm^{-2} for one electron transfer process determined by Pb-UPD stripping peak charge in this work. Furthermore, Co_3O_4 may promote Ag oxidation and reduction as mentioned before because when the Ag electrode are loaded with Co_3O_4, the Ag oxidation and reduction peaks do not become smaller but become larger than that of bare Ag electrode as shown in Fig. 3.11.

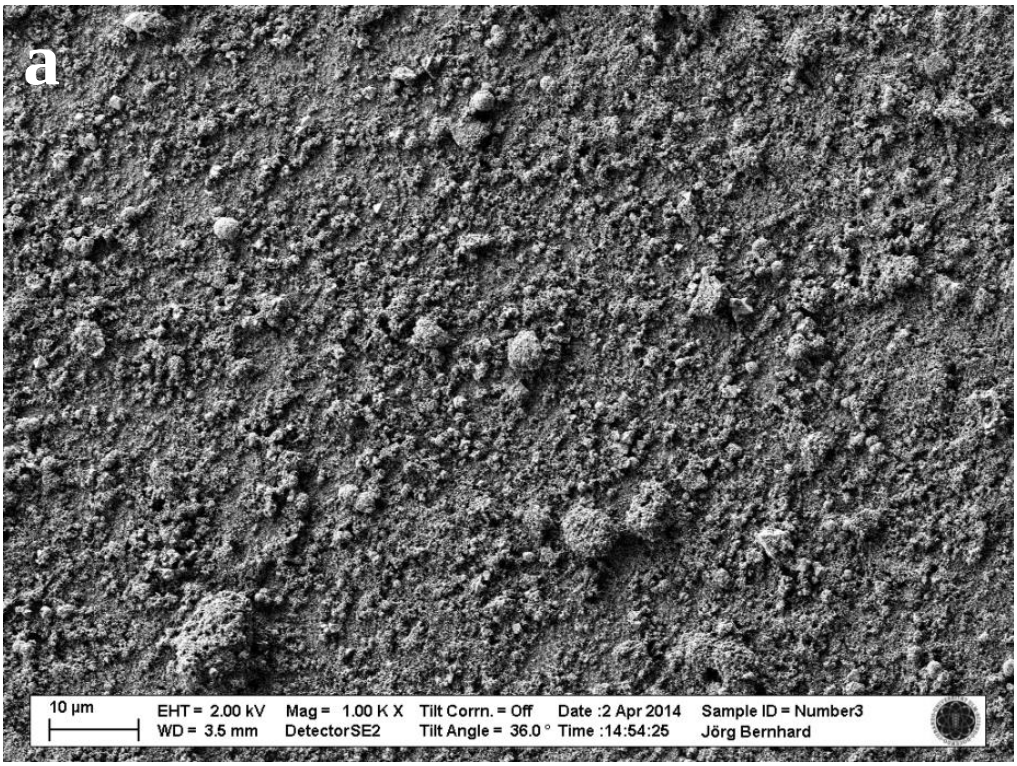
a
10 µm
EHT = 2.00 kV
WD = 3.5 mm
Mag = 1.00 K X
DetectorSE2
Tilt Corrn. = Off
Tilt Angle = 36.0 °
Date :2 Apr 2014
Time :14:54:25
Sample ID = Number3
Jörg Bernhard

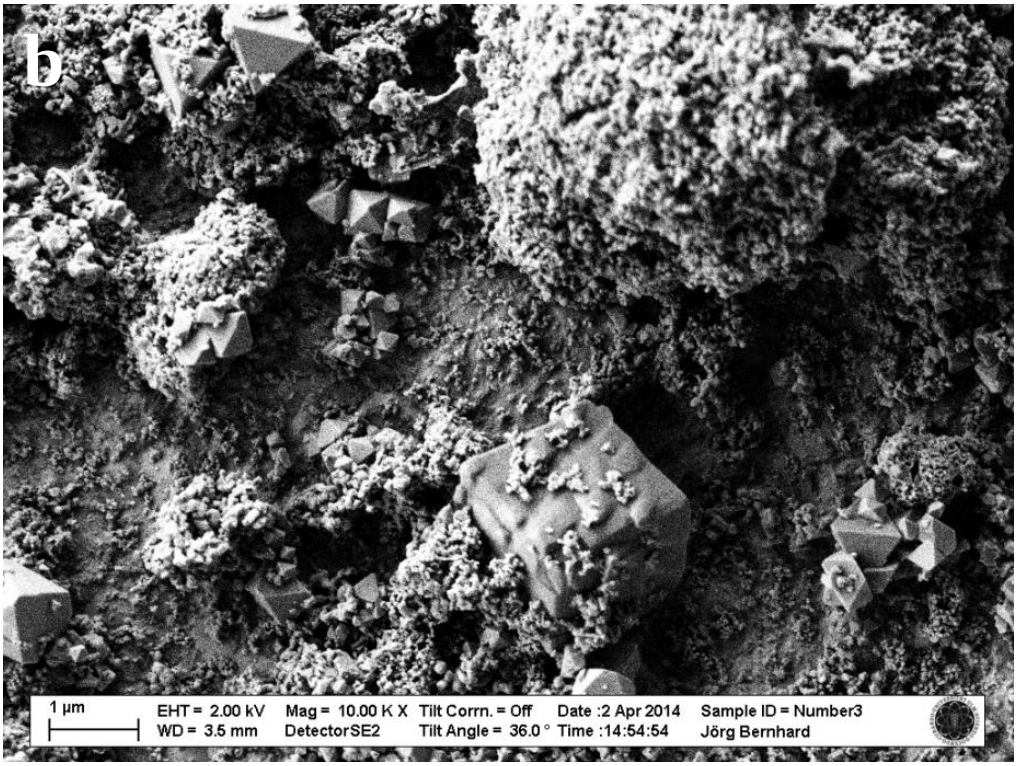
b
1 µm
EHT = 2.00 kV
WD = 3.5 mm
Mag = 10.00 K X
DetectorSE2
Tilt Corrn. = Off
Tilt Angle = 36.0 °
Date :2 Apr 2014
Time :14:54:54
Sample ID = Number3
Jörg Bernhard

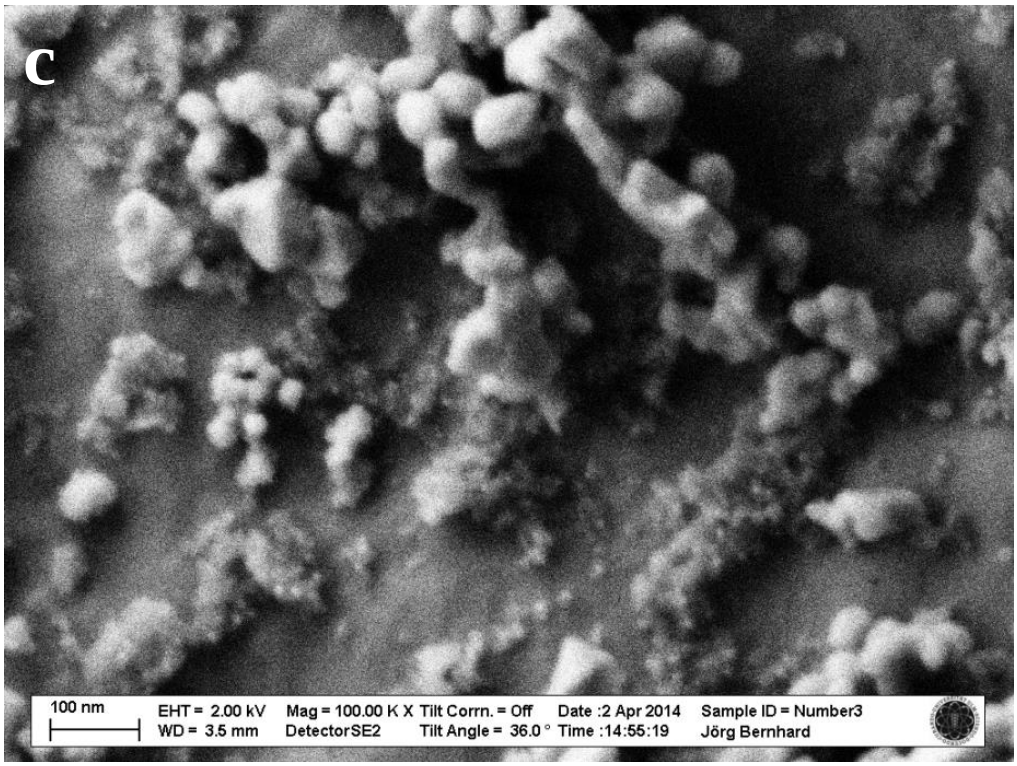

Fig. 3.9 SEM images of 800 µg cm^{-2} Co_3O_4/Ag disk electrode without Nafion binder before ORR and OER.

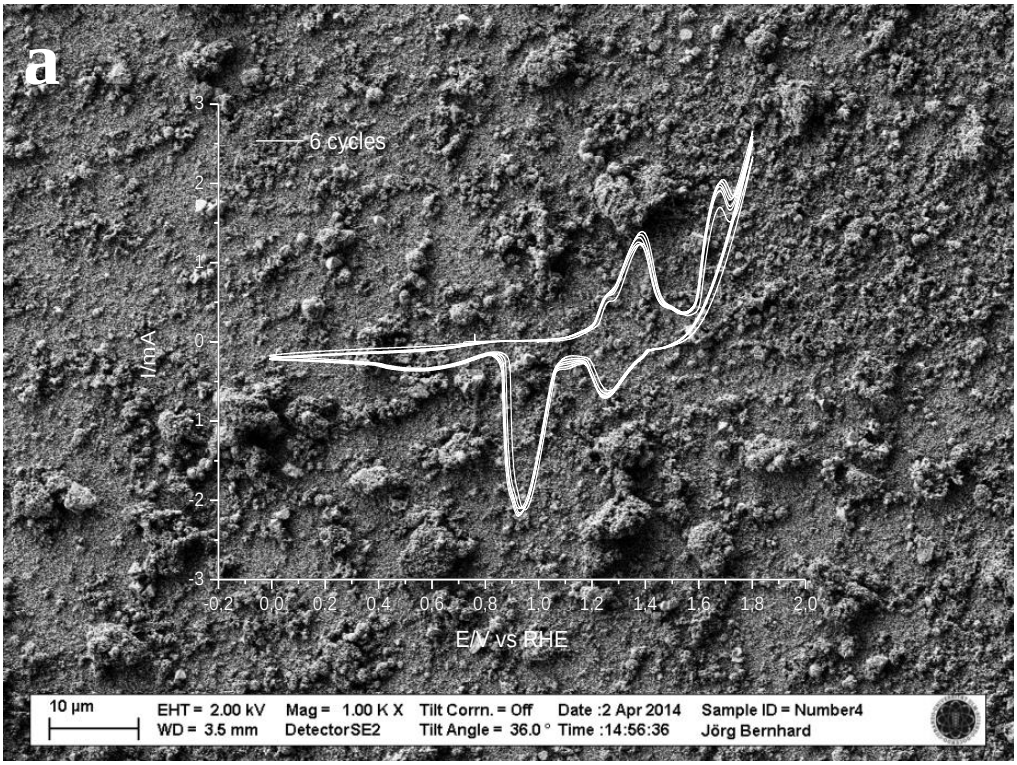

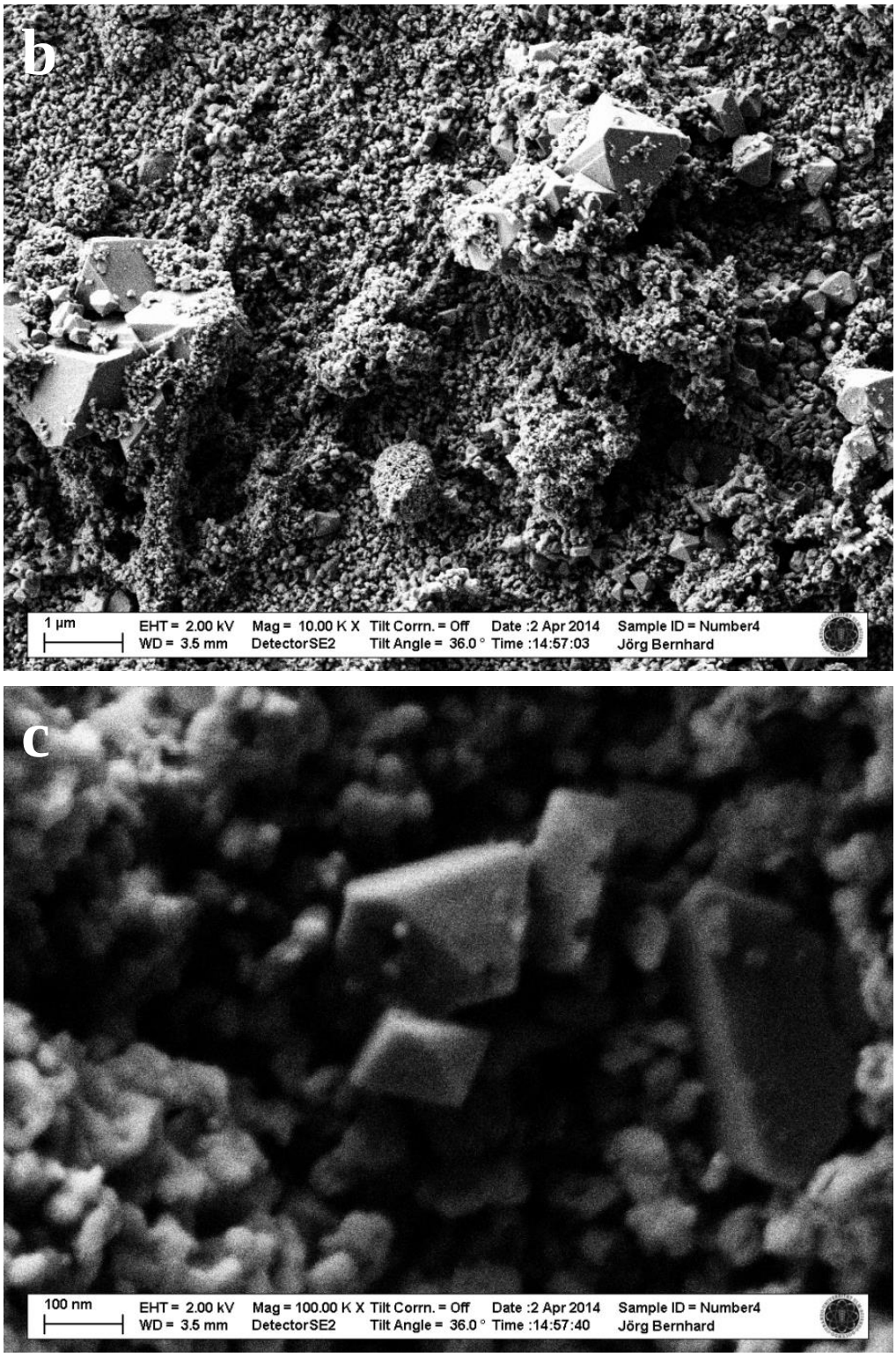

Fig. 3.10 SEM images of 800 µg cm^{-2} Co_3O_4/Ag disk electrode without Nafion binder after potential cycling in Ar saturated electrolyte, respectively. Inset of Fig. 3.9a is cyclic voltammogram of 800 µg cm^{-2} Co_3O_4/Ag electrode in 0.1 M LiOH with a sweep rate of 20 mV s^{-1}.

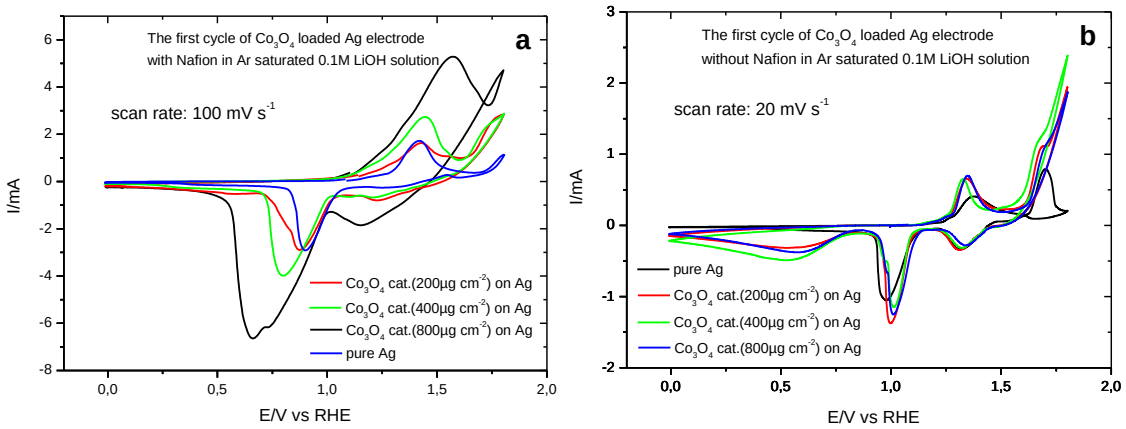

Fig. 3.11 Cyclic voltammograms of pure Ag, 200/400/800 µg cm^{-2} Co_3O_4/Ag, 800 µg cm^{-2} Co_3O_4/C electrode in Ar-saturated 0.1 M LiOH solution. (a) with Nafion binder, (b) without Nafion binder.

Determination of active and accessible Ag sites on the surface by Pb-UPD

Whereas for a Pt electrode the adsorption of a monolayer of CO or hydrogen can be used to determine the accessible sites of Pt, on Ag only UPD of another metal can be used for this propose. Pb_{upd}-stripping is a suitable method to determine the amount of surface active sites of Ag [25].

In order to determine the area of non-blocked silver on the electrode surface, Pb-UPD was carried out in the Pb containing solution to determine the amount of the active sites of silver. Considering that Nafion may influence on the Pb-UPD on active Ag surface, Nafion binder was not employed to bind Co_3O_4 nanoparticles on Ag electrode surface. As shown in Fig. 3.12c, Nafion has a large effect on Pb-UPD on the Ag electrode surface with the lower loadings of Co_3O_4 (< 400 µg cm^{-2}). However, it has an ignorable effect on the Ag electrode surface with the larger loadings of Co_3O_4 (≥ 400 µg cm^{-2}). Fig. 3.12a and b show the cyclic voltammograms of Pb-UPD obtained at the electrode surfaces without Nafion binder before and after potential cycling in Ar saturated electrolyte, respectively, in the solution of 0.1 M LiOH + 125 µM $Pb(NO_3)_2$ by holding the electrode potential at 0.23 V versus RHE for 5 min, and then cycling potential in UPD region at 10 mV s^{-1}, and the corresponding plots of Pb_{upd} stripping charges vs. the coverages of Co_3O_4 on Ag before and after potential cycling in Ar saturated electrolyte are shown in Fig. 3.12c and d, respectively. In the CVs, the reversible peak in the potential range from 0.25 to 0.5 V is related to the oxidation of Pb_{upd} to PbII and the reduction of PbII to Pb_{upd} in the anodic and cathodic scans, respectively. [45] A small

broad peak appears at ~0.5 V after potential cycling in Ar saturated electrolyte probably indicates Pb-alloy formation. The charge for monolayer formation of Pb-UPD on a smooth surface was found to be 260 µC cm^{-2} [46]. Therefore, on the pure Ag electrode in our experiment, the Pb_{upd}-stripping charge was found to be 430 µC cm^{-2} before ORR and OER, corresponding to an apparent roughness factor of ~1.65 (i.e. real surface area for Ag: ~1.65 cm^2 per cm^2 geometric area). By loading Co_3O_4 nanoparticles on Ag electrode surface, the surface area of the Ag electrode available for Pb-UPD is reduced. It is indicated by the reduced Pb_{upd} charge and Pb_{upd}-stripping charge for Pb_{upd} (Fig. 3.12c). According to the charge decrease during Pb_{upd}-stripping, 70% of the Ag surface area was blocked by loading 800 µg cm^{-2} Co_3O_4 on Ag electrode surface, which shows the highest catalytic activity in this work. It is slightly lower than the value for Ag311 + Co_3O_4 (10 wt%) nanoparticles, where about 88% of the Ag sites were blocked and which performed a best catalytic activity [23].

However, as shown in Fig. 3.12d, after potential cycling in Ar saturated electrolyte on the pure Ag electrode the Pb_{upd}-stripping charge was found to be 1750 µC cm^{-2}, around fourfold larger than that before ORR and OER. This is due to the increase in the surface roughness during oxidation and reduction of Ag. On Co_3O_4/Ag electrode, the ratio of the Pb_{upd}-stripping charge after potential cycling in Ar saturated electrolyte to the Pb_{upd}-stripping charge before ORR and OER increased from 4 (pure Ag) to 6 (800 µg cm^{-2} Co_3O_4/Ag) gradually. It indicates that there is change in the surface composition of the electrode, appearing to be consistent with our SEM results. The change in the surface composition is probably due to the migration of surface atom or molecules as mentioned before. It seems that Ag species were migrated to the surrounding Co_3O_4 nanoparticles surface. Nevertheless, the Pb_{upd}-stripping charge also decreases with the increase of the coverage of Co_3O_4 on Ag electrode. In addition, from the plot of Co_3O_4 coverage vs. $\log J_K$ (Fig. 3.12d), it shows that the kinetic current at 0.7 V on 800 µg cm^{-2} Co_3O_4/Ag electrode surface is the highest, indicating that the reaction rate is fastest, compared to others.

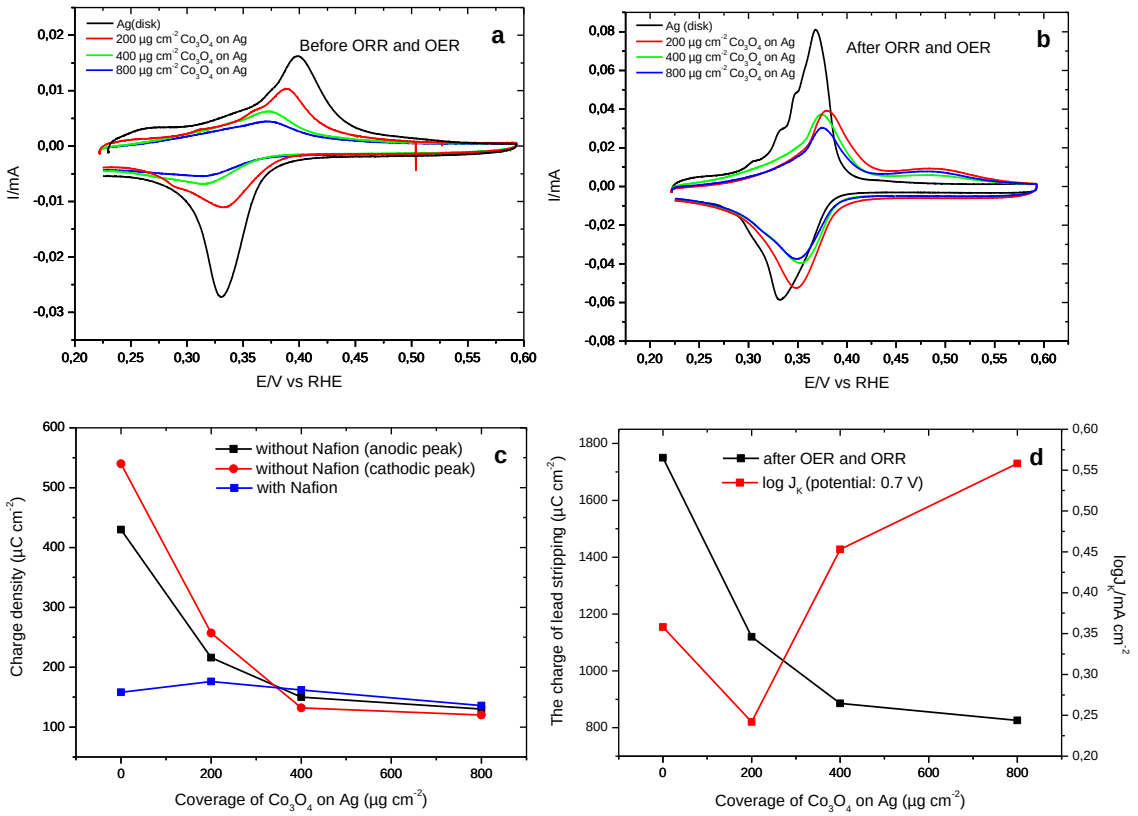

Fig. 3.12 Cyclic voltammograms of Pb-UPD at the Ag electrode covered with different amounts of Co_3O_4 without Nafion binder before (a) and after (b) potential cycling in Ar saturated electrolyte, respectively. The plots of Pb_{upd} and Pb_{upd} stripping charges vs. the coverages of Co_3O_4 on Ag before (c) and after (d) potential cycling in Ar saturated electrolyte, respectively, and the plot of coverage of Co_3O_4 on Ag vs. log J_K (d).

3.3 Conclusions

Co_3O_4 nanoparticles/Ag electrode was prepared by physical deposition and investigated for catalyzing oxygen reduction and evolution reactions in alkaline solution. Due to a synergistic effect the catalytic activity of Ag for ORR was greatly enhanced by Co_3O_4 and the catalytic activity of Co_3O_4 for OER was also enhanced by Ag. By comparison, 800 µg cm^{-2} Co_3O_4/Ag demonstrated better catalytic activity and stability for both ORR and OER. The mechanisms of both reactions were studied by RRDE experiments. For ORR, the yield of peroxide species (H_2O_2) was greatly reduced to less than 2% and the four-electron transfer process on this Co_3O_4/Ag electrode surface is preferred, which is comparable to the commercial Pt/C catalyst. Probably, the adsorption mode of the reactants or intermediates changed. For OER, no change in the mechanism was observed, but the current efficiency was improved significantly. Interestingly, the ratio of active sites of silver after potential cycling in Ar saturated electrolyte to that before

increased with the increase in the amount of Co_3O_4, suggesting that the electrode surface composition was changed, probably due to the migrations of surface species. By comparison with other catalysts for ORR and OER, even in the literatures, the hybrid bimetallic catalyst of Co_3O_4 nanoparticles/Ag possesses many advantages such as non-precious, bifunctional, higher catalytic activity and stability, etc.

References

[1] L. Demarconnay, C. Coutanceau, and J. M. Leger, Electrochimica Acta 49:4513 (2004).
[2] N. Markovic, H. Gasteiger, and P. N. Ross, Journal of the Electrochemical Society 144:1591 (1997).
[3] N. Ramaswamy and SanjeevMukerjee, Advances in Physical Chemistry 2012:491604 (2012).
[4] N. Imanishi and O. Yamamoto, Materials Today 17:24 (2014).
[5] P. G. Bruce, S. A. Freunberger, L. J. Hardwick, and J.-M. Tarascon, Nat Mater 11:19 (2012).
[6] P. Stevens, G. Toussaint, G. Caillon, P. Viaud, P. Vinatier, C. Cantau, O. Fichet, C. Sarrazin, and M. Mallouki, ECS Trans 28:1 (2010).
[7] L. Carlsson and L. Öjefors, J. Electrochem. Soc. 127:525 (1980).
[8] J.-S. Lee, S. Tai Kim, R. Cao, N.-S. Choi, M. Liu, K. T. Lee, and J. Cho, Advanced Energy Materials 1:34 (2011).
[9] B. B. Blizanac, P. N. Ross, and N. M. Markovic, Journal of Physical Chemistry B 110:4735 (2006).
[10] Q. Wang, X. Cui, W. Guan, L. Zhang, X. Fan, Z. Shi, and W. Zheng, Journal of Power Sources 269:152 (2014).
[11] E. J. Lim, S. M. Choi, M. H. Seo, Y. Kim, S. Lee, and W. B. Kim, Electrochemistry Communications 28:100 (2013).
[12] F. H. B. Lima, J. F. R. de Castro, and E. A. Ticianelli, Journal of Power Sources 161:806 (2006).
[13] M. Innocenti, G. Zangari, C. Zafferoni, I. Bencistà , L. Becucci, A. Lavacchi, F. Di Benedetto, S. Bellandi, F. Vizza, and M. L. Foresti, Journal of Power Sources 241:80 (2013).
[14] S.-A. Park, H. Lim, and Y.-T. Kim, Acs Catalysis 5:3995 (2015).
[15] S.-A. Park, E.-K. Lee, H. Song, and Y.-T. Kim, Scientific Reports 5 (2015).
[16] Y. Wang, X. Lu, Y. Liu, and Y. Deng, Electrochemistry Communications 31:108 (2013).
[17] Q.-Z. Xu, Y.-Z. Su, H. Wu, H. Cheng, Y.-P. Guo, N. Li, and Z.-Q. Liu, Current Nanoscience 11:107 (2015).
[18] Y. Meng, W. Song, H. Huang, Z. Ren, S.-Y. Chen, and S. L. Suib, Journal of the American Chemical Society 136:11452 (2014).
[19] A. J. Jeevagan, Y. Suzuki, T. Gunji, G. Saravanan, Y. Irii, T. Tsuda, T. Onobuchi, S. Kaneko, G. Kobayashi, and F. Matsumoto, ECS Transactions 58:9 (2014).
[20] G. Du, X. Liu, Y. Zong, T. S. A. Hor, A. Yu, and Z. Liu, Nanoscale 5:4657 (2013).
[21] N. Cheng, R. Kutz, C. Kemna, and A. Wieckowski, Journal of Electroanalytical Chemistry 705:8 (2013).
[22] T. S. Olson, S. Pylypenko, J. E. Fulghum, and P. Atanassov, Journal of the Electrochemical Society 157:B54 (2010).
[23] H. M. A. Amin, H. Baltruschat, D. Wittmaier, and K. A. Friedrich, Electrochimica Acta 151:332 (2015).
[24] D. A. Slanac, A. Lie, J. A. Paulson, K. J. Stevenson, and K. P. Johnston, The Journal of Physical Chemistry C 116:11032 (2012).
[25] H. M. A. Amin and H. Baltruschat, in preparation.
[26] T. Saito, T. H. Roberts, T. E. Long, B. E. Logan, and M. A. Hickner, Energy & Environmental Science 4:928 (2010).
[27] G. E. Totten and H. Liang, Surface Modification and Mechanisms: Friction, Stress, and Reaction Engineering, 2004.
[28] V. R. Stamenkovic, B. S. Mun, M. Arenz, K. J. J. Mayrhofer, C. A. Lucas, G.

Wang, P. N. Ross, and N. M. Markovic, Nature Materials 6:241 (2007).
[29] Y. Cai and R. R. Adzic, Advances in Physical Chemistry 2011:530397 (2011).
[30] V. Stamenkovic, B. S. Mun, K. J. J. Mayrhofer, P. N. Ross, N. M. Markovic, J. Rossmeisl, J. Greeley, and J. K. Nørskov, Angew. Chem., Int. Ed. 45:2897 (2006).
[31] J. Zhang, M. B. Vukmirovic, Y. Xu, M. Mavrikakis, and R. R. Adzic, Angew. Chem., Int. Ed. 44:2132 (2005).
[32] H. Lin, W. Tang, A. Kleiman-Shwarsctein, and E. W. McFarland, Journal of the Electrochemical Society 155:B200 (2008).
[33] Y. Liang, Y. Li, H. Wang, J. Zhou, J. Wang, T. Regier, and H. Dai, Nature Materials 10:780 (2011).
[34] Z. Wu, W. Li, Y. Xia, P. Webley, and D. Zhao, Journal of Materials Chemistry 22:8835 (2012).
[35] A. Holewinski and S. Linic, Journal of the Electrochemical Society 159:H864 (2012).
[36] J. X. Wang, J. Zhang, and R. R. Adzic, Journal of Physical Chemistry A 111:12702 (2007).
[37] N. A. Knott, Silver and silver-manganese cathode catalysts for alkaline fuel cells, 2007.
[38] N. Markovic, H. Gasteiger, and J. Philip N. Ross, Journal of the Electrochemical Society 144:1591 (1997).
[39] A. Damjanovic, Modern Aspects of Electrochemistry, 1969.
[40] R. Jinnouchi, K. Kodama, T. Hatanaka, and Y. Morimoto, Phys. Chem. Chem. Phys 13:21070 (2011).
[41] C. Iwakura, A. Honji, and H. Tamura, Electrochimica Acta 26:1319 (1981).
[42] R.-N. Singh, M. Hamdani, J.-F. Koenig, G. Poillerat, J. L. Gautier, and P. Chartier, Journal of Applied Electrochemistry 20:442 (1990).
[43] P. Rasiyah and A. C. C. Tseung, J. Electrochem. Soc. 130:365 (1983).
[44] A. Restovic, G. Poillerat, J. F. Koenig, and P. Chartier, Thin Solid Films 199:139 (1991).
[45] M. Hepel and S. Bruckenstein, Electrochimica Acta 34:1499 (1989).
[46] E. Kirowa-Eisner, Y. Bonfil, D. Tzur, and E. Gileadi, Journal of Electroanalytical Chemistry 552:171 (2003).

Chapter 4: ORR and OER on Co modified Ag electrode surface

To achieve a bimetallic bifunctional catalyst with high stability and efficiency in the cathode of Li-air battery, it is an alternative method to assemble catalysts by using electrochemical modification instead of physical modification. In this chapter, the bimetallic catalyst of the flower like Co/Ag prepared by electrochemical deposition was examined for catalysis the ORR and OER. The surface has been characterized by SEM and Pb-UPD techniques. An in-situ EC-STM was employed for observing the growth mechanism of Co on Ag surface.

4.1 Introduction:

Bimetallic catalysts [1-3] have been attracting significant attention in the field of heterogeneous catalysis because of their outstanding performance in the potential of enhancing catalytic activity and stability as compared to their monometal. However, as well known, the performance of catalyst is dominated by its structure, shape, size, components and its content, etc. It means that the preparation method is one of the important factors for obtaining a catalyst with high activity, stability and durability. Traditional way to prepare the bimetallic catalyst, such as impregnation [4-6] or co-impregnation [7, 8] of two metal salts and precipitation [9-11] have some disadvantages of reducing the catalyst active area due to high temperature sintering to form the alloy, suffering from an inability to carefully control the component content and homogeneity, and so on. Furthermore, most of these catalysts were bonded or supported on the electrode by using an adhesive, which probably covered the active sites of the catalyst leading to catalysts deactivation and could be decomposed during the reactions causing the loss of catalysts. Electroless deposition [12, 13] seems to be an effective method, but it is uncontrollable and normally requires strict conditions such as high temperature, noble metal, etc. In this paper, simple and controllable electrochemical deposition method was used to prepare the Co/Ag catalyst with high homogeneity, stability, reproducibility and bifunctional activity.

Recently, the bimetallic catalysts were widely used for catalyzing the ORR in metal-air batteries. Most of these studies were focused on the noble metal based bimetallic catalyst such as Ni or Co/Pt [14], Pt/Ru [15], Pt_3/M (Ag, Au, Co, Ni, etc.) [16], Pt/Pd [17], Ru/M(Se, Mo, W, Sn) [18], Pt/Au [19], etc, which can improve dramatically the catalytic activity for ORR compared to their monometal. However, the study of

bifunctional catalytic activity of catalyst for ORR and OER was absent except for Pt/Au [20] and these catalysts have a fatal disadvantage of high cost. To meet the requirement of the rechargeable battery, it is necessary to prepare a bifunctional catalyst, which can be used for both ORR and OER in metal-air battery. Most of these catalysts were based on the metal oxides [21-23], which have poor conductivity.

Silver is much less expensive than the usual noble metals. It was also widely used as excellent catalyst for ORR in metal-air battery due to its lower cost and high performance. To improve its catalytic activity, its different single crystal structure [24], size [25], shape [26, 27], modification [28-31] with other metal/metal oxide to form bimetallic catalysts, etc, have been studied. It is found that surface modification is one of the powerful approaches to improve its performance for ORR. Few of these studies were focused on bifunctional catalytic activity. Nanoporous Ag-embedded SnO_2 thin film [21] and Ag nanoparticle-modified MnO_2 nanorods [32] have been determined to possess a bifunctional catalytic activity for both ORR and OER, but the electron transfer numbers of ORR were found to be 3.7 and 3.1, respectively, and there was no study on the yield of peroxide and the stability of catalyst activity in both cases. Our previous studies revealed that the mixture of the Co_3O_4 and Ag311 particles [33] and Co_3O_4/Ag_{disk} (in chapter 3) have bifunctional catalysis activity for both ORR and OER, but these catalysts was prepared by physical modification, which cause particle uneven distribution and catalyst loss. However, the investigation of the bifunctional Co/Ag catalyst obtained by electrochemical modification for catalyzing both ORR and OER have never been reported yet.

In this work, we employed the electrochemical modification of Ag disk electrode with Co to achieve a bimetallic bifunctional catalyst for reversible oxygen reduction/evolution reaction in alkaline solution. The optimized composition was found by comparing the performance of the catalysts obtained by the electrochemical modification for different time. The mechanisms of oxygen reduction and evolution reactions on this catalyst were studied by rotating ring-disk electrode (RRDE) technique. The characterization of the catalyst surface was carried out by underpotential deposition of Lead (Pb_{UPD}) and scanning electron microscope (SEM). Furthermore, the mechanism of Co growth on Ag electrode was performed by an electrochemical-scanning tunneling microscope (EC-STM).

4.2 Experimental:

4.2.1 Preparation of Co/Ag bimetallic catalyst

Cobalt/silver bimetallic catalysts were prepared by electrochemical deposition through using a three electrodes system on silver electrode (0.196 cm^2) starts. The solution contained 0.05 mol L^{-1} $CoCl_2$ + 0.5 mol L^{-1} $B(OH)_3$ in Milli-Q water (18.2 MΩ cm, TOC of 5 ppm) and saturated with argon at room temperature. Reversible hydrogen electrode (RHE) prepared by electroanalysis the electrolyte of 0.05 mol L^{-1} K_2SO_4 + 0.5 mol L^{-1} $B(OH)_3$ in water was used as a reference electrode and separated from cobalt solution during electrochemical deposition; Pt foil (~1 cm^2) was used as counter electrode and Ag disk was used as work electrode. The different catalyst compositions (i.e. loading by Co) were achieved by holding the potential at the constant value of -0.42 V (vs. RHE) for 15 s, 30 s, 45 s, and 60 s. The catalysts were activated in 0.1 mol L^{-1} LiOH by conducting 10 potential cycles from 0 to 1.8 V, especially for catalyzing OER. For preparing the Co_3O_4 nanoparticles (< 50 nm)/Ag and GC were described in chapter 3.

4.2.2 Rotating ring-disk electrode (RRDE) measurements

Homemade RRDE setup combined with the disk electrode provided by the company (Pine Research Instrumentation, Pennsylvania, USA) and LabVIEW software (National Instruments GmbH, Munich, Germany) was employed for ORR and OER measurements. The measurements were conducted in a three-electrode-H-cell with three compartments for placing the reference electrode, counter electrode and working electrode (prepared before), respectively. The reference electrode was the reversible hydrogen electrode (RHE) which was prepared by electrolysis of 0.1 mol L^{-1} LiOH generating hydrogen in the glass bulb as described in chapter 2, the counter electrode was the Pt foil with the size of 1×1 cm and the working electrodes were Ag and glassy carbon (GC) electrodes. The electrolyte was 0.1 mol L^{-1} LiOH prepared with Milli-Q water and deaerated by purging ultra-high pure argon (99.999%, Air Liquide) or oxygen (99.9995%, Air Liquide) for at least 30 min before use. During the measurements, the rotation rate was varied from 10 to 40 Hz, the disk potential was linearly swept from 0 V to 1.8 V and the ring potential was held at a constant value of 1.2 V.

4.2.3 Surface characterization

Lead-UPD was employed for detecting the number of active sites of Ag. These

measurements were performed by holding the potential at 0.23V (vs. RHE) for 5 min in the electrolyte of 125 μmol L^{-1} $Pb(NO_3)_2$ + 0.1 mol L^{-1} LiOH saturated with argon, and then cycling in the potential range of UPD in the H-cell. SEM (Zeiss dual-beam NVISION 40 with an operating voltage of 5-30 kV) at the University of Ulm was employed to observe the surface morphology of the catalysts and theirs change after potential cycling in the ORR and OER potential region.

4.2.4 EC-STM measurement

Electrochemical-scanning tunneling microscopy (EC-STM) was used for study the growth mechanism of cobalt on silver and the morphology of the Co deposits. An Agilent 5500 Scanning Probe Microscope (Agilent Technologies, Chandler, AZ) equipped with a bipotentiostat provided by keysight was employed. The tip was prepared by the electroetching of the platinum/iridium (90:10) wire with diameter of 0.25 mm in the less toxic solution of 2 mol L^{-1} KOH + 4 mol L^{-1} KSCN; it was then isolated by hot-melt glue containing different types of polymer (provided by Steinel) to minimize faradaic leakage current [34]. A homemade three-electrode STM/AFM cell was fabricated from Kel-F. It contains a large cell volume and a small chamber for placing the reference electrode connected via a small hole to the main chamber as shown in chapter 2. A glass chamber was used for keeping the electrolyte under argon atmosphere control during the STM experiments.

Preparation of an atomic smooth Ag surface was carried out by the deposition of Ag on a well prepared Pt(111) single-crystal electrode with the diameter of 1 cm in argon saturated 10^{-4} mol L^{-1} Ag_2O + 10^{-3} mol L^{-1} H_2SO_4 solution. Cleanliness of the Pt(111) was checked in 0.1 mol L^{-1} H_2SO_4. To protect the Pt(111) surface, the monolayer of Ag was pre-deposited on the Pt(111) surface in the H-cell. It was then transferred into the STM setup. The smooth multilayer of Ag was obtained in 10^{-3} mol L^{-1} H_2SO_4 + 10^{-4} mol L^{-1} Ag_2O + 10^{-2} mol L^{-1} K_2SO_4 in the STM cell. For following deposition of Co on Ag, the silver containing electrolyte was exchanged carefully with cobalt containing electrolyte (10^{-3} mol L^{-1} $CoSO_4$, 10^{-2} mol L^{-1} K_2SO_4, 10^{-4} mol L^{-1} KCl and 10^{-3} mol L^{-1} H_2SO_4) in STM cell under potential control. In H cell, RHE and Pt foil was used as reference and counter electrode, respectively. In STM cell, Pt wires were used as reference and counter electrodes. All the electrolytes were saturated with argon. All the STM images were obtained in the constant-current mode.

4.3 Results and discussion

4.3.1 The Co/Ag bimetallic electrode preparation and determination of Co coverage

The Co/Ag bimetallic catalysts were obtained by electrochemical deposition of Co onto Ag disk electrode at the potential of -0.42 V (vs. RHE) in the electrolyte of 0.05 mol L^{-1} $CoCl_2$ + 0.5 mol L^{-1} $B(OH)_3$). By holding the potential at -0.42 V for different time (15 s, 30 s, 45 s and 60 s), it is difficult to determine the amount of Co deposited on Ag by current transient measurement because H_2 evolution also takes place at this potential, but the variation of the Co overage on Ag can be achieved for comparing the catalytic activity. The coverage of Co on Ag disk electrode was determined by conducting underpotential deposition of Pb (Pb-UPD) technique [35, 36] and Ag oxidation at the first potential cycle.

The Ag surface area exposed to the electrolyte after modification with Co was determined from the charge of Pb-UPD assuming a 1:1 ratio of Pb to Ag atoms. Vice versa, also the area blocked by Co on Ag (the Co coverage) is thus determined. Pb-UPD measurements were performed in the electrolyte of 125 μmol L^{-1} $Pb(NO_3)_2$ + 0.1 mol L^{-1} LiOH and the corresponding cyclic voltammograms are shown in Fig. 4.1a. The detailed explanation of the voltammetric feature is available in chapter 3. The charge densities of Pb_{UPD} peak and its stripping peak decreased with increasing in the deposition time of cobalt on silver, as shown in Fig. 4.1b. On smooth Ag electrode, it was found that the Pb monolayer formation requires 260 μC cm^{-2} [37]. In our measurement, the Pb_{UPD}-stripping charge was found to be 480 μC cm^{-2}, which gives the apparent roughness factor of ~1.85. The coverages of Co on Ag electrode surface were calculated and shown in the inset of Fig. 4.1b. These results are close to the values which were calculated by the charge densities of silver oxidation in the first potential cycle in the 0.1 M LiOH solution. The cyclic voltammograms of Co (deposition for 0, 15, 30, 45, 60 s) on Ag electrode in Ar-saturated 0.1 M LiOH before ORR/OER measurements are shown in Fig. 4.2. It shows that the Co coverages (θ_{Co}) of 58%, 83%, 93% and 96% on Ag were obtained in the case of holding the potential at -0.42 V (vs. RHE) for 15 s, 30 s, 45 s and 60 s, respectively, by using the following equation:

$$\theta_{Co} = \frac{Q^{o}_{Ag-oxi.} - Q^{Co/Ag}_{Ag-oxi.}}{Q^{o}_{Ag-oxi.}}$$

where, $Q^{o}_{Ag-oxi.}$ is the Ag oxidation charge on pure Ag electrode surface and $Q^{Co/Ag}_{Ag-oxi.}$ is

the Ag oxidation charge on Co modified Ag electrode surface.

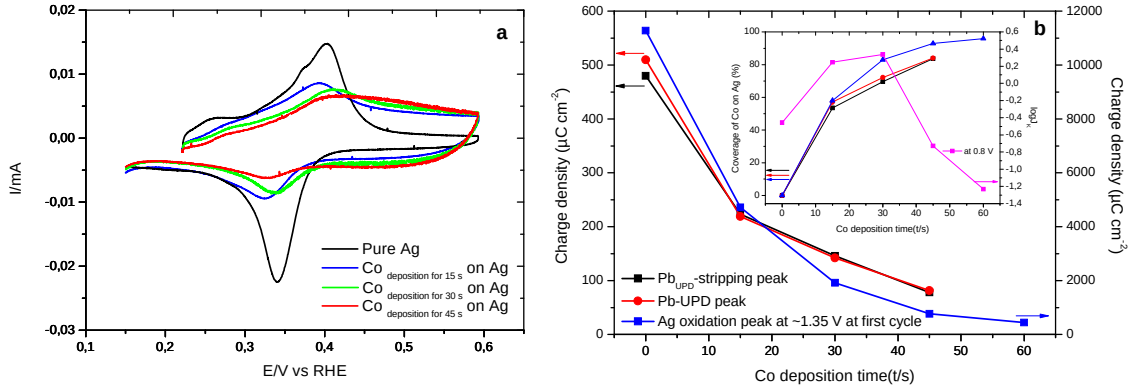

Fig. 4.1 a) Cyclic voltammograms of Pb-UPD on Ag disk electrode in the electrolyte of 125 μmol L^{-1} $Pb(NO_3)_2$ + 0.1 mol L^{-1} LiOH. b) The plots of the charges of Pb-UPD charge, its stripping charge and Ag oxidation charge vs. deposition times of Co on Ag, Inset: the deposition time dependence of the coverage of Co on Ag and ORR kinetic current.

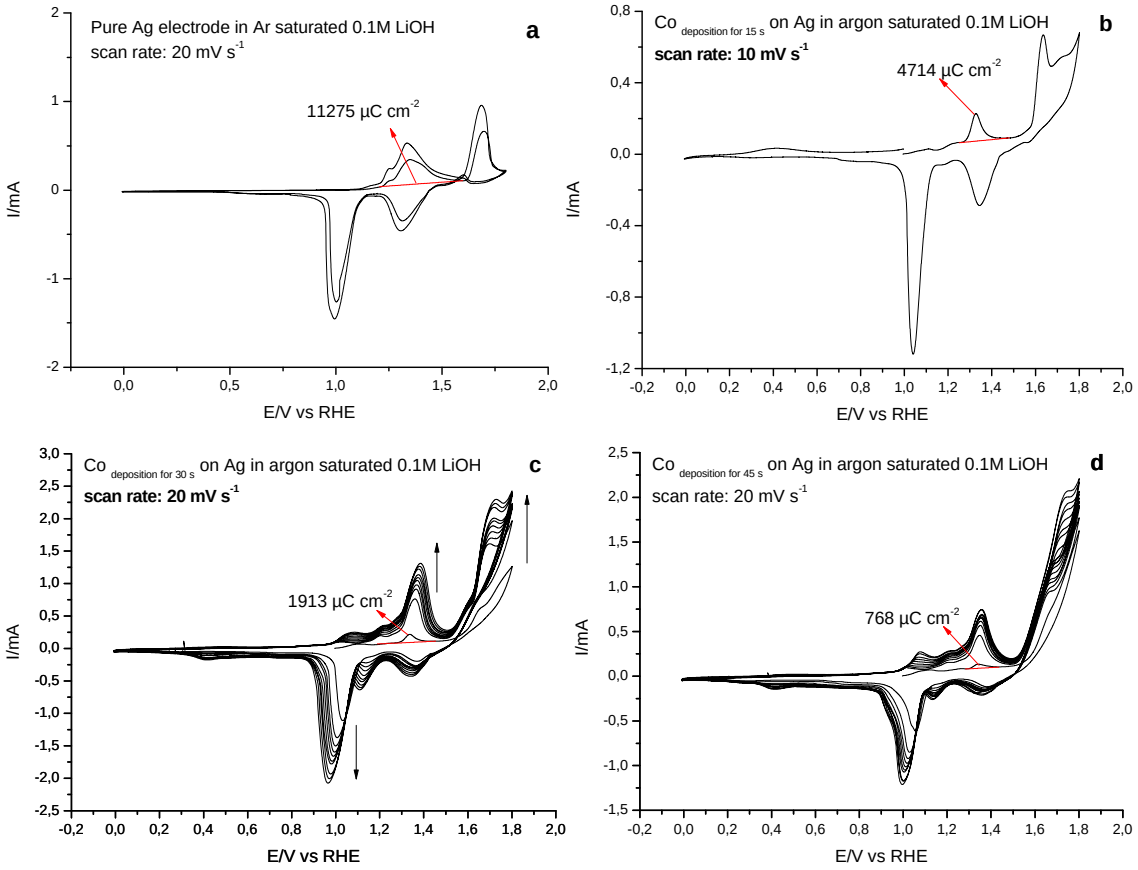

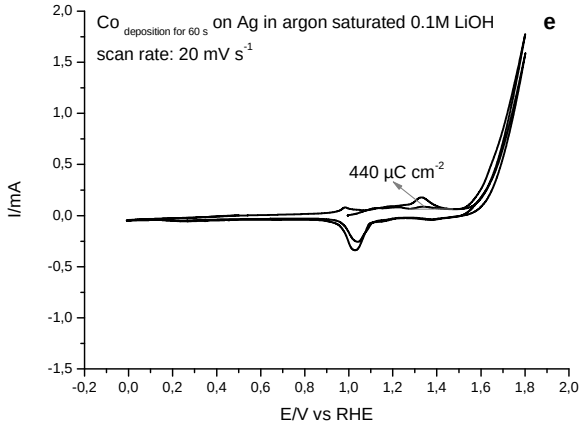

Fig. 4.2 Cyclic voltammograms of Co(deposition for 0, 15, 30, 45, 60 s)/Ag electrodes in Ar-saturated 0.1 M LiOH.

4.3.2 Electrochemical evaluation of the Co/Ag bimetallic electrode for ORR and OER

RRDE measurements have been conducted to determine the catalytic activity of these catalysts and the mechanisms of ORR and OER on these catalysts, which were prepared by electrochemical modification and physical modification (Co_3O_4/Ag and GC) for comparison.

4.3.2.1 ORR on Co/Ag bimetallic electrode

Comparation of catalytic activity of different electrode surface

For ORR on the Co/Ag bimetallic electrode surface, the onset potential of ORR shifts to more positive values with the increase of the deposition time of Co on Ag from 0 to 30 s, and then slightly shifts in negative direction with the further increase of the deposition time of Co on Ag to 45 s, as shown in Fig. 4.3. For the best Co deposition time (30 s) the ORR starts 60 mV earlier than that on pure Ag, very close to that on the commercial Pt/C catalyst. These results suggest that cobalt can enhance significantly the catalytic activity of silver for ORR. This enhancement of ORR catalytic activity is probably attributed to the shift of the d-band center caused by the change of the electronic structure of metal in the case of alloy formation with an additional metal or metal oxide [38, 39].

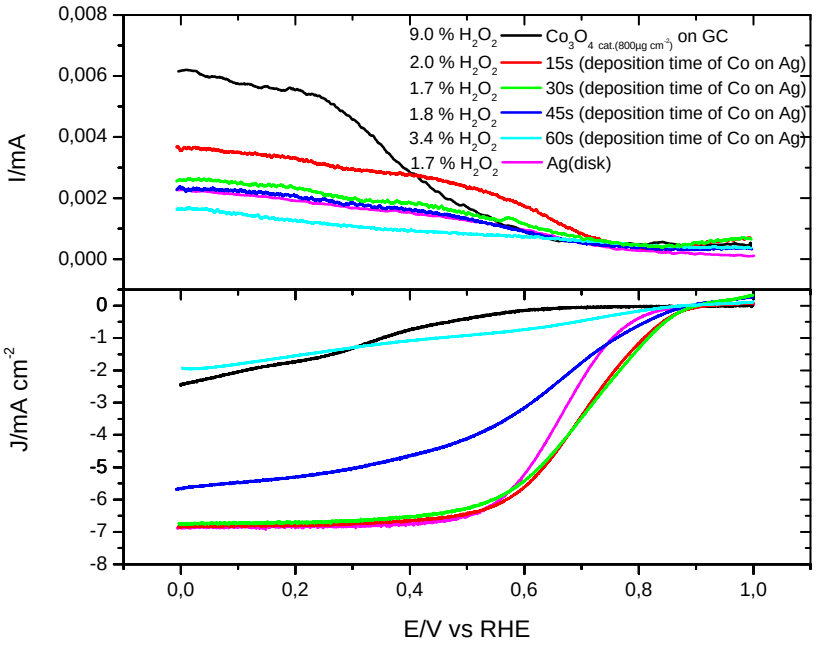

Fig. 4.3 RRDE voltammograms of ORR on Ag, 800 μg cm^{-2} Co_3O_4/Ag, 800 μg cm^{-2} Co_3O_4/C, Co(15 s, 30 s, 45 s and 60 s)/Ag electrodes in 0.1 M LiOH at the scan rate of 5 mV s^{-1} and a rotation rate of 40 Hz. Disk current density for ORR (up) and ring current (down). Inset: H_2O_2 yield.

The yield of H_2O_2 and electron transfer number

The yield of H_2O_2 was calculated by the disk current (i_D) and ring current (i_R) as shown in Fig. 4.3, using the following equation:

$$H_2O_2\% = \frac{2i_R}{Ni_D + i_R}$$ (N = 0.256, the theoretical collection efficiency)

The yield of H_2O_2 produced on the different catalysts were shown in the inset of Fig. 4.3. The results show that all the yields of H_2O_2 on the bimetallic Co/Ag catalysts are below 2% except that of Co(60 s)/Ag. In the case of using Co(30 s)/Ag as catalyst, the minimum of the H_2O_2 yield (1.5%) was obtained and the electron transfer number for ORR was calculated to be 3.97 by the following equaition:

$$n = \frac{4i_D}{i_D + i_R / N}$$

These results suggest that the Co/Ag bimetallic catalyst favours the $4e^-$ ORR pathway, which is consistent with the conclusions in the literatures [28, 31, 40].

Koutecky-Levich plots and Tafel plots

Koutecky-Levich plots and Tafel plots were obtained for the further study of the kinetics

and mechanisms of ORR and OER on this Co/Ag bimetallic catalyst, which were described by the Koutecky-Levich equation [41] and Tafel equation [42]:

$$1/j = 1/j_L + 1/j_K = 1/0.62nFC_0D_0^{2/3}\nu^{-1/6}\omega^{1/2} + 1/nFkC_0$$

$$\eta = a + b\log j_K \cdots\cdots \left(j_K = j/(1 - j/j_L) \right)$$

Where j, j_K and j_L ($mA \cdot cm^{-2}$) are the measured current density, kinetic current density and diffusion limited current density, respectively, n is the number of electron transferred in the ORR process, F is the Faraday constant (96,485 C mol^{-1}), k is the apparent rate constant, C_0 and D_0 are the concentration (0.9×10^{-6} mol cm^{-3}) and diffusion coefficient (2.0×10^{-5} cm^2 s^{-1}) of O_2 in 0.1 mol L^{-1} LiOH electrolyte at 25 ºC, respectively, ν is the kinematic viscosity of the electrolyte at 25 ºC (0.01 cm^2 s^{-1}), ω is the angular rotation speed of RRDE (rad s^{-1}), η is overpotential, a and b are constant values.

The typical ORR polarization curves on these Co(30 s)/Ag catalysts at the rotation speeds 10-40 Hz and the corresponding Koutecky-Levich plots at the different potentials were demonstrated in Fig. 4.4b. All the plots are linear and parallel dependence, which may indicate the first-order reaction with respect to oxygen concentration. The average value (3.01×10^3 cm^2 A^{-1} $s^{1/2}$) of the Koutecky-Levich slopes is very close to the theoretical value (2.93×10^3 cm^2 A^{-1} $s^{1/2}$), which has been calculated from 4 e^- transferred process. Direct four electrons transferred per oxygen molecule for ORR on this catalyst in this study is in a good agreement with results from the literature [43]. All of the RRDE voltammograms and corresponding Koutecky-Levich plots for different deposition time of Co on Ag as catalyst were shown in Fig. 4.4. When the Co deposition time reaches to 45 s, the intercept of K-L plot at 0.2 V significantly deviates from 0 (see. Fig. 4.4e), suggesting that the ORR process on this electrode surface is kinetically sluggish.

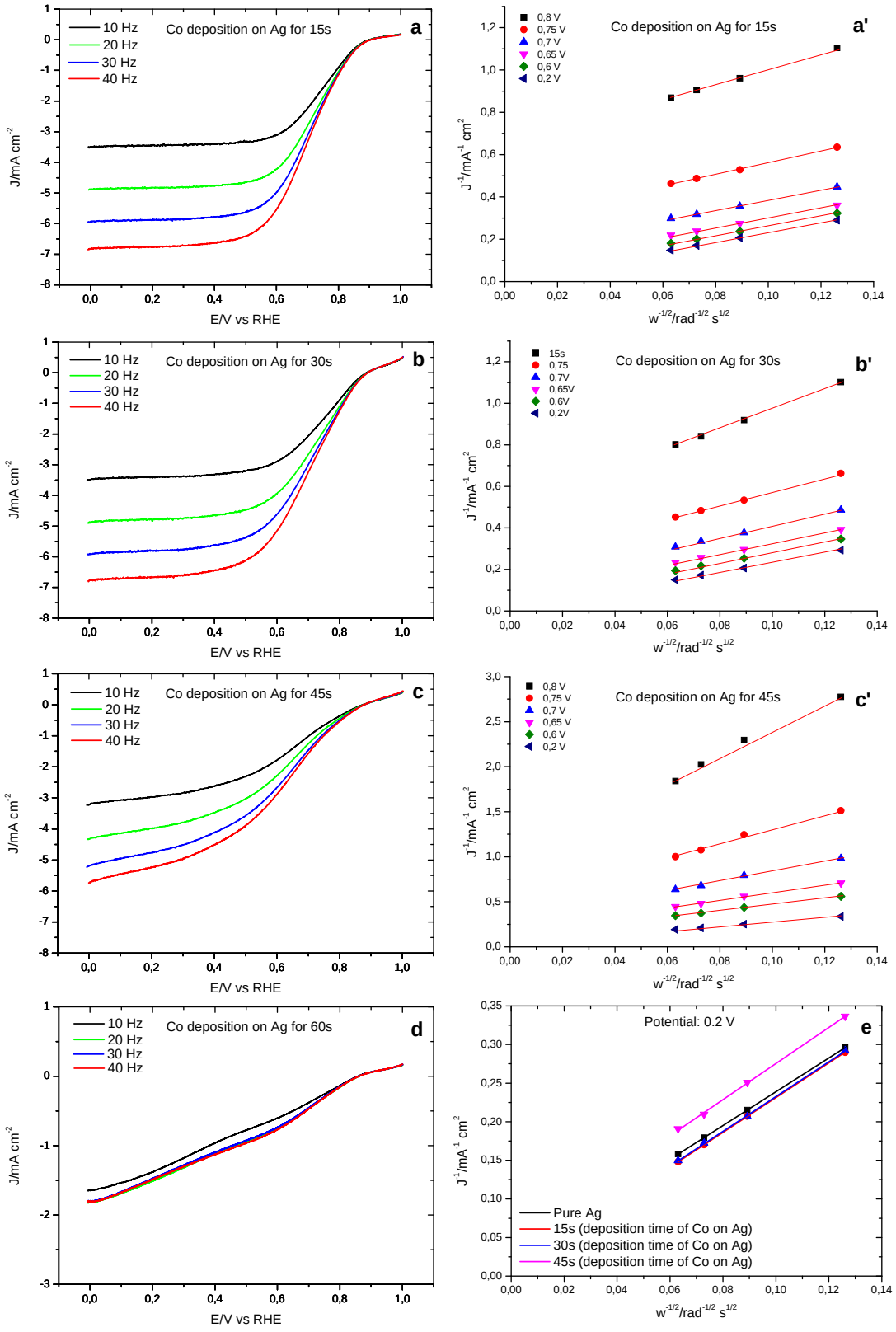

Fig. 4.4 RRDE voltammograms of ORR on Co(15 s (a), 30 s (b), 45 s (c) and 60 s (d))/Ag electrodes in 0.1 M LiOH at the scan rate of 10 mV s^{-1} and at different rotation rate indicated, and the corresponding Koutecky-Levich plots (J^{-1} vs. $\omega^{-1/2}$) at different potentials (E/V vs. RHE) showed in (a'), (b') and (c'). (e), the K-L plots at 0.2 V for different deposition time of Co on Ag electrode.

For ORR, the Tafel slopes were plotted by E vs. log (j_K) were shown in Fig. 4.5. Only one Tafel slope of 180 mV dec^{-1} was observed on Co_3O_4 catalyst. Two Tafel slopes were observed on the Co/Ag bimetallic and Ag catalysts at low and high overpotential, respectively. At low overpotential, the Tafel slopes obtained on Co/Ag bimetallic electrode surface are in the range of 70-84 mV dec^{-1}, suggesting that the rate determining step is the first electron transfer process. At high overpotential, the Tafel slopes increased from 118 mV dec^{-1} to 215 mV dec^{-1} with the increase of the deposition time of Co on Ag from 15 s to 60 s. This transition in Tafel slopes may be contributed to the change of the absorption model of intermediates [44-46] or the effect of the competitive adsorption from other adsorbates [47, 48]. However, the Tafel slopes obtained from the intercepts of corresponding K-L plots are slightly larger as shown in Fig. 4.5b, but the change of Tafel slope is similar as that observed in Fig. 4.5a.

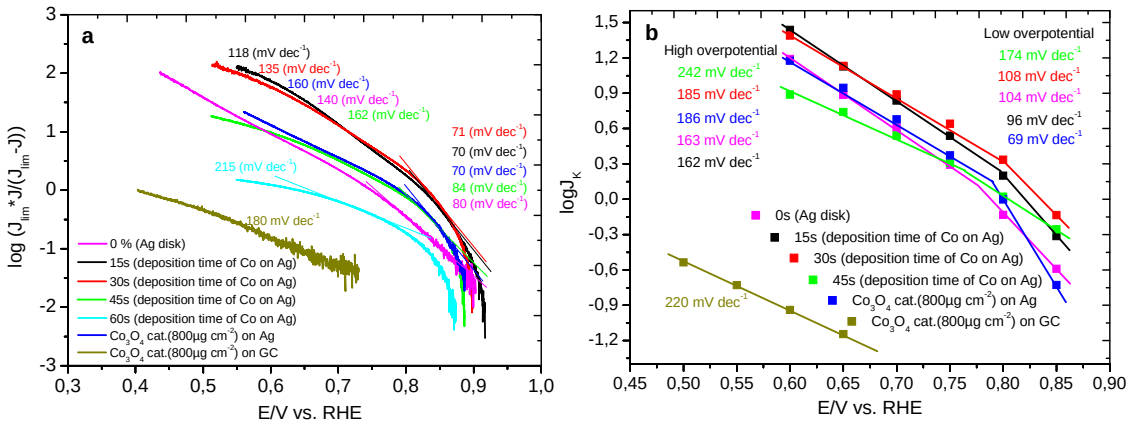

Fig. 4.5 a) iR-corrected Tafel plots of ORR for all the catalysts derived by the mass-transport correction of the corresponding RRDE data. b) non-iR-corrected Tafel plots in which the kinetic currents were obtained from the intercepts of corresponding K-L plots showed in Fig. 4.4.

4.3.2.2 OER on Co/Ag bimetallic electrode

Comparison of catalytic activity of different electrode surfaces

For OER, the polarization curves are shown in Fig. 4.6. The effect is very similar to ORR in that the onset potential of OER shifted in the direction of more negative values with the increase of the deposition time of Co on Ag from 0 to 30 s, then shifted to positive direction with further the increase of the deposition time of Co on Ag to 45 s and 60 s. It is found that in the case of using Co(30 s)/Ag as catalyst the onset potential of OER is 60 mV earlier than that of Co_3O_4 and the OER current at 1.8 V is improved by 17% compared to that of Co_3O_4, so the Co(30 s)/Ag could be best catalyst

composition for OER.

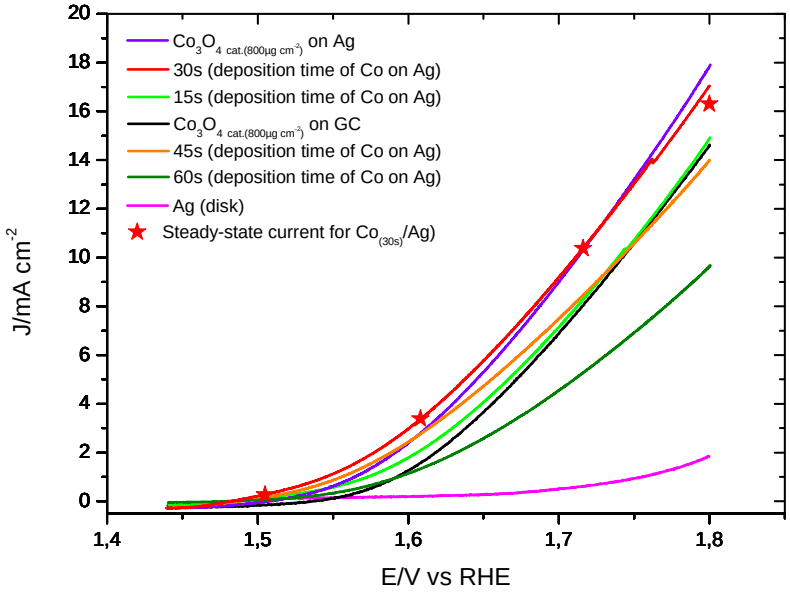

Fig. 4.6 OER polarization curves of Ag, 800 μg cm^{-2} Co_3O_4/Ag, 800 μg cm^{-2} Co_3O_4/C, Co(15 s, 30 s, 45 s and 60 s)/Ag electrodes in 0.1 M LiOH at the scan rate of 5 mV s^{-1} and a rotation rate of 40 Hz.

In practice, it was found that metal oxide is the most active catalyst for OER because it can provide more active sites for peroxide decomposition [49]. However, for bimetallic Co/Ag catalyst, the main reason for a higher performance to OER is probably that cobalt was oxidized into cobalt oxide or hydroxide species before or during OER in 0.1 mol L^{-1} LiOH electrolyte, which are more active for OER. It is worth to mention that OER became more active and its current at 1.8 V increased significantly in the first few cycles and then became stable, as shown in Fig. 4.2c and d. According to the Pourbaix diagram of Co shown in the literature [50], Co can be gradually oxidized to Co(II) ($Co(OH)_2$), Co(II, III) (Co_3O_4) and Co(III) ($Co(OH)_3$) in the high pH solution (pH > 9) and the small peak arised at ~0.4 V after few cycles and it is probably due to Co(III) reduction to Co(II) (see. Fig. 4.2c and d). It was found that 20% of the Co centers is converted to Co(III) at 0.3 V vs. MSE and 60% are Co(III) at 0.5 V vs MSE (E_{MSE} = +0.64 V vs. SHE) in 0.1 M KOH [51]. Switzer et al. [52] also found that $Co(OH)_2$ was converted to CoOOH during OER by Raman spectroscopy. However, these Co oxides can not be reduced into Co in this case. It means that the amount of the produced Co oxides was increased, so that the catalytic activity for OER was improved. This would be what is known as catalyst activation process.

Determination of the steady state activity of Co/Ag bimetallic electrode for OER

The steady state activity of this Co/Ag bimetallic electrode for OER was examed by chronoamperometry at the constant potentials of 1.5, 1.6, 1.7, 1.8 V in O_2-saturated 0.1 M LiOH solution (see. Fig. 4.7). The steady state current values are shown in the corresponding CV (see. the inset of Fig. 4.7) and in Fig. 4.6 and these values are as the same as those in the negative-going sweep, suggesting that the real oxygen evolution should be reflected by the polarization curve which recorded during negative-going scan. It is clear that the abrupt decrease in the current at 1.5 and 1.6 V is due to the continuous oxidation of silver and cobalt. However, when the potential was held at 1.7 and 1.8 V, the current showed serrated flow and declined slightly. It is attributed to the desorption of the produced oxygen at the active sites of catalyst and it is convinced that the OER current could be stable in the absence of adsorption of produced oxygen. The results suggest that the bimetallic electrode of Co/Ag has outstanding catalytic activity at steady state.

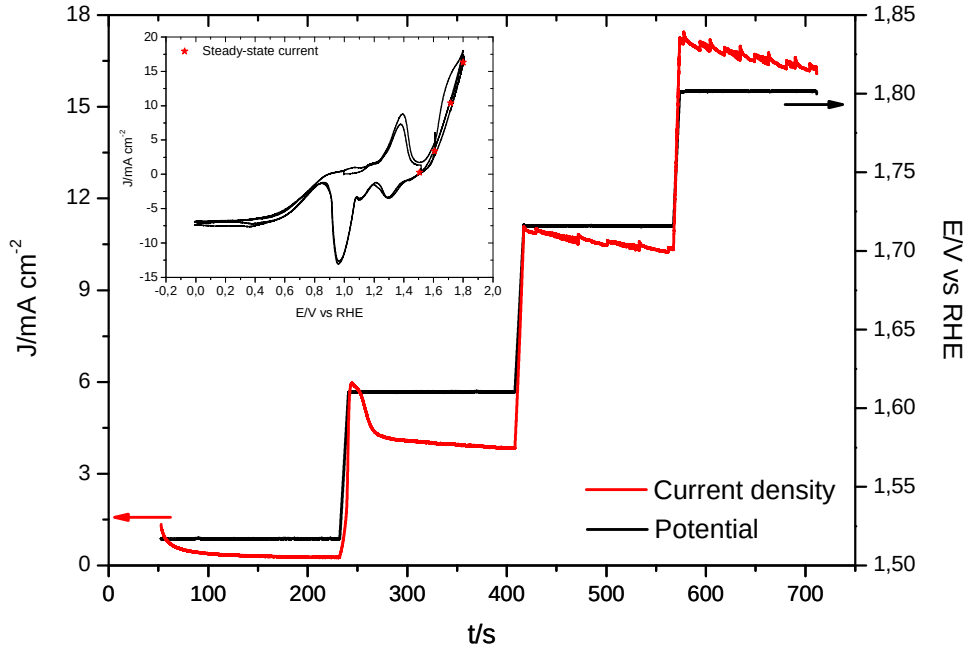

Fig. 4.7 Chronoamperometric response of the Co(30 s)/Ag electrode at 1.5, 1.6, 1.7, 1.8 V for ~3 min (in the positive-going scan) in O_2-saturated 0.1 M LiOH solution with the rotation rate of 40 Hz. Inset: the corresponding CVs.

Tafel plots for OER

For OER, the Tafel slopes were shown in Fig. 4.8. Only one Tafel slope of 60-76 mV dec^{-1} was obtained in all cases. It is very close to the values in the literatures. Rasiyah and Tseung [53] observed the Tafel slope of 60 mV dec^{-1} on Co_3O_4 and Li-doped Co_3O_4

Teflon-bonded anodes. Singh [54] also observed the Tafel slope of approximately 60 and 55 mV dec^{-1} on Co_3O_4 and $NiCo_2O_4$, respectively, in all different concentrations of 0.5-4 mol L^{-1} KOH, suggesting that the activation controlled process involving one electron transfer is the rate-determining step for oxygen evolution on oxide, and the mechanism for OER on Co_3O_4 was suggested.

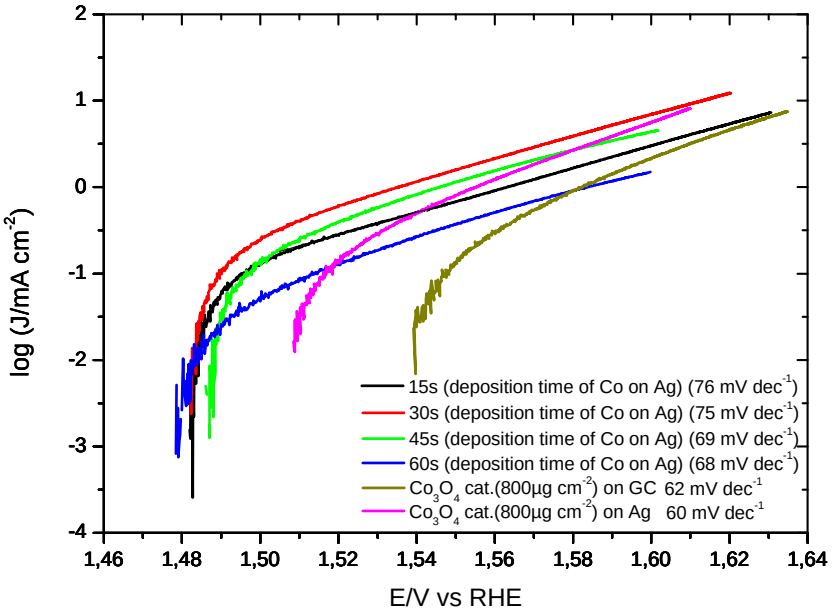

Fig. 4.8 iR-corrected Tafel plots of OER for all the catalysts obtained from the corresponding CVs in Fig. 4.6.

Evaluation and optimization of Co coverage on Ag

The plots of Co coverages vs. both current densities at 0 V (ORR) and 1.8 V (OER) are shown in Fig. 4.9. Both the potentials at 200 µA cm^{-2} (E_{200}) of ORR and OER are earliest on Co(83%)/Ag electrode. Furthermore, on Co(83%)/Ag electrode, the OER current at 1.8 V is the largest (see. Fig. 4.6) and the kinetic current of ORR is also the largest (see. in the inset of Fig. 4.1b). These results indicate that the best coverage (or deposition time) of the Co on Ag electrode is 83% (or 30 s) and it demonstrates a best synergistic catalytic effect.

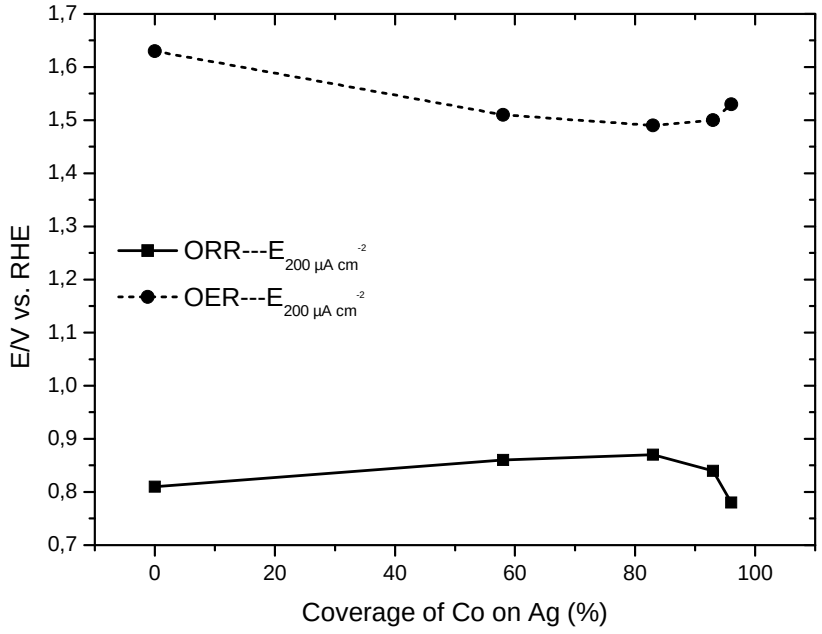

Fig. 4.9 The coverages of Co on Ag vs. both potentials at 200 μA cm^{-2} during ORR and OER, respectively.

4.3.3 Surface characterization by SEM

Scanning electron microscope (SEM) was employed to observe the morphology and structure of the deposited Co on Ag electrode and their changes after potential cycling in the ORR and OER potential region. The images were shown in Fig. 4.10. A large amount of cobalt with flower-like structure were formed and distributed uniformly on Ag disk electrode after deposition of Co on it in 0.05 mol L^{-1} $CoCl_2$ + 0.5 mol L^{-1} $B(OH)_3$ solution (see. Fig. 4.10a and a'). This structure was composed of several Co petals with a quite uniform thickness of ~10 nm radiating arrangement from the centre, leading to a porous surface formation. The flower-like Co structure was also observed by Lambert [23], Lv [55], Xie [56] and Li [57]. Unfortunately, this structure collapsed (see in Fig. 4.10b and b') after potential cycling in the ORR and OER potential region because Co and Ag suffered significant oxidation and reduction under these conditions [26, 58], but they still remained on the surface and the catalytic activity of this electrode surface was also determined to be very stable as discussed before. The change in the morphology probably will cause the change of the electrode surface component. More importantly, these reduction and oxidation products of Co and Ag species could play the important role in the enhancement of the catalytic activity for ORR and OER, respectively.

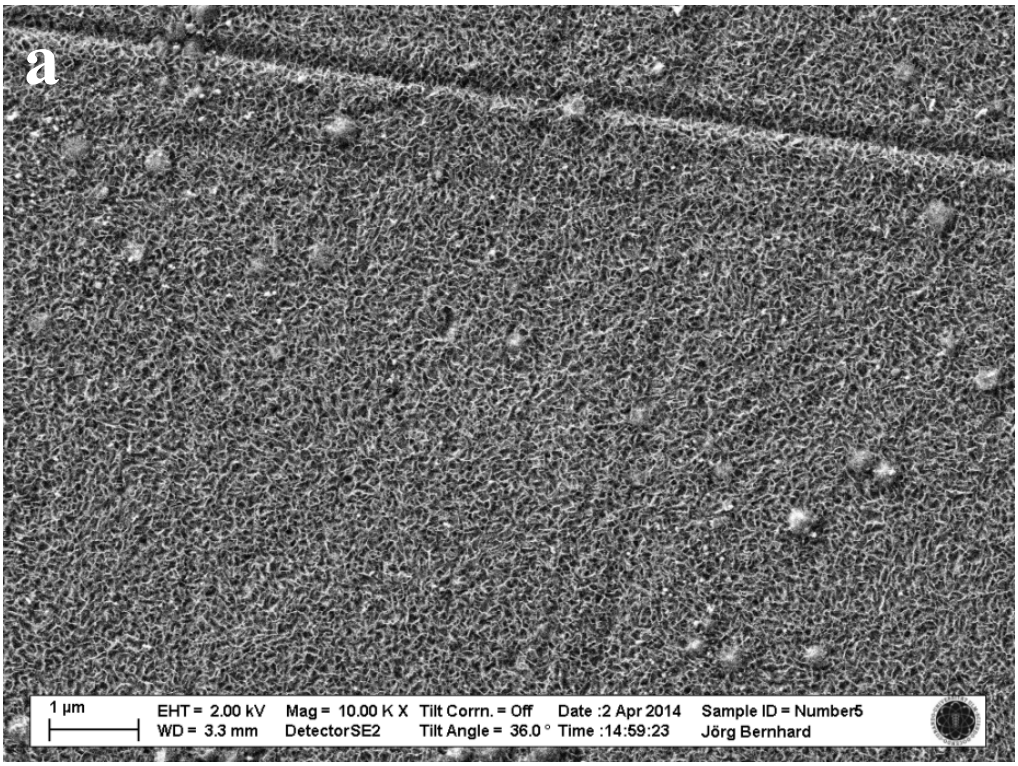
a
1 µm
EHT = 2.00 kV
WD = 3.3 mm
Mag = 10.00 K X
DetectorSE2
Tilt Corrn. = Off
Tilt Angle = 36.0 °
Date :2 Apr 2014
Time :14:59:23
Sample ID = Number5
Jörg Bernhard

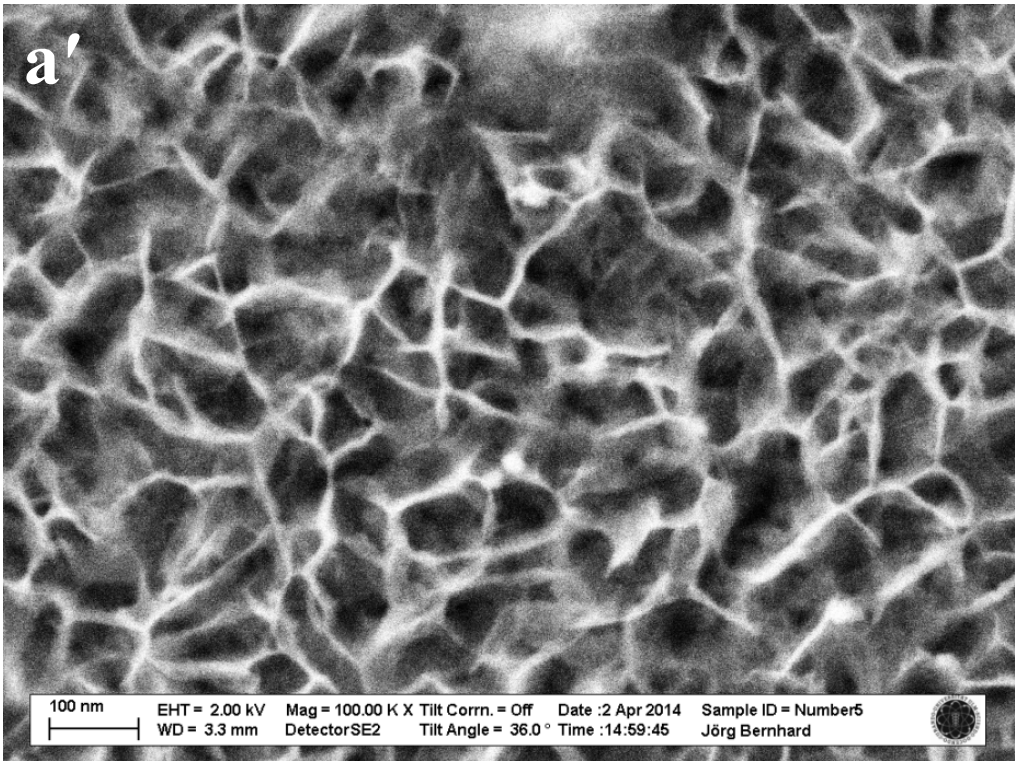
a′
100 nm
EHT = 2.00 kV
WD = 3.3 mm
Mag = 100.00 K X
DetectorSE2
Tilt Corrn. = Off
Tilt Angle = 36.0 °
Date :2 Apr 2014
Time :14:59:45
Sample ID = Number5
Jörg Bernhard

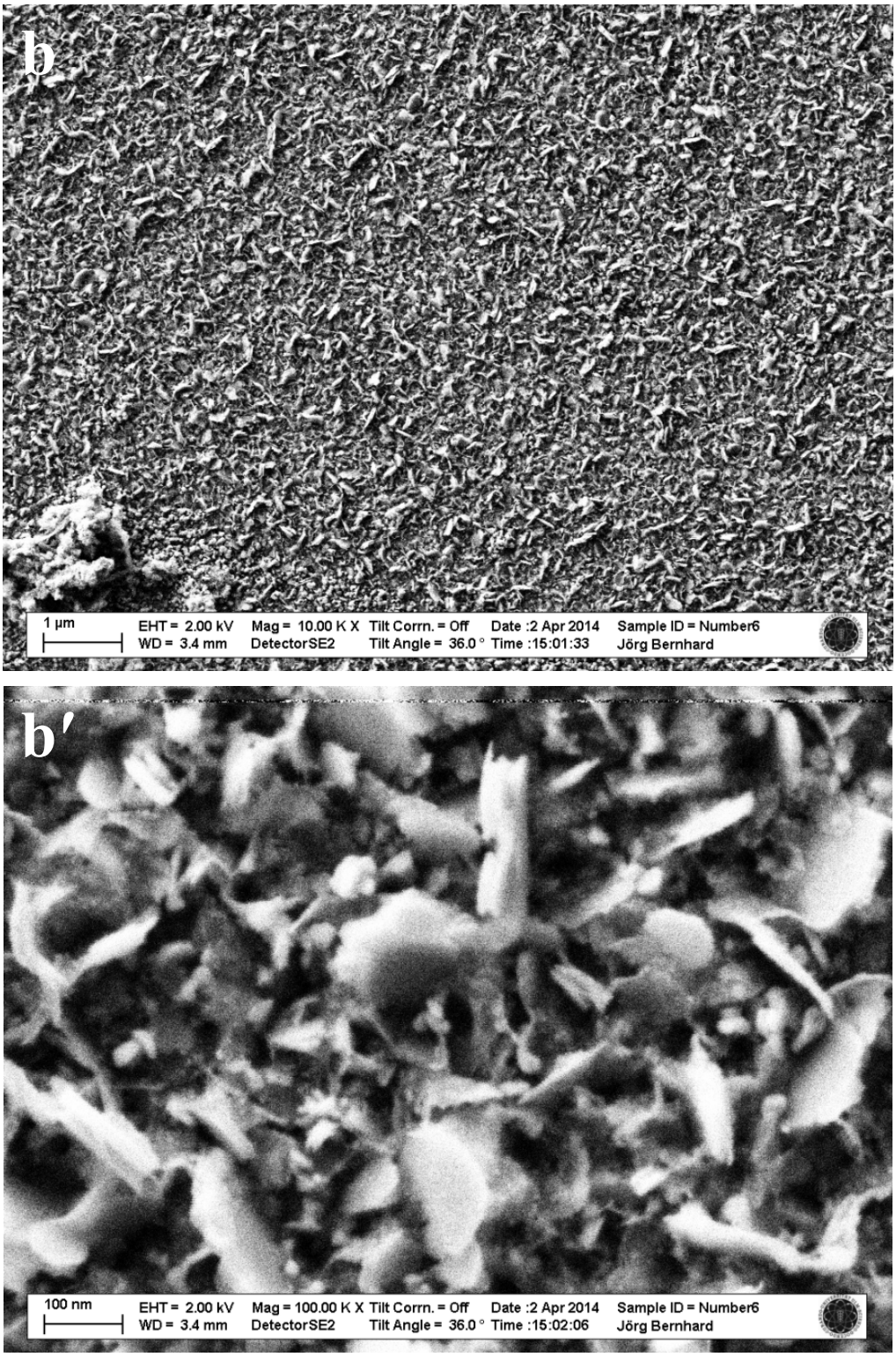

Fig. 4.10 SEM images Co(30 s)/Ag electrode before (a and a') and after (b and b') potential cycling in the ORR and OER region, respectively.

4.3.4 Electrochemical deposition of Co on Ag electrode

4.3.4.1 Electrochemical deposition of Co on Ag(pc) disk electrode

The cyclic voltammograms of Co deposition on Ag in a lower concentration of Co

contained solution (1 mM H_2SO_4 + 10 mM K_2SO_4 + 1 mM $CoSO_4$ + 0.1 mM KCl) in H cell was obtained and shown in Fig. 4.11.

Two cathodic peaks (C_1 at ~-1.45 V and C_2 at ~-1.64 V) and one anodic peak (A at ~-0.94 V) were observed in the potential range of -0.6 to -1.70 V. The anodic peak A was absent when the negative potential limit was -1.43 V, however, the small peak A appeared when the potential sweep was reversed at -1.52 V, indicating that the cathodic peak C_1 is not mainly due to cobalt deposition but to the proton reduction (or hydrogen evolution reaction) as reported by Allongue [59]. The cathodic peak C_2 at ~-1.64 V and the positive peak A at ~-0.75 V are related to bulk Co deposition and dissolution, respectively. The thickness of deposition layers of Co can be estimated by the charge density calculated by integration of the stripping peak. The charge densities of Co stripping at different potential ranges were shown in the table in the inset of Fig. 4.11. Allongue et al. [59] also reported that the monolayer charge of Co on Au(111) is 590 μC cm^{-2}, which is close to the value between 470 μC cm^{-2} and 677 μC cm^{-2} when the potential sweep was reversed at -1.52 V and -1.56 V, respectively, where is very close to the onset of the peak C_2.

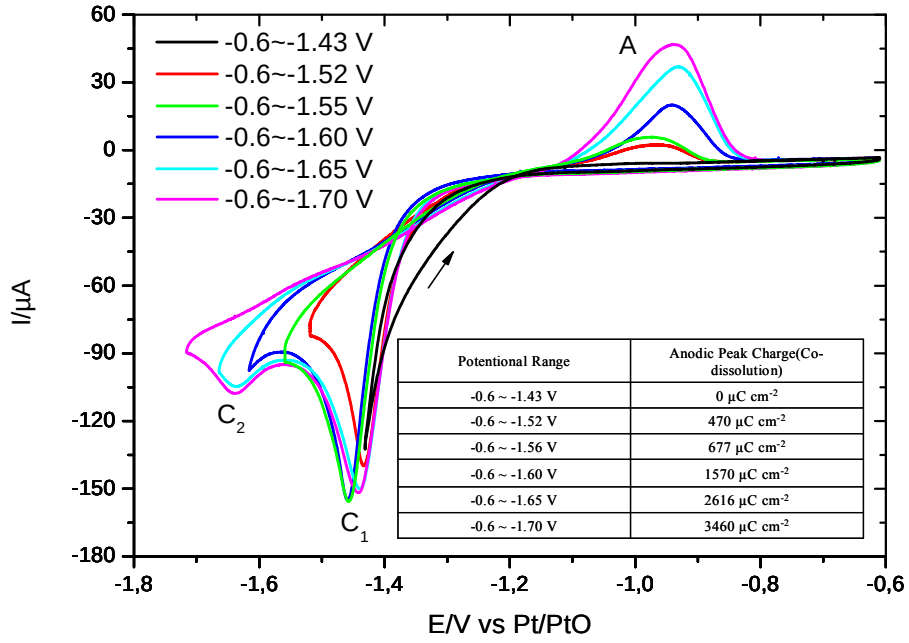

Potentional Range	Anodic Peak Charge(Co-dissolution)
-0.6 ~ -1.43 V	0 μC cm^{-2}
-0.6 ~ -1.52 V	470 μC cm^{-2}
-0.6 ~ -1.56 V	677 μC cm^{-2}
-0.6 ~ -1.60 V	1570 μC cm^{-2}
-0.6 ~ -1.65 V	2616 μC cm^{-2}
-0.6 ~ -1.70 V	3460 μC cm^{-2}

Fig. 4.11 Cyclic voltammograms of Co deposition on Ag(pc) in 1 mM H_2SO_4 + 10 mM K_2SO_4 + 1 mM $CoSO_4$ + 0.1 mM KCl solution saturated with Ar in H cell at 10 mV s^{-1}. Inset: the table of potential range vs. Co-dissolution charge. Arrow indicates the scan direction.

4.3.4.2 Electrochemical deposition of Ag on Pt(111)

For use with the STM, a smooth Ag surface was prepared by using a Pt(111) as a substrate and then depositing Ag on it. The procedures we employed have been described in detail in the experimental part. The cyclic voltammogram of Pt(111) in 0.1 M H_2SO_4 is shown in the inset of Fig. 4.12. The CVs of silver deposition on Pt(111) in 0.1 M H_2SO_4 + 10^{-4} M Ag_2O soultion are shown in Fig. 4.12. As usual, two peaks at 1.06 and 0.67 V (vs RHE) were observed in the UPD range indicating two steps of sliver-UPD. The total charge density of two UPD processes is around 248 μC cm^{-2}, which is very close to the value in the literature and suggests that two monolayers formed during the whole UPD process [60]. Silver bulk deposition starts at 0.65 V (vs RHE).

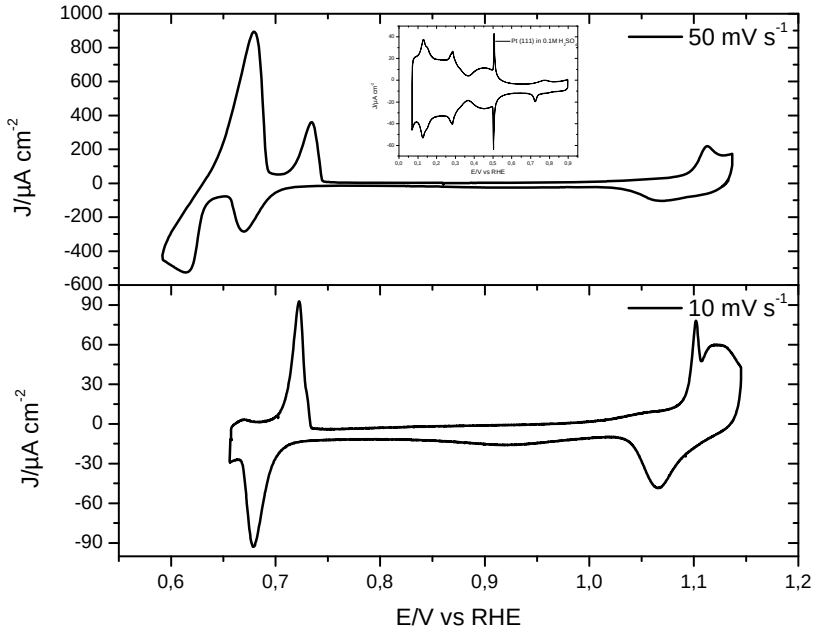

Fig. 4.12 Cyclic voltammograms of Ag deposition on Pt(111) in 0.1 M H_2SO_4 + 10^{-4} M Ag_2O solution in the potential range of the UPD region (down, scan rate: 10 mV s^{-1}) and UPD+OPD (overpotential deposition) region (up, scan rate: 50 mV s^{-1}). Inset: cyclic voltammogram of Pt(111) in 0.1 M H_2SO_4 solution saturated with Ar in H-cell at 50 mV s^{-1}.

4.3.4.3 Observation of Ag on Pt(111) by EC-STM

Electrochemical scanning tunneling microscopy (EC-STM) was employed to observe the mechanism of metal growth on a smooth substrate surface under potential control. As mentioned before, Ag monolayer was preformed and it is considered to be stable because the open circuit potential is -0.2 V (vs. Pt/PtO). A potential step method was

used to observe the bulk deposition of Ag on Pt(111) in the solution of 10^{-4} M Ag_2O, 10 mM K_2SO_4 and 1 mM H_2SO_4 in STM cell. It is shown that the bulk deposition of Ag starts at -0.22 V (see. the CV in Fig. 4.13). The typical in situ STM images for silver deposition is demonstrated in Fig. 4.14. From image a, b and c in Fig. 4.14, it is demonstrated that silver nucleates at the steps, then epitaxial growth to cover the whole terrace, resulting in a layer by layer growth mode (Frank-van der Merwe growth mode) [61]. With the further growth of silver (after at least ~6 monolayers), it starts to nucleate on the terraces, leading to the formation of silver islands as seen in the ellipses, which suggests that 3D growth mode (Stranski-Krastanov growth mode) was observed due to the accumulation of misfit [61].

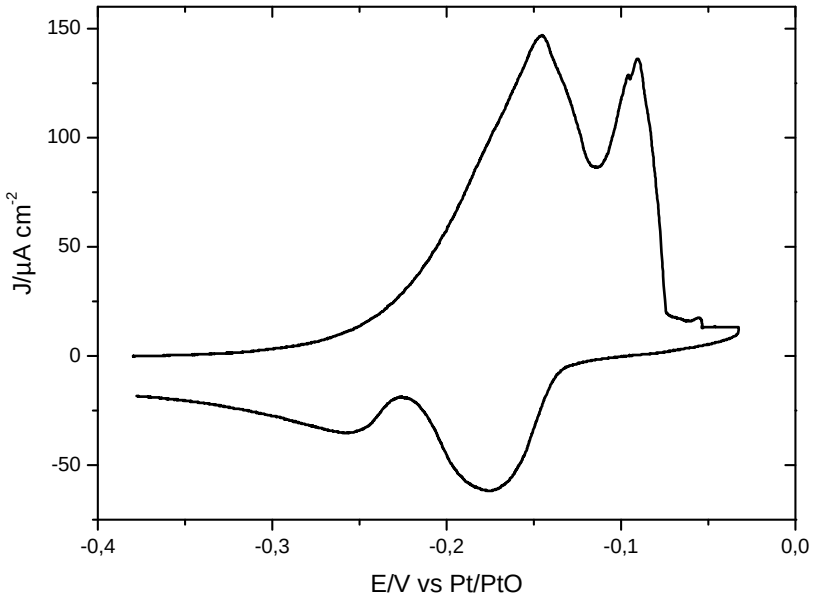

Fig. 4.13 Cyclic voltammogram of Ag depostion on Pt(111) in 1 mM H_2SO_4 + 10^{-4} M Ag_2O + 10 mM K_2SO_4 solution in STM cell at 30 mV s^{-1}.

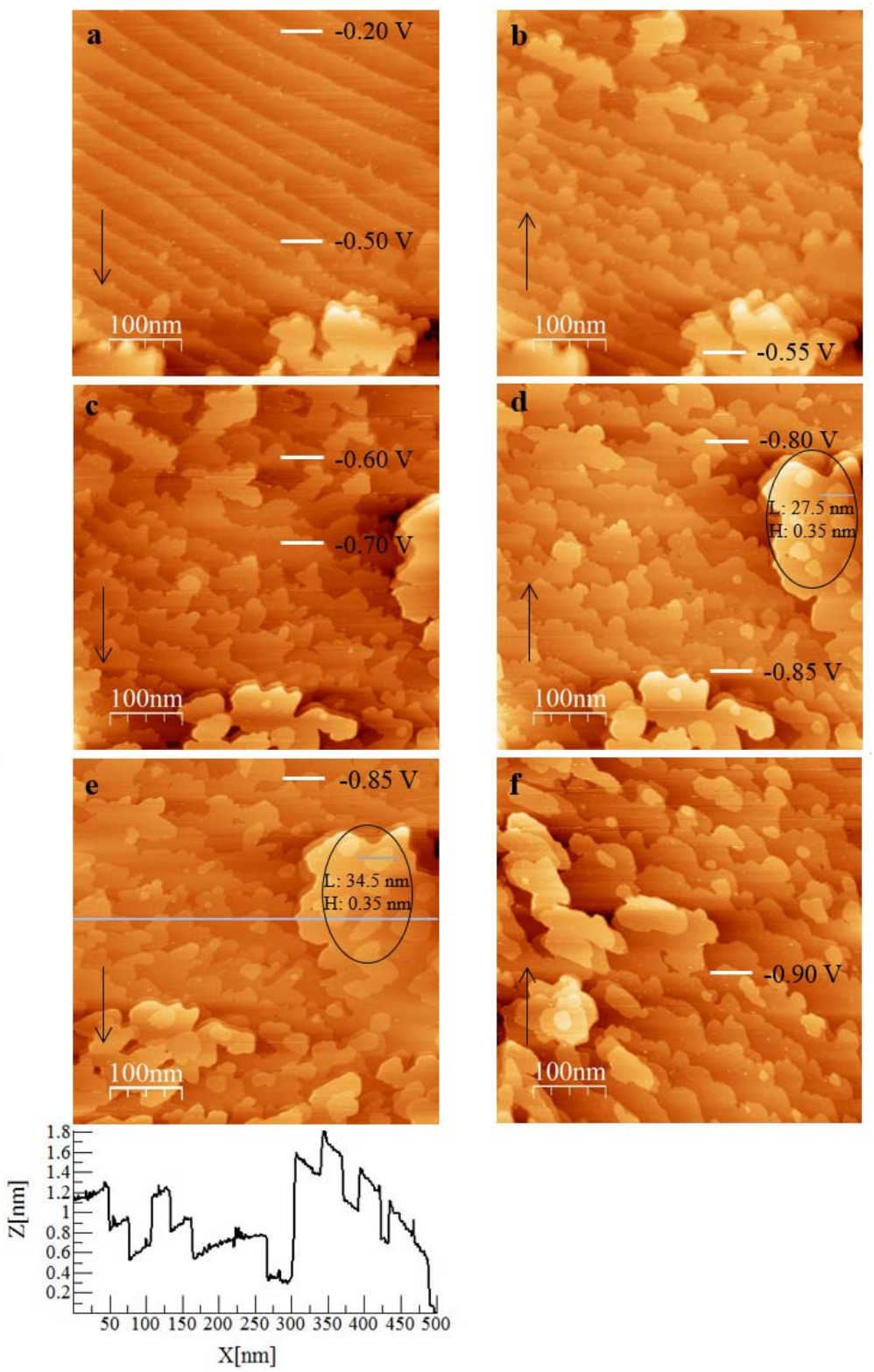

Fig. 4.14 The sequential in situ EC-STM images of Ag growth on Pt(111) surface under potential jumping control. (T: 298 K, E_{tip}: 0 mV, Setpoint: 0.5 V, I Gain: 2, P Gain: 3). (a) -0.25 to -0.50 V; (b) -0.55 V; (c) -0.55 to -0.60 to -0.70 V; (d) -0.70 to -0.80 to -0.75 V; (e) -0.85 V;(f) -0.85 to -0.90 V. Arrows indicate the scan direction. Cross section on image e is shown below.

4.3.4.4 Observation of Co on Ag by EC-STM

The well-prepared smooth bulk adlayers of Ag on Pt(111) was used as the substrate for the further investigation of the growth mechanism of Co on it. After almost all Ag^+ contained in the solution of 1 mM H_2SO_4 + 10^{-4} M Ag_2O + 10 mM K_2SO_4 in STM cell being deposited on Pt(111) (around 60 monolayers), the electrolyte was exchanged with Co containing solution (1 mM H_2SO_4 + 10 mM K_2SO_4 + 1 mM $CoSO_4$ + 0.1 mM KCl) under potential control at -0.9 V in STM cell carefully in order to maintain Ag bulk adlayers on Pt(111) surface. Similar cyclic voltammogram was recorded in the STM cell and shown in Fig. 4.15e. During the measurement, the tip potential was fixed at -0.85 V in order to avoid faradic current caused by the electrochemical reactions at the tip. A potential step method was also employed. The sequential in situ EC-STM images of Co deposition on Ag/Pt(111) electrode surface are shown in Fig. 4.15. As expected, smooth bulk adlayers of Ag are remain on the surface at the potential of -0.9 V after exchanging the solution (see. Fig. 4.15a). When the potential was jumped to -1.5 V, Co nucleated at steps and on terraces and grew in 3-D (Volmer-Weber growth mode) immediately, to form numerous islands of Co as shown in Fig. 4.15b. Morgenstern [62] was also observed that Co nucleation and growth take place at steps and on terraces of Ag(111). Co via three-dimensional (3D) growth (Volmer-Weber growth mode) to form islands was also observed on Ag/Ge(111) surface [63], Au(111) surface [64] and HOPG surface [65]. However, as seen in Fig. 4.15c, the smooth Ag surface reappeared once the potential was jumped to more positive values (-0.9 V), suggesting that this Co deposition and dissolution process is reversible. Continuous growth of Co on Ag/Pt(111) at -1.5 V was observed and the image was shown in Fig. 4.15d. Soon the surface was covered by numerous Co islands with an approximate height of 1.0 nm (around 4 layers) and width of 20 nm (see. Fig. 4.15f). The 3-D growth mode of Co on Ag/Pt(111) was observed, suggesting that the binding energy of Co-Ag is lower than that of Co-Co, and this may promote Co growth on Ag surface in the form of the flower like structure as shown in the SEM image before.

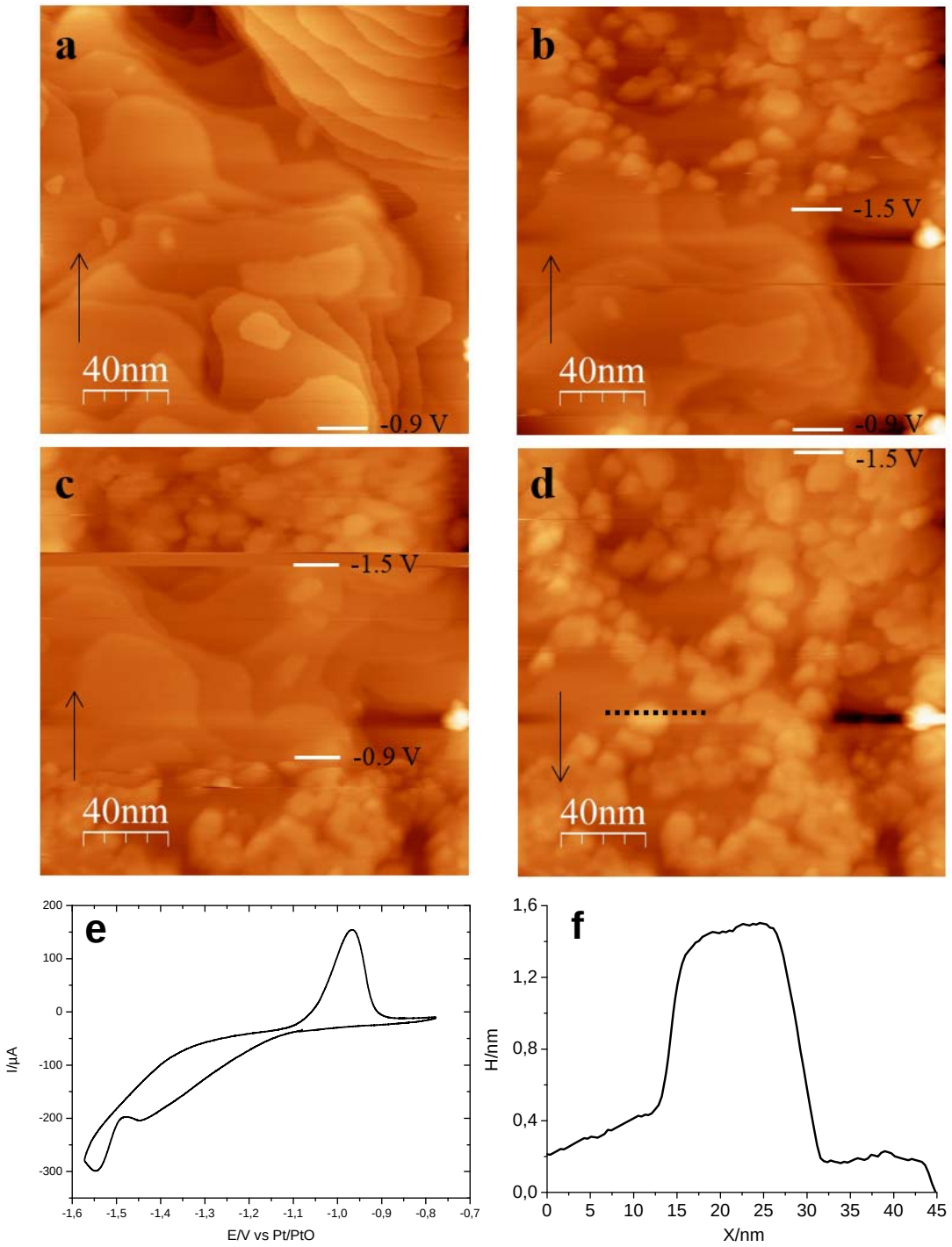

Fig. 4.15 Sequential in situ EC-STM images of Co deposition on Ag/Pt(111) electrode surface in 10 mM K_2SO_4 + 1 mM $CoSO_4$ + 0.1 mM KCl + 1 mM H_2SO_4 solution under potential control (T: 298 K, E_{tip}: -0.85 mV, Setpoint: 0.5 V, I Gain: 2, P Gain: 3).
(a) -0.90 V; (b) -0.90 to -1.50 V; (c) -1.50 to -0.90 to -1.50 V; (d) -1.50 V, (e) the cyclic voltammogram of Co deposition on Ag/Pt(111) electrode in 1 mM H_2SO_4 + 10 mM K_2SO_4 + 1 mM $CoSO_4$ + 0.1 mM KCl solution in STM cell at 30 mV s^{-1}, (f) the height of the particle along the black dot line on image d. Arrows indicate the scan direction.

4.3.4.5 Observation of the change of the surface morphology after potential cycling in the ORR and OER potential region by STM

After Co modification on Ag/Pt(111) electrode surface, the electrolyte in STM was exchanged with 0.1 M LiOH for investigating the change of the morphology of the Co/Ag/Pt(111) electrode surface after potential cycling in the ORR and OER potential region by STM. The CV is shown in the Fig. 4.16c. The anodic peak at ~+0.3 V is probably due to Co and Ag oxidation and at E > ~+0.6 V oxygen evolution takes place. The cathodic peak at ~+0.1 V is related to Ag reduction and a broad peak at ~-0.45 V is probably due to both reductions of Co oxides and oxygen molecules. The morphologies of Co/Ag/Pt(111) in 0.1 M LiOH before and after potential cycling in the ORR and OER potential region were shown in Fig. 4.16a and 4.16b, respectively. Before potential cycling, there is no change in the morphology of Co on Ag by comparing Fig. 4.16a with Fig. 4.15d. Many tiny Co particles on Ag/Pt(111) surface, the steps (the highest multistep height is 3 nm) of the smooth Ag islands and deep holes are visible. After potential cycling in 0.1 M LiOH (see. Fig. 4.16b), slight change in the distribution of particles on the surface is observed and it seems to become evenly distributed. Moreover, the deep holes and the steps of Ag islands disappear.

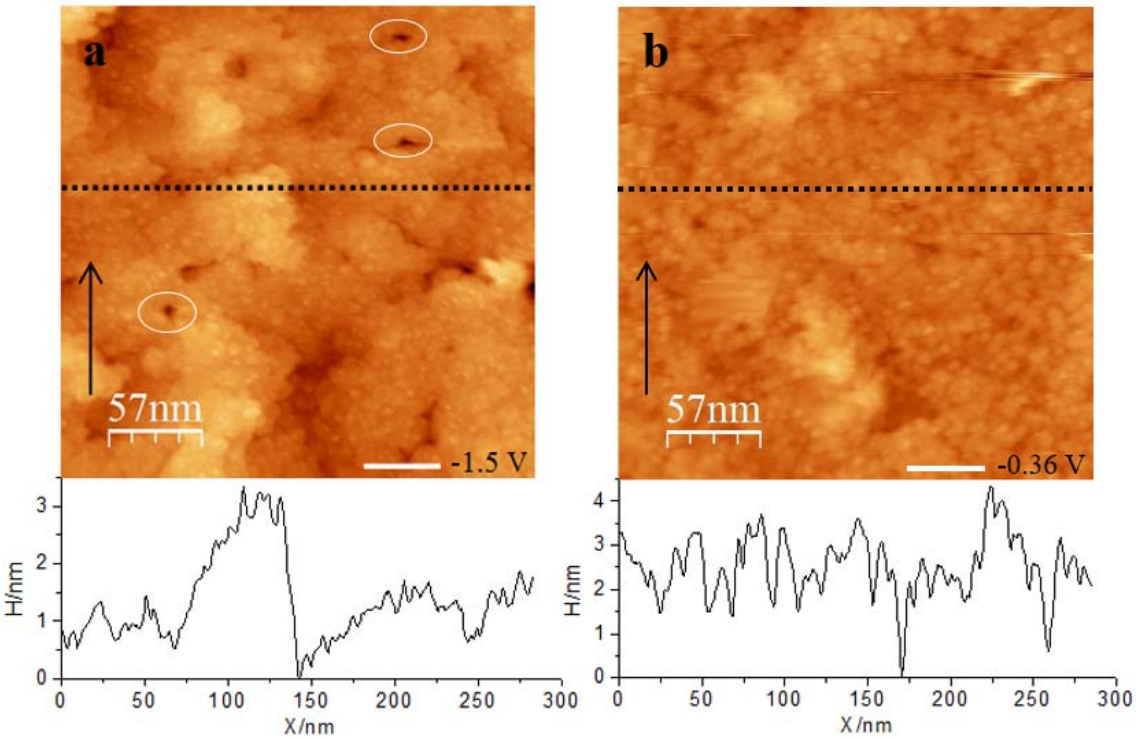

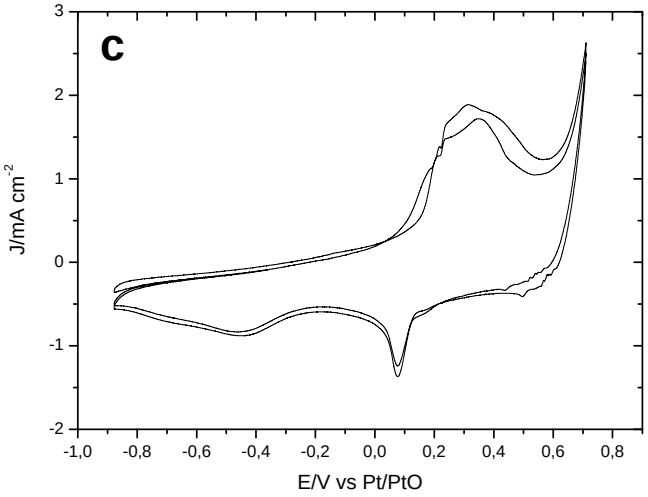

Fig. 4.16 EC-STM images of Co/Ag/Pt(111) electrode surface before (a) and after (b) potential cycling in ORR and OER potential region and the corresponding height of the particles along the black dot lines (under each image), (c) cyclic voltammograms of Co/Ag/Pt(111) in 0.1 M LiOH with air saturated at 30 mV/s.

4.4 Conclusions

Bimetallic cobalt/silver catalyst was synthesised by using an electrochemical deposition method, which is binder free, catalyst loss free, controllable and reproducible way to prepare catalysts. The coverage of Co was determined by Pb-UPD technique and Ag oxidation at first potential cycle and the morphology of this electrode surface was observed by SEM. Interestingly, the flower like cobalt was formed on polycrystalline silver disk electrode. In addition, EC-STM was employed to determine the mechanism of Co growth and observe its morphology on smooth Ag surface achieved by Ag deposition on Pt(111). The results demonstrated that Co prefer to start nucleation at the step edges of Ag and grow in the form of 3-D to form nanoparticles with a height of ~1 nm and width of ~20 nm, which probably give rise to the formation of flower like Co on Ag disk electrode.

More importantly, this bimetallic catalyst has bifunctional catalysis activity for both ORR and OER. It was found that the Co(30 s)/Ag (or Co(83%)/Ag) electrode performed the highest catalytic activity for both ORR and OER. In this case, the ORR starts 60 mV earlier than that of pure Ag and 10 mV earlier than that of 800 μg cm^{-2} Co_3O_4/Nafion/Ag in our previous work. And also the yield of H_2O_2 was only 1.5% and the ORR process follows a $4e^-$ pathway, similar to that of the commercial Pt catalyst, which has been considered to be the best catalyst for ORR. Furthermore, the OER starts

60 mV earlier than that of Co_3O_4 and the OER current efficiency was improved significantly comparing with that of Co_3O_4, which also is well known as one of the best catalysts for OER. These results suggests that the catalytic activity of this catalyst was enhanced not only for ORR but also OER, and the stability of the catalytic activity of this catalyst was determined to be highly stable. Therefore, this Co/Ag catalyst could be employed in metal-air battery because of its outstanding performance in bifunctional catalytic activity and stability.

References

[1] K. Bergamaski, E. R. Gonzalez, and F. C. Nart, Electrochimica Acta 53:4396 (2008).

[2] J. L. Fernandez, D. A. Walsh, and A. J. Bard, Journal of the American Chemical Society 127:357 (2005).

[3] S. M. A. Shibli and M. Noel, Journal of Applied Electrochemistry 23:1025 (1993).

[4] K. C. Neyerlin, G. Bugosh, R. Forgie, Z. Liu, and P. Strasser, Journal of the Electrochemical Society 156:B363 (2009).

[5] N. I. Andersen, A. Serov, and P. Atanassov, Applied Catalysis B: Environmental 163:623 (2015).

[6] U. I. Kramm, J. Herranz, N. Larouche, T. M. Arruda, M. Lefevre, F. Jaouen, P. Bogdanoff, S. Fiechter, I. Abs-Wurmbach, S. Mukerjee, and J.-P. Dodelet, Physical Chemistry Chemical Physics 14:11673 (2012).

[7] K. Zhang, Q. Yue, G. Chen, Y. Zhai, L. Wang, H. Wang, J. Zhao, J. Liu, J. Jia, and H. Li, The Journal of Physical Chemistry C 115:379 (2011).

[8] T. Masuda, H. Fukumitsu, K. Fugane, H. Togasaki, D. Matsumura, K. Tamura, Y. Nishihata, H. Yoshikawa, K. Kobayashi, T. Mori, and K. Uosaki, The Journal of Physical Chemistry C 116:10098 (2012).

[9] C.-W. Liu, Y.-W. Chang, Y.-C. Wei, and K.-W. Wang, Electrochimica Acta 56:2574 (2011).

[10] M. Yuasa, M. Nishida, T. Kida, N. Yamazoe, and K. Shimanoe, Journal of The Electrochemical Society 158:A605 (2011).

[11] M. Ramanathan, V. Ramani, and J. Prakash, Electrochimica Acta 75:254 (2012).

[12] K. C. Poon, D. C. L. Tan, T. D. T. Vo, B. Khezri, H. Su, R. D. Webster, and H. Sato, Journal of the American Chemical Society 136:5217 (2014).

[13] K. W. Kim, S. M. Kim, S. Choi, J. Kim, and I. S. Lee, Acs Nano 6:5122 (2012).

[14] N. M. Markovic, T. J. Schmidt, V. Stamenkovic, and P. N. Ross, Fuel Cells - From Fundamentals to Systems 1:105 (2001).

[15] H. Inoue, S. R. Brankovic, J. X. Wang, and R. R. Adzic, Electrochimica Acta 47:3777 (2002).

[16] Y. Ma and P. B. Balbuena, Surface Science 602:107 (2008).

[17] Z. Peng and H. Yang, Journal of the American Chemical Society 131:7542 (2009).

[18] A. Ezeta-Mejia, O. Solorza-Feria, H. J. Dorantes-Rosales, J. M. H. Lopez, and E. M. Arce-Estrada, International Journal of Electrochemical Science 7:8940 (2012).

[19] P. Hernandez-Fernandez, S. Rojas, P. Ocon, J. L. G. de la Fuente, J. S. Fabian, J. Sanza, M. A. Pena, F. J. Garcia-Garcia, P. Terreros, and J. L. G. Fierro, Journal of Physical Chemistry C 111:2913 (2007).

[20] Y.-C. Lu, Z. Xu, H. A. Gasteiger, S. Chen, K. Hamad-Schifferli, and Y. Shao-Horn, Journal of the American Chemical Society 132:12170 (2010).

[21] F. W. T. Goh, Z. L. Liu, X. M. Ge, Y. Zong, G. J. Du, and T. S. A. Hor, Electrochimica Acta 114:598 (2013).

[22] A. Garsuch, A. Panchenko, C. Querner, A. Karpov, S. Huber, and R. Oesten, Electrochemistry Communications 12:1642 (2010).

[23] T. N. Lambert, J. A. Vigil, S. E. White, D. J. Davis, S. J. Limmer, P. D. Burton, E. N. Coker, T. E. Beechem, and M. T. Brumbach, Chemical Communications 51:9511 (2015).

[24] B. B. Blizanac, P. N. Ross, and N. M. Markovic, Journal of Physical Chemistry B 110:4735 (2006).

[25] E. J. Lim, S. M. Choi, M. H. Seo, Y. Kim, S. Lee, and W. B. Kim, Electrochemistry Communications 28:100 (2013).

[26] T. Van Cleve, Gibara, E. and Linic, S., ChemCatChem published online: 4 DEC

2015 (2015).
[27] Q. Wang, X. Cui, W. Guan, L. Zhang, X. Fan, Z. Shi, and W. Zheng, Journal of Power Sources 269:152 (2014).
[28] F. H. B. Lima, J. F. R. de Castro, and E. A. Ticianelli, Journal of Power Sources 161:806 (2006).
[29] M. Innocenti, G. Zangari, C. Zafferoni, I. Bencistà , L. Becucci, A. Lavacchi, F. Di Benedetto, S. Bellandi, F. Vizza, and M. L. Foresti, Journal of Power Sources 241:80 (2013).
[30] S.-A. Park, E.-K. Lee, H. Song, and Y.-T. Kim, Scientific Reports 5 (2015).
[31] Y. Wang, X. Lu, Y. Liu, and Y. Deng, Electrochemistry Communications 31:108 (2013).
[32] Y. Yang, H. L. Fei, G. D. Ruan, L. Li, G. Wang, N. D. Kim, and J. M. Tour, Acs Applied Materials & Interfaces 7:20607 (2015).
[33] H. M. A. Amin, H. Baltruschat, D. Wittmaier, and K. A. Friedrich, Electrochimica Acta 151:332 (2015).
[34] F. P. Zamborini and R. M. Crooks, Langmuir 13:122 (1997).
[35] U. Schmidt, S. Vinzelberg, and G. Staikov, Surface Science 348:261 (1996).
[36] G. K. H. Wiberg, K. J. J. Mayrhofer, and M. Arenz, Fuel Cells 10:575 (2010).
[37] E. Kirowa-Eisner, Y. Bonfil, D. Tzur, and E. Gileadi, Journal of Electroanalytical Chemistry 552:171 (2003).
[38] V. R. Stamenkovic, B. Fowler, B. S. Mun, G. Wang, P. N. Ross, C. A. Lucas, and N. M. Markovic, Science 315:493 (2007).
[39] S.-A. Park, H. Lim, and Y.-T. Kim, Acs Catalysis 5:3995 (2015).
[40] C. Zafferoni, G. Cioncoloni, M. L. Foresti, L. Dei, E. Carretti, F. Vizza, A. Lavacchi, and M. Innocenti, Molecules 20:14386 (2015).
[41] B. Huskinson, M. P. Marshak, C. Suh, S. Er, M. R. Gerhardt, C. J. Galvin, X. D. Chen, A. Aspuru-Guzik, R. G. Gordon, and M. J. Aziz, Nature 505:195 (2014).
[42] T. Shinagawa, A. T. Garcia-Esparza, and K. Takanabe, Scientific Reports 5:21 (2015).
[43] F. Loglio, E. Lastraioli, C. Bianchini, C. Fontanesi, M. Innocenti, A. Lavacchi, F. Vizza, and M. L. Foresti, Chemsuschem 4:1112 (2011).
[44] N. Markovic, H. Gasteiger, and P. N. Ross, Journal of the Electrochemical Society 144:1591 (1997).
[45] A. Damjanovic, Modern Aspects of Electrochemistry, 1969.
[46] B. E. Conway, J. O. M. Bockris, E. Yeager, S. U. M. Khan, and R. E. White, Comprehensive Treatise of Electrochemistry, 1983.
[47] R. Jinnouchi, K. Kodama, T. Hatanaka, and Y. Morimoto, Phys. Chem. Chem. Phys 13:21070 (2011).
[48] V. Stamenkovic, T. J. Schmidt, P. N. Ross, and N. M. Markovic, Journal of Electroanalytical Chemistry 554:191 (2003).
[49] T. S. Olson, S. Pylypenko, S. Kattel, P. Atanassov, and B. Kiefer, The Journal of Physical Chemistry C 114:15190 (2010).
[50] E. M. Garcia, J. S. Santos, E. C. Pereira, and M. B. J. G. Freitas, Journal of Power Sources 185:549 (2008).
[51] D. A. Marsh, W. Yan, Y. Liu, J. C. Hemminger, R. M. Penner, and A. S. Borovik, Langmuir 29:14728 (2013).
[52] J. A. Koza, C. M. Hull, Y.-C. Liu, and J. A. Switzer, Chem. Mater. 25:1922 (2013).
[53] P. Rasiyah and A. C. C. Tseung, J. Electrochem. Soc. 130:365 (1983).
[54] R.-N. Singh, M. Hamdani, J.-F. Koenig, G. Poillerat, J. L. Gautier, and P. Chartier, Journal of Applied Electrochemistry 20:442 (1990).
[55] H. L. Lv, X. H. Liang, G. B. Ji, H. Q. Zhang, and Y. W. Du, Acs Applied Materials

& Interfaces 7:9776 (2015).
[56] Y. L. Xie, N. Xiao, Z. Ling, Y. Liu, C. Yu, and J. S. Qiu, Chinese Journal of Catalysis 33:1883 (2012).
[57] H. Li and S. J. Liao, Journal of Physics D-Applied Physics 41:7 (2008).
[58] H. Kim, J. Park, I. Park, K. Jin, S. E. Jerng, S. H. Kim, K. T. Nam, and K. Kang, Nature Communications 6:11 (2015).
[59] P. Allongue, L. Cagnon, C. Gomes, A. Gündel, and V. Costa, Surface Science 557:41 (2004).
[60] K. F. Domke, X.-Y. Xiao, and H. Baltruschat, Electrochimica Acta 54:4829 (2009).
[61] E. B. Budevski, G. T. Staikov, and W. J. Lorenz, Electrochemical Phase Fomation and Growth: An Introduction to the Initial Stages of Metal Deposition, Wiley-VCH, Weinheim, 1996.
[62] K. Morgenstern, J. Kibsgaard, J. V. Lauritsen, E. Laegsgaard, and F. Besenbacher, Surface Science 601:1967 (2007).
[63] X. L. Huang, C. L. Lin, A. Tomaszewska, C. R. Chen, and T. Y. Fu, Nanoscale Research Letters 7:7 (2012).
[64] M. Kleinert, H. F. Waibel, G. E. Engelmann, H. Martin, and D. M. Kolb, Electrochimica Acta 46:3129 (2001).
[65] S. W. Poon, J. S. Pan, and E. S. Tok, Physical Chemistry Chemical Physics 8:3326 (2006).

Chapter 5: Investigation of metal underpotential and overpotential deposition on Au(111) electrode surface in nonaqueous solution

In this chapter, underpotential and overpotential deposition (UPD and OPD) of Cu, Pb and Ag on Au(111) single crystals electrode surface in the solvents such as propylene carbonate (PC), acetonitrile (MeCN), tetrahydrofuran (THF), tetraglyme (G4) and some of their mixture based electrolytes have been investigated by cyclic voltammetric techniques. Based on the stability of Ag deposition process on Au(111) in non-volatile tetraglyme in air atmosphere, we have also performed an in-situ STM observation of the Ag-UPD and bulk deposition process on Au(111).

5.1 Introduction:

Underpotential deposition (UPD) [1, 2], is an electrochemical deposition phenomenon of a metal on a foreign metal substrate at the potential (E_{ads}) which is more positive than the equilibrium potential (or reversible Nernst potential, E_N) [3] for the reduction of the metal.

$$\Delta U = E_{ads} - E_N \geq 0$$

According to the definition of equilibrium potential, it also means that the metal is more easily deposited on the substrate material than on itself, indicating that the interaction energy between adsorbed metal atom and a foreign metal substrate surface (S-M) is larger than that of the deposited metal atom on its own surface (M-M) [4].

$$S - M_{ads} \geq M - M_{ads}$$

The process of UPD can be regarded as a charge transfer process at the interface between electrolyte and electrode accompanied with the adsorption and desorption or displacement of solvent molecules with solvated metal ions from the electrode surface [5].

So far, a lot of research on metal-UPD has been done in aqueous solution and some in ionic liquid, but little has been reported for organic solvents. The reason for this probably lies in the low solubility of salt, poor electric conductivity of organic solvents and the complex solvation process making the complexity of underpotential deposition process in non-aqueous solution, especially in organic solution. As is well known, the solvent plays an important role on surface reaction because of its effect on the solubility of salt, stability of electrolyte, reaction rate and thermodynamic and kinetic parameters

[6].

Solvents may have twofold effects during the underpotential deposition process, one is that the substrate surface may be covered by physisorbed solvent molecules and another one is that metal ion is solvated before deposition [7]. During the UPD process, the solvation layers on the substrate surface should be replaced by the solvated metal ion by adsorption accompanying with desorption of some solvent molecules. The process can be represented as:

$$\left[M\left(sol\right)_x\right]^{z+} + S\left(sol\right)_y + ze^- \rightarrow S - M + \left(x+y\right)sol \qquad (E > E_{Me/Me^{z+}})$$

The UPD process consists of the metal ion (M) with a positive charge of z (z+) solvated by x solvent (sol) molecules ($[M(sol)_x]^{z+}$) and solvent molecules (sol) penetrating from the solution into the inner Helmholtz layer. During this process, the adsorbed y solvent molecules on the substrate surface ($S(sol)_y$) and the solvation shell of metal ion are removed. (E is the actual electrode potential and $E_{Me/Me^{z+}}$ is the equilibrium potential of the Me/Me^{z+} electrode) Depending on the interaction between solvated metal ion and the substrate surface, the physisorption [8-10] or chemisorption [11-14] can be defined. The interfacial process of UPD becomes very complicate in nonaqueous solution because of the extensive co-adsorption of solvent and other species in solution [15, 16].

As mentioned before, solvent plays a crucial role in metal deposition. So, selecting a suitable solvent is very important to achieve a better behaviour of metal deposition and get better understanding of the mechanism of solvent effect on metal deposition. These studies could also make contribution to select a suitable nonaqueous electrolyte for metal-air or ion battery. However, in nonaqueous solution few reports on this topic can be found and most of these studies were done in ionic liquid and molten salts until now. Gofer [17] investigated Li-UPD on Au electrode from $LiClO_4$ contained poly(ethylene oxdie) solid polymer electrolyte in ultrahigh vacuum and Gasparotto [18] also observed the Li-UPD on Au(111) in the ionic liquid, 1-butyl-1-methylpyrrolidinium bis(trifluoromethylsulfonyl)amide ([Py1, 4]TFSA) which is stable in the air and water conditions, by in-situ STM. Stafford [19] and Moustafa [20] observed the Al-UPD on Au(111) electrode from the Lewis acidic aluminum chloride, 1-ethyl-3-methylimidazolium chloride ($AlCl_3$–EMImCl) and 1-butyl-1-methyl-pyrrolidinium bis(trifluoromethylsulfonyl)-amide, [Py1,4]Tf_2N or 1-ethyl-3-methyl-imidazolium

bis(trifluoromethylsulfonyl)amide, [EMIm]Tf_2N by STM, respectively. And some other metal-UPD in ionic liquid, for example, Germanium (Ge) [21], Cadmiun (Cd) [22], Lead (Pb) [23] and Silver (Ag) [24] have been investigated. But very few researches on metal-UPD in organic solvent were reported.

Xing [25] investigated the solvent effect on the UPD processes of Pb and Cd in propylene carbonate (PC), water, tetrahydrofuran (THF) and dimethoxyethane (DME) and Pekmez [26] investigated the Cu UPD on Au(111) in nonaqueous acetonitrile (MeCN) and examined the effect of water on Cu UPD process. They only used the cyclic voltammetric techniques, more detailed study of the interface process during UPD by other techniques such as STM [27, 28], AFM [29, 30], LEED [31, 32], XPS [33, 34], etc. are needed to unveil the details of UPD.

This manuscript's aim is to study the metal Cu, Pb, Ag-UPD phenomenon on Au(111) in the solvents such as MeCN, PC, THF and G4 (tetraglyme) or their mixture to get better understanding of the solvent effect on the interface reactions such as metal deposition and oxygen reduction in aprotic Li-air and Mg-air batteries.

5.2 Experimental

5.2.1 Chemicals and materials

Salts: $Cu(ClO_4)_2$ (Acros organics, 99.8%), $Pb(ClO_4)_2$ (Santa Cruz, 98%), Anhydrous $AgClO_4$ (Sigma-Aldrich, 97%), $AgNO_3$ (chemPUR 99%) and Anhydrous $LiClO_4$ (Alfa Aesar 95%).

Solvents: Tetraglyme (G4) (Acros organics, 99%), Acetonitrile (MeCN) (Acros organics, 99.9%, Extra Dry), Tetrahydrofuran (THF) (Sigma-Aldrich, ≥ 99.9%, inhibitor-free) and Propylene Carbonate (PC) (Sigma-Aldrich, 99.7%). All the solvents were used as received. All the electrolytes were prepared without pre-treatments of solvents and salts for drying (water contents are roughly in the range of 200~400 ppm) and cyclic voltammetry measurements were done in an argon-filled glove box (O_2 and H_2O < 1 ppm) which provided by Mbraun.

Cyclic voltammetric measurements were performed in a three-electrode cell and an EC-STM with a small amount of solution, made by the chemically inert Kel-F. The structure of our STM cell was described in chapter 2. The cell, which has a hole with the

diameter of 8 mm where the electrolyte and working electrode are contacted with each other, was employed. Cu, Pt or Ag wire was used as reference electrode in the corresponding system and Au wire was used as counter electrode. All these parts were kept in 5 M KOH bath for overnight to remove organic solvents, washed and then put into boiling 0.1 M H_2SO_4 solution and water for 5 min in turn to remove the residues salts, and then dried them in oven at the temperature below 80 °C before each use. The Au(111) (10 mm diameter) working electrode was cleaned in 0.1 M H_2SO_4 solution prepared with Milli-Q water and deaerated by purging ultra-high pure argon (99.999%, Air Liquide) in a glass H cell. A reversible hydrogen electrode (RHE) prepared by electroanalysis 0.1 M H_2SO_4 solution was used as reference electrode and an Au wire was used as counter electrode. The Au(111) electrode was prepared by flaming for 5 minutes and annealing for 8 minutes in argon atmosphere in a dried glass H cell.

5.2.2 EC-STM

An Agilent Technologies 5500 Scanning Probe Microscope combined with a built-in potentiostat was employed. The STM tip was prepared by electrochemical etching [35] of Pt/Ir (90/10) wire with the diameter of 0.25 mm in 2 M KOH + 4 M KSCN solution and sealed with hot-melt glue to minimize Faradaic current. The EC-STM measurement was performed in the STM cell in glass chamber purged with Ar gas at room temperature. Silver and gold wire was used as reference and counter electrode, respectively.

5.3 Results and discussion

Acetonitrile (MeCN), Tetrahydrofuran (THF), Tetraglyme (G4) and Propylene carbonate (PC) are polar aprotic solvents, which possess a good ability to dissolve salts and were widely used in the investigation field of batteries. In this chapter, MeCN, THF, G4 and PC solvents with different properties (for example, dielectric constant, donor and acceptor number, etc. as shown in Table. 5.1) were used as solvent for investigation of their effect on metal-UPD process on Au(111).

5.3.1 Cu-UPD on Au(111)

The cyclic voltammograms of Au(111) in acetonitrile containing 1 mM $Cu(ClO_4)_2$ + 0.1 M $LiClO_4$ recorded in the STM cell in an argon-filled glove box are shown in Fig. 5.1a. Four anodic peaks and the corresponding four cathodic peaks were observed. The cyclic

voltammetric feature is similar to that observed by Vaskevich and the detailed explanation was presented there [15]. However, the UPD peaks (A2/C2 and A3/C3) are not sharp, probably because the preparation quality of Au(111) surface is poor. It has also reported that under the same condition the gentle UPD peaks were observed on Au(pc) electrode [15]. The redox peak A1/C1 at around 1.1 V (vs. Cu/Cu^{2+}) is related to Cu^{+}/Cu^{2+} redox couple process and the relationship between the peak currents and the square root of the scan rate is linear (see. Fig. 5.1b). The peaks A4/C4 below 0 V are related to the bulk deposition and dissolution of copper.

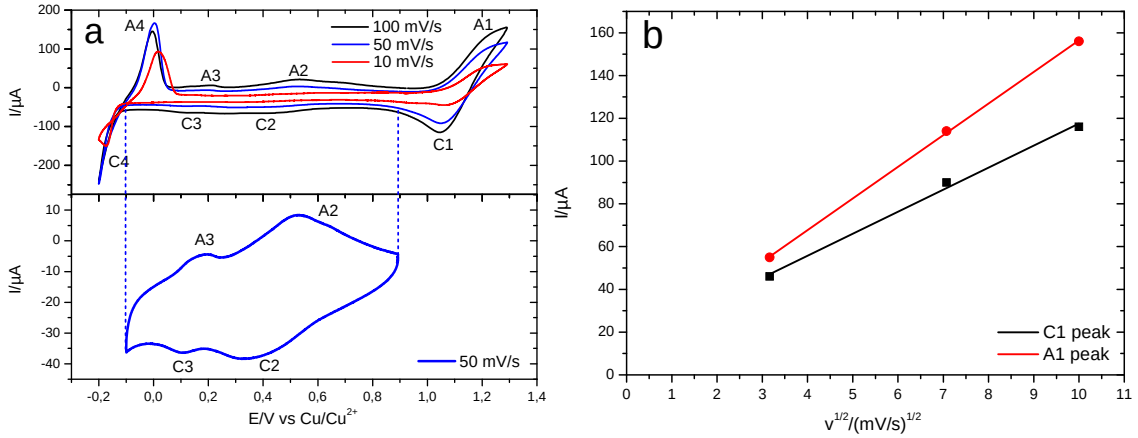

Fig. 5.1 a) Cyclic voltammograms of Au(111) in acetonitrile contained 1 mM $Cu(ClO_4)_2$ + 0.1 M $LiClO_4$ in STM cell in the argon-filled glove box at the scan rate of 10, 50 and 100 mV s^{-1}. b) Plots of i_p (peakcurrent) vs. $v^{1/2}$(square root of scan rate).

However, once the electrolyte was exposed to air, the characteristic polarization curve of Cu deposition on Au in this electrolyte disappeared as seen in Fig. 5.2. It indicates that this Cu deposition process is very sensitive to air in this case. This probably is due to the effect of oxygen, which would be reduced before Cu^{2+} reduction. It is worth to mention that the effect of water on Cu UPD on Au(111) process has been investigated [26] and interpreted that water changes the UPD mechanism from a two step (pure acetonitrile) to a one step (10 vol%, water content) process, but there is no OPD involved. The large current flowed after 0 V, but no corresponding anodic peak appeared. Therefore, it could be due to oxygen reduction [36] because it is well known that the standard potential of oxygen reduction is more positive than that of Cu^{2+}/Cu^{+} to Cu.

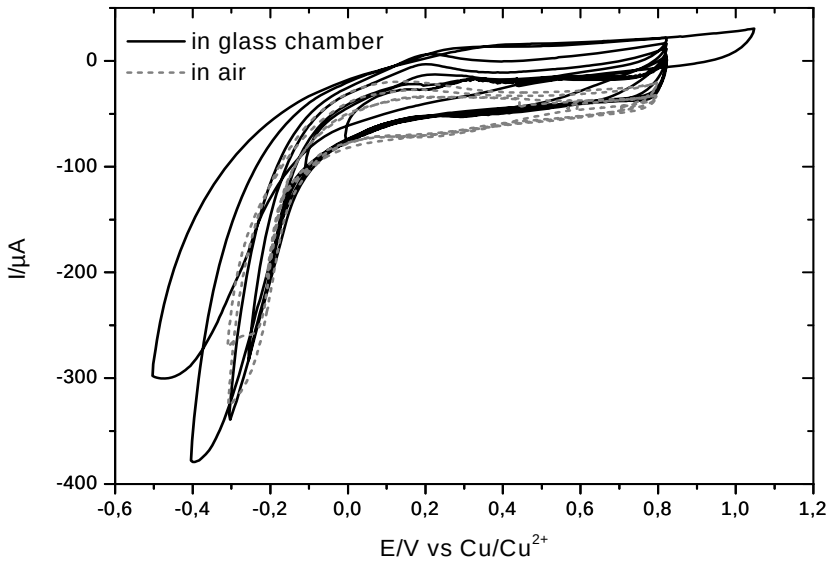

Fig. 5.2 Cyclic voltammograms of Au(111) in acetonitrile containing 1 mM $Cu(ClO_4)_2$ + 0.1 M $LiClO_4$ in STM cell in air and glass chamber at the scan rate of 50 mV s^{-1}.

5.3.2 Pb-UPD on Au(111)

Pb-UPD on Au(111) was investigated in tetrahydrofuran (THF) with low dielectric constant, its mixture with propylene carbonate (PC) with high dielectric constant or tetraglyme (G4) with low dielectric constant. In order to achieve better comparison, the investigation of Pb-UPD in pure G4 is very necessary, but unfortunately $Pb(ClO_4)_2$ can not be dissolved in pure G4. The cyclic voltammograms are shown in Fig. 5.3 respectively and the properties of these solvents were shown in table. 5.1. Pb-UPD on Au(111) in PC, THF and PC + THF based electrolyte has been studied by Xing and it has been found that solvent has a large effect on Pb-UPD process [25]. In pure PC (with high dielectric constant) based electrolyte the Pb-UPD process is very fast and the polarization curve is similar to that observed in aqueous electrolyte. In THF (with low dielectric constant) based electrolyte, the polarization curve was distorted and the Pb-UPD process becomes very sluggish. However, by adding small amounts of PC in THF the clearly defined feature in the polarization curve was observed, indicating that the solvent with high dielectric constant can accelerate the Pb-UPD process. The dielectric constant is the main factor to determine the conductivity of the electrolyte. The same results are also observed in this work. However, Pb-UPD in THF + G4 based electrolyte has never been studied. It is elusive that the polarization curve obtained in the mixture of THF and G4, both solvents with almost the same dielectric constant (see. table. 5.1), was similar to that obtained in THF/PC except for the slight changes in the sharpness and charge of peaks and the trend of the overlap of two peaks at around -0.5 V,

especially in THF/G4 (1:9, v:v) based electrolyte. It seems that not only dielectric constant but also other properties should also be taken into account. The charges of Pb-UPD stripping peaks between -0.6 and 0.1 V were calculated and shown in Table. 5.2. It shows that the lowest value (75 μC cm^{-2}, ~0.17 monolayer) of UPD stripping charge was obtained in THF, an intermediate value (~217 μC cm^{-2}, ~0.50 monolayer) was obtained in THF/G4 (9:1 and 1:9, v:v) and the highest value (398 μC cm^{-2}, ~0.90 monolayer), which is very close to the value obtained in aqueous solution in the literature [37], was obtained in THF/PC (9:1, v:v). Furthermore, the charges of the peaks at ~-0.5 V are also shown in table. 5.2. The lowest value was also obtained in THF based electrolyte.

Table. 5.1 The properties of solvents

solvent	Dc (ε, 25 °C)	DN (kcal/mol)	AN (kcal/mol)	η (cP, 25 °C)	DM (μ/D)
G4	7.79	16.6	11.8	4.05	2.47 (in benzene)
THF	7.52	20	8	0.48	1.75
PC	64	15.1	18.3	2.5	4.9
MeCN	38.8	14.1	19.3	0.334	3.92
Water	78.41	18	54.8	0.890	1.85

Note: Dielectric constant (Dc), Donor Number (DN), Acceptor Number (AN), Viscosity (η), Dipole Moment (DM).

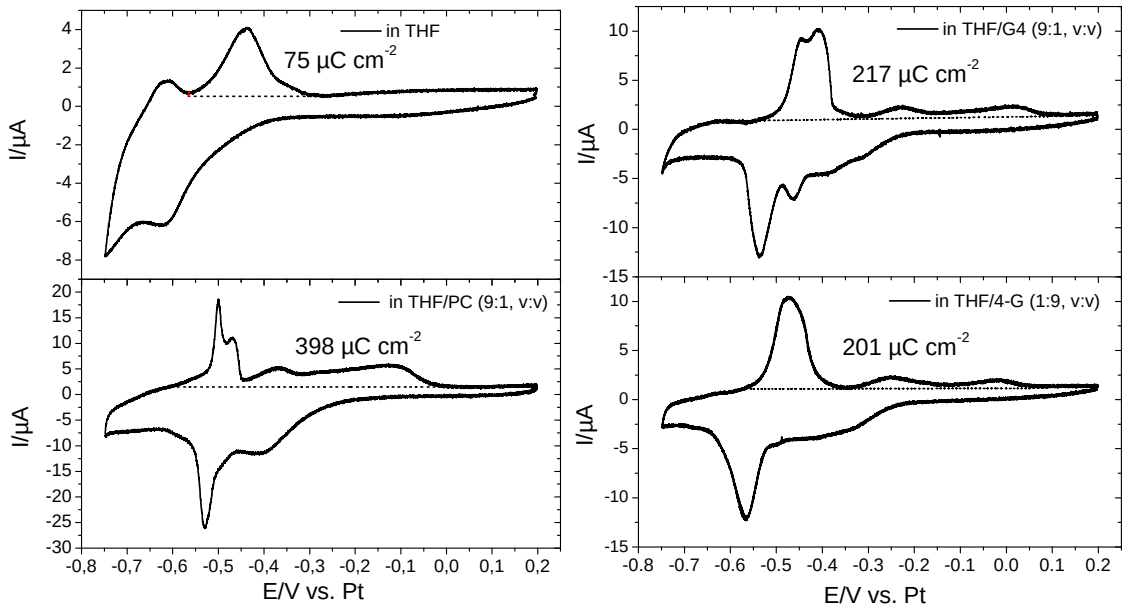

Fig. 5.3 Cyclic voltammograms of Pb-UPD on Au(111) in different solvents containing

5 mM $Pb(ClO_4)_2$ + 0.1 M $LiClO_4$ in STM cell at the scan rate of 10 mV s^{-1}.

Table. 5.2 Comparison of the charges of Pb-UPD and Pb-UPD stripping on Au(111) in the different electrolytes

solvent	UPD stripping peak (at ~0.5 V) charge	UPD stripping charge (between -0.6 and 0.1 V)
THF (pure)	75 μC cm^{-2}	75 μC cm^{-2}
THF/PC (9:1, v:v)	154 μC cm^{-2}	398 μC cm^{-2}
THF/G4 (9:1, v:v)	158 μC cm^{-2}	217 μC cm^{-2}
THF/G4 (1:9, v:v)	148 μC cm^{-2}	201 μC cm^{-2}
PC (pure) (+ 0.1 M TBAP)	350±20 μC cm^{-2} (between 2.9 and 3.1 V vs. Li/Li^+) [25]	

The reasonable explanation for the effect of solvent on metal UPD process is mainly due to the extent and type of formation of ion-pairs at the interface of the electrode and electrolyte and in the electrolyte. Fawcett et al. [38] investigated the effect of ion pairs on electrochemical kinetics. Nagaoka et al. [39, 40] and other authors [41, 42] suggested that ion-pairs adsorbed on the electrode surface may hinder the electron transfer, resulting in distortions in the polarization curves and shifts in the half-wave potentials. The formation of ion-pair was considered to be mainly related to the dielectric constant [43, 44], but other properties of the solvent cannot be ruled out. However, Schmid [45] considered that the dielectric constant can be determined by the donor number and acceptor number in a common aprotic solvents. For determining the extent of ion-pair formation in the solvent, the donor number (DN) and acceptor number (AN) should also be taken into account because the DN and AN indicate the ability of a solvent to solvate Lewis acids and cations and Lewis bases and anions, respectively. V. Gutmann [46] and Gonzalez [47] have found that the formation constant of ion pair is greater when both the donor number and acceptor number of solvent are decreased.

The relationship between UPD peaks and UPD-stripping peaks in different electrolyte was examined by reversing the direction of potential scan at different negative limiting potential and the cyclic voltammograms were shown in Fig. 5.4. But until now, there is no interpretation about these peaks. In aqueous solution, Motheo et al. observed five cathodic peaks (A1~A5) and five anodic peaks (D1~D5) and the detailed interpretation is available in the literature [48].

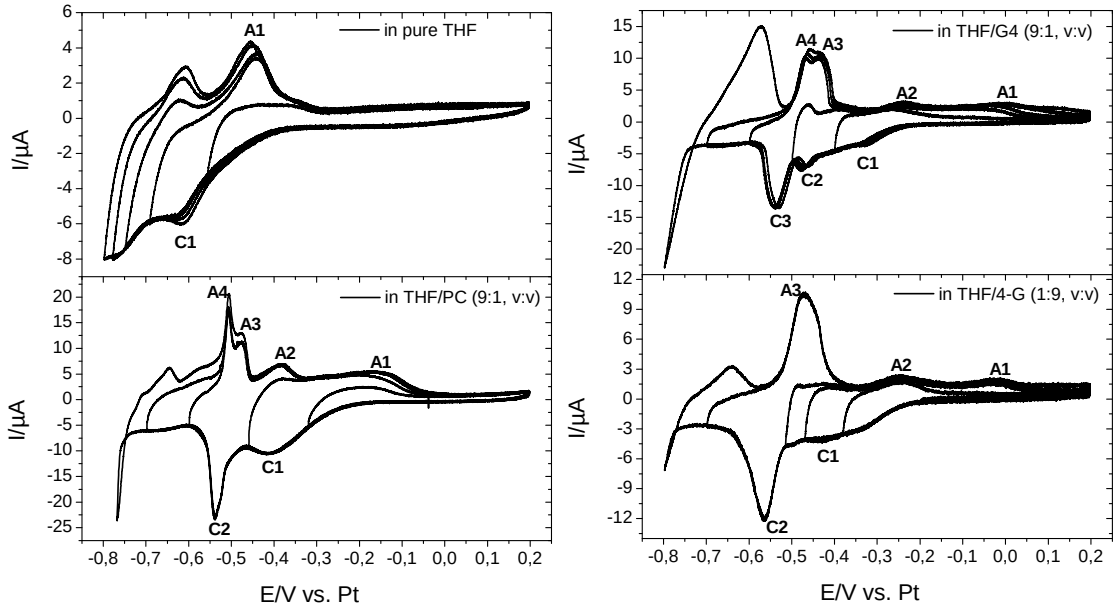

Fig. 5.4 Cyclic voltammograms of Au(111) in different solvents containing 5 mM $Pb(ClO_4)_2$ + 0.1 M $LiClO_4$ in STM cell in argon-filled glove box at the scan rate of 10 mV s^{-1}. C_n and A_n with n = 1, 2, 3, 4 denote cathodic adsorption and anodic desorption peaks, respectively.

Similar to the case of Cu-UPD in acetonitrile based electrolyte, the characteristic of the polarization curve of Pb-UPD disappeared and the large flowing currents on the electrode surface at negative potential (especially in THF/PC (9:1, v:v) based electrolyte) were observed in all cases once the electrolytes were exposed to air (see. Fig. 5.5). As mentioned before, it is probably due to the effect from water or oxygen or both. Oh et al. [49] found that oxygen reduction reaction also takes place during underpotential deposition of Pb in aqueous solution and its activity can be enhanced by Pb-UPD. In nonaqueous solution, Xing et al. [25] investigated the effect of water content (800 and 8000 ppm) on Pb-UPD in PC and found only the negative shift in potential but no distortion of polarization curve. That would mean that the effect on Pb-UPD process is mostly due to the presence of oxygen. According to our investigation of ORR in nonaqueous solution, the onset potential of ORR in 0.1 M $LiClO_4$/DMSO was found to be around -0.5 V (vs. Pt/PtO).

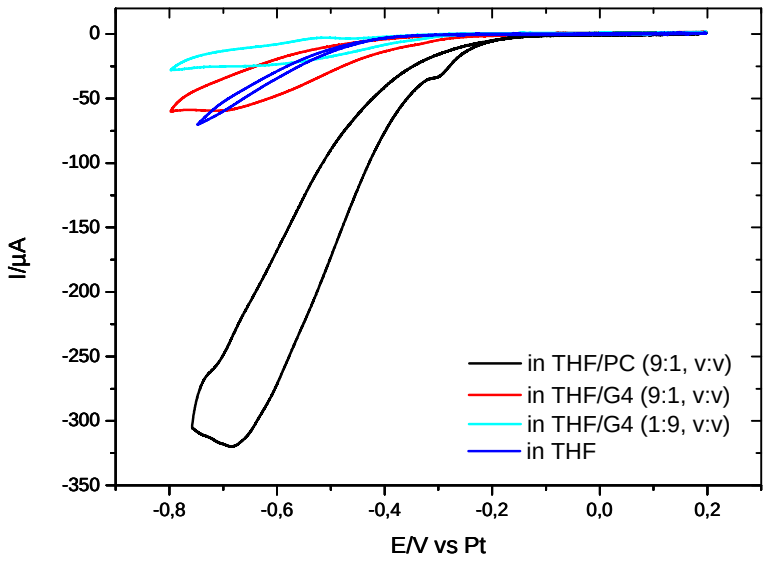

Fig. 5.5 Cyclic voltammograms of Au(111) in different solvents containing 5 mM $Pb(ClO_4)_2$ + 0.1 M $LiClO_4$ in STM cell in air at the scan rate of 10 mV s^{-1}.

5.3.3 Ag deposition on Au(111)

In this part, MeCN, THF and G4 were used as solvent for investigation of their effect on Ag-UPD on Au(111). These work have never been reported.

5.3.3.1 Ag deposition on Au(111) in the solvent with high dielectric constant

Ag deposition on Au(111) in acetonitrile containing 1 mM $AgNO_3$ + 0.1 M $LiClO_4$

Cyclic voltammograms (CVs) of Au(111) electrode in acetonitrile containing 1 mM $AgNO_3$ + 0.1 M $LiClO_4$ solutions at 10, 50, 100 mV s^{-1} were obtained in argon-filled glove box and air, respectively, as shown in Fig. 5.6. In both cases, two cathodic peaks and two corresponding anodic peaks were observed at the potential of ~0.61 and ~0 V (vs Ag/Ag^+), which are assigned to the Ag-UPD/UPD stripping and bulk deposition/stripping on Au(111) surface, respectively. By comparing the CVs obtained under argon to that under air condition, it suggests that the components of atmosphere (such as oxygen, water, etc.) have no effect on Ag deposition process, unlike in the case of Pb and Cu deposition in nonaqueous electrolytes discussed before, because the potential of Ag deposition is more positive than that of oxygen or water reduction.

It is well known that three major peaks at 0.52, 0.13 and 0.03 V (vs. Ag/Ag^+) in the UPD region were observed in aqueous solution. However, in acetonitrile, only one small and broad peak appeared in the UPD region at ~0.6 V and the charge calculated after

subtracting the double layer charge was found to be 42 μC cm^{-2}, which is less than that of monolayer (ML) formation of Ag (222 μC cm^{-2}) [50, 51]. It suggests that only 0.19 ML formed on Au(111) surface during the UPD process in this electrolyte. Perhaps, this is due to the effect of co-adsorption or competitive adsorption of solvent, anions or contaminations present in the electrolyte at the electrode surface. Vaskevich [15] reported that acetonitrile adsorbs on the Au surface strongly. Cunha et al. [52], observed that nitrate ions and NO_2^-, which is the product of reduction of nitrate ions at ~0.05 V (vs. Pd|H_2), adsorbed on Au surface at the potential above 0.8 V. And other anions (sulfate ion and halide ions) co-adsorption on Au(111) surface in aqueous systems have also been reported in the literature [51, 53-55].

In general, the peak current (i_p) in cyclic voltammetry depends not only on the concentration and diffusion of the electroactive species but also on the scan rate. In the diffusion controlled reversible or quasi-reversible electrochemical reaction, the peak current follows Randles-Sevcik equation [56, 57].

$$i_p = 0.4463nFAC\left(\frac{nF\upsilon D}{RT}\right)^{\frac{1}{2}}$$

When the electrolyte is at room temperature (25 °C), the equation can be described as follow: $i_p = 268{,}600n^{\frac{3}{2}}AD^{\frac{1}{2}}C\upsilon^{\frac{1}{2}}$

Where, i_p is the peak current (A); n is the electron transfer number; A is the electrode area (cm^{-2}); F is the Faraday constant (C mol^{-1}); D is the diffusion coefficient (cm^2 s^{-1}); C is the concentration (mol cm^{-3}); υ is the scan rate (V s^{-1}); R is the Gas constant (J K^{-1} mol^{-1}); T is the temperature (K).

In bulk deposition region, the peak currents as a function of the square root of scan rates were plotted and shown in Fig. 5.6b. In all cases, the plots exhibited linear and the intercepts are very close to zero. The diffusion coefficient of Ag^+ in this solution is calculated to be 4.28×10^{-11} cm^2 s^{-1}, which is much smaller than the typical value (within a range of minus five orders of magnitude) of ion diffusion coefficient in electrolyte.

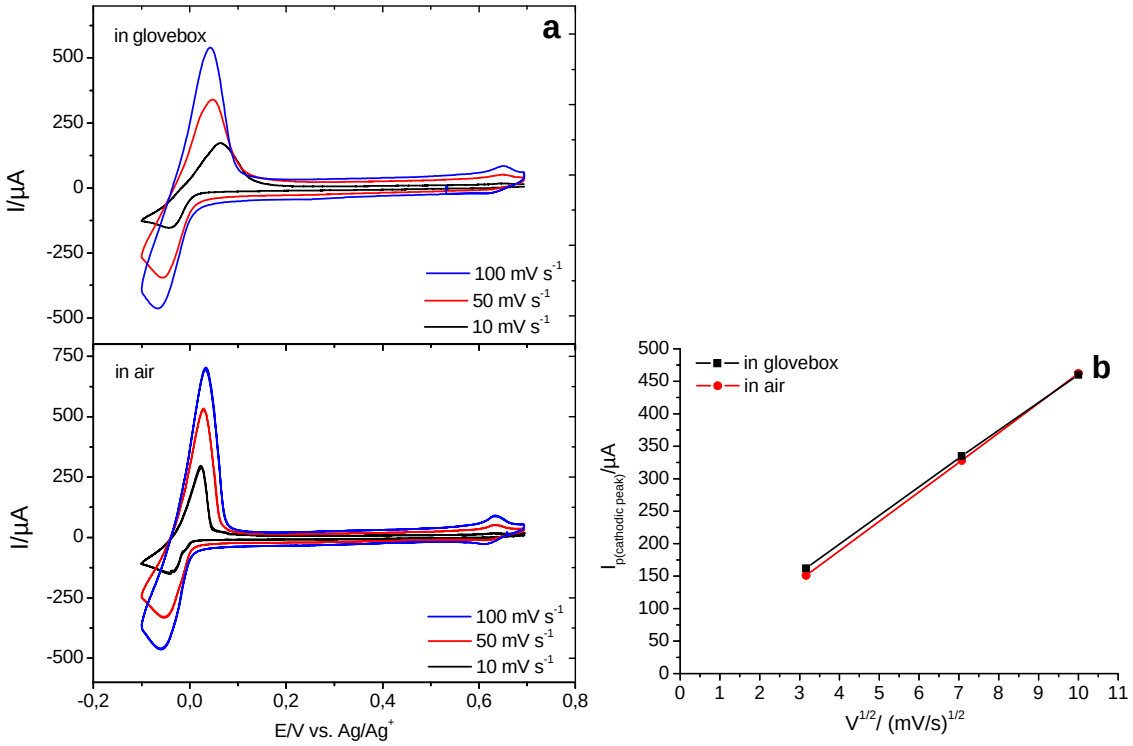

Fig. 5.6 a) Cyclic voltammograms of Ag deposition on Au(111) in acetonitrile containing 1 mM $AgNO_3$ + 0.1 M $LiClO_4$ in STM cell at the scan rate of 10, 50 and 100 mV s^{-1}: (top) in argon-filled glove box, (bottom) in air. b) Plots of i_p (peak current) vs. $\nu^{1/2}$ (square root of scan rate).

Ag deposition on Au(111) in acetonitrile containing 1 mM $AgClO_4$ + 0.1 M $LiClO_4$

In order to compare the effect of anions (ClO_4^- and NO_3^-) on UPD of Ag on Au(111), $AgClO_4$ instead of $AgNO_3$ was used as salt in acetonitrile containing 0.1 M $LiClO_4$. Similar cyclic voltammograms of Ag deposition on Au(111) were obtained in 1 mM $AgClO_4$ + 0.1 M $LiClO_4$ in acetonitrile and shown in Fig. 5.7. But the UPD peak became obvious and the charge (65 µC cm^{-2}, ~0.3 ML) of UPD peak became large by comparing with the electrolyte in the presence of NO_3^-. It suggests that the influence of ClO_4^- anion on Ag-UPD on Au(111) process is less than that of NO_3^- anion. This is probably due to that the adsorption strength of NO_3^- or solvated NO_3^- on Au(111) surface is stronger than that of ClO_4^- or solvated ClO_4^- [58] and the amount of NO_3^- species in the double layer is larger than that of ClO_4^-. However, the UPD charge is still smaller than that of monolayer formation because acetonitrile adsorbs on the surface as discussed before and the adsorption of ClO_4^- anion or solvated anion could also not be excluded. Hamm [59] and Kolb [60] et al. found that perchlorate ions show a weak specific adsorption on Au(111) surface. Furthermore, a relatively stable process of Ag

deposition on Au(111) in air atmosphere was also observed in this case (see. Fig. 5.7). The linear relationship between the peak currents and the square root of scan rates and zero intercept were also obtain in both cases as well (see. Fig. 5.7b). The diffusion coefficient of Ag^+ in this solution is calculated to be 2.39×10^{-11} cm^2 s^{-1}, which is close to the value obtained in 1 mM $AgNO_3$ based electrolyte.

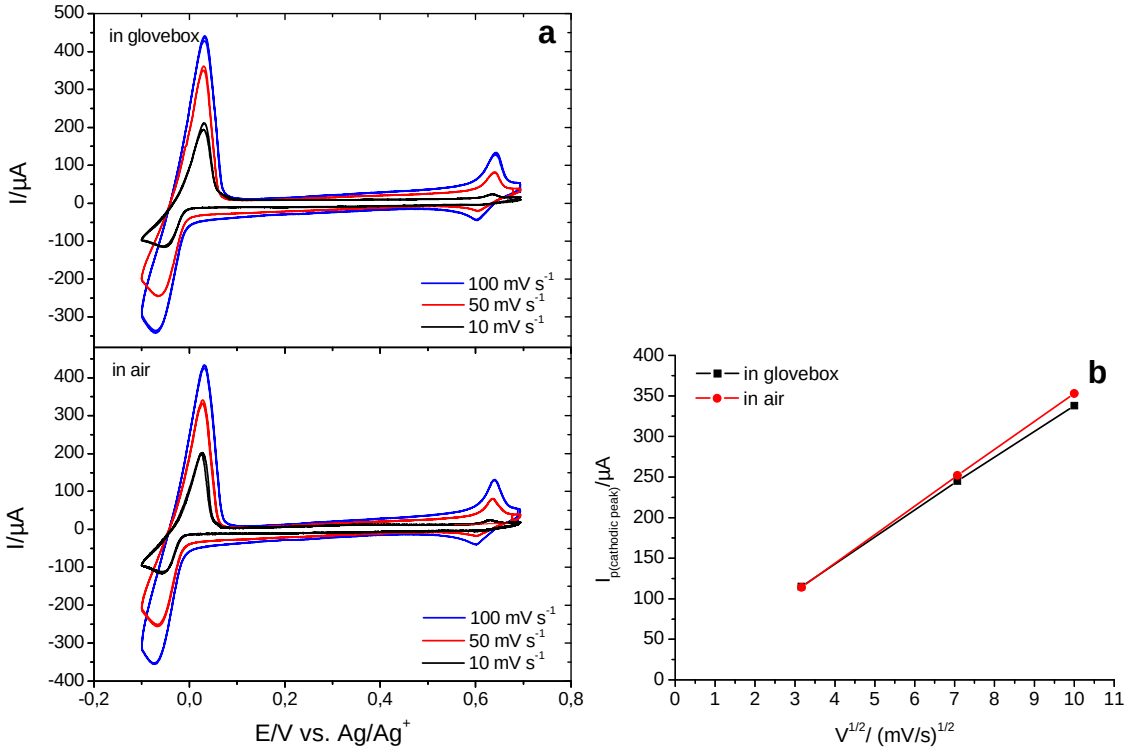

Fig. 5.7 a) Cyclic voltammograms of Ag deposition on Au(111) in acetonitrile containing 1 mM $AgClO_4$ + 0.1 M $LiClO_4$ in STM cell at the scan rate of 10, 50, 100 mV s^{-1}: (top) in argon-filled glove box, (bottom) in air. b) Plots of i_p (peak current) vs. $v^{1/2}$ (square root of scan rate).

5.3.3.2 Ag deposition on Au(111) in the solvents with low dielectric constant

Ag deposition on Au(111) in tetrahydrofuran containing 1 mM $AgClO_4$ + 0.1 M $LiClO_4$

Fig. 5.8 shows the cyclic voltammograms of Ag deposition on Au(111) in tetrahydrofuran containing 1 mM $AgClO_4$ + 0.1 M $LiClO_4$ in both air and argon-filled glove box. The cyclic voltammograms obtained in both cases are similar and the UPD charges both are around 60 µC cm^{-2}, except that the peaks are slightly sharp under air atmosphere comparing to under argon atmosphere. This could be due to the effect of water, which has a high dielectric constant of 78.41 at 25°C, suggesting that in the solvent with low dielectric constant, the effect of water is relatively obvious by

comparing with that in the solvent with high dielectric constant, because the difference in the dielectric constant is larger.

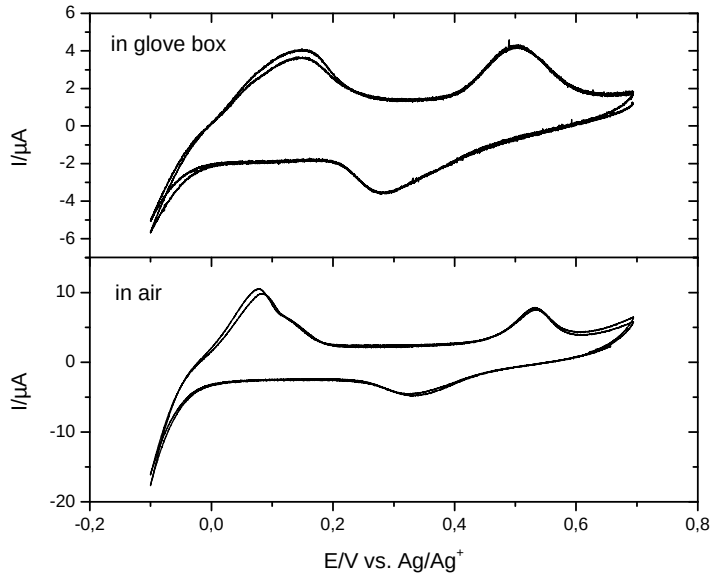

Fig. 5.8 Cyclic voltammograms of Ag deposition on Au(111) in tetrahydrofuran containing 1 mM $AgClO_4$ + 0.1 M $LiClO_4$ in STM cell at the scan rate of 10 mV s^{-1}: (top) in argon-filled glove box, (bottom) in air.

Ag deposition on Au(111) in tetraglyme containing 1 mM $AgClO_4$ + 0.1 M $LiClO_4$

Ag deposition on Au(111) was also carried out in tetraglyme containing 1 mM $AgClO_4$ + 0.1 M $LiClO_4$. The similar cyclic voltammograms were obtained in both air and glove box and shown in Fig. 5.9. The slight change in CVs between the electrolyte under air and argon is similar to that observed in tetrahydrofuran. A small peak and broad peak were observed at the potential of 0.45 and 0.1 V in UPD region, respectively. The CVs are almost stable under argon atmosphere but it is not the case under air. Under air atmosphere, the intensity of the first UPD peak (at 0.45 V) increased and its corresponding stripping peak decreased and the second peak (at ~0.1 V) gradually disappeared with cycles, and then the CV became stable after several cycles. The total UPD charge is around 94 μC cm^{-2}, indicating that 0.42 monolayer of Ag formed on Au(111) surface. It is worth to mention that two separated dissolution peaks at around 0.06 V and 0.12 V were observed in both cases and they are probably related to the dissolution of bulk and second layer, respectively. The charges of the anodic peaks at ~0.13 V were calculated by integrating the red shaded area to be 194 and 152 μC cm^{-2} under argon atmosphere and air atmosphere, respectively.

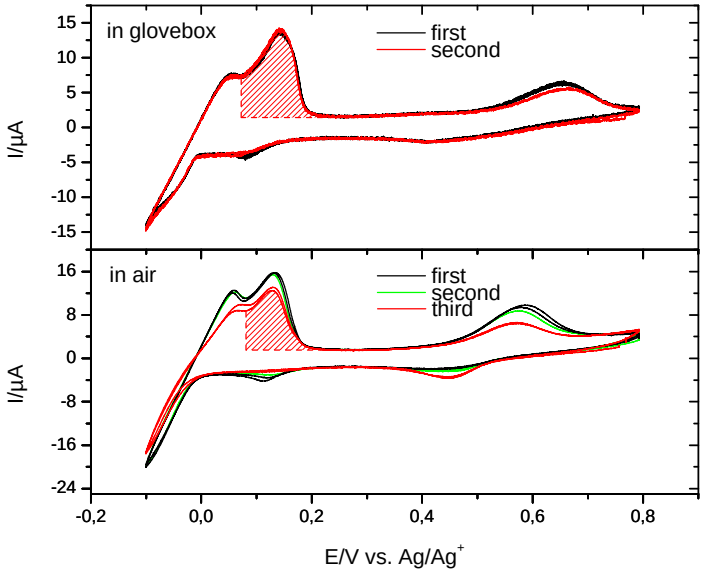

Fig. 5.9 Cyclic voltammograms of Ag deposition on Au(111) in tetraglyme containing 1 mM $AgClO_4$ + 0.1 M $LiClO_4$ in STM cell at the scan rate of 10 mV s^{-1}: (top) in argon-filled glove box, (bottom) in air.

5.3.3.3 Comparison of the effect of the solvents on Ag-UPD process

Ag-UPD on Au(111) have been done in MeCN(ε, 38.8), G4(ε, 7.79) and THF(ε, 7.52) based electrolytes. The cyclic voltammograms are shown in Fig. 5.10. It is obvious that the potential of UPD peaks is at 0.6, 0.41 and 0.28 V in MeCN, G4 and THF based electrolyte, respectively, suggesting that the UPD peak potential was shifted in the negative direction or the kinetics of UPD process is sluggish in the electrolyte based on the solvents with low dielectric constant (such as G4), and especially with high donor number (such as THF) was used. Furthermore, the distorted polarization curve was observed in the electrolyte, which is based on the solvent with low dielectric constant as well. It agrees with the results of Pb UPD on Au(111) as discussed before. These could be attributed to the formed adsorbates (such as ion pair, solvated ions, etc.) adsorbed at the electrode surface modifying the energetics and kinetics of the UPD process [61-63] in the electrolyte based on the solvent with low dielectric constant. More specifically, these adsorbates (including solvent) adsorbed at the electrode surface could block the metal nucleation sites and hinder its growth [64] and the amount of co-adsorbed species determines the UPD charge. The change in the amount of co-adsorbed species could cause the variation of the UPD charge. The lowest UPD stripping charge was obtained in MeCN base electrolyte, but the double large is the largest and the Ag bulk deposition is very fast in this case. The highest value was obtained in G4 based electrolyte, which

is still less than the theoretical value for monolayer formation and the experimental value in aqueous solution [29, 65]. The coverages were calculated by considering that the Ag monolayer formation on Au(111) requires the charge of 240 μC cm^{-2} and are also shown in Fig. 5.10. As mentioned before, the dielectric constant is the main factor to determine the extent of ion pair formation, and the ion pair plays a role in determining the conductivity of electrolyte, kinetic behaviour of the reaction, etc. [66] Generally, it is found that extensive ion pair formed in the electrolyte, which is based on the solvent with low dielectric constant [67, 68]. Triple cations and triple anions have also been observed in THF [69]. Na^{+},G,$N^{\bullet -}$ loose ion pair was found in tetraglyme containing sodium naphthalene [70].

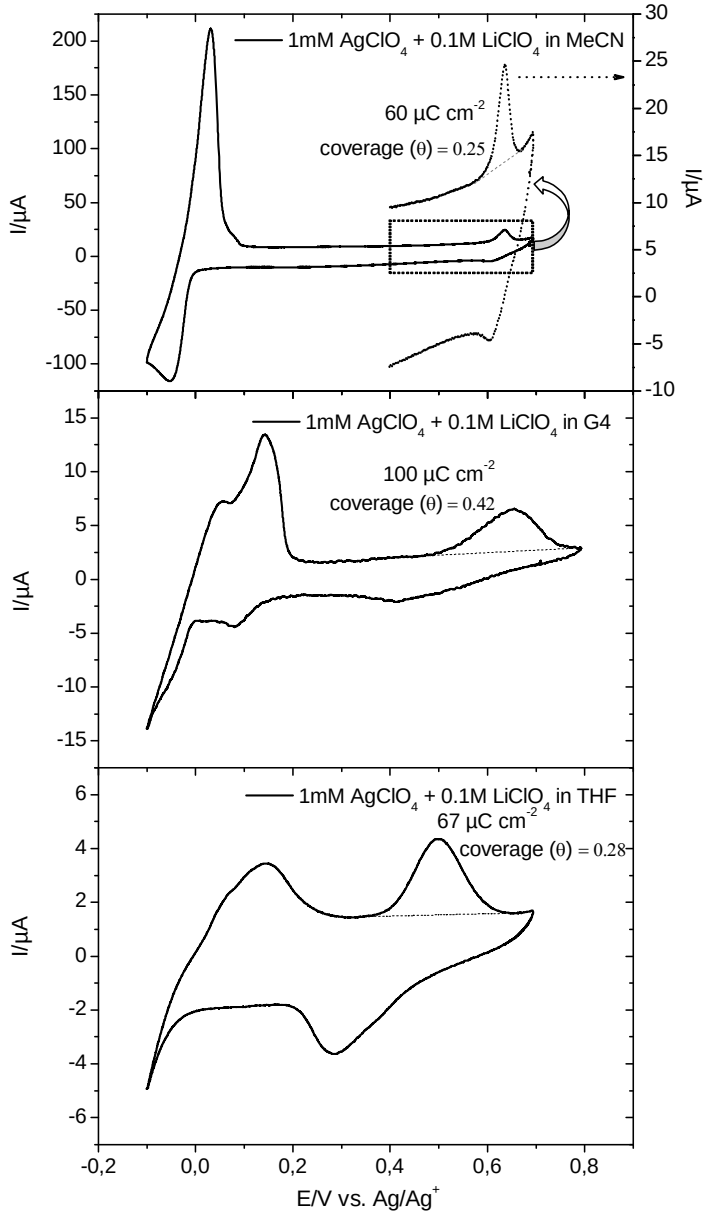

Fig. 5.10 Cyclic voltammograms of Ag deposition on Au(111) in acetonitrile (top), tetraglyme (middle) and tetrahydrofuran (bottom) containing 1 mM $AgClO_4$ + 0.1 M

$LiClO_4$ in STM cell in argon-filled glove box at the scan rate of 10 mV s^{-1}.

5.3.3.4 EC-STM observation of Ag deposition in tetraglyme containing 1 mM $AgClO_4$ + 0.1 M $LiClO_4$ electrolyte

An in-situ observation of Ag deposition on Au(111) in tetraglyme containing 1 mM $AgClO_4$ + 0.1 M $LiClO_4$ electrolyte were performed by electrochemical scanning tunnelling microscopy (EC-STM). The similar cyclic voltammogram was obtained and shown in Fig. 5.11.

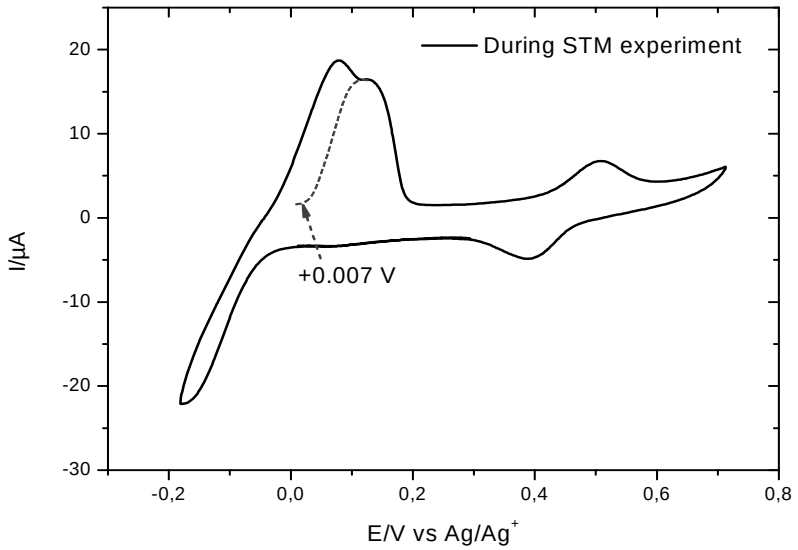

Fig. 5.11 Cyclic voltammogram of Ag on Au(111) in tetraglyme containing 1 mM $AgClO_4$ + 0.1 M $LiClO_4$ in STM cell at the scan rate of 10 mV s^{-1} during STM measurement.

Fig. 5.12 shows the morphology of Au(111) electrode surface in tetraglyme containing 1 mM $AgClO_4$ + 0.1 M $LiClO_4$ during the discontinuous potential scanning in the range of +0.2 to +0.66 (UPD region). The open circuit potential (OCP) or rest potential was found at +0.33 V vs. Ag/Ag^+, where is more negative than the UPD peak potential, meaning that Ag atoms are already adsorbed on the surface at OCP. Once the potential was swept to positive direction and then reversed in negative direction, it was observed clearly that the dissolution process started at around +0.5 V and deposition started at around +0.45 V, respectively, and these are consistent with the results observed in cyclic voltammogram as shown in Fig. 5.11. The step heights after monolayer deposition and stripping are measured and shown in Fig. 5.12. It suggests that Ag deposition prefer to occur on the terraces. Furthermore, after stripping it is visible that some adsorbate molecules remained on Au(111) surface. These adsorbates are probably pre-adsorbed on

Au(111) surface. The pre-adsorbates and co-adsorbates would lead to irregular deposition of Ag on Au(111) surface as shown in Fig. 5.12 and small UPD charge of 96 μC cm^{-2} in Fig. 5.11. As described previously, these adsorbates could be solvent molecules, ion pairs, solvated ions, etc. In addition, the larger bright dots are probably Au islands as a result of the lifting of the thermally induced surface reconstruction at positive potential [71] or contaminations.

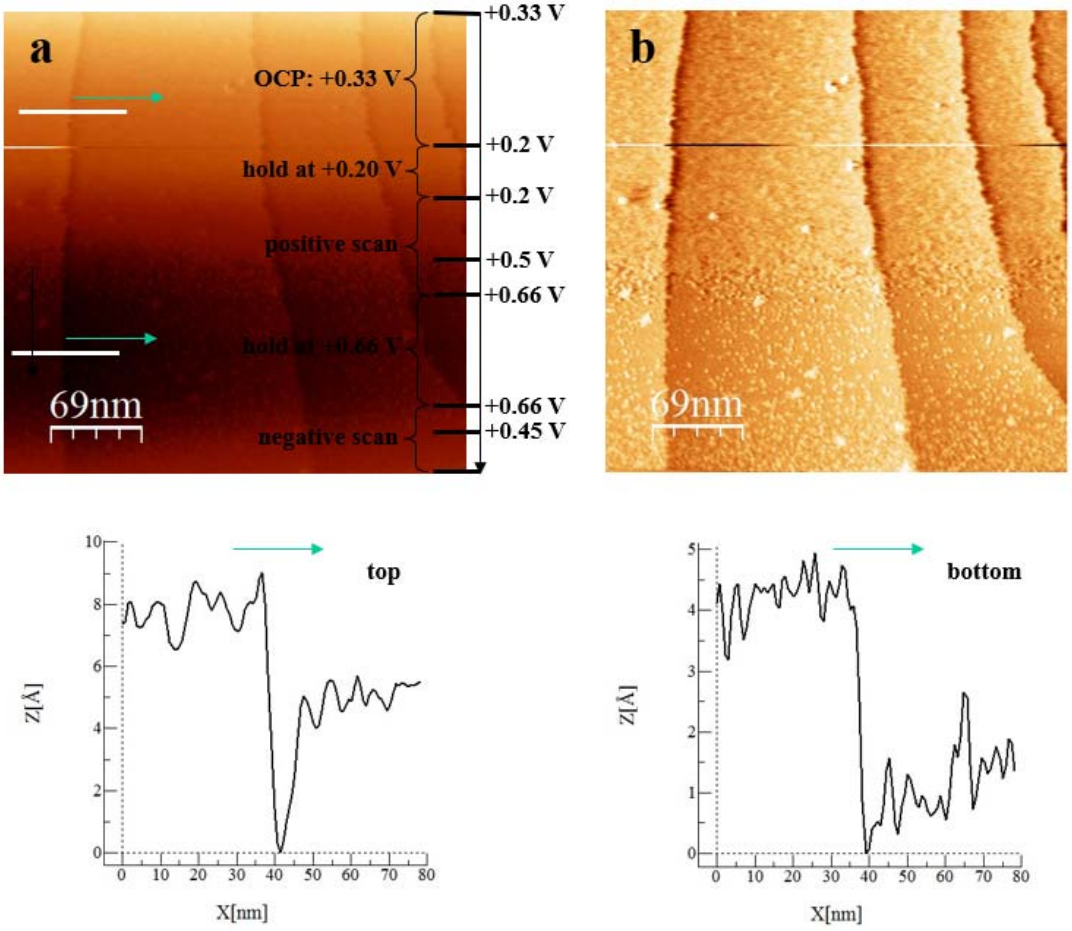

Fig. 5.12 Typical STM images of the Ag UPD on Au(111) in tetraglyme containing 1 mM $AgClO_4$ and 0.1 M $LiClO_4$ electrolyte at the scan rate of 3.04 ln/s. Integral gain: 2 and proportional gain: 3. Arrows indicate scan direction. Plane correction is used for image a and line by line correction is used for image b. Two cross sections show the height change along the white lines on image a.

A detailed in-situ EC-STM observation of Ag-UPD on Au(111) is shown in Fig. 5.13. The results are consistent with those previously observed. While the potential was swept from 0.62 to 0.13 V vs. Ag/Ag^+, a random nucleation and growth process of Ag on Au(111) terrace and accompanying with pre-adsorption and co-adsorption of other species to form a monolayer were observed again as shown in Fig. 5.13a, b and c. On

this monolayer, it is very difficult or even impossible to get atomic resolution images. The rough Ag-UPD adlayer has been also observed in aqueous solution by Hamm [59], who believes that the apparent charge deficit and the rough surface were caused by the co-adsorption of anions induced by the expected shift in point of zero charge (pzc) during Ag deposition. Once the potential was swept back from 0.13 to 0.62 V, an Ag-UPD adlayer stripping process was observed as shown in Fig. 5.13d. After stripping, some pre-adsorbed adsorbates became very visible on Au(111) again as shown in Fig. 5.13d and e, and caused a rougher surface (see. Fig. 5.13c) comparing to that of Ag-UPD adlayer (see. Fig. 5.13e). It is well known that these adsorbates have a larger effect on metal-UPD process, modify the energetics and kinetics of the metal-UPD process, and make it complicated.

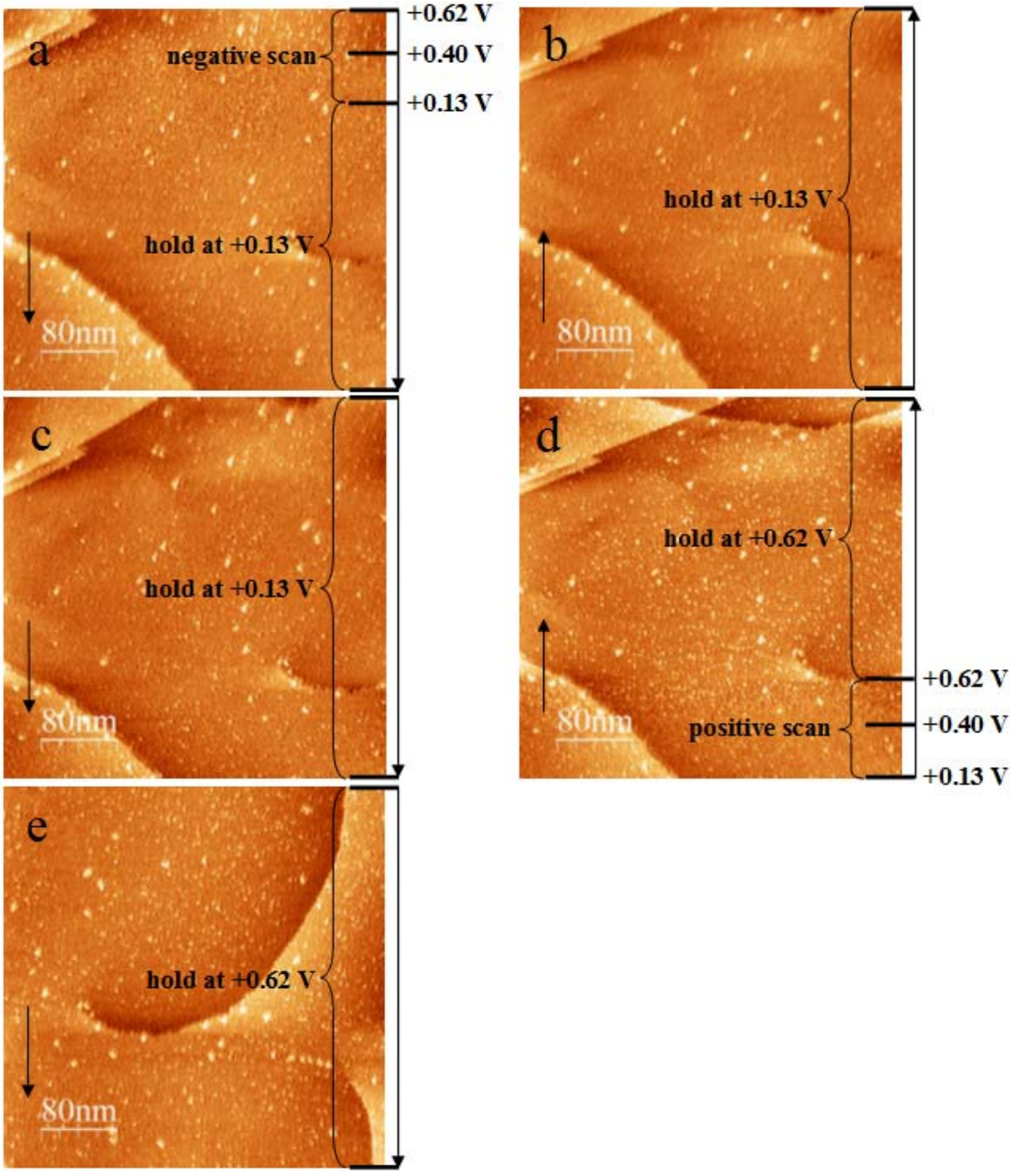

Fig. 5.13 Typical in-situ STM images of Ag-UPD on Au(111) in tetraglyme containing 1 mM $AgClO_4$ + 0.1 M $LiClO_4$ electrolyte at the scan rate of 3.04 ln/s. (a) from 0.62 to 0.13 V, (b) 0.13 V, (c) 0.13 V, (d) from 0.13 to 0.62 V, (e) 0.62 V. Integral gain: 2 and proportional gain: 3. Arrows indicate scan direction. Line by line correction is used for above images.

The Ag-OPD on Au(111) process was also observed by EC-STM. Fig. 5.14 demonstrates the sequential in-situ STM images recorded at different overpotentials. Similar morphology of Ag-UPD adlayer was observed at +0.3 V as shown in Fig. 5.14a. A few bright dots were also observed on this surface. As mentioned before, these are probably Au islands. When the potential was held at -0.025 V where is slightly more negative than 0 V (the onset potential of OPD), the initial nucleation of Ag preferring to start at the energetically favorable binding sites such as island rims as indicated by comparing the size of the islands in elliptic region of Fig. 5.14a and Fig. 5.14b), holes and step edges was observed in Fig. 5.14b, similar to that in aqueous solution [72]. However, the deposition process is very slow at such low overpotential. With the further increase of overpotential to -0.055 V, a continuous epitaxial growth to form a completely closed layer was observed obviously (see. Fig. 5.14c), then 3D growth started (see. Fig. 5.14d and e). These results suggested that Ag growth on Au(111) in this nonaqueous electrolyte follows a layer-by-layer growth (or “Frank-van der Merwe” growth [1]) only up to two monolayers initially, then following by 3D growth (or “Stranski-Krastanov” growth [1]) because of the non-uniform distribution of interfacial energy and the accumulated lattice misfit [19]. This growth mode is different from that in aqueous electrolyte, in which a layer-by-layer growth up to at least ten monolayers was observed [72]. The height of the formed Ag island in Fig. 5.14e was measured to be ~1.1 nm, which suggests that around three monolayers formed on the second adlayer. It is worth to mention that it need ~2.8 min to generate one image. When the potential was swept back to +0.106 V, Ag adlayers deposited at overpotenital were dissolved completely and the bright dots with the same size and same position reappeared on the surface (see. Fig. 5.14a and f/g).

Rapid deposition and dissolution of Ag on Au(111) under the control of a continuous potential scan is demonstrated in Fig. 5.15a and a′. The Ag-OPD started at around 0 V and it was dissolved completely at ~+0.157 V. It is certain that the higher overpotential

will lead to faster deposition rate, so that it seems that a "Stranski-Krastanov" growth mode was excited immediately once OPD started. The height of Ag deposited on Au(111) during this process is around 5.4 nm (see. the cross section on image a′). A complete dissolution of Ag adlayers was confirmed again as shown in Fig. 5.15b.

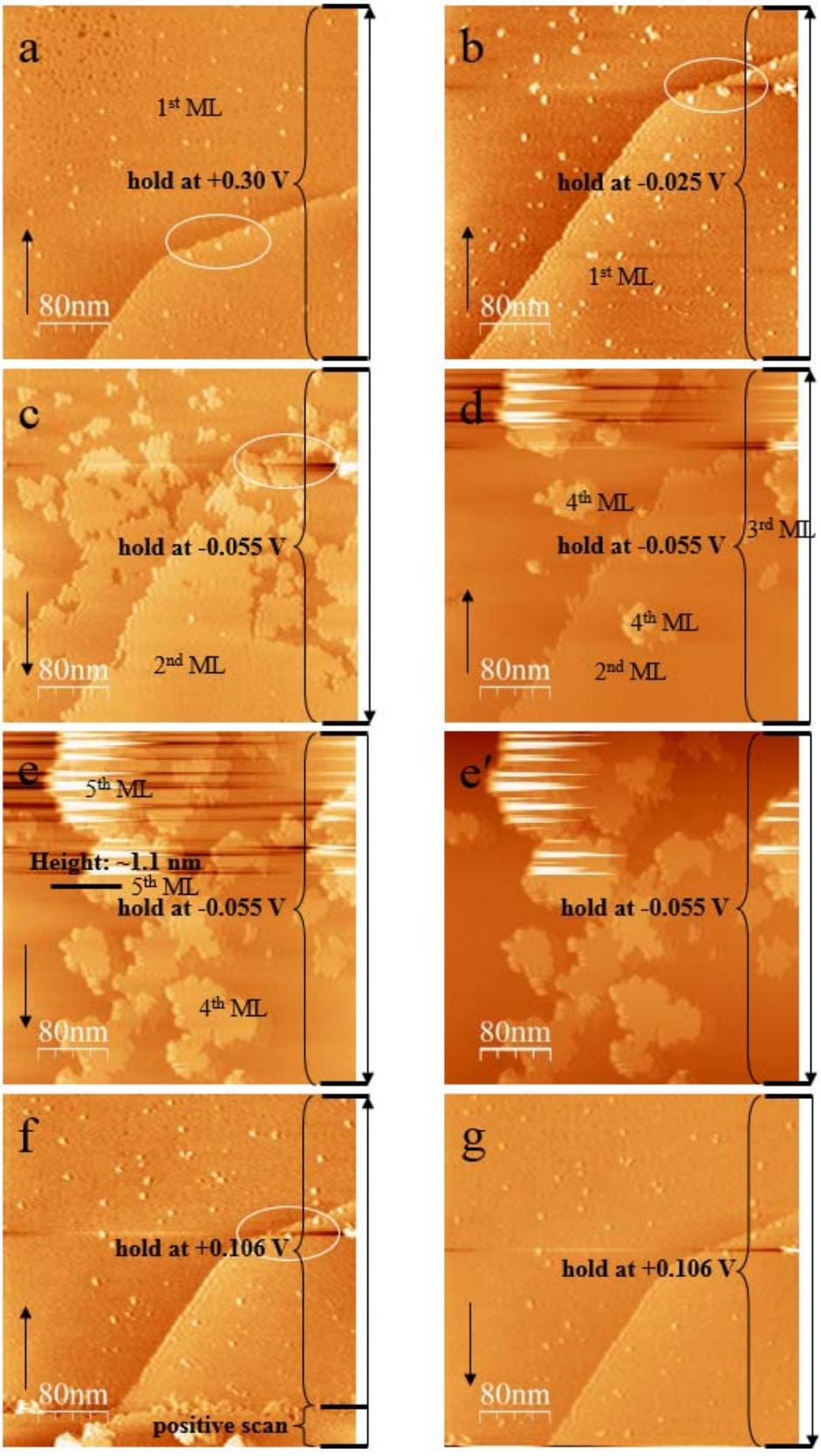

Fig. 5.14 Typical in-situ STM images of the Ag-OPD on Au(111) in tetraglyme containing 1 mM $AgClO_4$ + 0.1 M $LiClO_4$ electrolyte at the scan rate of 3.04 ln/s. (a) +0.298 V, (b) -0.025 V, (c) -0.055 V, (d) -0.055 V, (e) -0.055 V, (e') -0.055 V, (f) from -0.055 to +0.106 V, (g) +0.106 V. Integral gain: 2 and proportional gain: 3. Arrows indicate scan direction. Line by line correction is used for images a-g. Plane correction is used for image e′.

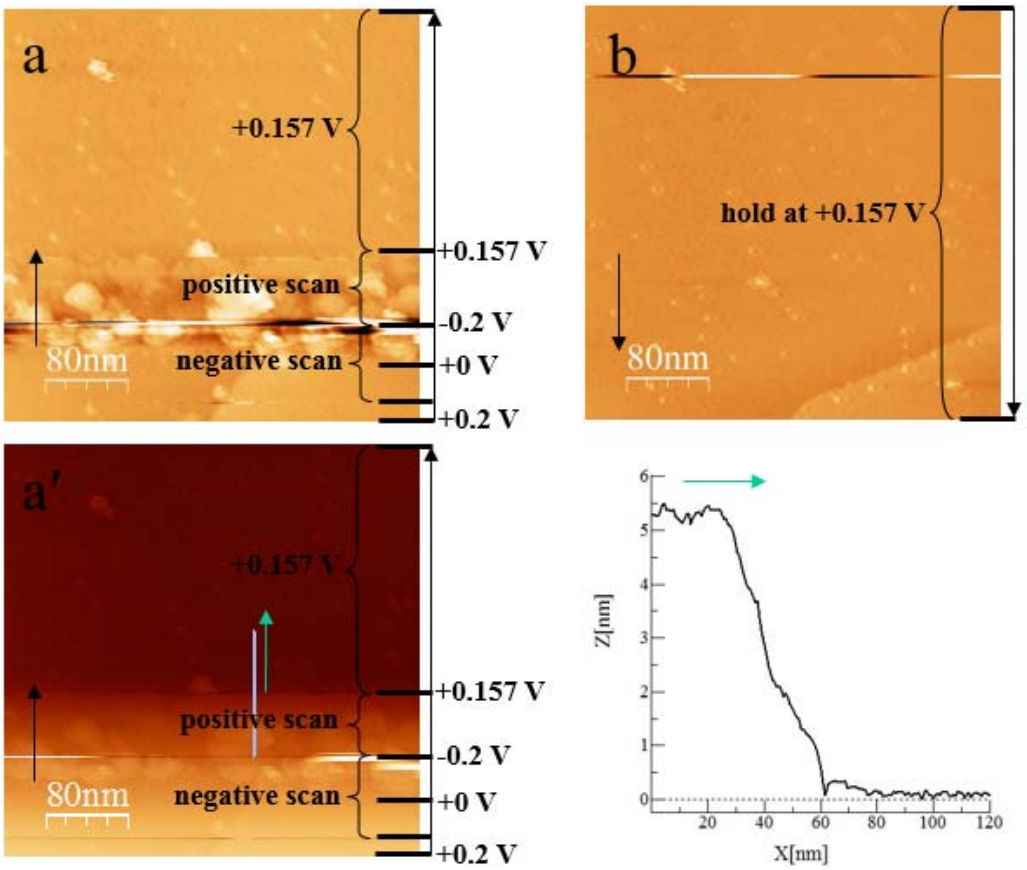

Fig. 5.15 STM images of Ag-OPD on Au(111) in tetraglyme containing 1 mM $AgClO_4$ + 0.1 M $LiClO_4$ electrolyte at the scan rate of 3.04 ln/s. (a) from -0.2 to +0.2 V, (b) +0.157 V. Integral gain: 2 and proportional gain: 3. Arrows indicate scan direction. Line by line correction is used for above images a and b. Plane correction is used for image a′.

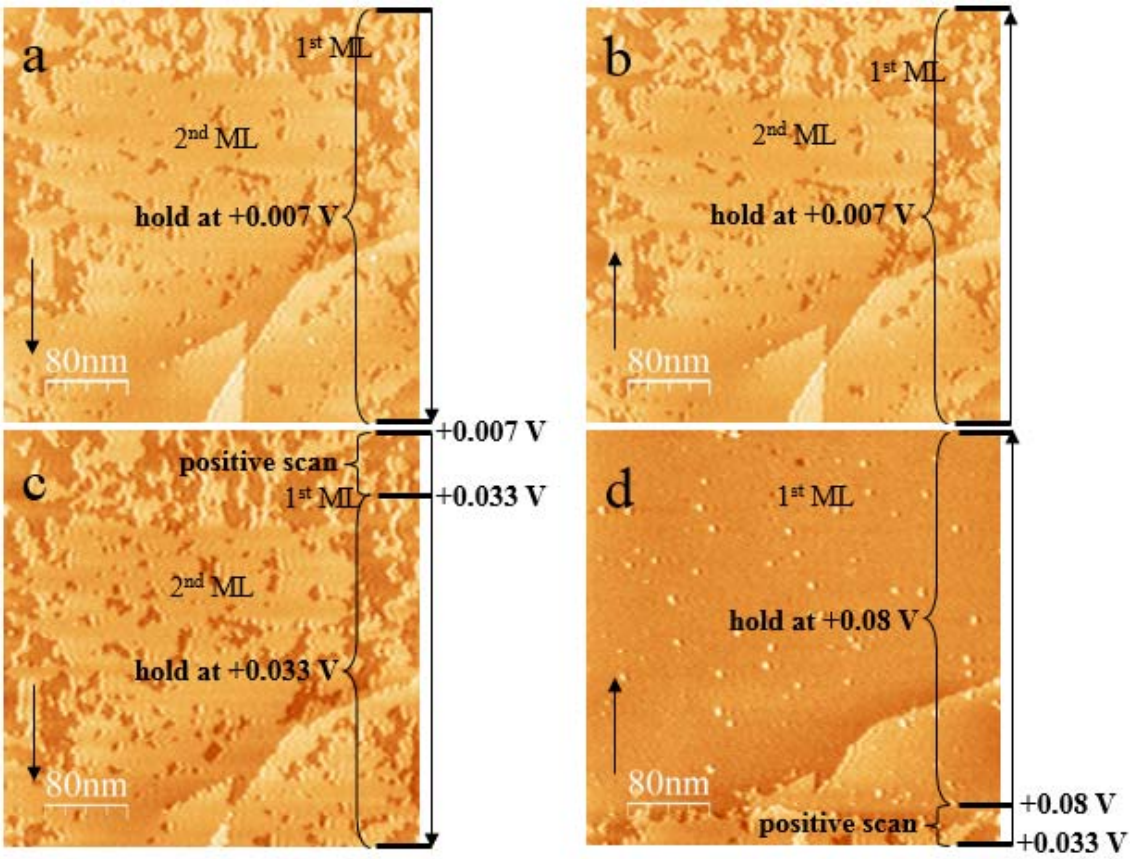

Fig. 5.16 in-situ STM images of Ag-OPD on Au(111) in tetraglyme containing 1 mM $AgClO_4$ + 0.1 M $LiClO_4$ electrolyte at the scan rate of 3.04 ln/s. (a) +0.007 V, (b) +0.007 V, (c) from +0.007 to +0.033 V, (d) from +0.033 to +0.08 V. Integral gain: 2 and proportional gain: 3. Arrows indicate scan direction. Line by line correction is used for above images.

As discussed before, two anodic peaks at 0.06 V and 0.12 V were observed in the cyclic voltammogram and they are probably related to Ag bulk dissolution and second layer dissolution, respectively. It is confirmed by the STM results, which were shown in Fig. 5.16. When the potential was held at +0.007 V where is very close to the onset potential of the second Ag adlayer dissolution (see. the dot curve in Fig. 5.11), the second Ag adlayer remained on the surface and it is stable over time as seen in Fig. 5.16a and b. Furthermore, very slow dissolution was observed at the potential of +0.033 V (see. Fig. 5.16). However, once the potential was swept to more positive value of +0.08 V, the dissolution of Ag took place very quickly and completely as shown in Fig. 5.16d. The images which were shown in Fig. 5.14, Fig. 5.15 and Fig. 5.16 were obtained from almost the same surface area if observed carefully.

5.4 Conclusions

This chapter focused on the study of underpotential and overpotential deposition of metal (Cu, Pb and Ag) on Au(111) electrode surface in different solvents such as acetonitrile (MeCN), tetrahydrofuran (THF), propylene carbonate (PC), tetraglyme (G4) and some mixture of them based nonaqueous electrolytes by cyclic voltammetry and EC-STM (only for Ag-UPD and OPD in tetraglyme based electrolyte).

For copper, Cu deposition behavior was investigated only in acetonitrile based electrolyte. It was found that the redox peak at ~1.1 V (vs. Cu/Cu^{2+}) is related to Cu^{2+}/Cu^{+} redox couple, two gentle UPD peaks indicate two step UPD process and the bulk deposition appears below 0 V. However, the characteristic polarization curve of copper deposition was distorted seriously or even disappeared when the electrolyte was exposed to air. This is probably due to the effect of oxygen reduction at more positive potential.

For lead, Pb deposition behavior in tetrahydrofuran and its mixture with propylene carbonate and tetraglyme based electrolytes was studied. The large distortion in the polarization curve and the small UPD charge were observed in pure THF based electrolyte and slightly distortion in the polarization curve was observed in THF/G4 (1:9 or 9:1) based electrolyte. This phenomenon could be caused by extensive co-adsorption of other species such as the formed ion-pair, solvated anion and extremely polar molecules in the electrolyte which consists only of the solvent with lower dielectric constant, and especially higher donor number. Similar to that in the case of Cu deposition in acetonitrile based electrolyte, the characteristic polarization curve of Pb deposition in these electrolytes was also distorted seriously or even disappeared when the electrolyte was exposed to air.

For silver, Ag deposition behavior in acetonitrile, tetraglyme and tetrahydrofuran (with different properties) based electrolytes was investigated. Similarly, the distorted polarization curve was observed again in the electrolyte based on the solvent with low dielectric constant, and especially with high donor number. However, unlike Cu and Pb deposition, the stable polarization curves of Ag deposition on Au(111) in these electrolyte under air atmosphere were observed. Base on this point and non-volatile tetraglyme, an in-situ STM observation of the Ag-UPD and OPD on Au(111) in

tetraglyme based electrolyte was performed. The results showed that the first Ag adlayer containing some pre-adsorbed and co-adsorbed species was formed and observed at the UPD region, a layer-by-layer growth (Frank-van der Merwe growth) up to only 2 monolayers, and then 3D growth were observed at low overpotential. In addition, the second Ag adlayer remained stable on the surface when the potential was held at ~+0.007 V, where is very close to the onset potential of the second Ag adlayer dissolution. It is consistent with the result observed in cyclic voltammetry.

References

[1] E. Budevski, G. Staikov, and W. J. Lorenz, Electrochemical Phase Formation and Growth: An Introduction to the Initial Stages of Metal Deposition, VCH, Weinheim, New York, Basel, Cambridge, Tokyo, 1996.

[2] D. M. Kolb, M. Przasnyski, and H. Gerischer, Journal of Electroanalytical Chemistry 54:25 (1974).

[3] V. S. Bagotsky, Fundamentals of Electrochemistry, 2nd Edition, wiley, 2005.

[4] S. Szabo, International Reviews in Physical Chemistry 10:207 (1991).

[5] R. F. Probstein, ed., Physicochemical Hydrodynamics: An Introduction, 2nd Edition, wiley, 2003.

[6] M. S. Singh, ed., Reactive Intermediates in Organic Chemistry: Structure, Mechanism, and Reactions, wiley, 2014.

[7] O. A. Oviedo, L. Reinaudi, S. G. García, and E. P. M. Leiva, Underpotential Deposition-From Fundamentals and Theory to Applications at the Nanoscale, Springer International Publishing, 2016.

[8] M. H. Hölzle, D. M. Kolb, D. Krznaric, and B. Cosovic, Ber. Bunsenges. Phys. Chem. 100:1779 (1996).

[9] J. Noh, T. Murase, K. Nakajima, H. Lee, and M. Hara, Journal of Physical Chemistry B 104:7411 (2000).

[10] K. Kunimatsu, H. Hanawa, H. Uchida, and M. Watanabe, Journal of Electroanalytical Chemistry 632:109 (2009).

[11] C. P. Wilde and M. Zhang, Electrochimica Acta 39:347 (1994).

[12] J. Kua and W. A. G. III, Journal of Physical Chemistry B 102:9481 (1998).

[13] Y. Tsai, C. Xu, and B. Koel, Surface Science 385:37 (1997).

[14] G. Dodero, L. De Michieli, O. Cavalleri, R. Rolandi, L. Oliveri, A. Dacca, and R. Parodi, Colloids and Surfaces a-Physicochemical and Engineering Aspects 175:121 (2000).

[15] A. Vaskevich and I. Rubinstein, Journal of Electroanalytical Chemistry 491:87 (2000).

[16] D. Aurbach, Nonaqueous Electrochemistry, CRC Press, Ramat-Gan, 1999.

[17] Y. Gofer, R. Barbour, Y. Y. Luo, D. Tryk, D. A. Scherson, J. Jayne, and G. Chottiner, Journal of Physical Chemistry 99:11739 (1995).

[18] L. H. S. Gasparotto, N. Borisenko, N. Bocchi, S. Z. El Abedin, and F. Endres, Physical Chemistry Chemical Physics 11:11140 (2009).

[19] G. R. Stafford and C. R. Beauchamp, Journal of the Electrochemical Society 155:D408 (2008).

[20] E. M. Moustafa, S. Z. El Abedin, A. Shkurankov, E. Zschippang, A. Y. Saad, A. Bund, and F. Endres, Journal of Physical Chemistry B 111:4693 (2007).

[21] F. Endres and S. Z. El Abedin, Physical Chemistry Chemical Physics 4:1649 (2002).

[22] W. Freyland, Coulombic Fluids-
Bulk and Interfaces, Springer-Verlag Berlin Heidelberg, 2011.

[23] F. X. Wang, G. B. Pan, Y. D. Liu, and Y. Xiao, Chemical Physics Letters 488:112 (2010).

[24] H. Wang, X. H. Qu, J. X. Lu, A. M. Bond, and C. Zhao, Crystengcomm 13:4762 (2011).

[25] X. Xing, I. T. Bae, and D. A. Scherson, Electrochimica Acta 40:29 (1995).

[26] K. Pekmez, E. Avci, H. G. Baumgartel, and C. Donner, Zeitschrift Fur Physikalische Chemie-International Journal of Research in Physical Chemistry & Chemical Physics 226:953 (2012).

[27] B. Hayden and I. Nandhakumar, Journal of Physical Chemistry B:7751 (1997).

[28] K. F. Domke, X.-Y. Xiao, and H. Baltruschat, Physical Chemistry Chemical Physics 10:1555 (2008).
[29] C. Chen, S. Vesecky, and A. Gewirth, Journal of the American Chemical Society 114:451 (1992).
[30] F. Hausen, M. Nielinger, S. Ernst, and H. Baltruschat, Electrochimica Acta 53:6058 (2008).
[31] Y. Shingaya, H. Matsumoto, H. Ogasawara, and M. Ito, Surface Science 335:23 (1995).
[32] Y. Nakai, M. S. Zei, D. M. Kolb, and G. Lehmpfuhl, Berichte Der Bunsen-Gesellschaft-Physical Chemistry Chemical Physics 88:340 (1984).
[33] D. M. Anjos, M. A. Rigsby, and A. Wieckowski, Journal of Electroanalytical Chemistry 639:8 (2010).
[34] J. K. Lee, H. Jeon, S. Uhm, and J. Lee, Electrochimica Acta 53:6089 (2008).
[35] J. Lindahl, T. Takanen, and L. Montelius, Journal of Vacuum Science & Technology B 16:3077 (1998).
[36] P. L. Claessens, Proceedings of the International Symposium on Electrometallurigical Plant Practice 1990.
[37] J. Tang, M. Petri, L. A. Kibler, and D. M. Kolb, Electrochimica Acta 51:125 (2005).
[38] W. R. Fawcett and A. Lasia, J. Phys. Chem. 82:1114 (1978).
[39] T. Nagaoka, S. Okazaki, and T. Fujinaga, Journal of Electroanalytical Chemistry 133:89 (1982).
[40] T. Nagaoka and S. Okazaki, Journal of Electroanalytical Chemistry 158:139 (1983).
[41] J. S. Jaworski, Journal of Electroanalytical Chemistry 219:209 (1987).
[42] S. B. Khoo, J. K. Foley, and S. Pons, Journal of Electroanalytical Chemistry 215:273 (1986).
[43] V. V. Even and M. C. Haulait-Pirson, Journal of Solution Chemistry 6:757.
[44] E. V. Anslyn and D. A. Dougherty, Modern Physical Organic Chemistry, 2006.
[45] R. Schmid, Journal of Solution Chemistry 12:135 (1983).
[46] V. Gutmann and G. Resch, Lecture Notes on Solution Chemistry, World Scientific Pub Co Inc (September 1995), 1995.
[47] G. Gonzalez, U. Mayer, and V. Gutmann, Inorganic & Nuclear Chemistry Letters 15:155 (1979).
[48] A. J. Motheo, E. R. Gonzalez, G. Tremilliosi, A. Rakotondrainibe, J. M. Leger, B. Beden, and C. Lamy, Journal of the Brazilian Chemical Society 9:31 (1998).
[49] I. Oh, A. A. Gewirth, and J. Kwak, Journal of Catalysis 213:17 (2003).
[50] D. Borissov, C. L. Aravinda, and W. Freyland, Journal of Physical Chemistry B 109:11606 (2005).
[51] K. Itaya, Nanotechnology 3:185 (1992).
[52] M. daCunha, M. Weber, and F. C. Nart, Journal of Electroanalytical Chemistry 414:163 (1996).
[53] P. Mrozek, Y. E. Sung, and A. Wieckowski, Surface Science 335:44 (1995).
[54] H. D. Abruna, J. M. Feliu, J. D. Brock, L. J. Buller, E. Herrero, J. Li, R. Gomez, and A. Finnefrock, Electrochimica Acta 43:2899 (1998).
[55] Y. E. Sung, S. Thomas, J. A. Tanzer, and A. Wieckowski, Proceedings - Electrochemical Society 96-8:28 (1996).
[56] P. Zanello, Inorganic Electrochemistry: Theory, Practice and Application, Royal Society of Chemistry, 2003.
[57] N. S. Neghmouche and T. Lanez, Recent Trends in Physical Chemistry: An International Journal 1:1 (2013).

[58] F. Silva and A. Martins, Journal of Electroanalytical Chemistry 467:335 (1999).
[59] U. W. Hamm, D. Kramer, R. S. Zhai, and D. M. Kolb, Journal of Electroanalytical Chemistry 414:85 (1996).
[60] D. M. Kolb and J. Schneider, Electrochimica Acta 31:929 (1986).
[61] P. Zelenay, L. M. Ricejackson, A. Wieckowski, and J. Gawlowski, Surface Science 256:253 (1991).
[62] D. B. Parry, M. G. Samant, H. Seki, M. R. Philpott, and K. Ashley, Langmuir 9:1878 (1993).
[63] Z. Shi and J. Lipkowski, Journal of Electroanalytical Chemistry 364:289 (1994).
[64] F. Endres, D. MacFarlane, and A. Abbott, Electrodeposition from Ionic Liquids, John Wiley&Sons. Inc., 2008.
[65] K. Ogaki and K. Itaya, Electrochim Acta 40:1249 (1995).
[66] Liang Fang, Honglei Xi, and D. Cun, in Formation of Ion Pairs and Complex Coacervates (Nina Dragicevic and H. I. Maibach, eds.), Springer Berlin Heidelberg, 2015, p. 175.
[67] Michael Mendolia, H.Cai, and G. C. Farrington, in Applications of Electroactive Polymers (G. Stienen, ed.), Springer Netherlands, 1993, p. 113.
[68] S.M.Khopkar, in Basic Concepts of Analytical Chemistry, New Age Science; 3rd edition (November 15, 2008), 2008, p. 91.
[69] P. Bacelon, J. Corset, and C. D. Loze, Journal of Solution Chemistry 9:129 (1980).
[70] K. Hofelman, Jagurgro.J, and M. Szwarc, Journal of the American Chemical Society 91:4645 (1969).
[71] A. S. Dakkouri, Solid State Ionics 94:99 (1997).
[72] M. J. Esplandiu, M. A. Schneeweiss, and D. M. Kolb, Physical Chemistry Chemical Physics 1:4847 (1999).

Chapter 6: Investigation of oxygen reduction and evolution in nonaqueous electrolyte

This chapter focuses on the mechanism investigation of oxygen reduction and oxygen evolution on Au and Pt electrode and the observation of the surface morphology of oxygen reduction products on Au(111) and Pt(111) electrodes in dimethyl sulfoxide (DMSO) based electrolyte containing Mg^{2+} or Li^{+} ion.

6.1 Introduction:

Rechargeable metal-air batteries have been considered as the most promising energy storage devices in the practical application, especially in the field of electric vehicles because of their remarkably high theoretical energy density. However, until now, many issues (instability of the electrolytes, the limited reversibility of the reaction process, sudden death of battery, etc.) still exist which limit their performance and application in practice [1]. In order to make a contribution to understand the working principle of this kind of battery and effectively improve the performance, it is particularly important to study all reactions, which take place during the charge and discharge processes. Currently, intense research focuses on the mechanistic study of the oxygen reduction reaction at air cathode in rechargeable metal-air batteries, especially in rechargeable Li-air batteries [2-7]. The electrochemical reaction $2Li^{+} + O_2 \leftrightarrow Li_2O_2$ was considered to be reversible or partial reversible in most of the nonaqueous electrolytes in Li-air batteries, oxygen is drawn through the gas diffusion electrode, and then reduced at the electrode surface to form Li_2O_2 during the discharge or oxygen reduction process. During the charge or oxygen evolution process, the discharge product Li_2O_2 is electrochemically oxidized to Li ions and oxygen [8]. Specifically, two conceivable pathways for formation of Li_2O_2 were mentioned by Bondue [9]: one is the direct pathway in which oxygen accepts two electrons and combines with Li^{+} ions to form Li_2O_2, the other one is the indirect pathway that O_2^{-} species are formed electrochemically and then induced by Li^{+} ion to disproportionate into Li_2O_2 and O_2 in the electrolyte. However, Reinsberg described that oxygen can be also reduced directly to Li_2O_2 [10]. These different mechanisms of oxygen reaction depend on the property of reactants, solvent [5], electrode [11], catalyst [12], etc. Laoire [5, 13] et al. have investigated the effect of solvents and cations on the mechanism of oxygen reduction reaction and found that the superoxide (O_2^{-}) is formed and exist more stable in all the electrolytes containing TBA^{+}, which was classified as a soft acid and weakly solvated by solvent, so that the more

naked TBA^+ exists and stabilizes the O_2^- (soft base) to form an ion pair complex in these electrolytes, and unstable superoxide decomposes rapidly into peroxide (O_2^{2-}) in the electrolytes containing hard acid Li^+ ions. However, Bondue considered that the strength of acid Lewis acids and Lewis bases play an important role to stabilize superoxide in bulk electrolyte [3]. Laoire and Trahan [14] also found that superoxide is stable in the solvents with high donor number such as dimethyl sulfoxide (DMSO, DN = 29.8), but in the solvents with low donor number such as acetonitrile (MeCN, DN = 14.1) and tetraethylene glycol dimethyl ether (TEGDME, DN = 16), the superoxide decomposes or undergoes electrochemical reaction quickly into peroxide [15], even oxide in the presence of Li^+. However, in DMSO based electrolyte containing Li^+, the LiO_2 is found to be an intermediate product and it can be further reduced chemically and electrochemically into Li_2O_2 [5].

For lithium air battery, Li_2O_2 was confirmed as the main product of oxygen reduction not only by cycle voltammetric techniques but also by DEMS [2], XRD [16], XPS [17], and its morphology was observed by SEM [18], AFM [19], etc. In ether based electrolyte, the morphology of Li_2O_2 is dependent on the discharge current density. The toroid-like Li_2O_2 was observed at low current density [18, 20, 21], whereas other shapes such as small particle [21, 22], thin film [18] or disc [20] was observed at high discharge current density. However, IBM members claimed that they never observed the toroid-like particles under the same conditions [21] and Wen [23, 24] only observed a Li_2O_2 film formed on both HOPG and polycrystalline Au electrode by AFM. Recently, Schwenke [16] and Aetukuri [25] found that the morphology of Li_2O_2 is also dependent on the water content in the electrolyte and that water might promote the toroid-like Li_2O_2 particles formation. In DMSO based electrolyte, Herrera [26] only observed Li_2O_2 nanoparticles formed on HOPG, and other [27] observed toroid-like Li_2O_2 particles formed during the gradual discharge process, but it seems unstable in the case of prolonging exposure to electrolyte and further converts into flake-like LiOH particles. Geaney [28] suggested that LiOH is the product of H_2O reactions with Li_2O_2 in DMSO based electrolyte.

However, unfortunately the formed Li_2O_2 is insoluble [29, 30] and an electronic insulator [31] (with a considerable band gap [32, 33]) and other products such as Li_2O, LiOH, Li_2CO_3, etc, are even worse and irreversible. It was found experimentally and

theoretically that a "sudden death" phenomenon in charge transport appears once the thickness of the formed Li_2O_2 film reaches to the maximum value of ~5 to 10 nm [31], which determines the maximum discharge capacity, Q_{max}. In addition, these batteries also suffer from the decomposition of electrolyte [27, 34-38], instability of electrode [39-41], side reactions [42-45] to form more insoluble and irreversible products, etc.

Compared with Li-air battery, Mg-air battery has more advantages such as no dendritic formation on Mg anode during charge [46, 47], higher volumetric energy density, higher safety, and so on. Based on these advantages, Mg-air battery could be constructed as an excellent energy storage device. To my knowledge, the first primary Mg-air battery was constructed in the neutral NaCl solution by General Electric in the 1960s. Over the following decades, only a few studies [48] have been done in this field. Ma et al. [49] investigated the performance of Mg-14Li-1Al-0.1Ce as anode in neutral 3.5% NaCl electrolyte for Mg-air battery. Khoo et al. [50, 51] found that the phosphonium chloride based ionic liquid electrolyte could be a promising electrolyte for Mg-air battery. However, these are not rechargeable. To achieve a rechargeable Mg-air battery, reversible oxygen reduction and evolution reactions at cathode are required. For oxygen reactions in nonaqueous electrolyte (DMSO based electrolyte), Shiga et al. [52] found that MgO was formed as a main product of oxygen reduction reaction (discharging) via a four-electron reaction and it can be decomposed during charging by adding I_2 into the electrolyte to form the iodine-DMSO complex, which was considered as an oxygen cathode catalyst to achieve a rechargeable Mg-air battery. It was also found that oxygen undergoes a stepwise reduction from superoxide to peroxide in DMSO based electrolyte [53]. Moreover, it was suggested that superoxide is formed in THF based electrolyte and the final ORR products are consisting of MgO_2 and MgO with a volume ratio of 1:2. However, achieving oxygen evolution in Mg^{2+} containing nonaqueous electrolyte seems a little discouraging.

However, considering present research, there are still some aspects that need to be further studied, such as optimization of electrolyte composition, improvement of the reversibility of oxygen reactions, elimination of side reactions, observation of products morphology, etc. Therefore, in this chapter, we investigated the mechanism of oxygen reduction on Au/Pt electrode and the morphology of oxygen reduction products by EC-AFM and EC-STM in DMSO based electrolyte containing Li or Mg salt for Li/Mg-air

battery.

6.2 Experimental:

6.2.1 Chemicals

All organic electrolytes were prepared in a MBraun glovebox filled with Ar (H_2O < 5 ppm and O_2 < 5 ppm). The water content in freshly prepared electrolytes was determined by a coulometric Karl-Fischer titrator (C20, Metler Toledo) to be around 50 ppm. The error for determining water content in DMSO based electrolyte was estimated by adding a water standard and included in these presented values [9]. A syringe sealed by inserting the needle into rubber block was used to transfer the electrolyte.

Extra dry DMSO (99.7%, over molecular sieve, Acros Organics) and $LiClO_4$ (battery grade, Sigma-Aldrich) were used as received. $Mg(ClO_4)_2$ (≥ 99%, Sigma-Aldrich) was dried at 245 °C under low pressure (10^{-2} mbar) before usage. Highly pure Argon (Air Liquid, 99.999%,) and oxygen (Air Liquid, 99.999%) were employed to deaerate the vessels and electrolytes. For the RRDE measurements, the mixture gas of oxygen (20%) and argon (80%) was produced by using two flowmeters (Krohne Duisburg) and used to saturate the electrolytes. For the AFM/STM measurements, pure oxygen was used to deaerate the environmental control glass chamber.

6.2.2 Electrochemical measurements

Electrochemical measurements were carried out in the classical H-cell.

For Li^+ containing organic electrolyte, the electrochemical measurements were carried out under argon, oxygen and air conditions. Freshly prepared Au(111) was used as working electrode. Two large Pt foils were used as counter and reference electrodes.

For RRDE measurements in Mg^{2+} containing organic electrolyte, the well-cleaned and dried glass H-cell was deaerated by continuously purging Ar before injecting electrolyte inside, and then the electrolyte was deaerated and saturated by continuously purging an Ar-O_2 mixture. A polycrystalline Pt electrode (0.5 cm, diameter) and a large Pt foil (1×1 cm) were used as a working and counter electrode, respectively. An Ag/Ag^+ electrode was constructed by inserting a silver wire into DMSO containing 0.1 M $AgNO_3$ electrolyte and used as reference electrode, which has to be placed in the compartment separated from working compartment by a wet surface of a closed, rough glass stopcock at Luggin capillary between two compartments to prevent diffusion of Ag^+ ions. The

electrolytes with different water contents were prepared by using an Eppendorf-Pipette to add the trace amounts of Milli-Q water (18.2 MΩ cm, TOC of 5 ppm, MILLIPORE, Schwalbach, Germany) into electrolyte. After each RRDE measurements, the water contents in working electrolyte were also determined by KF-titrator and the Pt electrode was freshly polished.

6.2.3 Preparation of Au(111) and Pt(111) single crystal electrodes

A traditional way of annealing was used to prepare the Au(111) and Pt(111) which both have a diameter of 10 mm and provided by Mateck company. 0.1 M H_2SO_4 was prepared from 18.2 MΩ Milli-Q water, deaerated with high purity argon gas (99.999%) and used to clean the electrode before its preparation. Electrochemical experiments were carried out in the classical H-cell. An Au wire and a large Pt foil were used as a counter electrode, respectively, and the reversible hydrogen electrode(RHE) was used as a reference electrode.

6.2.4 EC-AFM/STM measurements

All EC-AFM/STM measurements were performed by an Agilent Technologies 5500 Scanning Probe Microscope (SPM) combined with the built in bipotentiostat or Nanoscope III E controller (Digital Instruments, Santa Barbara, CA) connected with a separate potentiostat and a commercially available STM and AFM scanner (Molecular Imaging/Agilent Technologies) fitted with a homemade electrochemical cell (so called AFM/STM cell as described before). A Pt or Au wire was used as the counter electrode in the case of using Pt(111) or Au(111) as working electrode, respectively. A Pt wire was used as quasi reference electrode ($E_{Pt/PtO}$ = ~-0.45 V vs. Ag/Ag^+). All the AFM measurements were carried out with soft cantilevers (n^+-doped Si cantilever, PPP-CONT-10, k_n = 0.09 N/m) provided by Nanosensors. All the EC-STM measurements were performed by using Pt/Ir (90:10) tips with a diameter of 0.25 cm, which were prepared by etching in a 2 M KOH + 4 M KSCN bath and coated with hot-melt glue to minimize faradaic current. All the EC-AFM/STM measurements were done in glass chamber purged with oxygen at room temperature.

6.3 Results and discussion

6.3.1 ORR in 0.1 M $Mg(ClO_4)_2$ containing DMSO based electrolyte

The mechanism of ORR and particularly the effect of water on ORR in Mg^{2+}-containing

DMSO based electrolyte was investigated by RRDE technique and an in-situ observation of potential-dependent surface morphology were performed by EC-STM.

6.3.1.1 Investigation of ORR on Pt(pc) by RRDE technique

The cyclic voltammograms of Pt(pc) in Mg^{2+}-containing DMSO based electrolyte saturated with argon and oxygen were recorded and showed in Fig. 6.1. In argon saturated electrolyte a redox peak appears at ~-0.75 V after several cycles and the magnitude of the redox peak and the electrolyte decomposition both increase with increasing number of potential cycles. It seems that the redox peak is due to the reduction and oxidation of the produced species by the decomposition of electrolyte at more positive potential. Comparing to the CVs recorded in argon saturated electrolyte, in oxygen saturated electrolyte it is obvious that oxygen reduction starts at -0.8 V, which is more negative than the reduction potential of the decomposition products. However, the oxygen reduction current decreases with increasing number of potential cycles, and this could be the result of accumulation of inert oxygen reduction species blocking the active site on the electrode surface. However, by comparing the short dash curves (in Ar saturated electrolyte) with the black solid curves (in O_2 saturated electrolyte) in the potential range of 0.5 to 1.0 V, a mild shoulder appears and it probably due to the partial oxidation of these inert oxygen reduction species but it is too slowly. Unfortunately, there was no indication of oxygen evolution in this electrolyte.

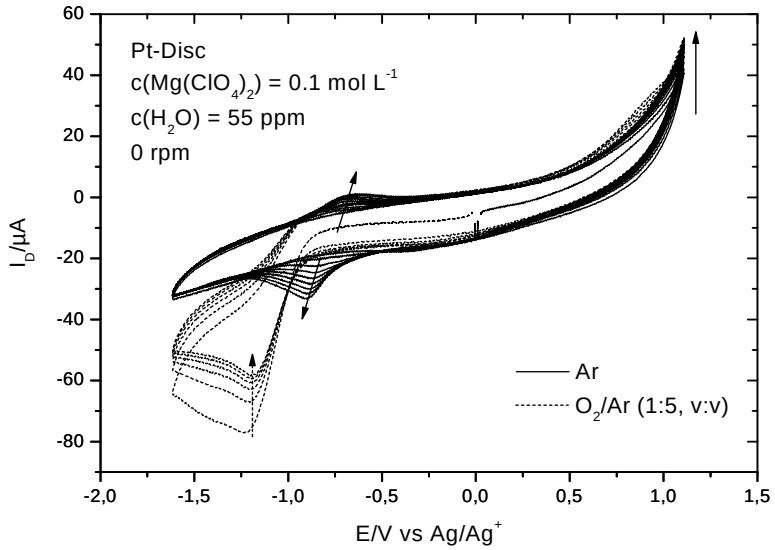

Fig. 6.1 Cyclic voltammograms of Pt disc electrode in 0.1 M $Mg(ClO_4)_2$ containing DMSO based electrolyte saturated with Ar (black solid curves) and 20% O_2 (short dash curves) at the scan rate of 120 mV s^{-1}.

To investigate the mechanism of oxygen reduction reaction in Mg^{2+}-containing DMSO electrolyte, RRDE measurements were performed. Similar investigation of ORR in low water content (approx. 40 ppm) Mg^{2+}-DMSO electrolyte has been done by Reinsberg in our group [53]. Fig. 6.2 shows the RRDE voltammograms of ORR on Pt electrode in the electrolyte with a water content of 65 ppm. Part of the formed species by oxygen reduction at disc electrode are soluble and can be detected and oxidized at the ring electrode at the potential of +0.3 V. The onset potential of the oxidation of these species detected at ring electrode is almost the same as that of ORR and both currents at the disc and ring electrodes are almost simultaneously reaching the limiting current. Furthermore, no decrease in ring current was observed. This suggests that these species are formed continuously during the overall oxygen reduction process in this potential range. However, no oxidation peak was observed at the disc electrode at the potential of +0.3 V on anodic branch after oxygen reduction reactions, because these species are unstable or they are transported away due to convection.

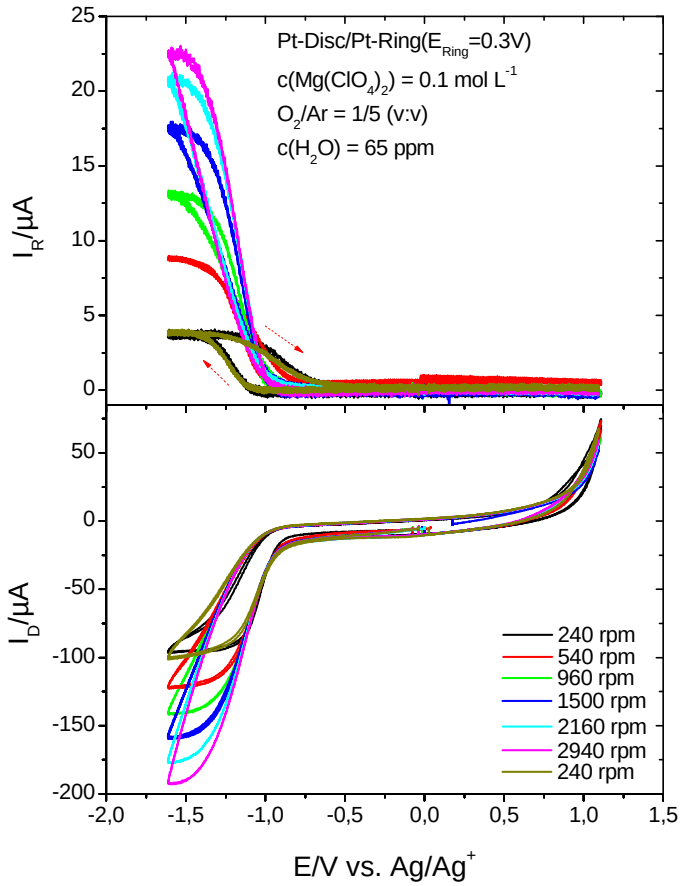

Fig. 6.2 RRDE voltammograms of ORR on Pt disc electrode in 0.1 M $Mg(ClO_4)_2$ containing DMSO based electrolyte (water content, 65 ppm) saturated with 20% O_2 at the scan rate of 120 mV s^{-1}.

The collection efficiency is the fraction of the amount of the species collected subsequently at ring electrode to the amount of the species formed at the disc electrode, which could be represented by the ring current (i_R) and disc current (i_D), respectively, as following:

$$N = -i_R / i_D$$

The theoretical collection efficiency value was calculated by the geometry parameters of RRDE and found to be 0.256. However, in our experiments the collection efficiencies at the potential of -1.5 V have been found to be dependent on the rotation frequency (f), it increased with increasing rotational frequency and the maximum value was calculated to be 51% of the theoretical value as shown in Fig. 6.3a. This increase of collection efficiencies with increasing rotational frequency was also observed by Reinsberg, however, the maximum collection efficiency value he obtained is around 35% of the theoretical value [53]. The species which was detected at ring electrode could be regarded as intermediates or final products of ORR at disc electrode which are not stable. Moreover, these species could further react electrochemically (as intermediates) at disc electrode or chemically (as intermediates and final product) in the electrolyte, which can cause a relative increase in current at disc electrode or a relative decrease in current at ring electrode compared to an ideal electrochemical reaction, resulting in low collection efficiency. Considering the fact that the collection efficiency is dependent on the rotational frequency and some of these species can still be detected at ring electrode at even low rotation frequency, it means that the further reaction rate of these species at disc electrode or in the electrolyte could be slow. More specifically, if these species were further reduced electrochemically at the disc electrode, the collection efficiency could be mainly determined by detachment rate of these species from the disc electrode surface which is dependent on rotational frequency, so that the collection efficiency increases with increasing rotational frequency. If these species reacted chemically in the electrolyte, the collection efficiency could be mainly determined by the transition time of these species through the gap between disc electrode and ring electrode, which is also dependent on rotational frequency; of course, there are probably other reasons for the rotational frequency-dependent collection efficiency as well.

It has been reported that the plot of 1/N vs. $\omega^{-1/2}$ can provide some information to distinguish the reaction pathway, a single pathway (without intermediate) or two parallel pathways (with the formation of intermediate in one of these pathways) [54]. In our

measurements, when 1/N was plotted as a function of $\omega^{-1/2}$, almost straight lines with a same intercept of $1/N_0$ and potential-dependent slope were observed as shown in Fig. 6.3b, which suggests that the reaction proceeded along a single pathway with intermediate which can react further and the further reaction of intermediate is potential-dependent (disc electrode potential), respectively. Therefore, it is reasonable that the collection efficiency decreases with increase of the potential, especially obvious at high rotational frequency, because the rate of further reaction of intermediate at disc electrode at high overpotential is higher than that at low overpotential. Therefore, ORR in Mg^{2+}-DMSO based electrolyte is probably via a single pathway, along with formation of intermediate which would react further.

In order to further analyse the ORR mechanism, the experimental data of Fig. 6.2 were plotted as Koutecky-Levich plots and are shown in Fig. 6.3c. The fitting lines at -1.1 V and -1.3 V are parallel to each other. However, the fitting line at -1.5 V is not parallel to those at -1.1 V and -1.3 V and the intercepts at -1.5 V (at diffusion region) is not zero, indicating that ORR at disc electrode is kinetically limited reaction or diffusion of reactant or electron transfer in the film or solid layer or whatever which formed at the electrode surface limited reaction. The diffusion limiting current of 152 μA (25 Hz) obtained after deducting the double layer current in our experiment is lower than the theoretical value (290 μA at 25 Hz) for four electron transfer process. Assuming that the diffusion limiting only exists in the electrolyte and the surface reaction is very fast, the theoretical diffusion limiting can be calculated by using the equation as follow:

$$i_L = 0.62nFAD^{2/3}\nu^{-1/6}c_0\sqrt{2\pi}f^{1/2}$$

Where, n is the number of electrons transferred; F is Faradic constant (9.64858×10^7 mA s mol^{-1}); A is the surface area of disc electrode (0.196 cm^2, geometric surface area); D is diffusion coefficient (15.8×10^{-6} cm^2s^{-1}) [55]; c_0 is solubility of oxygen (0.40 mol m^{-3}); ν is the kinematic viscosity (0.018 cm^2s^{-1}) [56] and f is the rotation frequency.

The slope of Koutecky-Levich plots can be used to determine the number of electrons transferred during ORR at disc electrode by the equation as follows:

$$Slope = \frac{1}{0.62nFAD^{2/3}c_0\nu^{-1/6}\sqrt{2\pi}}$$

The theoretical slope for two electrons transfer was calculated to be 33.7 mA^{-1} $s^{1/2}$, which is nearly twice as large as the experimental values as shown in Fig. 6.3c. The

ORR is probably via an indirect four-electron transfer process in this measurement. However, the experimental slope of 31 $mA^{-1}\ s^{1/2}$ was obtained on Pt electrode in Mg^{2+}-DMSO based electrolyte with water content of approx. 40 ppm by Reinsberg [53] and the mechanism of ORR in Mg^{2+} containing electrolyte is very complex and still unknown.

The Tafel slope for ORR was obtained from the plot of kinetic currents ($i_K = (i_L \cdot i)/(i_L - i)$) as a function of potential (Fig. 6.3d) and found to be around 125 mV dec^{-1}, which is very close to the value obtained from DMSO containing Li^+ or TBA^+ electrolyte and suggests that the rate determining step is the first one electron transfer [5, 12]. But it was also considered that the rate determining step could be the second electron transfer once the saturation of the surface was taken into account [53].

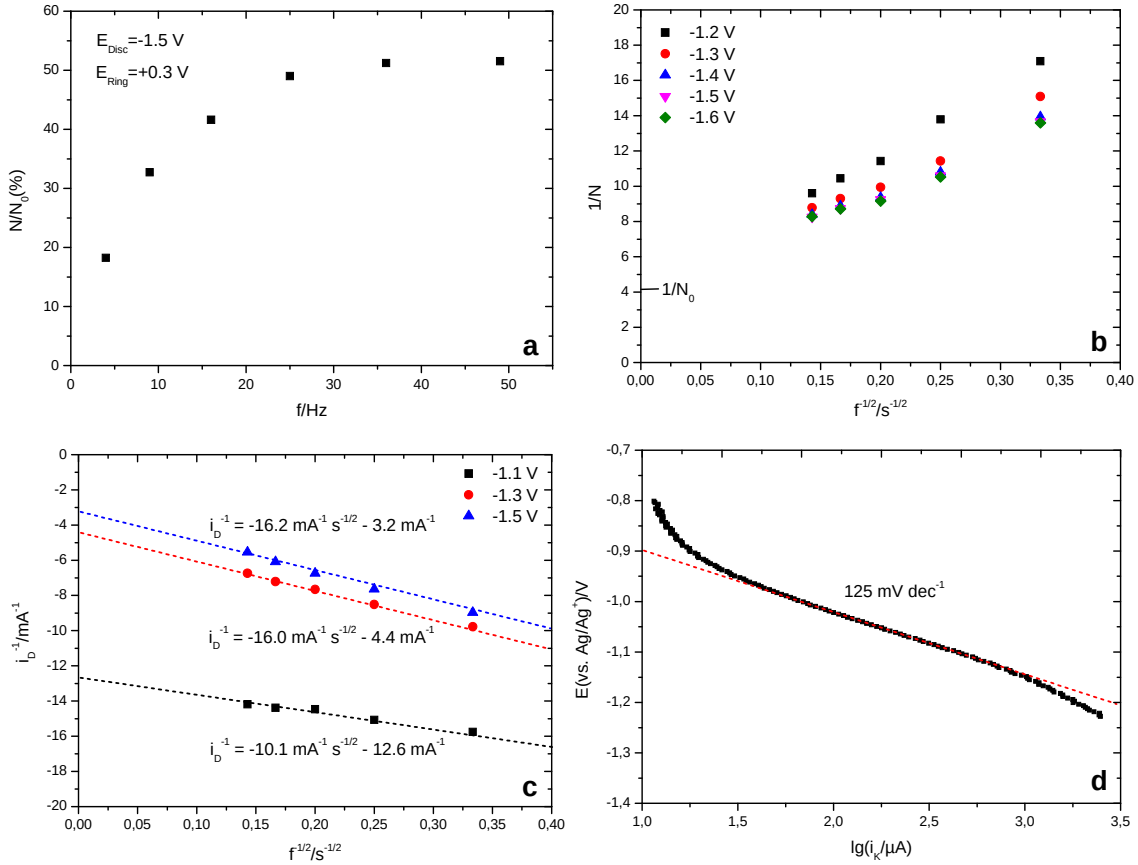

Fig. 6.3 a) Collection efficiencies (N) with respect to the theoretical efficiency (N_0 = 0.256) as a function of the rotation frequency (f), b) Plot of 1/N vs. $f^{-1/2}$ at different disc potentials, c) Koutecky–Levich plots (J^{-1} vs. $\omega^{-1/2}$) at different potentials (E/V vs. Ag/Ag^+) and d) Tafel plot of ORR for Pt electrode derived by the mass-transport correction. All these plots based on the data in Fig. 6.2.

However, once the electrolyte contains 175 ppm water, the limiting current is increasing with rotation frequency at lower rotation frequencies but it is decreasing at higher rotation frequency; the ring current behaves similar (see. Fig. 6.4a). Further investigations of the effect of higher water contents (1200 ppm) on ORR show that the limiting current is completely independent of the rotation frequency, even at lower rotation frequency, and is very low as shown in Fig. 6.4b. This indicates that in the electrolyte with higher water content the deactivation of electrode surface was observed, especially in the case of higher rotation frequency because the higher rotation frequency can produce larger amounts of inert species on electrode surface. A detailed discussion about the effect of water on ORR in Mg^{2+}-DMSO based electrolyte will be presented next.

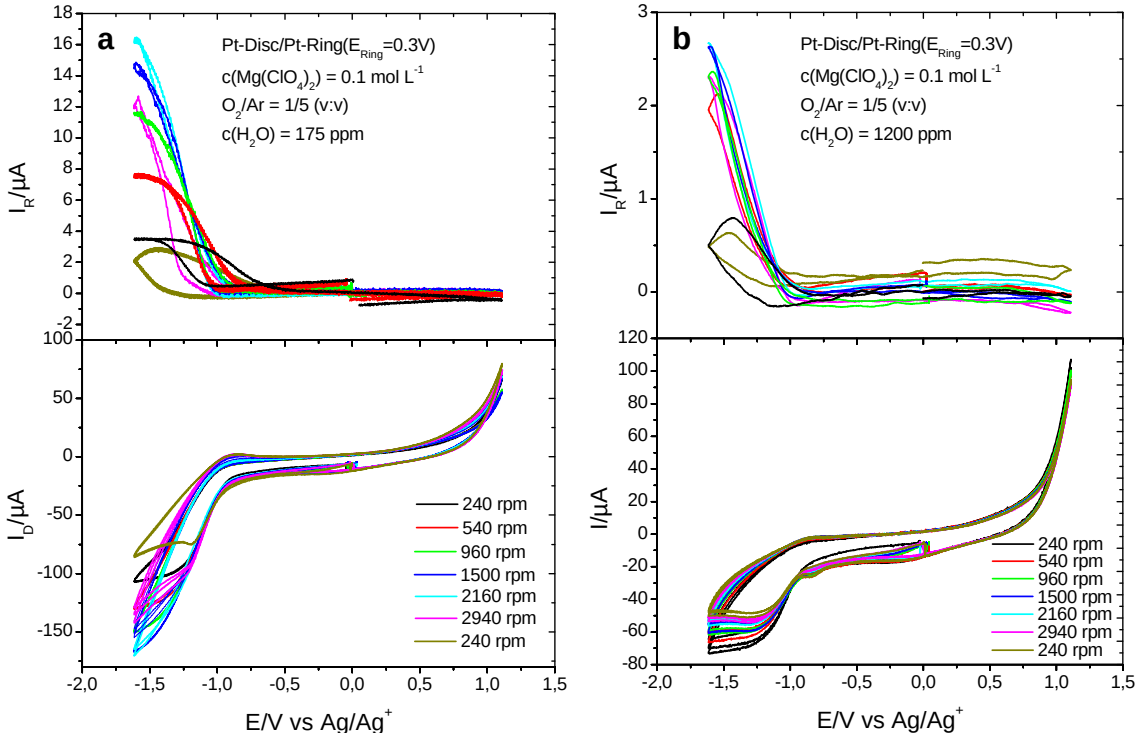

Fig. 6.4 RRDE voltammograms of Pt disc electrode in 0.1 M $Mg(ClO_4)_2$ containing DMSO based electrolyte (water content, (a) 175 ppm and (b) 1200 ppm) saturated with 20% O_2 at the scan rate of 120 mV s^{-1}.

When the potential scan was restricted to potentials in the range of ORR, a strong deactivation of electrode surface was observed, as seen in Fig. 6.5. During continuous cycling, the onset potential for ORR is shifted to more negative values and the current at -1.5 V is decreased, suggesting that the inert species were formed during ORR and accumulated continuously on the electrode surface, resulting in deactivation

phenomenon of electrode surface. However, when the potential was scanned to +1 V, a slight reactivation of electrode surface was observed during ORR (see. Fig. 6.4b).

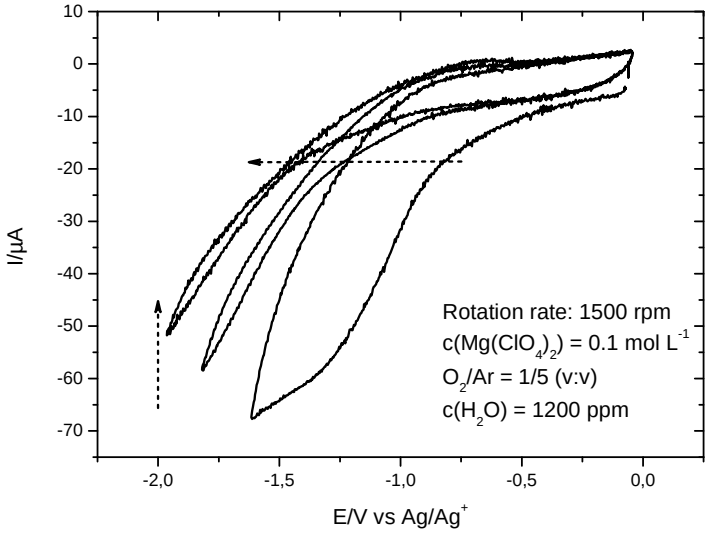

Fig. 6.5 Cyclic voltammograms of Pt disc electrode in 0.1 M $Mg(ClO_4)_2$ containing DMSO based electrolyte saturated with 20% O_2 at the scan rate of 120 mV s^{-1}.

Scan rate, potential range, rotation rate and water content dependent deactivation of active sites on the electrode surface was observed in this electrolyte. It could be related to the competition between accumulation (formation) and consumption (decomposition) of this kind of inert species adsorbed on the electrode surface. In order to systematically study the effect of water content on ORR, the following experimental conditions were chosen: scan rate of 120 mV s^{-1}, potential range of -1.6~+1.1 V vs. Ag/Ag^+, rotation rate of 4 Hz (or 240 rpm) [53] and a freshly polished electrode. The RRDE voltammograms of ORR in 0.1 M $Mg(ClO_4)_2$ containing DMSO based electrolyte with different water content were obtained and shown in Fig. 6.6a. The results show that water has a large effect on the diffusion limiting current, collection efficency and decomposition of electrolyte. A detailed analysis was performed by the plots of collection efficiency and the diffusion limiting current as the function of water content (see. Fig. 6.6b). It shows that the limiting current increases with the initial increase of the water content from 65 to 660 ppm, decreases with the following increase of water content from 660 to 2611 ppm, and then increases again with the further increase of water content from 2611 to 13000 ppm. A maximum and minimum value of limiting current appears at 660 ppm and 2611 ppm, respectively. Obviously, the effect of water content on ORR could be divided into three conditions. First, in low water content electrolyte (~65-660 ppm), there is a small amount of inert species formed on the electrode surface to form a

blocking layer. As water content increases, the solubility of ORR products may be increased and the kinematic viscosity of this thin blocking layer may be decreased, which are the determinants of diffusion limiting current. Second, in medium water content electrolyte (~660-2611 ppm), the blocking layer may be formed quickly and becomes thick with further increase of water content. It may consist of different components (e.g. probably $Mg(OH)_2$) from that formed in the electrolyte with low water content (e.g. probably MgO_2, Mg_2O_2 and MgO) or the composition of the blocking layer on the electrode surface may be changed. These are probably the reasons for the decrease of the limiting current. Third, in high water content electrolyte (above 2611 ppm), the measurement condition is similar to that in aqueous electrolyte. Lee [57] has found that in nonaqueous electrolyte with higher water content, the ORR behaviour approaches to that of observed in aqueous electrolyte. Furthermore, the decomposition current at upper limiting potential is always increasing with increase in the water content.

The onset potentials of ORR on water contents (< 2611 ppm) start at almost the same potential. However, the onset potential of ORR in the electrolyte with water content of 13000 ppm starts earlier. The increase of current at upper limiting potential (at +1.1 V) with the increase in water content suggests that water promotes the dissolution of the inert species at the electrode surface or electrolyte decomposition. Furthermore, the collection efficiency decreases with the increase of water content, suggesting that the intermediate or the ORR product which can be detected at ring is less stable in the electrolyte with high water content. In the literatures, it was found that superoxide is unstable in some cases [9, 58], especially in aqueous electrolyte [59, 60]. It is also possible that ORR is via a direct 4-electron transfer pathway in the high water content electrolyte. However, the diffusion limiting current is still smaller than the theoretical value for 4-electron transfer because the blocking layer is still formed in this case.

The Tafel slopes were obtained corresponding to the data (in Fig. 6.6a) recorded from different water content electrolyte and shown in Fig. 6.7. A Tafel slope of 125, 145 and 214 mV dec^{-1} was obtained in the electrolyte containing water content of 65, 660 and 1200 ppm, respectively. This behaviour of the increase of Tafel slope with the increase of water content was also observed in aprotic ionic liquid 1-butyl-2,3-dimethylimidazolium triflate (C_4dMImTf) electrolyte by Zeller [61]. The increase in

Tafel slope suggests that water may change the mechanism of ORR. The change of ORR mechanism with the increase of water content in nonaqueous electrolyte was also reported by others [57].

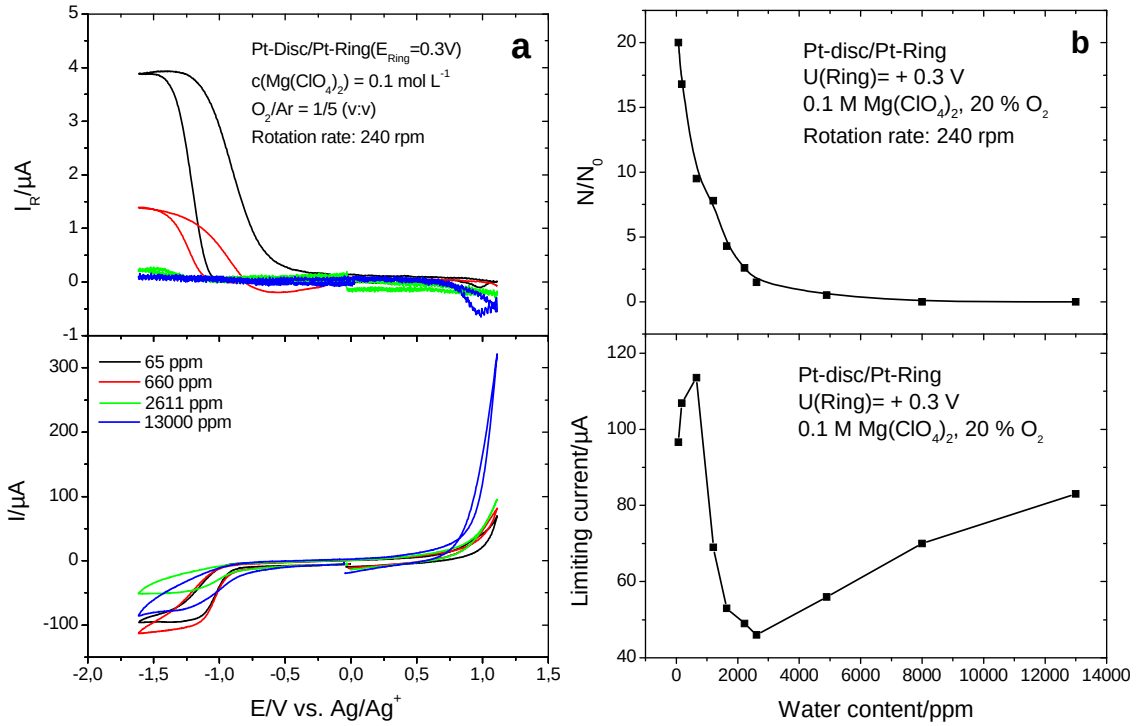

Fig. 6.6 a) RRDE voltammograms of Pt disc electrode in 0.1 M $Mg(ClO_4)_2$ containing DMSO based electrolyte with the water content of 65 ppm, 660 ppm, 2611 ppm and 13000 ppm saturated with 20% O_2 at the scan rate of 120 mV s^{-1} and the rotation rate of 240 rpm. b) The plots of collection efficiency, N% (up) and limiting current (down) vs. water content in ppm.

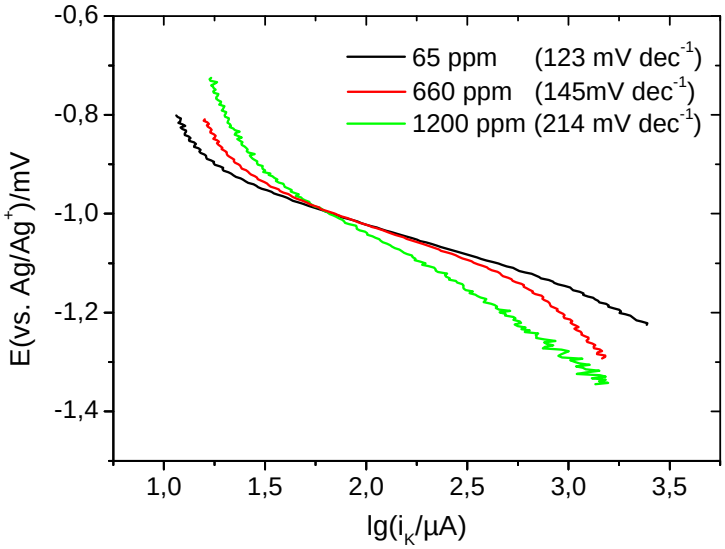

Fig. 6.7 Tafel plots of ORR for Pt disc electrode derived by the mass-transport correction corresponding to the data in Fig. 6.6.

6.3.1.2 Investigation of ORR on Au(111) by EC-STM

Investigation of oxygen reduction products in Mg^{2+}-DMSO based electrolyte by EC-STM was first carried out on Au(111) electrode. The cyclic voltammograms for ORR on Au(111) in Mg^{2+}-DMSO based electrolyte were recorded during EC-STM measurement and shown in Fig. 6.8. The overpotential of ORR increases and the current of ORR at -1.0 V decreases with the increase in the number of cycles. It indicates that the inert species probably formed on the electrode surface hinders charge transfer or ion diffusion and modifies the energetics and kinetics of the ORR process. The small peak with the charge of 40 μC cm^{-2} was observed at ~0 V (vs. Pt/PtO) where probably Au dissolves. Unfortunately, as mentioned before, oxygen evolution did not take place under these conditions.

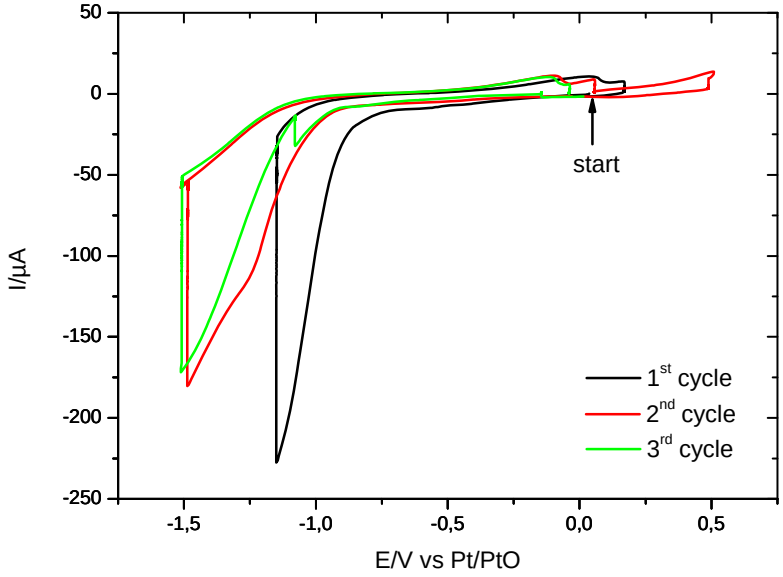

Fig. 6.8 Cyclic voltammograms of ORR on Au(111) electrode in 0.1 M $Mg(ClO_4)_2$ containing DMSO based electrolyte in STM cell in O_2 purged glass chamber at the scan rate of 50 mV s^{-1} during the STM measurement.

The freshly prepared Au(111) surface with smooth and large terraces was inspected at open circuit potential in this electrolyte (see. Fig. 6.9a). Once the potential was held at -1.15 V, it seems that a film was initially formed on some parts of the electrode surface and then covered the whole surface (see. Fig. 6.9b and c). This film is probably consisting of the oxygen reduction species, solvent and Au, which is regarded as the blocking layer to hinder the following reaction. When the potential was held at +0.17 V after the first cycle, the clear steps and terraces with small dots on were observed at the different area (see. Fig. 6.9d). The same surface morphology at the negative potential of

-1.49 V at the second cycle was observed again as shown in Fig. 6.9f.

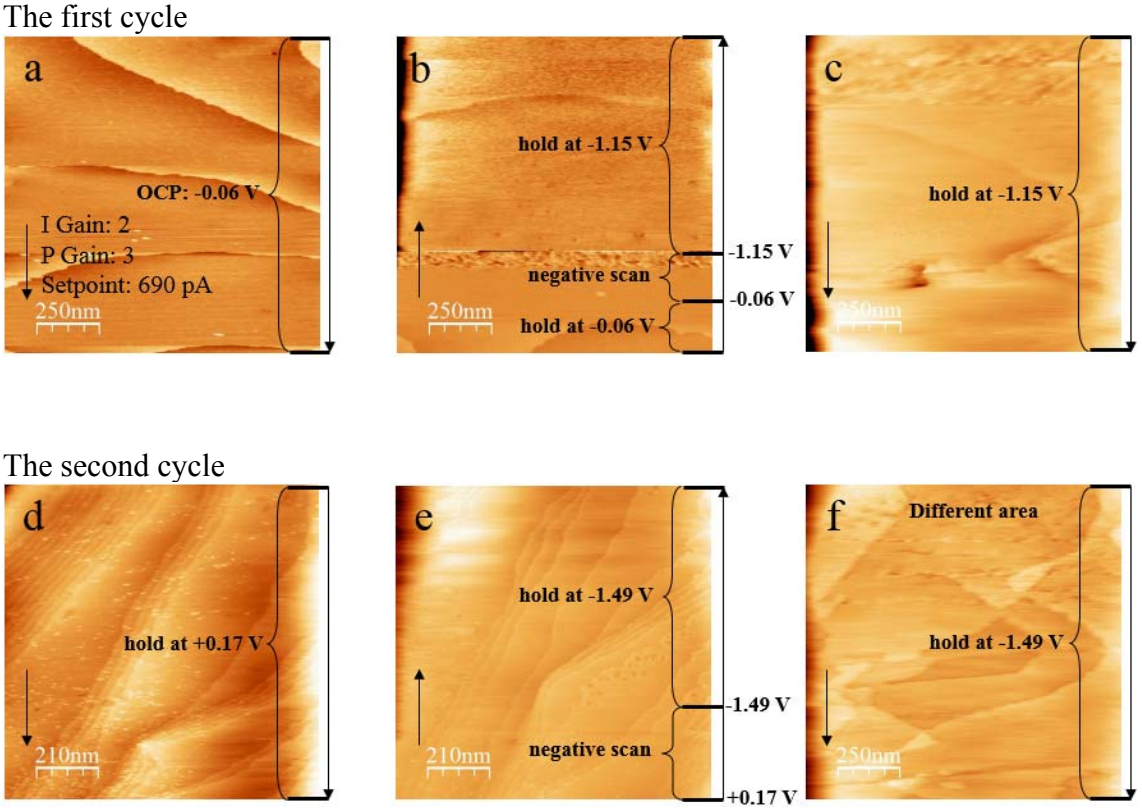

Fig. 6.9 STM images of Au(111) during ORR in 0.1 M $Mg(ClO_4)_2$ containing DMSO based electrolyte. Sample bias of 50 mV, set point = 0.69 nA & scan rate of 5 Hz. Arrows indicate scan direction. Line by line correction is used for above images.

An in-situ observation of surface morphology is demonstrated in the following images (see. Fig. 6.10 and Fig. 6.11) obtained in the subsequent potential cycles to show the process of film formation. Many holes with a height of 0.7 nm and a diameter of 10~30 nm scale appeared on the surface which is probably due to Au dissolution (see. Fig. 6.10a). It has been reported that Au dissolution may be facilitated in donor-acceptor organic and aqueous-organic Au-DMSO-RX systems (where R = H or Bu, and X = Cl or Br) [62]. In our electrolyte, it is not excluded that magnesium perchlorate may contain small amounts of Cl^- ions. When the potential was held at -1.08 V around the onset of ORR potential, the density of small holes decreased (see. Fig. 6.10b and c). Further decreasing the potential to -1.51 V, small holes disappeared but some larger holes with the height of 1.2 nm and the diameter of 40-60 nm appeared on the surface (see. Fig. 6.10d). This phenomenon may be caused by the surface shrinkage because of the change in surface tension and accompanying with the formation of the ORR species

to form a thicker film on the electrode surface. By the comparison of Fig. 6.10c, d, e, f, it is seen that the thickness of this film increased gradually from 0.7 nm to 2.5 nm over time. As the potential is scanned positively to -0.04 V, the decomposition of this film seems to prefer to start at the edges of the steps and it is decomposed into small pieces as shown in Fig. 6.10g and h. Quickly, almost the whole surface is covered by these inert decomposition products with the height of 0.8 nm (see. Fig. 6.10h), which will be one of the components of new film formation in the following cycle, as demonstrated later.

The third cycle

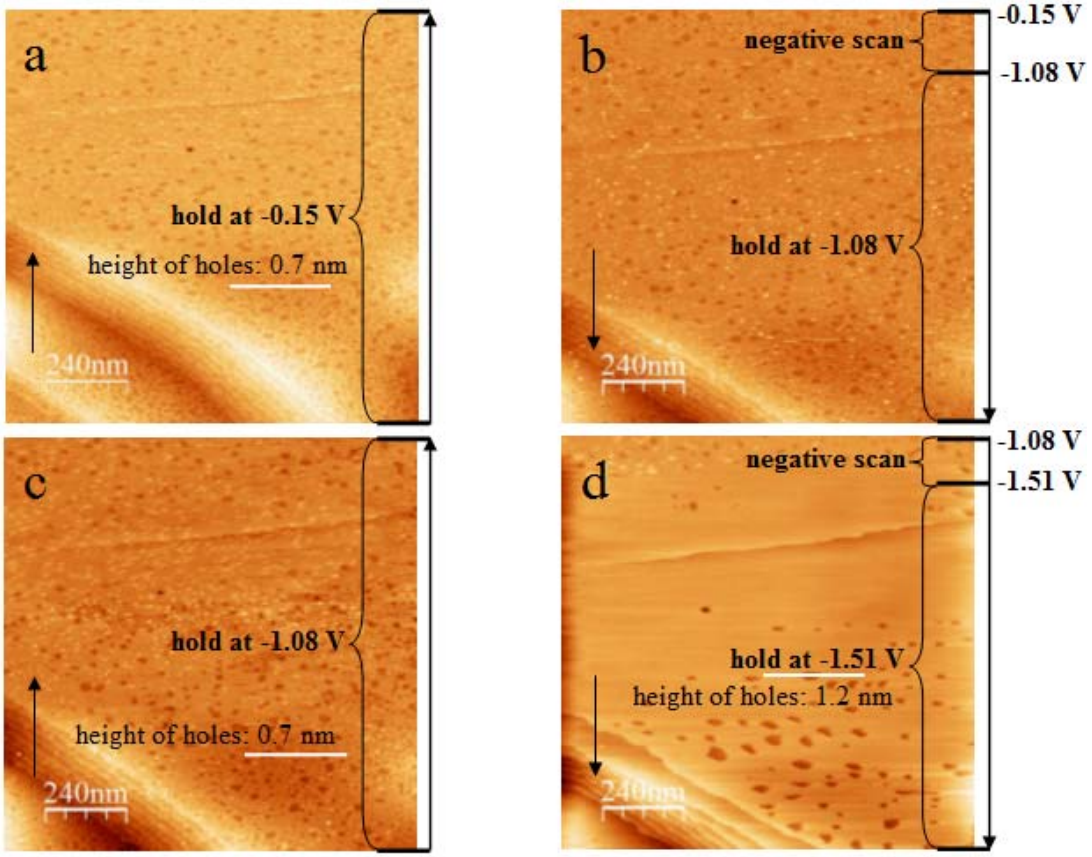

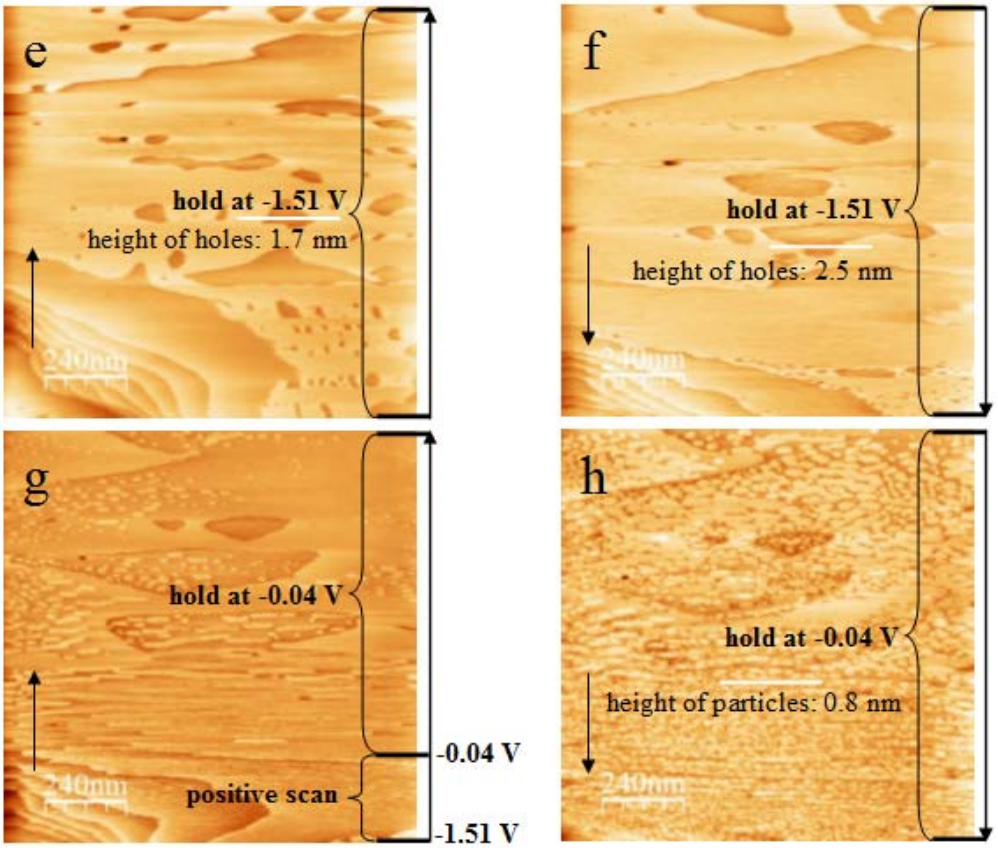

Fig. 6.10 STM images of Au(111) during ORR in 0.1 M $Mg(ClO_4)_2$ containing DMSO based electrolyte. Sample bias of 50 mV, set point = 0.69 nA & scan rate of 5 Hz. The height of the holes and pieces on the surface is indicated by the cross section on image a, c, d, e, f and h. Arrows indicate scan direction. Line by line correction is used for above images.

The fourth cycle

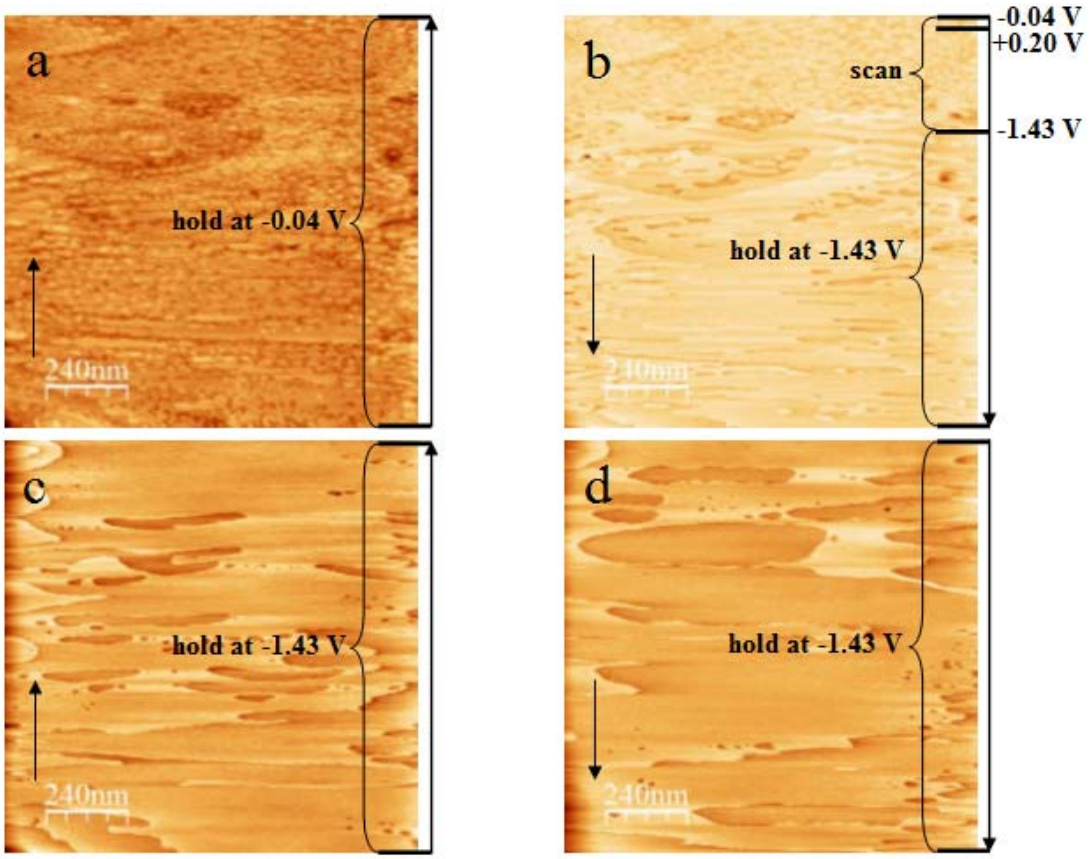

Fig. 6.11 STM images of Au(111) during ORR in 0.1 M $Mg(ClO_4)_2$ containing DMSO based electrolyte. Sample bias of 50 mV, set point = 0.69 nA & scan rate of 5 Hz. Arrows indicate scan direction. Line by line correction is used for above images.

Fig. 6.11 shows the images which were subsequently recorded at the same area of electrode surface as shown in Fig. 6.10. With further decomposition, these pieces became smaller and smaller as seen in Fig. 6.11a comparing to that in Fig. 6.10h. As the potential is scanned negatively to -1.43 V, these small pieces, probably with the produced ORR species and other species start to reform a new film on the electrode surface. The new film formation process and its continuous growth were demonstrated in Fig. 6.11b and Fig. 6.11c and d, respectively. With the growth of this film, the ORR activity became weaker and weaker so that the current decreased rapidly when the potential was held at ORR range as shown in Fig. 6.8. This film may be consisting of adsorbed DMSO molecules [63] and $DMSO_2$ which was considered as the product of the electrolyte decomposition [27, 37], some solvated cation (Mg^{2+}) and anions [26] (O^{2-} and O_2^{2-}), ion-pairs and small amounts of redeposited Au, and thus it exhibits a poor electrical conductivity. Yu reported that Li^+ ions solvated by DMSO combine with superoxide to form ion-pairs [11]. Briefly, the formation of this kind of film on the

electrode surface was found during ORR and it inhibited ORR. In addition, this kind of film could be partly decomposed at positive potential.

6.3.1.3 Investigation of ORR on Pt(111) by EC-STM

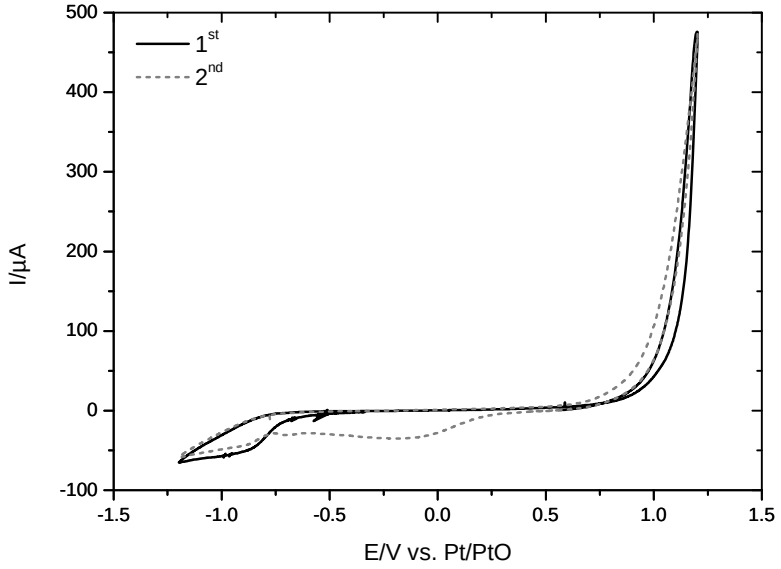

Fig. 6.12 Cyclic voltammograms of ORR on Pt(111) electrode in 0.1 M $Mg(ClO_4)_2$ containing DMSO based electrolyte in STM cell in O_2 purged glass chamber during the STM measurement. Scan rate: 10 mV s^{-1}.

The cyclic voltammograms of ORR on Pt(111) in 0.1 M $Mg(ClO_4)_2$ containing DMSO based electrolyte were recorded during EC-STM measurement and are shown in Fig. 6.12. The oxygen reduction reaction and electrolyte decomposition start at ~-0.6 and +0.7 V vs. Pt/PtO, respectively. At the second cycle, a broad peak appears around -0.1 V, which probably is due to the reduction of the species produced by electrolyte decomposition at positive potential.

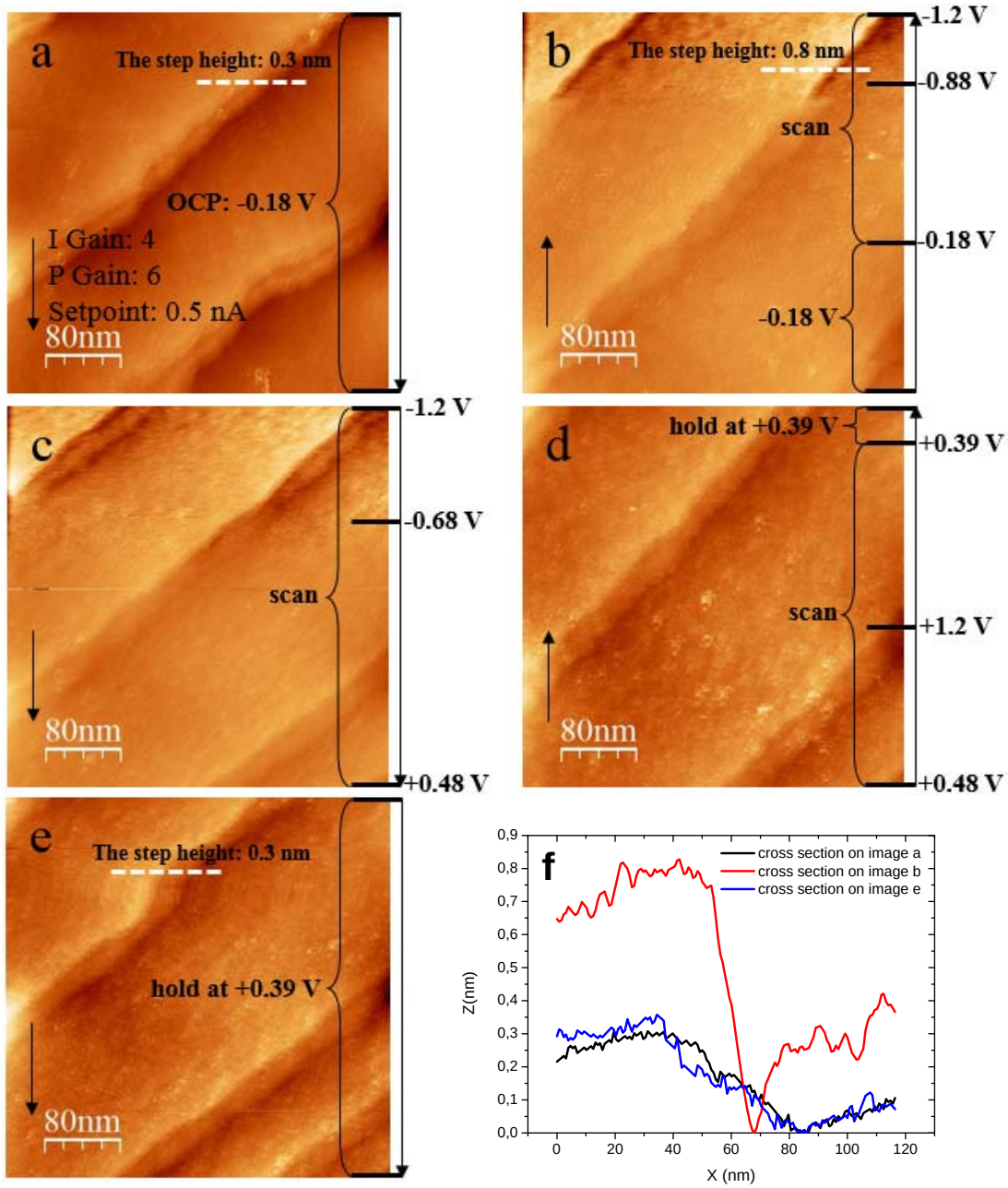

Fig. 6.13 STM images of Pt(111) electrode surface during ORR in 0.1 M $Mg(ClO_4)_2$ containing DMSO based electrolyte (a, b, c, d and e). Sample bias of 50 mV, set point = 0.5 nA & scan rate of 3.04 ln/s. Arrows indicate scan direction. Line by line correction is used for above images. f) The cross sections on image a b and e (dot white lines).

A freshly prepared Pt(111) electrode surface is shown in Fig. 6.13a. The surface morphologies of Pt(111) electrode in 0.1 M $Mg(ClO_4)_2$ containing DMSO based electrolyte during continuous potential scanning in the range of -1.2 to +1.2 V (vs. Pt/PtO) is shown in Fig. 6.13b, c and d. As the potential was scanned negatively to ORR region, the step started to become more obvious and its height increased from 0.3 nm to 0.8 nm (see. Fig. 6.13f). It seems that some pre-adsorbed adsorbates on the surface

especially at the step (see. the graph as follow) are decomposed as shown in Fig. 6.13b. However, according to the results of RRDE measurements, a blocking layer which possesses poor conductivity or even is nonconductive should be formed during ORR. If this kind of blocking layer was formed on the surface, the STM tip was probably very close to or even in this blocking layer during scanning. The step height we observed during ORR should be of the same height as Pt(111) step, but its increase is elusive. As the potential was scanned positively, the Pt(111) surface recovered at around -0.69 V, but the surface roughness increased(see. Fig. 6.13c and d). It seems that some adsorbates were still adsorbed on the surface. When the potential was scanned to up limiting potential (+1.2 V) and then back to +0.39 V, there was no obviously change in surface morphology (see. in Fig. 6.13d and e).

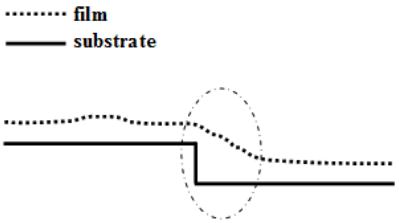

The graph of the film formation on the substrate

As mentioned before a broad cathodic peak appeared around -0.1 V during the second cycle is probably related to the reduction of decomposition products formed at more positive potential. The surface morphologies before (at +0.39 V) and after (at -0.4 V) the peak were shown in Fig. 6.14a and Fig. 6.14b and the corresponding root mean square roughness (R_{RMS}) was calculated to be 0.79 and 0.1, respectively. It seems that the tiny bare grains appeared on the surface after this reduction process. With further decreasing the potential to -1.19 V, similar surface phenomenon was observed again as observed before (see. Fig. 6.14c). It is unusual that the height of the step increased to ~2 nm. This large change at the steps was not only observed on the topographic images but also on current images by comparing Fig. 6.15 to Fig. 6.16. Furthermore, the current change at the steps in case of the tip climbing the step is large than that of passing down the step (see. Fig. 6.16). Probably, it is due to this nonconductive (or poor-conductive) film formed on the surface.

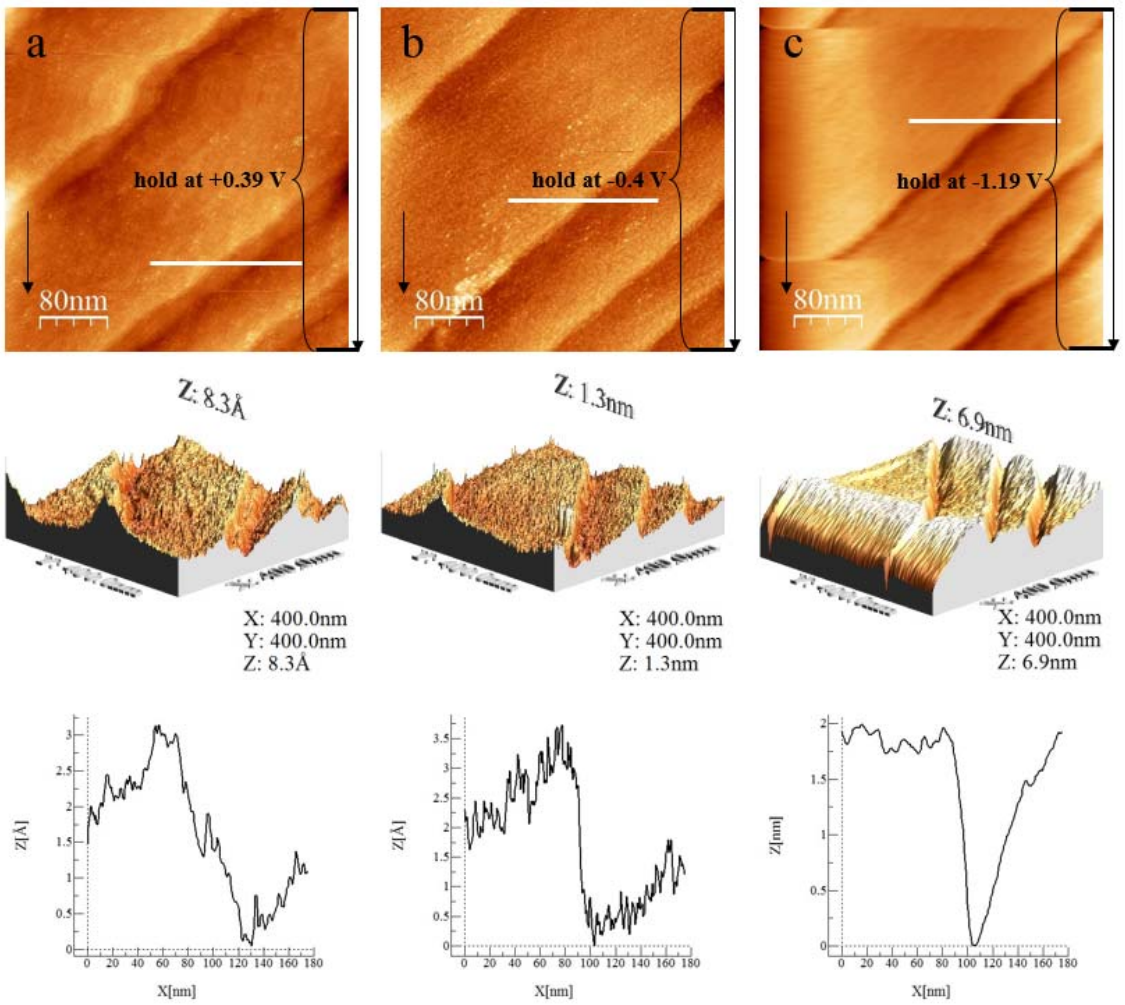

Fig. 6.14 Topographic and the corresponding 3D STM images of Pt(111) electrode surface during ORR in 0.1 M $Mg(ClO_4)_2$ containing DMSO based electrolyte. Sample bias of 50 mV, set point = 0.5 nA & scan rate of 3.04 ln/s. The heights of the steps indicated by the cross section on image a, b and c are shown below. Arrows indicate scan direction. Line by line correction is used for above images.

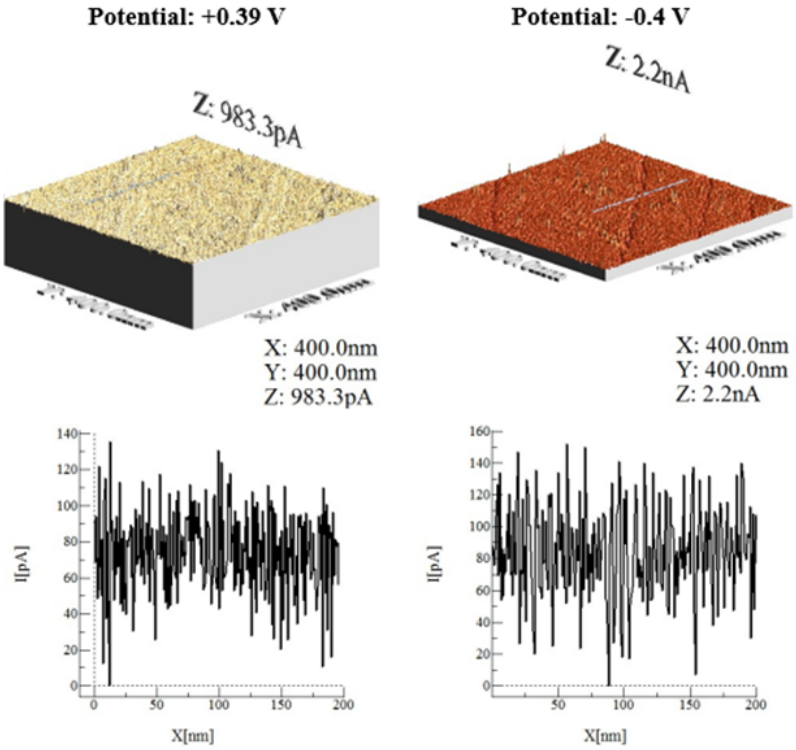

Fig. 6.15 Current trace images (without any correction) of the electrode surface at +0.39 V and -0.4 V in 0.1 M $Mg(ClO_4)_2$ containing DMSO based electrolyte. Sample bias of 50 mV, set point = 0.5 nA & scan rate of 3.04 ln/s.

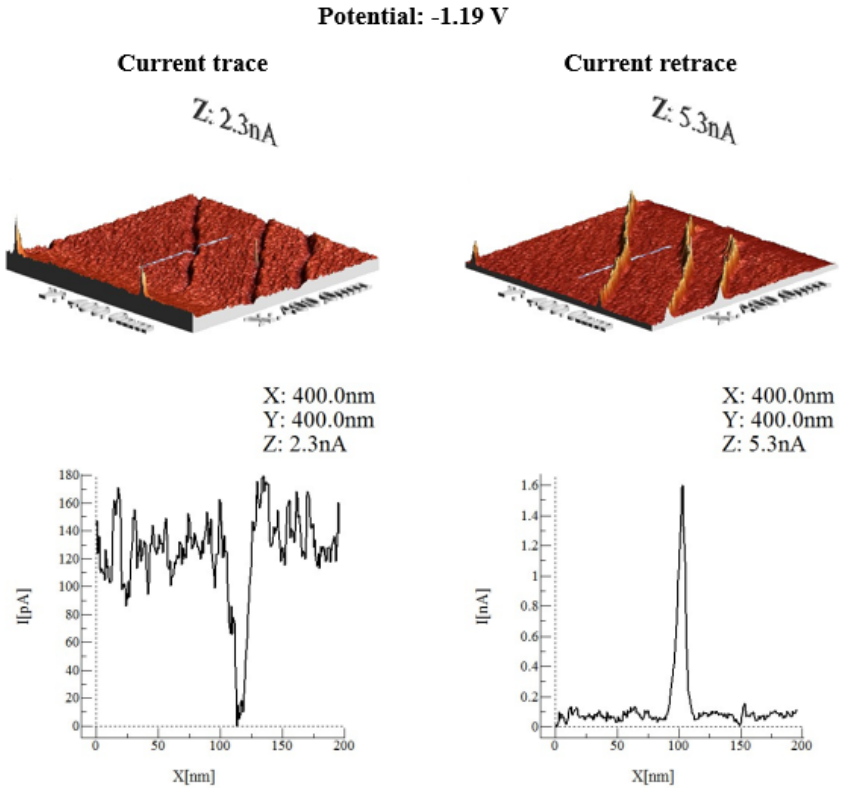

Fig. 6.16 Current trace and retrace images (without any correction) of the electrode surface at -1.19 V in 0.1 M $Mg(ClO_4)_2$ containing DMSO based electrolyte. Sample bias of 50 mV, set point = 0.5 nA & scan rate of 3.04 ln/s.

6.3.2 ORR in 0.1 M $LiClO_4$ containing DMSO based electrolyte

Investigation of ORR and OER on Au electrode in Li^+-containing DMSO electrolyte under different conditions was carried out by cyclic voltammetry and an in-situ observation of potential-dependent surface morphology were performed by EC-STM.

6.3.2.1 Investigation of ORR and OER on Au by cyclic voltammetry

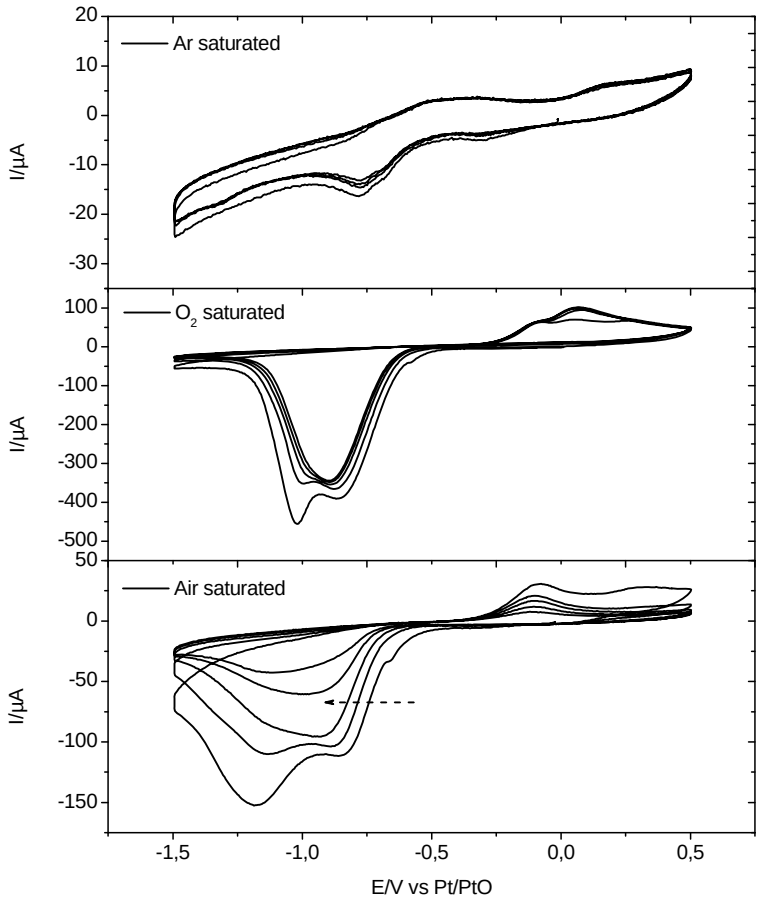

Fig. 6.17 Cyclic voltammograms of Au electrode in 0.1 M $LiClO_4$ containing DMSO based electrolyte saturated with Ar, O_2 and air in H cell at the scan rate of 50 mV s^{-1}.

Oxygen reduction and oxygen evolution have been achieved successfully in DMSO containing Li^+ electrolyte, but there are still some issues (e.g. reversibility, stability, products property, etc.) that need to be addressed. The cyclic voltammograms recorded in Li^+-containing DMSO electrolyte saturated with argon, oxygen and air are shown in Fig. 6.17. In Ar saturated electrolyte, no obvious peaks were observed except a small cathodic peak at ~-0.75 V and anodic peak at -0.4 V, and they are probably due to the reduction and oxidation of electrolyte or residual oxygen reduction and evolution, respectively. In oxygen saturated electrolyte, two ORR peaks appeared at -0.85 and -1.0

V in the initial two cycles, probably related to superoxide and peroxide formation [11], respectively, and then overlapped into one peak. Slightly negative shift in the onset potential and decrease in peak current were observed. In addition, the charge densities of oxygen reduction peak and oxygen evolution peak were calculated to be around 2575 and 685 μC cm^{-2}, respectively, indicating that the reversibility of ORR and OER is around 26.6%. The poor reversibility might be due to the effect of the side reactions or superoxide diffusing away from the electrode. Assuming that all the charge of OER peak was related to the decomposition of Li_2O_2 and the ratio of Li_2O_2 to Au atoms is one to one, it would mean that only around one to two monolayers of Li_2O_2 were formed on Au surface. Comparing to the cyclic voltammogram recorded in oxygen saturated electrolyte, in air saturated electrolyte the potential gap between two ORR peaks at the initial two cycles became larger and the ORR and OER peak currents were smaller and decreased rapidly with potential cycle numbers. Furthermore, the reversibility of ORR and OER (the average value) in this case was found to be around only 10%, which is less than the value obtained in oxygen saturated electrolyte. It is probably due to the effect of water.

6.3.2.2 Investigation of ORR on Au(111) by EC-AFM

Freshly prepared Au(111) surface with the atomically flat terraces and steps at the potential of -0.06 V is shown in Fig. 6.18a and a'. As the potential was scanned to -1.0 V in the ORR region, no toroid-like Li_2O_2 was observed (see. Fig. 6.18b and b'). It was reported that toroid-like Li_2O_2 formation is dependent on the magnitude of water content [16] and discharge current [20]. Moreover, IBM members also claimed that they never observed the toroid-like Li_2O_2 formation at any discharge current with optimally anhydrous and purified ether electrolytes [21].

Fig. 6.19 shows the topographic and friction images on the electrode surface at different potentials. The upper part of the image was obtained under potential control of -0.9 V and the lower part was obtained under potential control of -1.0 V. The friction at steps at -1.0 V is suddenly changed as compared to that at -0.9 V (see. the friction trace and retrace images in Fig. 6.19). It is reversible when the potential was scanned from -1.0 V to -0.9 V. The cross section analysis of the different positions on the friction trace, retrace images and retrace-trace image are also shown in Fig. 6.19. It shows no obvious change in the friction. The effective normal force (F_N) and the frictional force (F_L) are

calculated to be 3.2 nN and 4.45 nN, respectively, which give the friction coefficient (μ) of 1.4. However, a large change in the friction at step is observed on the electrode surface at the potential of -1.0 V. The increase in the friction at the steps is due to the Schwoebel-barrier effect [64].

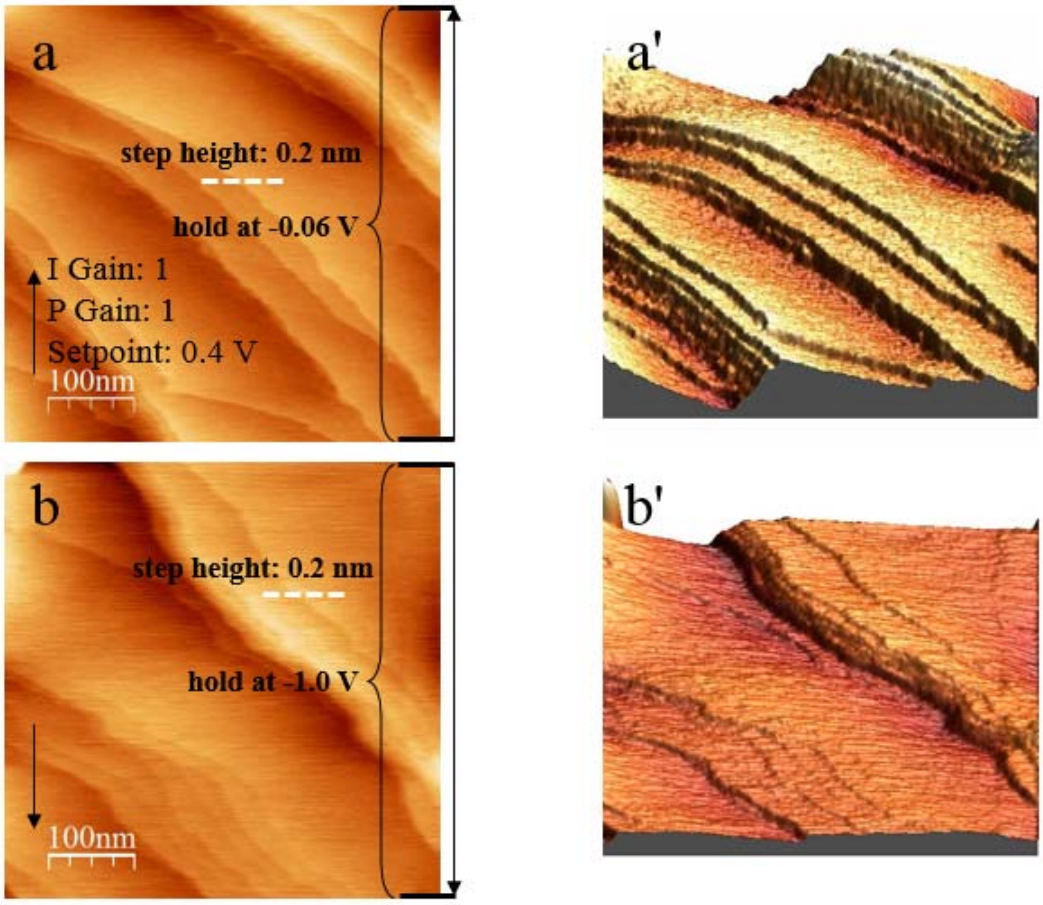

Fig. 6.18 Topographic AFM images and the corresponding 3D images of Au(111) electrode surface in 0.1 M $LiClO_4$ containing DMSO based electrolyte during the first potential cycle. Set point = 0.4 V (or F_N = 3.2 nN) & scan rate of 5 Hz. Arrows indicate scan direction. Line by line correction is used for above images.

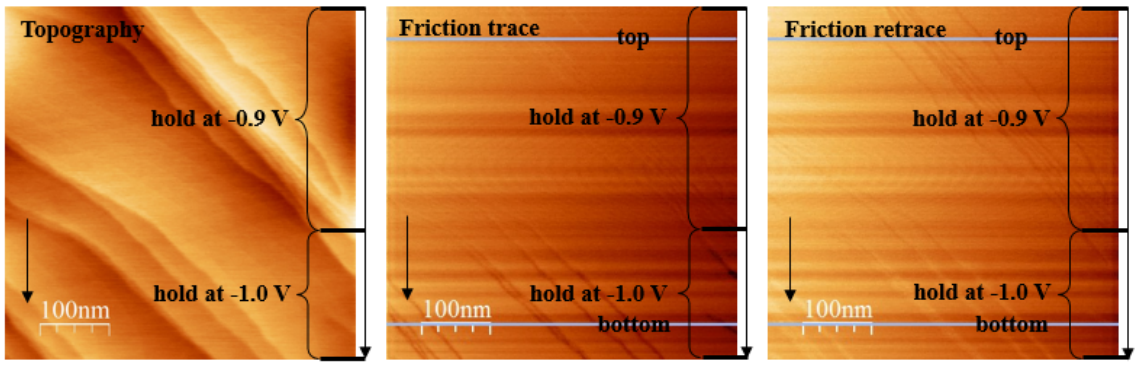

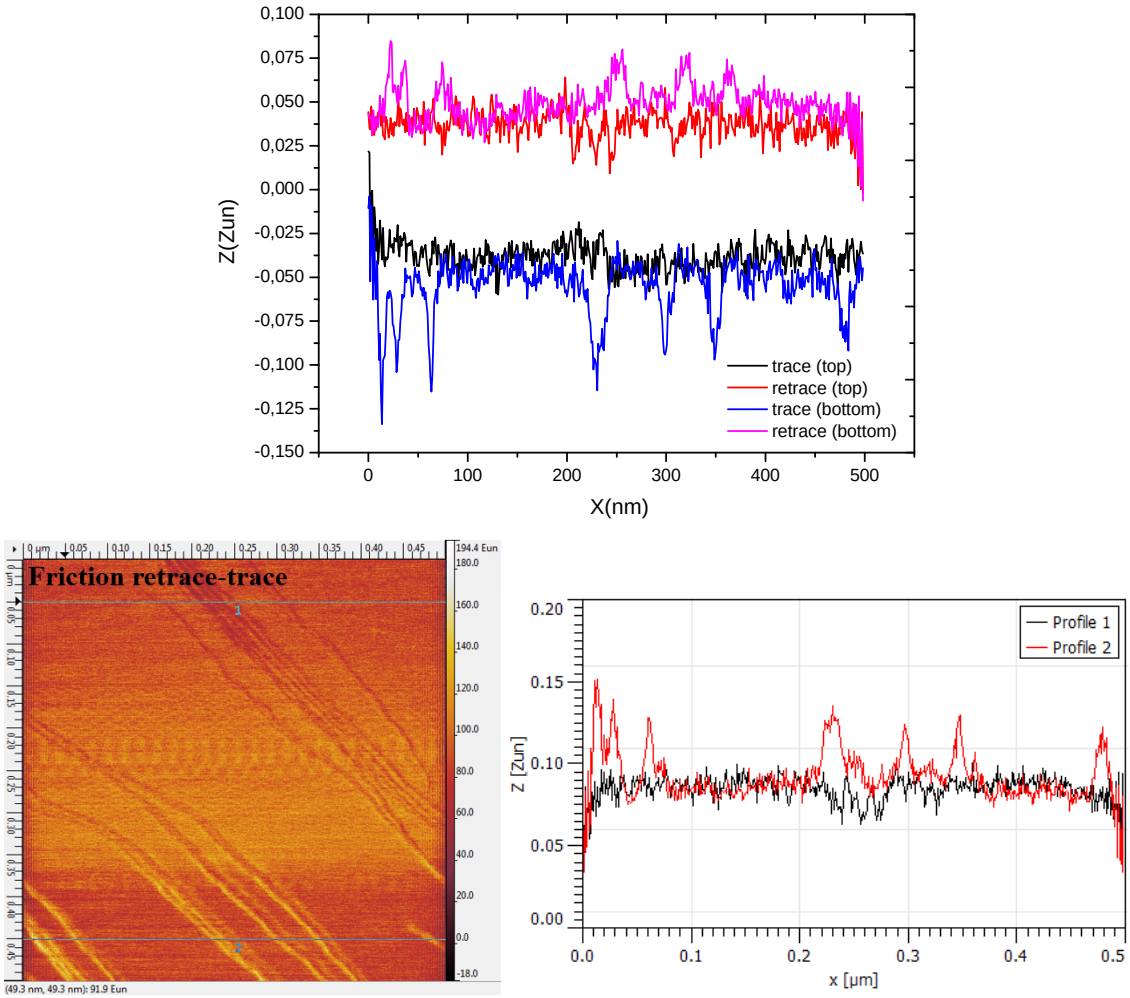

Fig. 6.19 Topographic AFM image (line by line corrected) and the corresponding friction images (without any correction) of Au(111) electrode surface in 0.1 M $LiClO_4$ containing DMSO based electrolyte at the potential step of -0.9 V and -1.0 V. Set point = 0.4 V (or F_N = 3.2 nN) & scan rate of 5 Hz. Arrows indicate scan direction.

In addition, during the second potential cycle, some small particles with the height of 0.2~0.4 nm and the average diameter of 10 nm are formed on the surface during the potential scanning from -0.23 V to -1.3 V (vs. Pt/PtO) as shown in Fig. 6.20b, and they are almost completely dissolved when the potential was scanned positively to +0.02 V (see. Fig. 6.20 c and d). These particles probably are Li_2O_2 or redeposited Au. As mentioned before, Au can be dissolved in DMSO based electrolyte, and it is also confirmed by our AFM results as shown in Fig. 6.21. The friction image is shown in Fig. 6.21b′. The section analysis shows that the friction forces on the substrate and at the bottom of the hole are nearly the same and this would suggest that it is probably Au dissolution. The obvious change (from 0.04 to 0.06) in the friction on the image (see. Fig. 6.21b′) is at steps and it is due to the Schwoebel-barrier effect as mentioned before.

However, Calvo et al. observed that nanoparticle like Li_2O_2 formed on HOPG in $LiPF_6$–dimethyl sulfoxide (DMSO) electrolyte [26]. Fig. 6.20b′ shows the friction image of Fig. 6.20b. In the area where the potential was held at -1.3 V the friction on the substrate is much lower than on the particles where the friction is slightly lower than on Au(111) surface. It may suggest that some Li_2O_2 are formed on the electrode surface.

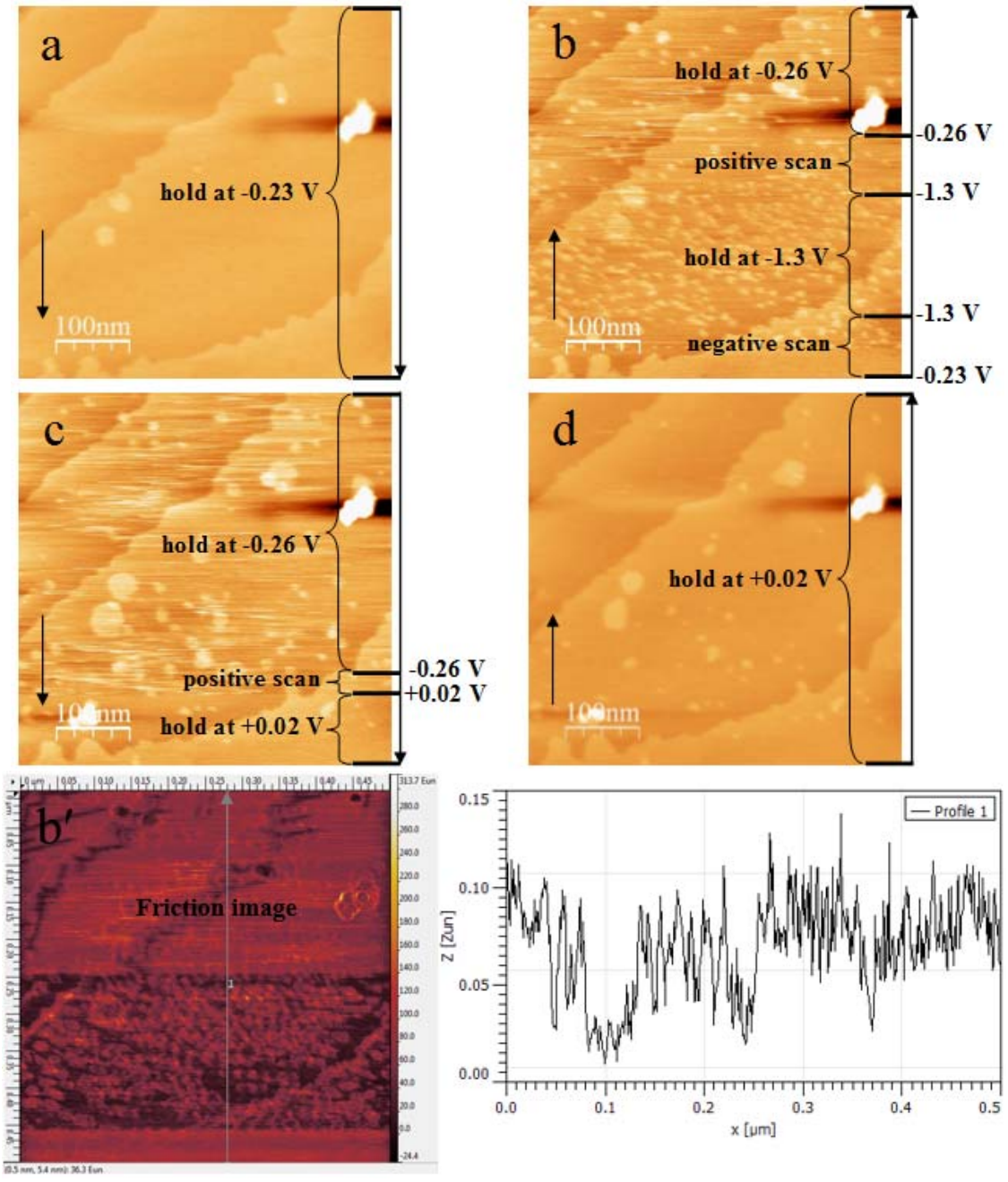

Fig. 6.20 Topographic AFM image images (a, b, c and d) and friction image (b′) of the electrode surface in 0.1 M $LiClO_4$ containing DMSO based electrolyte during the second potential cycle. Set point = 0.4 V (or F_N = 3.2 nN) & scan rate of 5 Hz. Arrows indicate scan direction. Line by line correction is used for above topographic images and friction image is used without any correction.

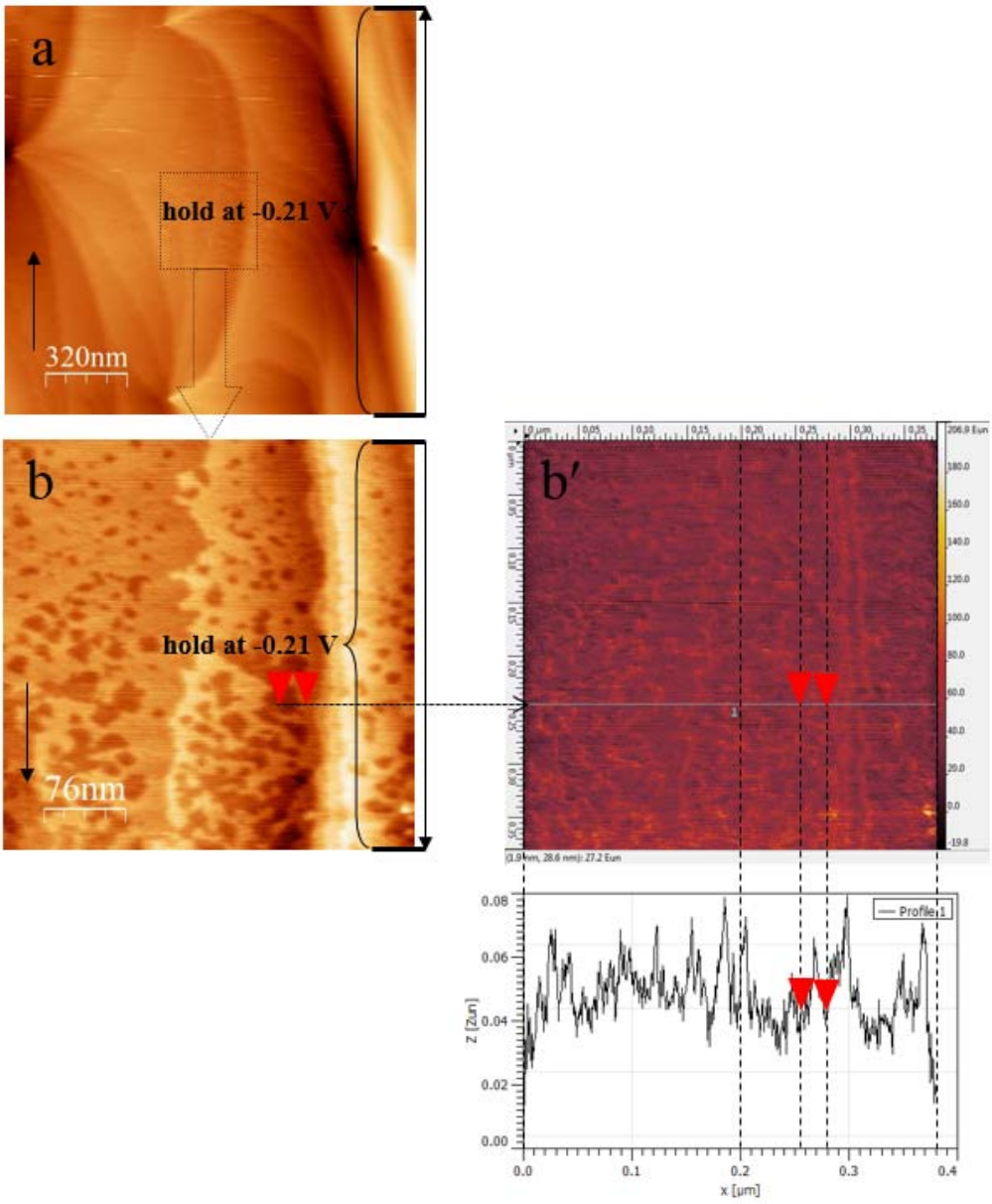

Fig. 6.21 Topographic AFM images (a and b) and friction image (b′) of Au dissolution in 0.1 M $LiClO_4$ containing DMSO based electrolyte. Set point = 0.4 V (or F_N = 3.2 nN) & scan rate of 5 Hz. Arrows indicate scan direction. Line by line correction is used for above topographic images and friction image is used without any correction.

6.3.2.3 Investigation of ORR on Au(111) by EC-STM

The morphology of ORR products on Au(111) in 0.1 M $LiClO_4$ containing DMSO based electrolyte was also observed by the EC-STM. The cyclic voltammogram recorded in STM cell is similar to that recorded in H cell, except a slight shift in potential (see. Fig. 6.22 and Fig. 6.17). The detailed explanation has already been given before.

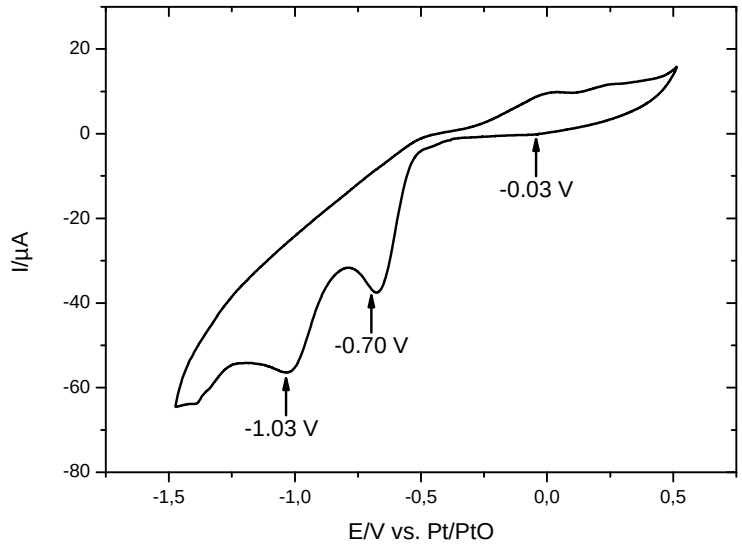

Fig. 6.22 Cyclic voltammograms of ORR on Au(111) electrode in 0.1 M $LiClO_4$ containing DMSO based electrolyte in STM cell in O_2 purged glass chamber at the scan rate of 10 mV s^{-1}.

The electrode surface morphologies during potential scanning from OCP to -1.4 V and then to -0.03 V at the first cycle are demonstrated in Fig. 6.23. The Au(111) surface with atomically flat terraces and steps decorated by some small Au islands was clearly observed (see. Fig. 6.23a). No change in surface morphology during the potential scan over the first peak was observed (see. Fig. 6.23b). However, when the potential was scanned over the second peak and then back to around -0.8 V, it seems that some species formed on the surface disturb the tip scan (see. Fig. 6.23b and c). With the further increase in the potential to positive direction, the clearly Au(111) was observed again. Furthermore, as seen in Fig. 6.23c and d, a lot of tiny holes appeared after -0.2 V which are probably due to Au dissolution.

Fig. 6.24 shows the electrode surface morphology during the second potential scan. When the potential was jumped to -0.72 V where the first peak appears, there is no obvious change in surface morphology except slowly recovering of the holes (see. Fig. 6.24a-c). Once the potential was scanned to -1.06 V where the second peak appears, almost all the holes were recovered probably due to Au re-deposition and the step height increased slightly with time (see. Fig. 6.24d-f). A suddenly increase and then decrease in the step height in the topographic image and a large variation in the tunneling current at step in the current image are observed as shown in Fig. 6.25, which are quite similar to what I observed in Mg^{2+}-DMSO based electrolyte. The detailed discussion on the

appearance of this phenomenon was presented before.

It is well known that in a series circuit the magnitude of the electric current decreases quickly with the increase of the thickness of insulator at a fixed voltage [65]. Similarly, for the tunneling current in STM, when there is nonconductive film and its thickness increase with time on the electrode surface, the tunneling current will become smaller and smaller, and the gradient of the recession in tunneling current is larger in the nonconductive film comparing to that in vacuum when the distance between the tip and sample surface is constant. However, in the STM measurements, the formed film is probably not nonconductive, it may has low conductivity. When the constant tunneling current is kept constant and this kind of film grow on the electrode surface, the distance between the tip and the surface of the film formed on the electrode surface should be smaller than the distance between the tip and bare electrode surface. Furthermore, as mentioned before the film formed at the steps is slight thicker than on the terrace. Therefore, when the tip was scanned over the step along the direction of trace or forward direction (from left to right), the tunneling current first increased rapidly (see. Fig. 6.25b), probably because of the slow feedback control and the shortly contact of the tip with the film surface at the steps. Afterwards, the feedback system responds to this current change to adjust the height of the tip drastically to keep the tunneling current constant. The great adjustment of the tip height (increase) at the step is probably the reason for the large change at the step height on the topographic image (see. Fig. 6.25a).

Conversely, when the tip was scanned over the steps along the direction of retrace or backward direction (from right to left), the tunneling current decreased rapidly because of the slow feedback control and the large recession of the tunneling current in this film (see. Fig. 6.25d). Afterwards, it is similar to the case of trace direction that the feedback system responds to this current change to adjust the height (decrease) of the tip drastically to keep the tunneling current constant, probably causing the large change at the step height on the topographic image (see. Fig. 6.25c).

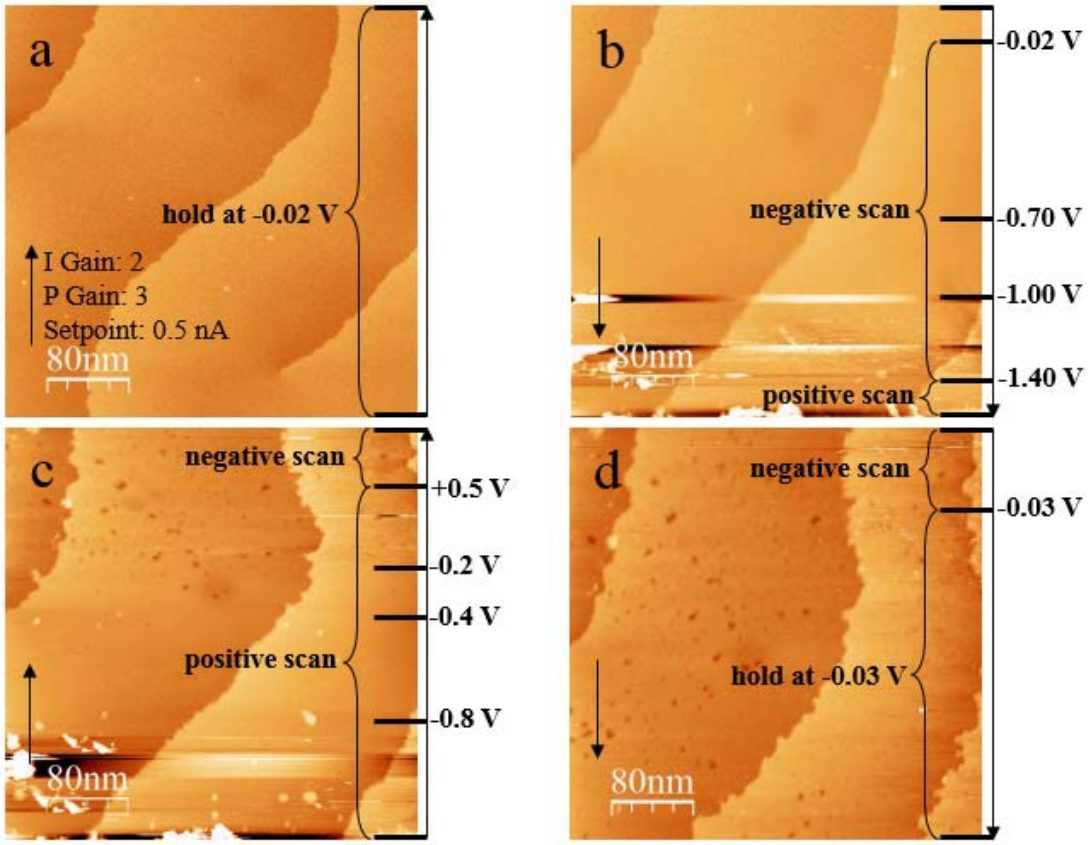

Fig. 6.23 Topographic STM images of the electrode surface in 0.1 M $LiClO_4$ containing DMSO based electrolyte at the different potential in O_2 purged glass chamber. Sample bias of 50 mV, set point = 0.5 nA & scan rate of 3.04 ln/s. Arrows indicate scan direction. Line by line correction is used for above images.

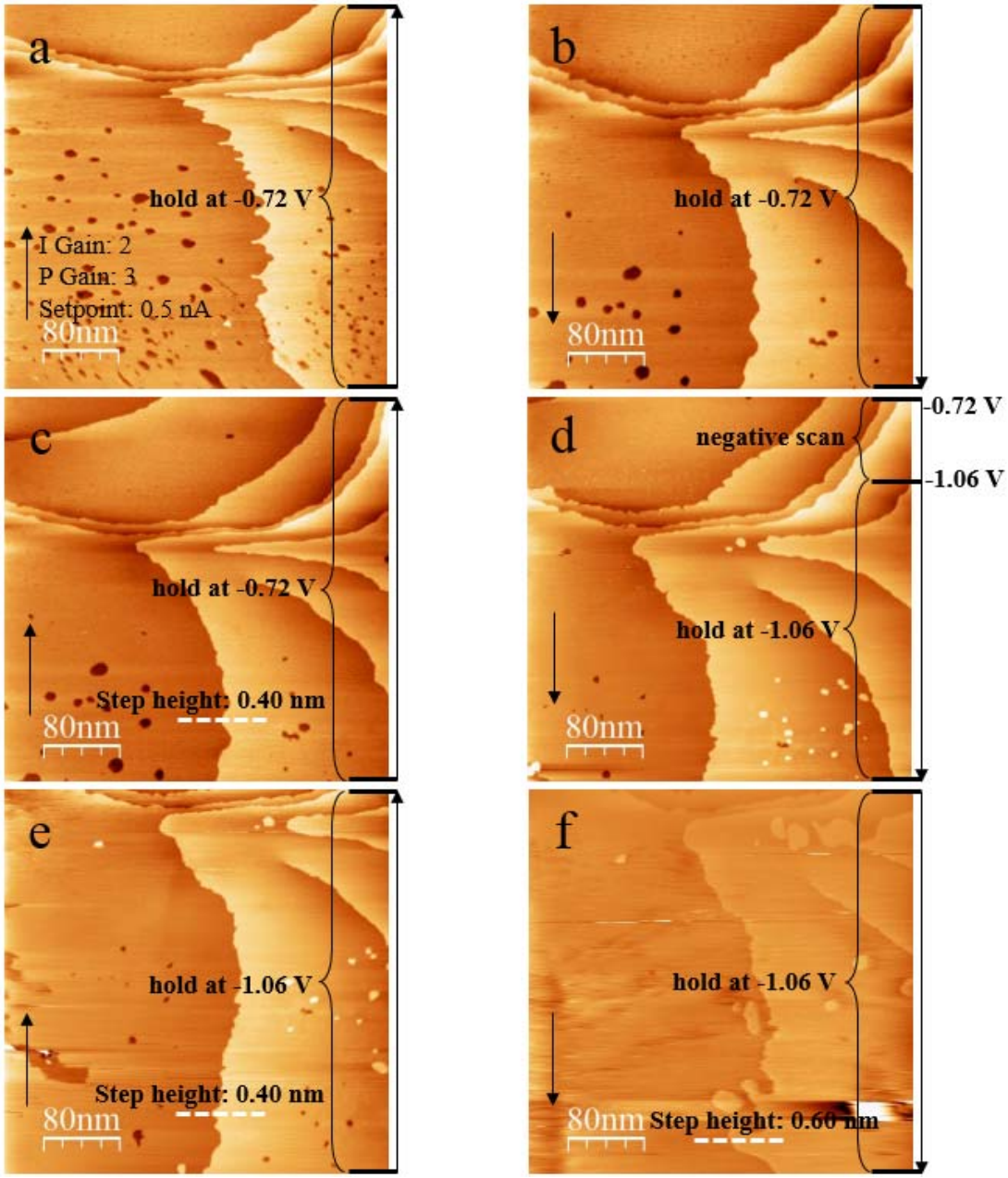

Fig. 6.24 Topographic STM images of the electrode surface in 0.1 M $LiClO_4$ containing DMSO based electrolyte at the potential of -0.72 V and -1.06 V in O_2 purged glass chamber. Sample bias of 50 mV, set point = 0.5 nA & scan rate of 3.04 ln/s. Arrows indicate scan direction. Line by line correction is used for above images.

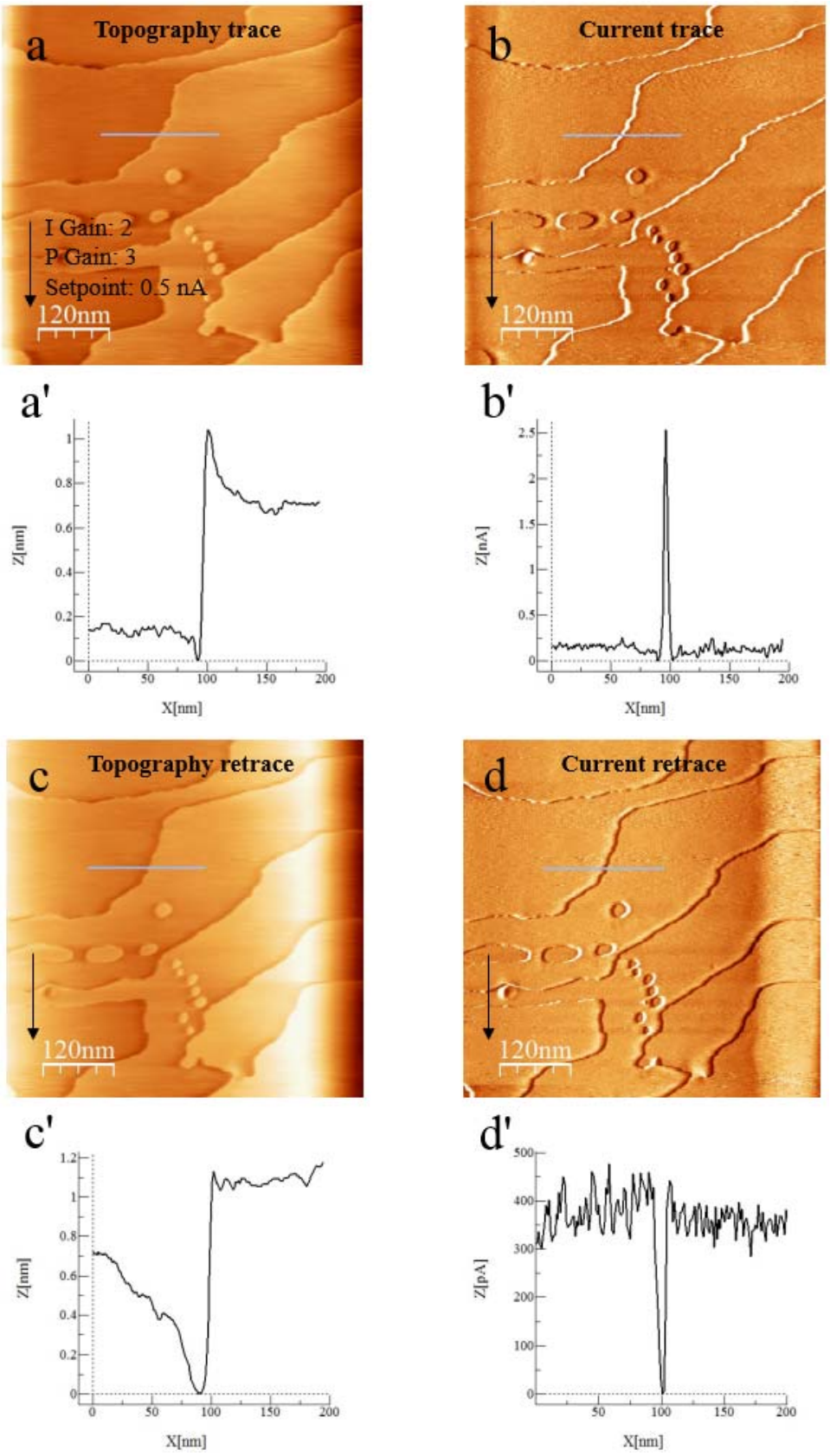

Fig. 6.25 Topographic and current (trace and retrace) images of Au(111) electrode surface in 0.1 M $LiClO_4$ containing DMSO based electrolyte at the potential of -1.06 V in O_2 purged glass chamber. Sample bias of 50 mV, set point = 0.5 nA & scan rate of

3.04 ln/s. Arrows indicate scan direction. The change in height and current are indicated by the cross section on image a, b, c and d and shown in a', b', c' and d', respectively. Line by line correction is used for above topographic images and current images are used without any correction.

The continuous growth of this kind of film at the potential of -1.06 V (in ORR range) with the time was observed. It prefers to grow along the step edges as seen in the focused area (in the ellipses) in Fig. 6.26. This kind of film may consist of ORR products (e.g. insoluble Li_2O_2, etc.), Au and some other species which are produced during the decomposition of electrolyte.

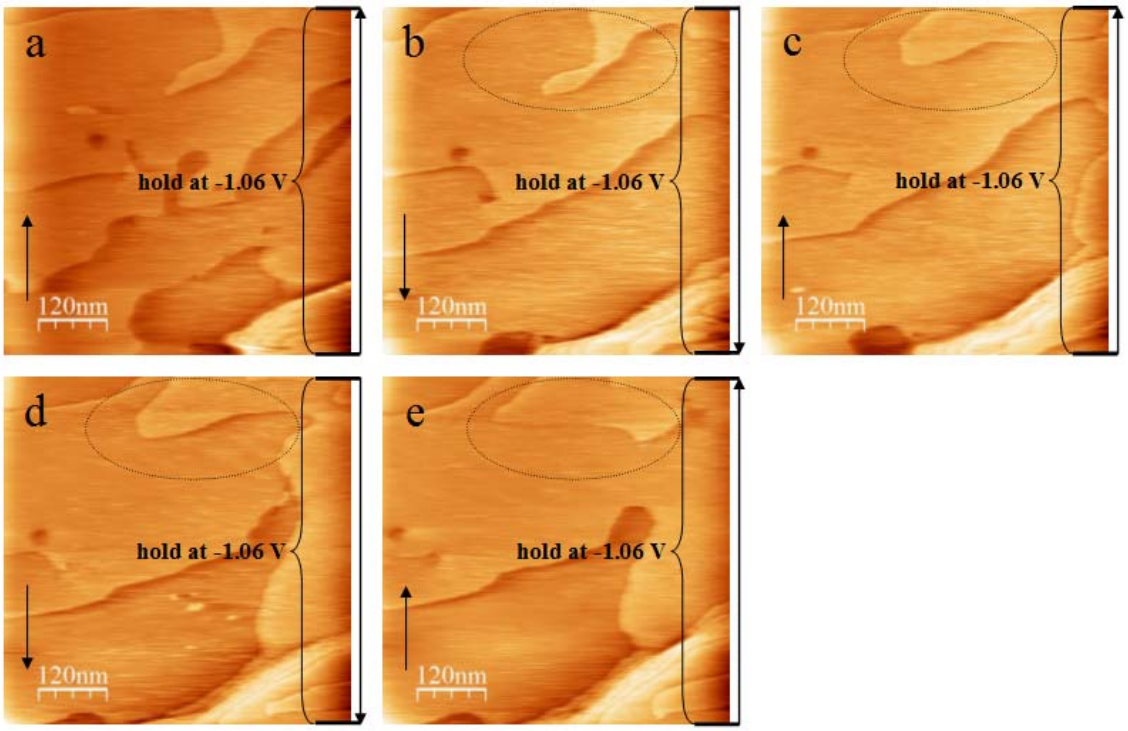

Fig. 6.26 The consecutive STM images of film growth on Au(111) electrode surface in 0.1 M $LiClO_4$ containing DMSO based electrolyte at the potential of -1.06 V in O_2 purged glass chamber. Sample bias of 50 mV, set point = 0.5 nA & scan rate of 3.04 ln/s. Arrows indicate scan direction. Line by line correction is used for above images.

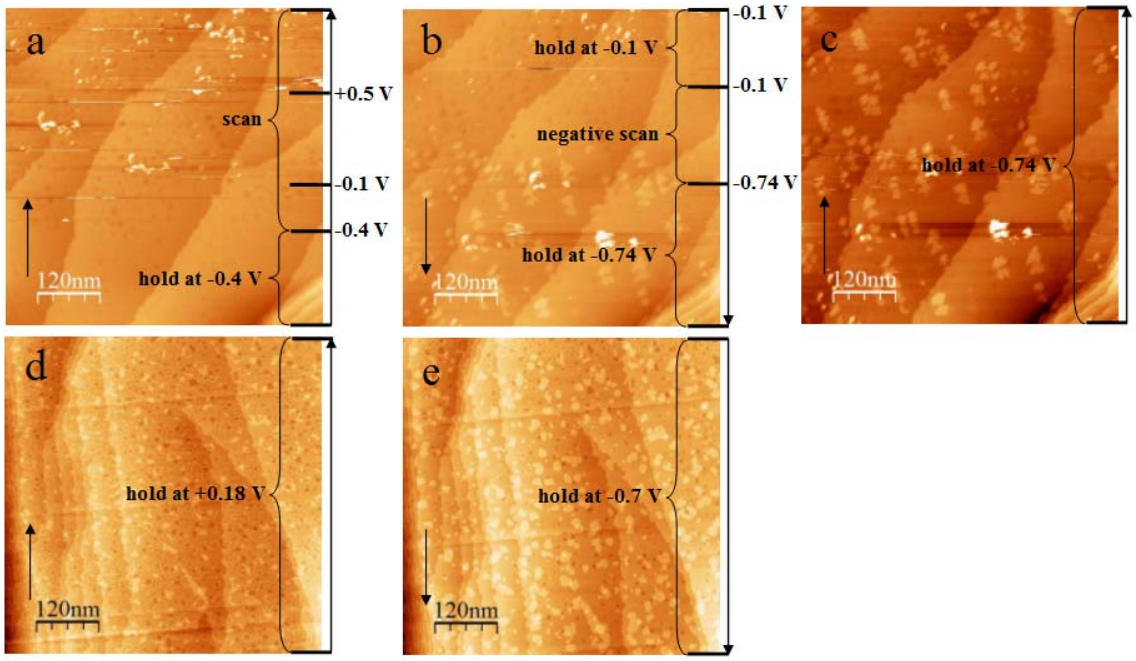

Fig. 6.27 STM images of Au dissolution and redeposition in 0.1 M $LiClO_4$ containing DMSO based electrolyte in O_2 purged glass chamber. Sample bias of 50 mV, set point = 0.5 nA & scan rate of 3.04 ln/s. Arrows indicate scan direction. Line by line correction is used for above images.

Au dissolution and redeposition were also observed during the potential scan in this electrolyte as shown in Fig. 6.27. Some holes start to appear at around -0.2 V, then some particles start to appear at around -0.5 V in the following potential cycle. As mentioned before, these holes are probably due to the Au dissolution and these particles are probably redeposited Au rather than Li_2O_2. With further increase in potential cycle numbers, the dissolution and redeposition phenomenon were clearly observed as shown in Fig. 6.27d and Fig. 6.27e, respectively. This is in good consistent with our AFM results (see. Fig. 6.20 and Fig. 6.21).

6.4 Conclusions:

We investigated the mechanisms of oxygen reduction and oxygen evolution on Au and Pt electrode and the morphology of oxygen reduction products on Au(111) and Pt(111) electrodes in Mg^{2+}/Li^{+}-DMSO based electrolyte.

In Mg^{2+}-DMSO based electrolyte:

The mechanism of ORR on Pt electrode was studied by RRDE. In the electrolyte which contains the water content of 65 ppm, the RRDE results revealed that oxygen reduction

is probably via a total four-electron transferring to form peroxide in this electrolyte. Some of the ORR products could be detected at the ring electrode when the ring potential was held at +0.3 V. The collection efficiency was found that it increased with the increase in rotation rate and its highest value was around 51% of the theoretical value. Furthermore, the deactivation of electrode surface was observed, suggesting that some of the ORR products are formed at the electrode surface and they are insoluble, and this deactivation layer may hinder the charge transfer or the diffusion of electroactive species. The Tafel slope was determined to be 125 mV dec^{-1}, suggesting that the first electron transfer could be as the rate determining step.

The water effect on ORR was also investigated and the results indicated that water has a large effect on the diffusion limiting current, collection efficency and decomposition of electrolyte. With the increase in water content from 65 ppm to 13000 ppm, the diffusion limiting current first was increased slightly and then decreased, and finally increased again, the collection efficency was always decreased and the decomposition intensity of electrolyte was also always increased. Moreover, the Tafel slope was found to be increased with the increase in water content, it would suggest that water content probably has an effect on the mechanism of ORR in this electrolyte. Unfortunately, no OER was observed in these Mg^{2+}-DMSO based electrolytes.

The morphology of ORR products on Au(111) and Pt(111) was studied by EC-STM. On Au(111) surface, the step height is increasing with time during ORR. It seems that a thin film was formed on the electrode surface (especially, at the steps) during ORR and it may consist of ORR products, polar solvent molecules, Au, etc. Furthermore, this film can be partly decomposed into small pieces at the positive potential. However, when the potential was scanned back to the ORR range, these small pieces will participate in the formation of new thin film. The conductivity of this kind of film is probably very poor or even nonconductive. In addition, Au dissolution and probably redeposition were observed during the potential scan in this electrolyte. On Pt(111) surface, the step height is also increasing during ORR as what observed on Au(111). However, Pt dissolution did not observed in this electrolyte.

In Li^{+}-DMSO based electrolyte:

Two ORR peaks were observed at the initial two potential cycles, which are probably

related to superoxide and peroxide formation, respectively, and then overlapped into one peak. In the electrolyte saturated with oxygen, it was suggested that probably only one to two monolayers Li_2O_2 was formed on the electrode surface by assuming that the charge of OER peak (685 μC cm^{-2}) was only contributed by decomposition of Li_2O_2. The reversibility of ORR and OER was found to be around 26.6%. Furthermore, it was also found that the impurity from air (probably, water) has large effect on ORR and OER. Comparing to those in oxygen saturated electrolyte, in air saturated electrolyte the ORR activity recession is very obviously and the reversibility is worse. Only ~10% reversibility was obtained.

Similar surface phenomenon to that in Mg^{2+}-DMSO based electrolyte was also observed in Li^+-DMSO based electrolyte. No toroid-like or particle-like Li_2O_2 was observed during ORR. Moreover, Au dissolution and re-deposition was also observed in this case, which is consistent with the results presented previously.

References

[1] J. Hassoun, H.-G. Jung, D.-J. Lee, J.-B. Park, K. Amine, Y.-K. Sun, and B. Scrosati, Nano Letters 12:5775 (2012).

[2] C. J. Bondue, A. A. Abd-El-Latif, P. Hegemann, and H. Baltruschat, Journal of the Electrochemical Society 162:A479 (2015).

[3] C. J. Bondue, P. P. Bawol, A. A. Abd-El-Latif, P. Reinsberg, and H. Baltruschat, J. Phys. Chem. C 121 8864 (2017).

[4] C. J. Barile and A. A. Gewirth, Journal of the Electrochemical Society 160:A549 (2013).

[5] C. O. Laoire, S. Mukerjee, K. M. Abraham, E. J. Plichta, and M. A. Hendrickson, Journal of Physical Chemistry C 114:9178 (2010).

[6] C. J. Allen, J. Hwang, R. Kautz, S. Mukerjee, E. J. Plichta, M. A. Hendrickson, and K. M. Abraham, Journal of Physical Chemistry C 116:20755 (2012).

[7] Z. Peng, S. A. Freunberger, Y. Chen, and P. G. Bruce, Science 337:563 (2012).

[8] Z. Peng, S. A. Freunberger, L. J. Hardwick, Y. Chen, V. Giordani, F. Bardé, P. Novák, D. Graham, J.-M. Tarascon, and P. G. Bruce, Angewandte Chemie International Edition 50:6351 (2011).

[9] C. Bondue, P. Reinsberg, A.-E.-A. A. Abd-El-Latif, and H. Baltruschat, Physical Chemistry Chemical Physics (2015).

[10] P. Reinsberg, A. Weiss, P. P. Bawol, and H. Baltruschat, Journal of Physical Chemistry C 121:7677 (2017).

[11] Q. Yu and S. Ye, The Journal of Physical Chemistry C 119:12236 (2015).

[12] Y.-C. Lu, H. A. Gasteiger, and Y. Shao-Horn, Journal of the American Chemical Society 133:19048 (2011).

[13] C. O. Laoire, S. Mukerjee, K. M. Abraham, E. J. Plichta, and M. A. Hendrickson, Journal of Physical Chemistry C 113 20127 (2009).

[14] M. J. Trahan, I. Gunasekara, S. Mukerjee, E. J. Plichta, M. A. Hendrickson, and K. M. Abraham, Journal of the Electrochemical Society 161:A1706 (2014).

[15] M. Safari, B. D. Adams, and L. F. Nazar, The Journal of Physical Chemistry Letters 5:3486 (2014).

[16] K. U. Schwenke, M. Metzger, T. Restle, M. Piana, and H. A. Gasteiger, Journal of the Electrochemical Society 162:A573 (2015).

[17] R. Younesi, M. Hahlin, F. Björefors, P. Johansson, and K. Edström, Chemistry of Materials 25:77 (2012).

[18] B. D. Adams, C. Radtke, R. Black, M. L. Trudeau, K. Zaghib, and L. F. Nazar, Energy & Environmental Science 6:1772 (2013).

[19] F. Marchini, S. Herrera, W. Torres, A. Y. Tesio, F. J. Williams, and E. J. Calvo, Langmuir 31:9236 (2015).

[20] R. R. Mitchell, B. M. Gallant, Y. Shao-Horn, and C. V. Thompson, The Journal of Physical Chemistry Letters 4:1060 (2013).

[21] A. C. Luntz and B. D. McCloskey, Chemical Reviews 114:11721 (2014).

[22] B. M. Gallant, D. G. Kwabi, R. R. Mitchell, J. Zhou, C. V. Thompson, and Y. Shao-Horn, Energy & Environmental Science 6:2518 (2013).

[23] R. Wen, M. Hong, and H. R. Byon, Journal of the American Chemical Society 135:10870 (2013).

[24] R. Wen and H. R. Byon, Chemical Communications 50:2628 (2014).

[25] N. B. Aetukuri, B. D. McCloskey, J. M. García, L. E. Krupp, V. Viswanathan, and A. C. Luntz, Nat Chem 7:50 (2015).

[26] S. E. Herrera, A. Y. Tesio, R. Clarenc, and E. J. Calvo, Physical Chemistry Chemical Physics 16:9925 (2014).

[27] D. G. Kwabi, T. P. Batcho, C. V. Amanchukwu, N. Ortiz-Vitoriano, P. Hammond,

C. V. Thompson, and Y. Shao-Horn, The Journal of Physical Chemistry Letters 5:2850 (2014).
[28] H. Geaney and C. O'Dwyer, Physical Chemistry Chemical Physics 17:6748 (2015).
[29] Y. G. Zhu, C. Jia, J. Yang, F. Pan, Q. Huang, and Q. Wang, Chemical Communications 51:9451 (2015).
[30] D. Kundu, R. Black, B. Adams, and L. F. Nazar, ACS Central Science 1:510 (2015).
[31] V. Viswanathan, K. S. Thygesen, J. S. Hummelshoj, J. K. Norskov, G. Girishkumar, B. D. McCloskey, and A. C. Luntz, Journal of Chemical Physics 135:10 (2011).
[32] M. D. Radin, J. F. Rodriguez, F. Tian, and D. J. Siegel, Journal of the American Chemical Society 134:1093 (2011).
[33] J. S. Hummelshøj, J. Blomqvist, S. Datta, T. Vegge, J. Rossmeisl, K. S. Thygesen, A. C. Luntz, K. W. Jacobsen, and J. K. Nørskov, Journal of Chemical Physics 132:071101 (2010).
[34] F. Mizuno, S. Nakanishi, Y. Kotani, S. Yokoishi, and H. Iba, Electrochemistry 78:403 (2010).
[35] S. A. Freunberger, Y. Chen, N. E. Drewett, L. J. Hardwick, F. Barde, and P. G. Bruce, Angewandte Chemie-International Edition 50:8609 (2011).
[36] W. Xu, K. Xu, V. V. Viswanathan, S. A. Towne, J. S. Hardy, J. Xiao, D. Hu, D. Wang, and J.-G. Zhang, Journal of Power Sources 196:9631 (2011).
[37] D. Sharon, M. Afri, M. Noked, A. Garsuch, A. A. Frimer, and D. Aurbach, The Journal of Physical Chemistry Letters 4:3115 (2013).
[38] R. Imhof and P. Novak, Journal of the Electrochemical Society 146:1702 (1999).
[39] D. G. Kwabi, N. Ortiz-Vitoriano, S. A. Freunberger, Y. Chen, N. Imanishi, P. G. Bruce, and Y. Shao-Horn, Mrs Bulletin 39:443 (2014).
[40] I. C. Jang, S. Ida, and T. Ishihara, Chemelectrochem 2:1380 (2015).
[41] B. D. McCloskey, A. Speidel, R. Scheffler, D. C. Miller, V. Viswanathan, J. S. Hummelshøj, J. K. Nørskov, and A. C. Luntz, The Journal of Physical Chemistry Letters 3:997 (2012).
[42] S. R. Gowda, A. Brunet, G. M. Wallraff, and B. D. McCloskey, The Journal of Physical Chemistry Letters 4:276 (2013).
[43] H.-K. Lim, H.-D. Lim, K.-Y. Park, D.-H. Seo, H. Gwon, J. Hong, W. A. Goddard, H. Kim, and K. Kang, Journal of the American Chemical Society 135:9733 (2013).
[44] F. Barde, Y. Chen, L. Johnson, S. Schaltin, J. Fransaer, and P. G. Bruce, Journal of Physical Chemistry C 118:18892 (2014).
[45] S. Meini, Vol. PhD, TUM, Munich, 2013.
[46] D. Aurbach, Y. Cohen, and M. Moshkovich, Electrochemical and Solid State Letters 4:A113 (2001).
[47] M. Matsui, Journal of Power Sources 196:7048 (2011).
[48] I. V. Barsukov, C. S. Johnson, J. E. Doninger, and V. Z. Barsukov, New Carbon Based Materials for Electrochemical Energy Storage Systems: Batteries, Supercapacitors and Fuel Cells, Springer Netherlands, 2006.
[49] Y. B. Ma, N. Li, D. Y. Li, M. L. Zhang, and X. M. Huang, Journal of Power Sources 196:2346 (2011).
[50] T. Khoo, P. C. Howlett, M. Tsagouria, D. R. MacFarlane, and M. Forsyth, Electrochimica Acta 58:583 (2011).
[51] T. Khoo, A. Somers, A. A. J. Torriero, D. R. MacFarlane, P. C. Howlett, and M. Forsyth, Electrochimica Acta 87:701 (2013).

[52] T. Shiga, Y. Hase, Y. Kato, M. Inoue, and K. Takechi, Chemical Communications 49:9152 (2013).
[53] P. Reinsberg, C. Bondue, and H. Baltruschat, Electrochimica Acta 200:214 (2016).
[54] Damjanov.A, M. A. Genshaw, and J. O. Bockris, Journal of Chemical Physics 45:4057 (1966).
[55] M. Khodayari, P. Reinsberg, A. A. Abd-El-Latif, C. Merdon, J. Fuhrmann, and H. Baltruschat, ChemPhysChem 17:1647 (2016).
[56] R. G. LeBel and D. A. I. Goring, J. Chem. Eng. Data 7:100 (1962).
[57] S. H. Lee, R. A. DeMayo, K. J. Takeuchi, E. S. Takeuchi, and A. C. Marschilok, Journal of the Electrochemical Society 162:A69 (2015).
[58] W. Torres, N. Mozhzhukhina, A. Y. Tesio, and E. J. Calvo, Journal of the Electrochemical Society 161:A2204 (2014).
[59] E. Pelizzetti and N. Serpone, Homogeneous and Heterogeneous Photocatalysis, Springer Netherlands, 1986.
[60] C. E. M. Berger, H. K. Dattaa, and B. R. Horrocks, Physical Chemistry Chemical Physics 13:5288 (2011).
[61] R. A. Zeller, Arizona State University, Lake Havasu, 2011.
[62] G. A. Nifontova and I. P. Lavrentev, Bulletin of the Russian Academy of Sciences-Division of Chemical Science 41:391 (1992).
[63] N. Ikemiya and A. A. Gewirth, The Journal of Physical Chemistry B 104:873 (2000).
[64] F. Hausen, M. Nielinger, S. Ernst, and H. Baltruschat, Electrochimica Acta 53:6058 (2008).
[65] J. M. S. Al-fahdawi, International Journal of Science and Research 4:1986 (2015).

Chapter 7: Investigation of surface morphology and adlayer structure of Sb on Au(111) by EC-STM and insertion of magnesium at the Sb modified Au electrode

This chapter demonstrates the monolayer structure of antimony (Sb) on Au(111) surface by electrochemical-scanning tunneling microscope (EC-STM) and the change of the bulk adlayer structure from the double row to particle-like structure with the increase in the surface roughness caused by accumulation of irreversible adsorption Sb species with potential cycles. Furthermore, insertion/extraction of magnesium ion into the Sb modified Au electrode was investigated.

7.1 Introduction:

The initial study of antimony electrochemical deposition on Au electrode was done by cyclic voltammetry by Rhee [1], who found that antimony deposition on Au(100) and Au(111) in acid electrolyte undergoes two electrochemical processes involving an irreversible adsorption and underpotential deposition. This irreversible adsorption was attributed to oxygenous Sb(III) species, probably SbO^+, which is formed in acid electrolyte and is adsorbed irreversibly on Au surface at the potential more positive than the UPD potential [2]. Later, the fundamental research of this phenomenon of this irreversible adsorption and UPD of Sb was investigated by EC-STM. A detailed study on the structure of the irreversibly adsorbed oxygenous Sb(III) species and the Sb adlayer on Au(100) was carried out by Itaya and Mao [2, 3]. Rhee only investigated the structure of the irreversibly adsorbed oxygenous Sb(III) species on Au(111) surface by an in situ STM [4] and Mao also [5] investigated the electrodeposition of Sb on Au(111). However, no detailed investigations on adlayer structure and morphology of Sb on Au(111) were presented. Moreover, the detailed study of magnesium deposition/dissolution at Sb modified Au electrode surface has never been reported.

It is well known that Sb [6-9], Bi [10-12], etc. can be used to form bimetallic semiconductors. These semiconductors possess an interesting property and were widely used in the field of electrocatalysis and materials. Recently, Sb, Sn, Bi have been suggested as insertion materials [13-15], which could be used as an anode material in rechargeable Mg batteries because magnesium can form intermetallics with these materials with a high energy density. In addition, Bi and Sb have rhombohedral crystal

structures which can form alloys in a wide composition range [14, 13]. High initial capacity of 298 mAh/g at 1 C rate has been reported for electrochemical magnesiation at electrodeposited $Bi_{0.88}Sb_{0.12}$ by Arthur et al. [13]. However, the capacity declined to 215 mAh/g after 100 cycle. Insertion/de-insertion of Mg at electrochemically deposited Bi in $Mg(TFSI)_2$/acetonitrile solution has been also investigated. Powdered Tin electrode has been used by Singh et al. as an anode for Mg-ion insertion/extraction [16]. However, they found a higher capacity close to the theoretical value (903 mAh/g) and low voltage difference for Mg insertion/extraction (+0.15/0.20 V), the capacity dropped to 200 mAh/g after 10 cycles at 0.05 C rate. They attributed the low columbic efficiency to the material pulverization after the severe volume change. Bi-nanotubes as an anode material for Mg insertion/de-insertion showed a superior cycling stability and rate performance [17]. The high cycleability upon Mg insertion/extraction was attributed to effectiveness of Bi-nanotubes in combat volume change. Recently, a high specific initial capacity of 180 mAh/g dropped to 50 mAh/g after 3 cycles in $Mg(ClO_4)_2$/MeCN electrolyte has been observed at Bi-CNT composite materials for magnesium battery anodes prepared by electrodeposition technique [18]. Among Ge, Si, and Sn as anode materials for Mg insertion, Si could provide the lowest insertion voltage (0.15 eV vs. Mg) and the highest specific capacity of 3827 mAh/g according to DFT calculations. However, it is so hard to overcome the slow diffusion of Mg into Si and the huge volume expansion (216%). On the other hand, Sn can provide a competitive volumetric energy density (7.4 Wh/cc) under 100% volume expansion [19]. In general, according to our information, there is no literature about the values of diffusion coefficient of Mg in the insertion materials. The superiority of insertion materials as anode material in the field of rechargeable batteries is also one of the reasons, which drive this work as does interest in study of the morphology and structure of Sb deposited on Au(111) electrode.

In this work, we studied systematically the electrochemical behavior of Sb deposition on Au(111) electrode by cyclic voltammetry and EC-STM techniques. Furthermore, we also studied the insertion of Mg into multilayers of Sb in nonaqueous electrolyte (MACC in tetraglyme). The apparent diffusion coefficient of Mg in the solid state was determined and the cycling reversibility of insertion/de-insertion was demonstrated.

7.2 Experimental:

Preparation of Au(111) single crystal electrode

The Au(111) single crystal electrode (Mateck, Germany) is a cylinder, 10 mm in diameter and 3 mm in thickness with a thin gold wire attached to its rear for handling. It was polished with roughness < 0.01 micron and orientation accuracy < 0.4 deg. by Mateck and prepared by cooling down after annealing in pure argon (Air Liquid, 99.999%) atmosphere as described elsewhere [20]. A polycrystalline Au electrode with a similar size was also employed. All aqueous electrolytes were prepared by 18.2 MΩ Milli-Q water and de-aerated with high purity argon gas for at least 15 min before use. Electrochemical measurements in 0.1 M H_2SO_4 (spectro pure grade) were carried out in a conventional three electrode glass H-cell consisting of three compartments, where are used for placing working electrode, reference electrode and counter electrode, respectively. The working electrode is placed in the central compartment and contacted with solution in a hanging meniscus configuration, the reference electrode is placed in the compartment, where is connected to the central compartment with a Luggin capillary and the counter electrode is placed in the compartment, where is separated from the central compartment by a glass frit. A large Pt sheet (1×1 cm) was used as the counter electrode, a reversible hydrogen electrode (RHE) prepared by electrolyzing 0.1 M H_2SO_4 electrolyte was used as the reference electrode and the Au(111) was used as working electrode. The electrochemical deposition behaviour of antimony on Au electrode was studied in the same glass H-cell containing 0.25 mM Sb_2O_3(99.999%, Aldrich) + 0.5 M H_2SO_4 electrolyte. All electrochemical measurements were carried out by a bi-potentiostat purchased from Pine Instruments Inc. model AFBPC1 in combination with LabVIEW software (National Instruments GmbH, Munich, Germany) for recording cyclic voltammograms (CVs). The coverages are given as a ratio of the adsorbed Sb species to the number of surface Au-atoms assuming a one to one ratio of Sb to Au atoms.

EC-STM measurements

All EC-STM measurements were performed with an Agilent Technologies 5500 Scanning Probe Microscope (SPM) and a commercially available STM scanner (Molecular Imaging/Agilent Technologies) fitted with an electrochemical cell so called STM/AFM cell as described before. A Pt and Au wire was used as a quasi reference electrode ($E_{Pt/PtO}$ = 0.9 V vs. RHE) and a counter electrode, respectively. The reference electrode was immersed in a small compartment filled with the same electrolyte and separated from main compartment by a capillary. Pt/Ir (90:10) STM tips with a diameter

of 0.25 cm were prepared by etching in a 2 M KOH + 4 M KSCN bath and coated with hot-melt glue containing different types of polymer (provided by Steinel) to minimize faradaic current. All the EC-STM measurements were done in glass chamber purged with argon at room temperature.

Magnesium electrochemical deposition measurements

All chemicals were purchased from Sigma-Aldrich. The tetraglyme (G4) was distilled over sodium and stored over molecular sieves (3 Å) until the water content reaches to an amount less than 5 ppm. The water content has been determined by Karl Fischer titration. $MgCl_2$ was heated overnight under vacuum at 290 °C and then stored under thionyl chloride for 1 week. At low pressure the thionyl chlorid was removed completely. All materials were handled in an Argon filled glovebox. The MACC electrolyte was prepared by adding tetraglyme (20.5 ml) to $MgCl_2$ (0.966 g). While stirring the $AlCl_3$ (1.368 g) was added slowly and portion wise. The whole mixture was then stirred overnight after addition of a suitable amount of MgH_2 to reduce the water content. Finally, the water content of this well prepared electrolyte did not exceed 50 ppm.

A polycrystalline Au electrode and an antimony modified Au electrode (~30 monolayer of Sb on Au) were used as working electrodes for Mg deposition measurements. Magnesium foil was used as a counter electrode and another one as a reference electrode. All the magnesium electrochemical deposition measurements were carried out in the MBraun glovebox (H_2O < 0.5 ppm, O_2 < 0.5 ppm).

7.3 Results and discussion

7.3.1 Electrochemistry of antimony on Au(111)

A typical cyclic voltammogram of Au(111) in 0.1 M H_2SO_4 is shown in Fig. 7.1. The interpretation of the voltammetric feature of Au(111) has been reported before [21-23].

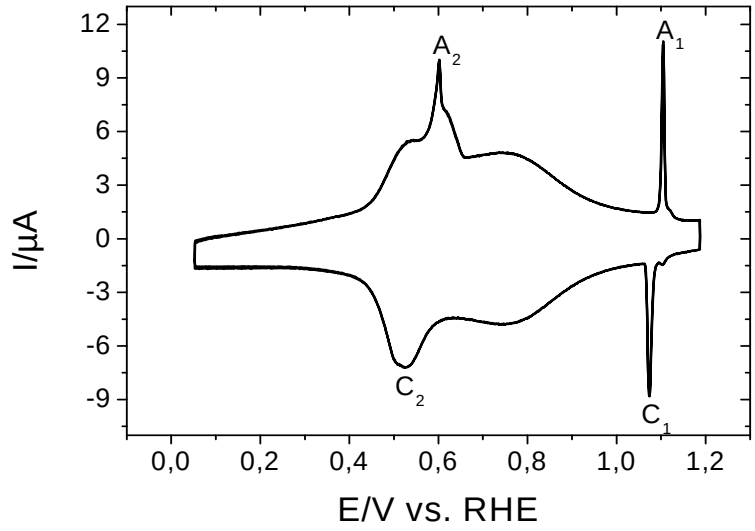

Fig. 7.1 Cyclic voltammogram of Au(111) in 0.1 M H_2SO_4 solution saturated with Ar in H-cell at the sweep rate of 50 mV s^{-1}.

The recorded cyclic voltammograms of Sb underpotential deposition and overpotential deposition on Au(111) in 0.5 M H_2SO_4 containing 0.25 mM Sb_2O_3 electrolyte saturated by argon are shown in Fig. 7.2. Two peaks were observed in the underpotential deposition region. The first cathodic peak C1 (~+0.3 V) is due to the reduction of preadsorbed oxygenous Sb(III) species (SbO^+). In a highly acidic electrolyte ($0 < pH < 1$), the main species of antimony is SbO^+ as reported by Wu et al. [5]. The following small peak C2 (~+0.28 V) is due to the reduction of oxygenous Sb(III) species from bulk solution.

The total charge density of peaks C1 and C2 (~320 μC cm^{-2}) suggests that the coverage of a monolayer is around 0.44 by assuming a one to one ratio of Sb to Au atoms, which is close to the reported value of 0.43 [1]. However, Itaya and coworkers [2] have investigated the Sb structure at Au(100) and they found the total charge due to Sb UPD and irreversible adsorption corresponding to the coverage of 0.63, which should be the influence of anions due to the co-adsorption. A corresponding dissolution peak A1 was observed at +0.34 V and its charge was calculated to be 290 μC cm^{-2}. The columbic efficiency (the ratio between the anodic and cathodic charges) in the first potential cycle for Sb stripping/deposition in UPD region gives a value of 90%. Furthermore, the columbic efficiency decreased to 70% in the fifth potential cycle in the potential range of 0.2 V to 0.5 V. This suggests that irreversible process took place in UPD region and the irreversibly adsorbed species and probably some Au-Sb surface alloys were

accumulated with the increase of the potential cycles. According to the relevant studies, the irreversible process was attributed to the irreversible adsorption of oxygenous Sb(III) species [2, 3, 5, 24]. In the potential range of overpotential deposition, a cathodic peak C3 was observed at ~0.1 V. The peak C3 and the corresponding anodic peak A2 are attributed to the bulk Sb deposition and dissolution, respectively. It is worth noting that the peak A1 became small and the peak A0 appeared in the fifth cycle after sweeping the potential to more negative value at the Sb-bulk deposition region. We attributed the presence of anodic peak (A0) to the stripping of Sb from $AuSb_2$ alloy which has been reported before by Stegemann [25].

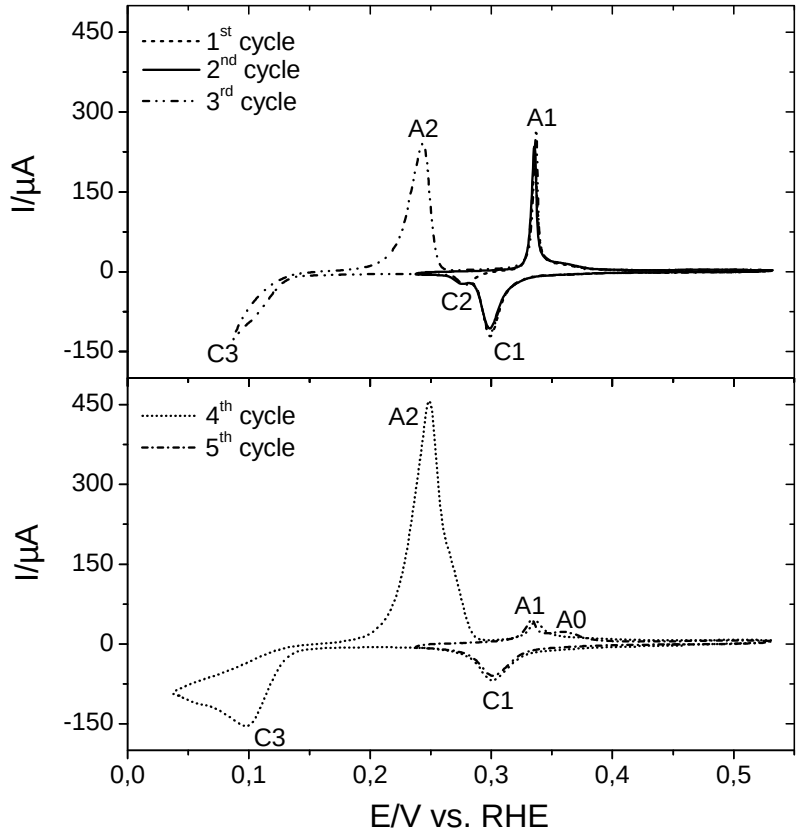

Fig. 7.2 Cyclic voltammograms of Sb deposition on Au(111) in 0.25 mM Sb_2O_3 + 0.5 M H_2SO_4 electrolyte saturated with Ar in H cell at the sweep rate of 10 mV s^{-1}.

After carrying out the deposition and dissolution of Sb for several potential cycles in Sb containing electrolyte as seen in Fig. 7.2, the potential was held at +0.5 V and the Au(111) was rinsed with plenty of 0.1 M H_2SO_4 electrolyte and transferred into 0.1 M H_2SO_4 electrolyte. The corresponding cyclic voltammograms were recorded and are shown in Fig. 7.3. A large cathodic peak with a weak shoulder was observed at +0.3 V in the first potential cycle, and then it was separated obviously into two peaks which decreased with the increase of the cycle number. This means that the process of

deposition/dissolution of Sb on Au(111) is irreversible and the deposited Sb species can not be dissolved completely at the positive potential of +0.5 V in Sb containing electrolyte. However, with the continuous potential scan in the blank electrolyte, it was indicated by sulfate adsorption/desorption spike at ~1.1 V that most of the adsorbed Sb species can be dissolved and the Au(111) surface reappeared again due to the rearrangement of surface Au atoms. The decrease in the charge of the spike at ~1.1 V is probably due to the increase in the roughness of the surface. Two cathodic peaks C1 and C2 appeared after the first potential cycle and they are probably attributed to the reduction of preadsorbed Sb(III) species and Sb(III) species from the electrolyte, respectively. As shown in Fig. 7.2, the peak C1 is corresponding to the peak A2 and peak C2 is corresponding to the peaks A1 and A3.

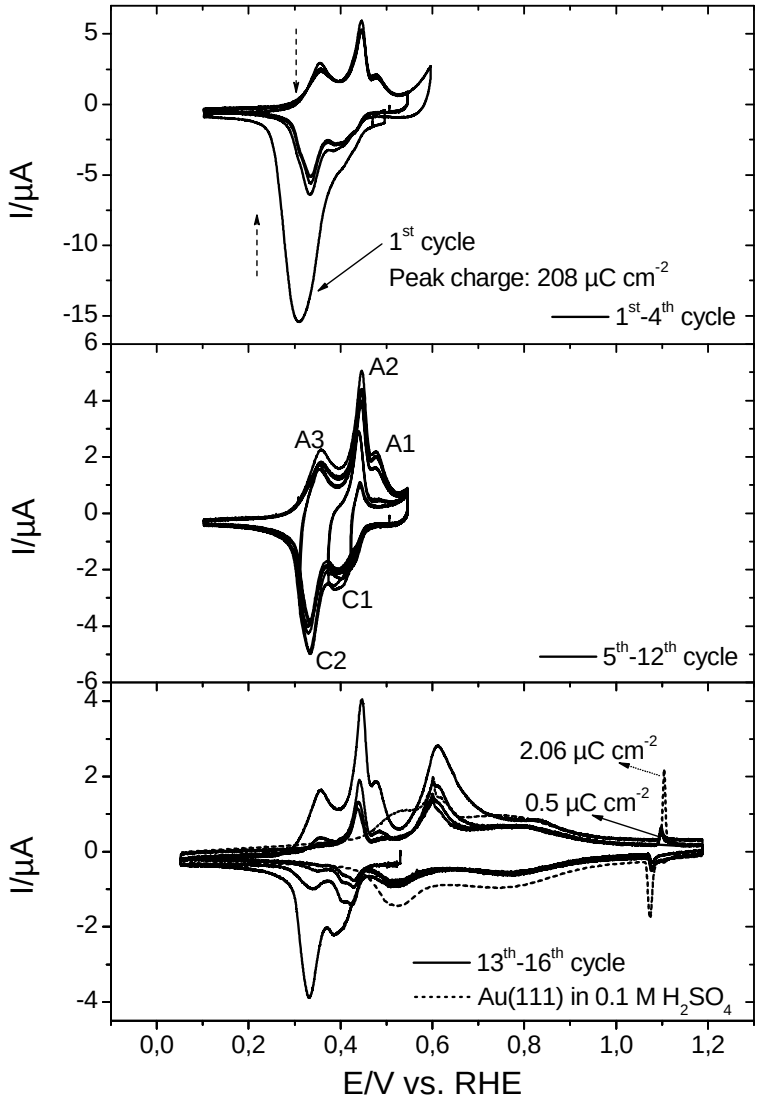

Fig. 7.3 Cyclic voltammograms of Sb species/Au(111) in 0.1 M H_2SO_4 electrolyte saturated with Ar in H cell at the sweep rate of 10 mV s^{-1}. The Sb species/Au(111) was obtained after carrying out bulk deposition and dissolution of Sb on Au(111) in Sb

containing electrolyte, as shown in Fig. 7.2. The CV of fresh prepared Au(111) in 0.1 M H_2SO_4 electrolyte saturated with Ar in H cell at the sweep rate of 10 mV s^{-1} (bottom, the dot curve).

Fig. 7.4 shows the cyclic voltammograms of Sb species/Au(111) electrodes which was induced by immersing the electrode surface into the Sb containing electrolyte in the hanging meniscus configuration for 1, 3 and 5 min at open circuit potential, in 0.1 M H_2SO_4 electrolyte. The electrode was rinsed with plenty of 0.1 M H_2SO_4 electrolyte before recording the CVs. The reduction and oxidation of Sb species on Au(111) were observed, suggesting that irreversible adsorption of Sb species on Au(111) starts once the Au(111) surface is in contact with the Sb containing electrolyte at open circuit potential. All the cyclic voltammograms are similar and the charges of the cathodic peak in the first potential cycle in these three cases (contact for 1, 3 and 5 min) are around 210 μC cm^{-2}, indicating that the irreversible adsorption process is very fast and the coverage of the irreversibly adsorbed Sb species on Au(111) is around 0.30 (assuming a $3e^-$ transfer), which is in good consistence with the value obtained in the literature [4]. It was also observed that the prolonged contact time (≥ 1 min) did not affect on the CV on Au(100) electrode surface [2].

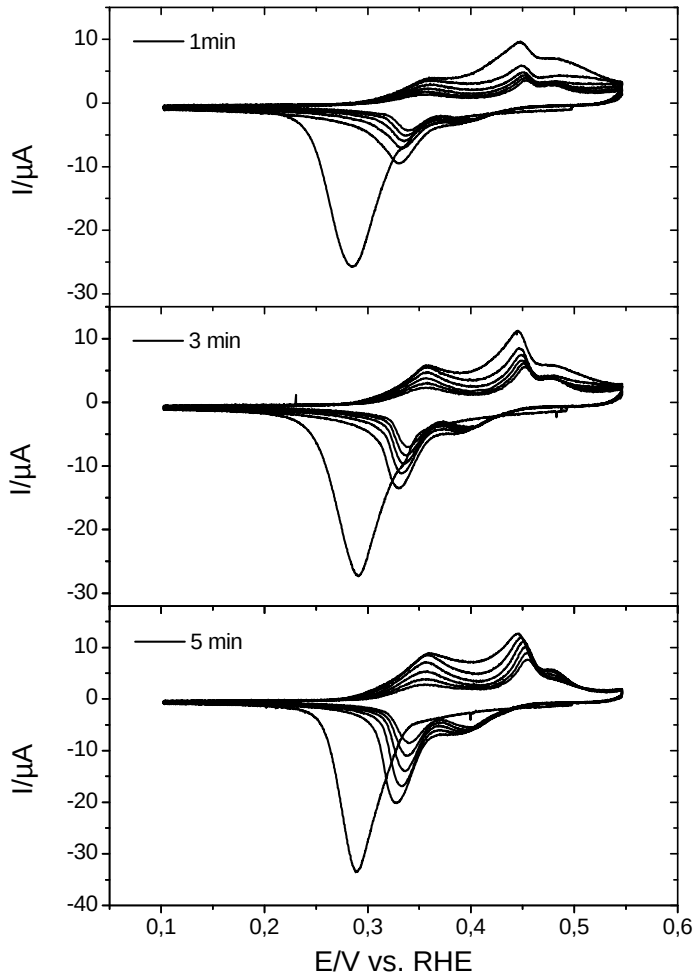

Fig. 7.4 Cyclic voltammograms of Sb species/Au(111) in 0.1 M H_2SO_4 electrolyte saturated with Ar at the sweep rate of 10 mV s^{-1}. The irreversible adsorption of Sb species on Au(111) was induced after the electrode surface contact with Sb containing electrolyte in the hanging meniscus configuration for 1, 3 and 5 min at open circuit potential (~0.6 V).

7.3.2 Investigation of Sb deposition on Au(111) by EC-STM

7.3.2.1 Electrochemistry of antimony on Au(111) in STM cell

Similar cyclic voltammogram of Sb deposition on Au(111) in 0.25 mM Sb_2O_3 + 0.5 M H_2SO_4 electrolyte was obtained in STM cell during the STM measurements as shown in Fig. 7.5. It is almost identical to that recorded in H cell when the potential is converted to that versus reversible hydrogen electrode (RHE) using E (Pt/PtO)= 0.9 V vs RHE.

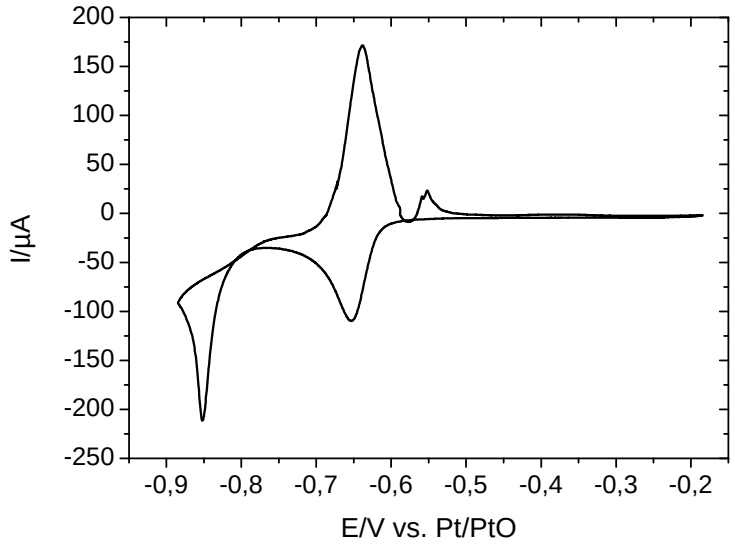

Fig. 7.5 Cyclic voltammogram of Sb deposition on Au(111) in 0.25 mM Sb_2O_3 + 0.5 M H_2SO_4 electrolyte in STM cell at the sweep rate of 10 mV s^{-1}.

7.3.2.2 Underpotential deposition of Sb on Au(111)

An in situ observation of Sb underpotential deposition/dissolution on Au(111) in 0.5 M H_2SO_4 containing 0.25 mM Sb_2O_3 electrolyte in STM cell is shown in Fig. 7.6. In all EC-STM measurements, Pt/PtO electrode was used as reference electrode and the potential was scanned from -0.24 V (open circuit potential) to -0.74 V, which is in the potential range of UPD. At open circuit potential, the Au(111) surface decorated by the tiny spots and some small islands was observed as shown in Fig. 7.6a. These small islands might be the Au islands. When the potential was scanned negatively, the massive nucleation on the terraces and epitaxial two dimensional (2D) growth started at ~0.6 V (see. Fig. 7.6b). The Sb monolayer-islands were formed with the height of ~0.35 nm. As seen in Fig. 7.6a, the step height of the fresh prepared Au(111) obtained by our setup is also ~0.35 nm, which is higher than the value it should be (0.2 nm). With the continuous growth at the potential of -0.74 V, a complete monolayer was formed within approximately 3.5 min as shown in Fig. 7.6c and d. However, this monolayer can be dissolved quickly when the potential was scanned positively to -0.31 V (see. Fig. 7.6e). But some islands and visible tiny spots appeared on the surface after dissolution as shown in Fig. 7.6f, which means that some residual Sb species consisting of irreversible Sb species and Au-Sb alloy remained on surface and can not be dissolved completely. This confirms the result obtained in electrochemical measurement.

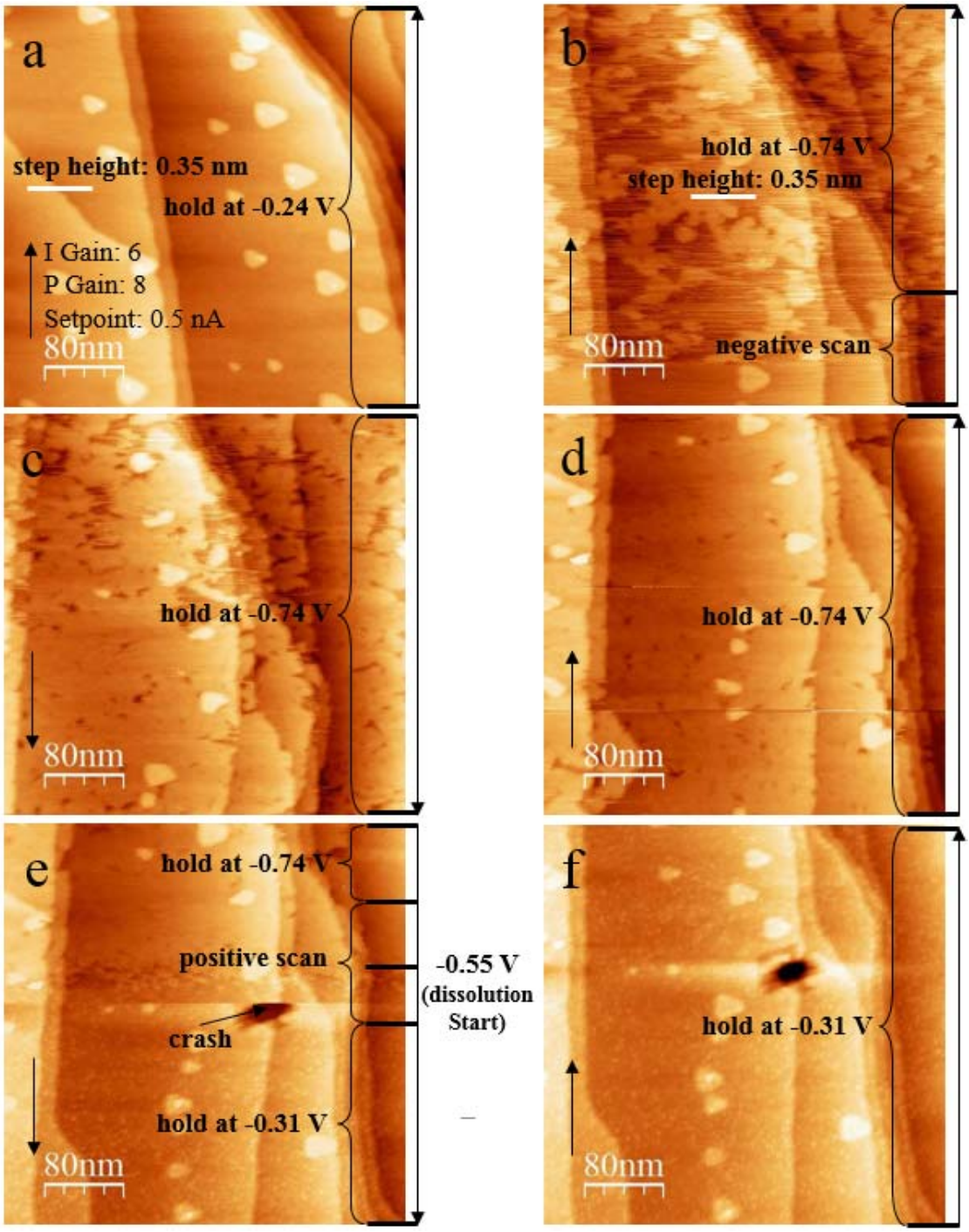

Fig. 7.6 Sequential STM topographic images of Sb deposition/dissolution on Au(111) in 0.25 mM Sb_2O_3 + 0.5 M H_2SO_4 electrolyte. (a) Initial Au(111) surface at open circuit potential of -0.24 V, (b) the electrode potential was scanned from -0.24 to -0.74 V and then stopped at -0.74 V, the height of Sb adlayer was shown with cross section on the image b, (c-d) the electrode potential was held at -0.74 V, formation of complete monolayer, (e) the electrode potential was scanned back from -0.74 to -0.31 V and then stopped at -0.31 V, dissolution of monolayer (f) the electrode potential was held at -0.31 V. sample bias of 50 mV, set point = 0.5 nA & scan rate of 3.04 ln/s. Integral gain: 6 and

proportional gain: 8. Arrows indicate scan direction. Line by line correction is used for above images.

7.3.2.3 Adlayer structure of Sb on Au(111)

The atomic resolution of Sb adlayer structure on Au(111) surface was obtained at the potential of -0.74 V and is shown in Fig. 7.7. As discussed before, two peaks corresponding to two deposition processes were observed in the UPD region. The initial process is the reduction of the preadsorbed oxygenous Sb(III) species and it has been investigated and found that the formed adlayer has a $\left(\sqrt{3}\times\sqrt{3}\right)R30^\circ$ structure on Au(111) [4]. The second process is the UPD process or the reduction of oxygenous Sb(III) species, which are from the bulk electrolyte. It was also investigated by other researchers [1, 5], but the structure of underpotentially deposited adlayer was not resolved. In this work, we observed that the Sb adlayer possesses a double row structure as shown in Fig. 7.7. Specifically, as shown in Fig. 7.7a, an orientated 2D growth along three different directions to form the double row structure with the width of ~2.4 or 3.2 nm was observed and the angle between two different oriented rows was found to be around 120°, suggesting that this structure is probably aligned along the densely packed atom rows of the (111) plane. Moreover, the channels appeared between two parallel rows, which is probably due to oxygen removal from the in-plane orientated SbO^+ layer [5]. The height of the UPD adlayer is shown in Fig. 7.7c. The distance between two adjacent Sb atoms along the black dot line on image b is shown in Fig. 7.7d. To get accurate lattice parameters, the error induced by the thermal drift was eliminated by drift calibration and the Sb adlayer lattice vectors were corrected by using the calibration matrix from the known adlayer lattices of sulfate on Au(111) (see. appendix A). The orientation of the substrate was kept almost the same (± 10°) for each experiment. The corrected distances between the two adjacent atoms along vector a and vector b (see. Fig. 7.7b) were found to be 1.076 nm and 0.821 nm, respectively. Both vectors included angle is 128.5° close to 120°. A proposed Sb adlayer structure model is shown in the appendix A. The initial Sb adlayer was formed by the reduction of the adsorbed oxygenous Sb species with the structure of $\left(\sqrt{3}\times\sqrt{3}\right)R30^\circ$ and coverage of 0.33, and then the UPD adlayer was formed with the structure shown in the model and coverage of ~0.11 (see. appendix A). The total coverage calculated from the proposed model is almost the same as the value calculated from the charge of the peaks. However, in practice the structure of UPD adlayer probably is compressed or expanded, so that it

is shown a local certain structure in our STM image as like the Moiré pattern. Similar investigation has been done on Au(100) in perchloric acid electrolyte by Itaya [2], who found that the irreversibly adsorbed SbO^+ adlayer has a quasi (2×2) structure and two adlayer structures, $(2\sqrt{2}\times\sqrt{5})$ and $(\sqrt{2}\times\sqrt{5})$ observed at 0.3 and 0.25 V, respectively.

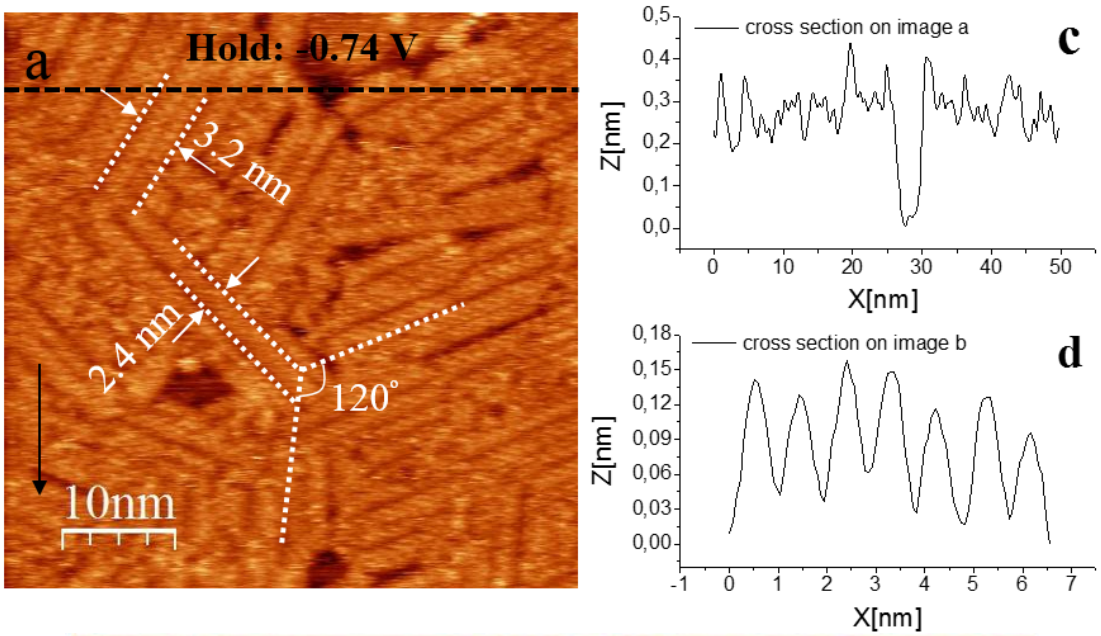

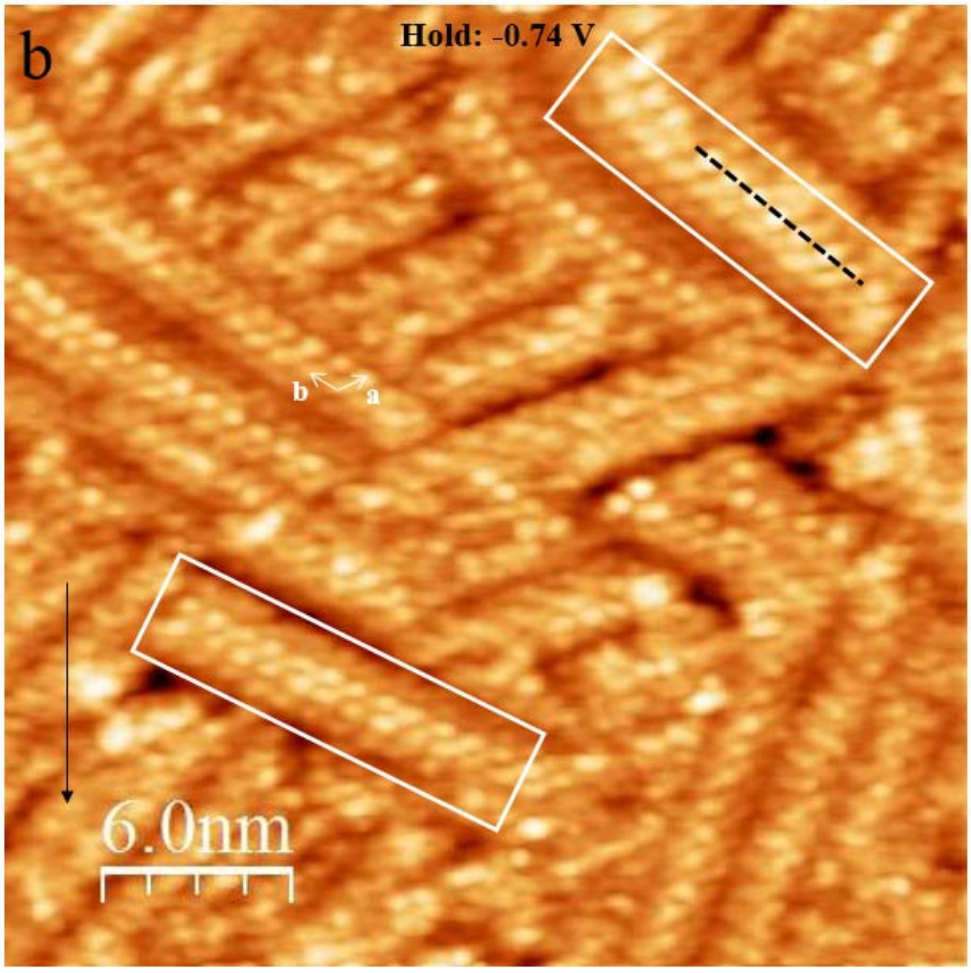

Fig. 7.7 STM images of the Sb adlayer structure on Au(111) in 0.25 mM Sb_2O_3 + 0.5 M H_2SO_4 electrolyte at -0.74 V. (a) 50 × 50 nm; (b) 30 × 30 nm; (c) the cross section on image a; (d) the cross section on image b. Sample bias of 50 mV, set point = 0.5 nA & scan rate of 12 ln/s. Integral gain: 2 and proportional gain: 3. Arrows indicate scan direction. Line by line correction is used for above images.

7.3.2.4 Overpotential deposition of Sb on Au(111)

A freshly prepared Au(111) surface was employed for observing the bulk adlayer structure of Sb formed on its surface. The bulk deposition process was demonstrated in Fig. 7.8. The Au(111) surface at the potential of -0.35 V in the Sb^+ containing electrolyte is shown in Fig. 7.8a, and is similar to that observed before in Fig. 7.6a. As the potential was scanned negatively from -0.35 to -0.88 V (see. Fig. 7.8b, c and c′), the bulk deposition of Sb starts at ~0.78 V (vs. Pt/PtO) and both regular and irregular three dimensional (3D) nucleation and growth were observed, which lead to the bulk adlayer formation with different structures, double row and particle-like structure, respectively. The increase in the height of the Sb deposits with the increase in the potential initially and then with the holding time at -0.88 V is shown in Fig. 7.8d. The horizontal cross section on Fig. 7.8b is shown in Fig. 7.8e. It shows that ~1 nm height of Sb deposits was formed at that time. At the bottom of Fig. 7.8b, the height of the Sb deposits reaches to ~6 nm, which is around 15 layers based on that the height of the Sb monolayer obtained in this measurement is ~0.4 nm (see. Fig. 7.8d). A typical Volmer-Weber growth was observed during overpotential deposition.

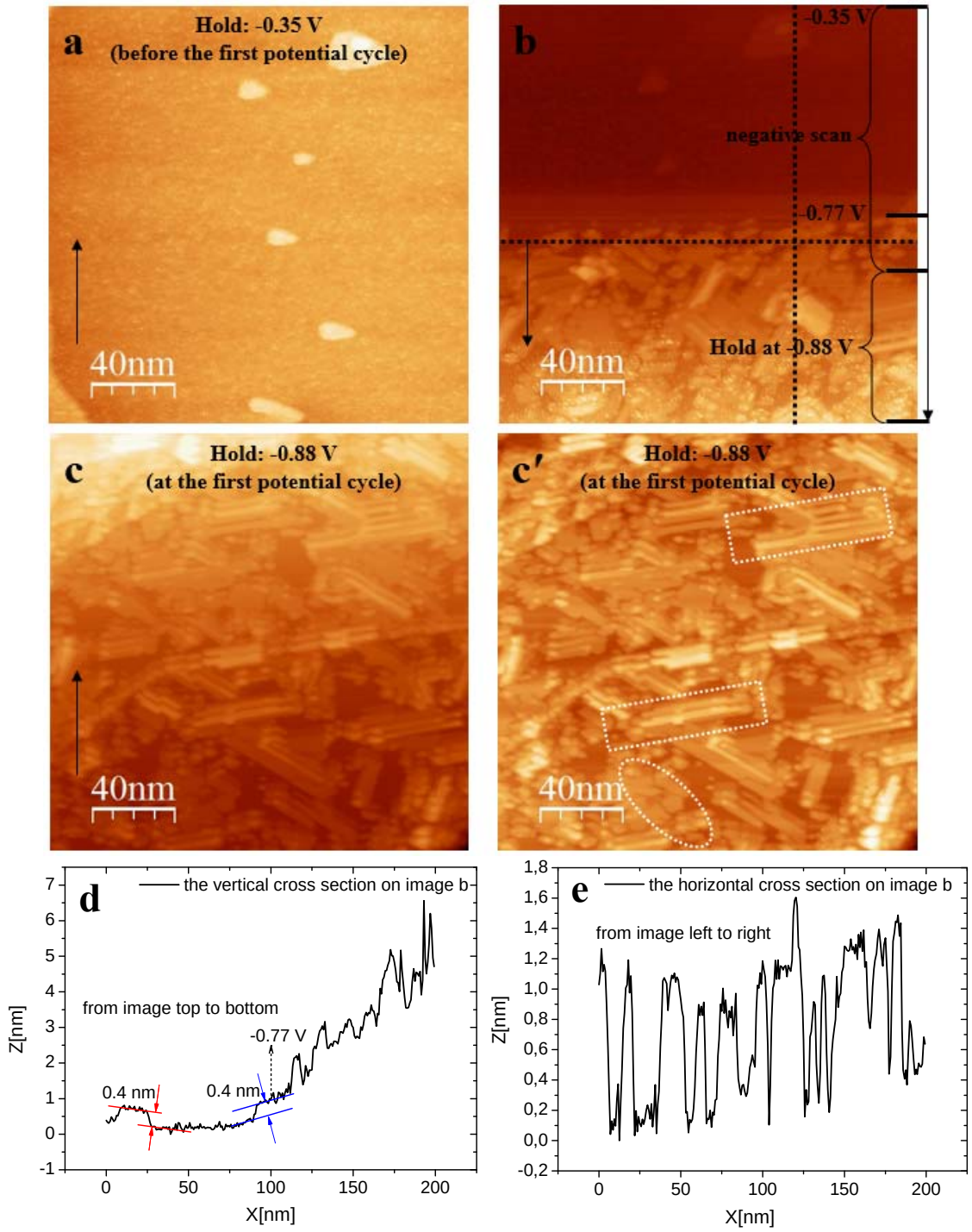

Fig. 7.8 STM images of Sb overpotential deposition on Au(111) at the first potential cycle in 0.25 mM Sb_2O_3 + 0.5 M H_2SO_4 electrolyte. (a) Initial Au(111) surface at the potential of -0.35 V, (b) the electrode potential was scanned negatively from -0.35 to -0.88 V and then stopped at -0.88 V, (c) and (c′) the electrode potential was held at -0.88 V, (d) the cross section on the image b (black vertical dot line), (e) the cross section on the image b (black horizontal dot line). Sample bias of 50 mV, set point = 0.5 nA & scan rate of 3.04 ln/s. Integral gain: 6 and proportional gain: 8. Arrows indicate scan direction. Plane correction is used for images a, b and c. Line by line correction is used

for image c′.

Fig. 7.9a shows the Au(111) surface after stripping of Sb at -0.21 V in the first potential cycle. It shows that the tiny particles with an approximialy 0.25 nm height appeared on the entire surface, which resulted in a slightly rough surface and would induce the structure change of the Sb deposits. As seen in Fig. 7.10, which shows the adlayer structures of Sb deposited on Au(111) at -0.88 V during potential holds within subsequent potential cycles, with the increase the cycle number, the change of Sb adlayer structure from the double row (see. Fig. 7.8c′ and Fig. 7.10a) to particle-like (see. Fig. 7.10b and c) structure was observed. However, some deposited Sb with the double row structure could still be found (see. Fig. 7.10d). Fig. 7.9b and c shows the Au(111) surface after stripping of Sb at positive potential in the continuous potential cycles. By comparison, it is clear that surface roughness increased with the increase of the potential cycles, or rather cycle numbers of continuous deposition and dissolution of antimony, which is an indication of $AuSb_2$ alloy formation [3, 25, 26]. As shown in Fig. 7.9d, the Au(111) surface is full of the species with a height of 0.3~0.6 nm after the third potential cycle. Therefore, it is obvious that the Sb adlayer structure depends on the roughness of the substrate surface as shown in Fig. 7.10. The result is quite consistent with the CV results.

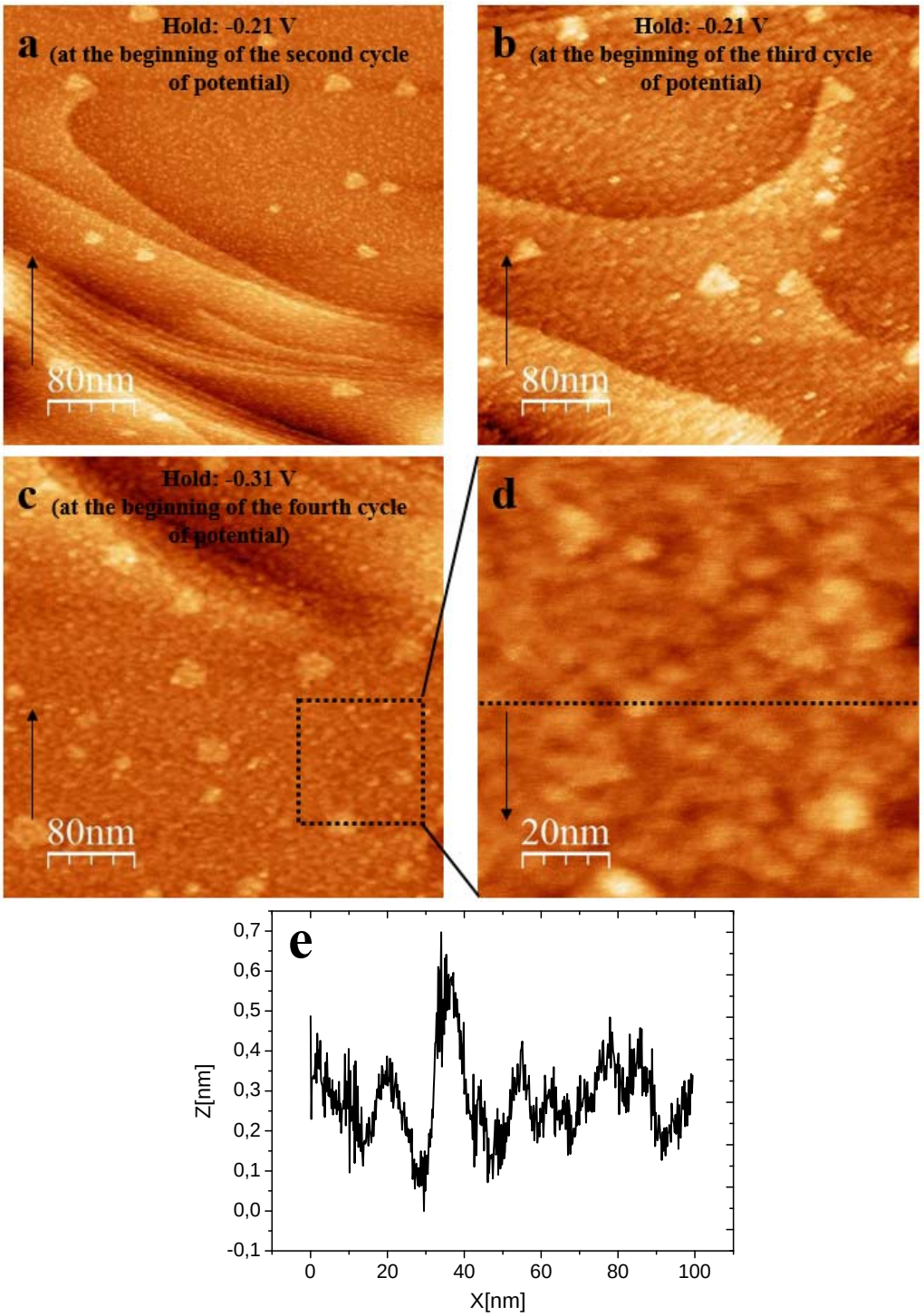

Fig. 7.9 STM images of Au(111) surface after Sb stripping in 0.25 mM Sb_2O_3 + 0.5 M H_2SO_4 electrolyte. (a) the potential was held at -0.21 V after the first potential cycle, (b) the potential was held at -0.21 V after the second potential cycle, (c) the potential was held at -0.31 V after the third potential cycle, (d) the zoomed in image on the image c (black box) and (e) the cross section on the image d (black dot line). Sample bias of 50 mV, set point = 0.5 nA & scan rate of 3.04 ln/s. Integral gain: 6 and proportional gain: 8. Arrows indicate scan direction. Line by line correction is used for above images.

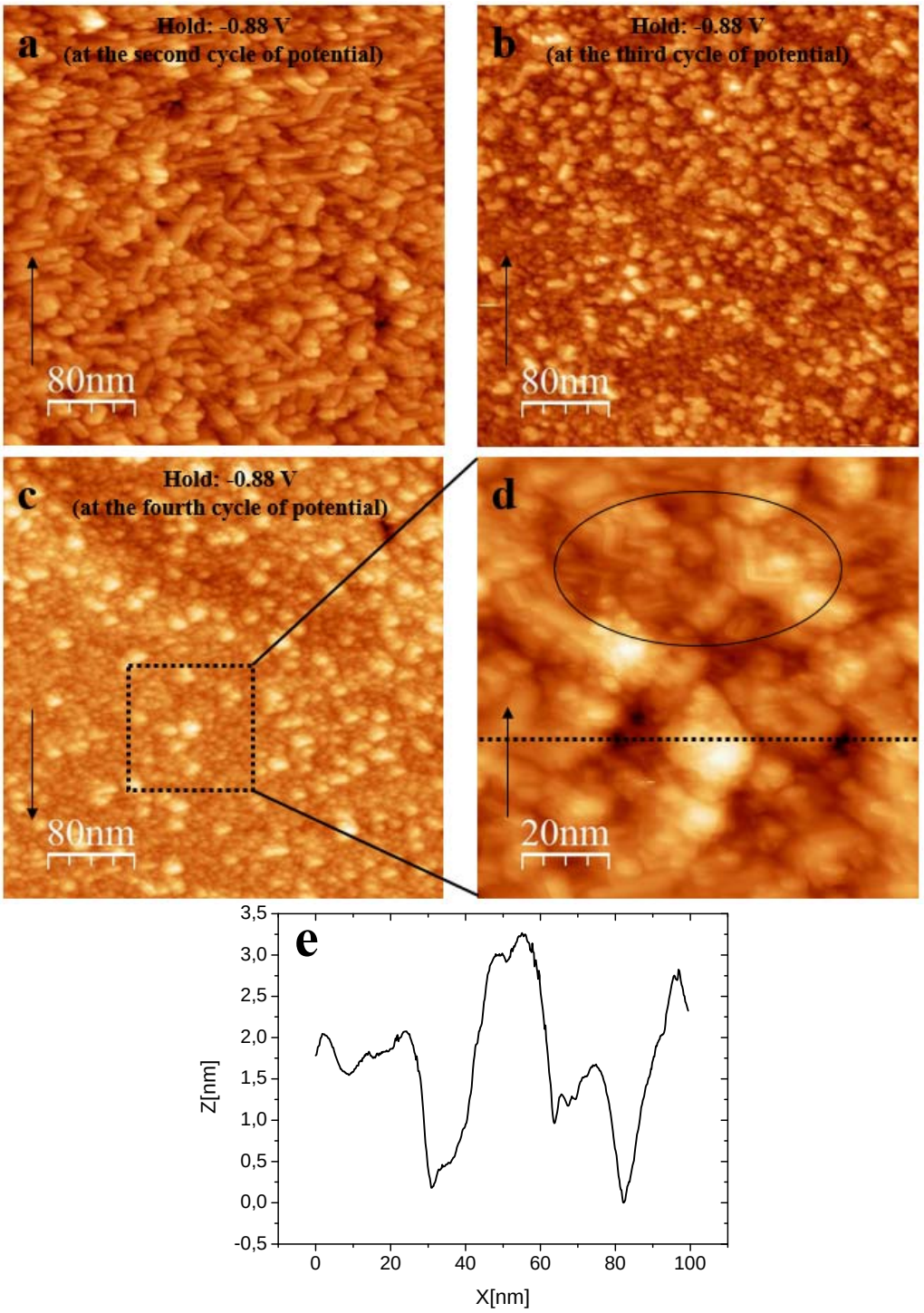

Fig. 7.10 STM images of Sb overpotential deposition on Au(111) in 0.25 mM Sb_2O_3 + 0.5 M H_2SO_4 electrolyte. (a) the potential was held at -0.88 V at the second potential cycle, (b) the potential was held at -0.88 V at the third potential cycle, (c) the potential was held at -0.88 V at the fourth potential cycle, (d) the zoomed in image on the image c (black box) and (e) the cross section on the image c (black dot line). Sample bias of 50 mV, set point = 0.5 nA & scan rate of 3.04 ln/s. Integral gain: 6 and proportional gain: 8. Arrows indicate scan direction. Line by line correction is used for above images.

7.3.3 Insertion of Mg into Sb modified Au electrode

One of the main targets to develop Mg batteries is the selection of anode material. Insertion materials such as Sb, Sn and Bi have been suggested to be the advanced electrode materials for Mg batteries [13, 15]. However, they just tested the performance of the cell, which employed these materials as the anode. The detailed mechanism of insertion and the diffusion coefficient were not investigated.

7.3.3.1 Preparation of Sb modified Au electrode

The cyclic voltammogram of electrochemical deposition of bulk Sb at polycrystalline Au electrode is shown in Fig. 7.11. It is similar to that observed at Au(111) electrode (see. Fig. 7.2) except for the much broader monolayer stripping peak. The detailed explanation about the voltammetric feature of Sb electrochemical deposition on Au electrode was discussed in the previous section. To form a thick layer of Sb deposited on Au electrode, the potential was held at 0 V vs. RHE for 10 min during the bulk deposition in the cathodic going sweep. The number of moles of Sb deposited at Au electrode was calculated to be ~70 nmol/cm^2 from the integrated charge density of 20.2 mC cm^{-2}. Afterwards, the Sb-modified Au electrode has been transferred to the glovebox under inert atmosphere where the electrochemical insertion of Mg from MACC electrolyte will be done.

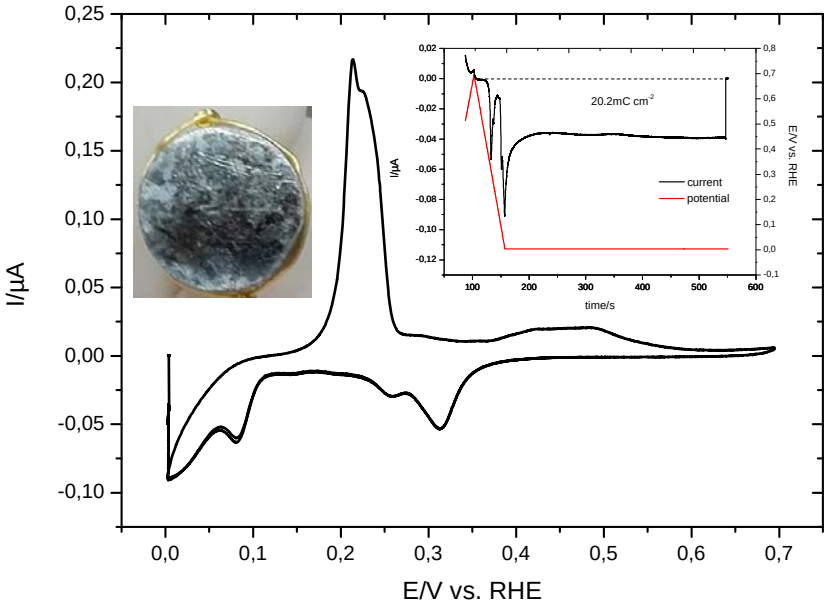

Fig. 7.11 Cyclic voltammograms of polycrystalline Au in 0.25 mM Sb_2O_3 + 0.5 M H_2SO_4 electrolyte at the sweep rate of 10 mV s^{-1}. Inset: current transition when the potential was held at 0 V and a photo of Au surface modified by large amount of Sb.

7.3.3.2 Mg insertion and deposition

Fig. 7.12 shows the comparison of electrochemical deposition and stripping behavior of Mg at bare gold electrode and at Sb-modified gold electrode in 0.5 M $MgCl_2$ + 0.5 M $AlCl_3$ in tetraglyme. At bare Au-electrode (see black curve), a slight increase in the current in the potential range of -0.25 V to -0.6 V (vs. Mg) was observed. It probably is due to the reduction of oxides or a blocking layer which inhibits nucleation of Mg. Then, an abrupt increase in the current at the potential below -0.6 V is observed due to bulk deposition of Mg. On the anodic going sweep, the current is still negative in the potential range of -1 to -0.25 V due to the continuous deposition of Mg. At E > equilibrium potential (-0.25V), Mg dissolution took place. However, at Sb-modified gold electrode (see red and blue curves), a pre-cathodic peak has been observed before the bulk deposition started. We attributed the pre-cathodic peak to the insertion of Mg into Sb-adlayers and formation of magnesiated binary phase of antimony (Mg_3Sb_2), where the onset potential is 320 mV lower than that of bulk deposition at bare Au electrode. The formation of magnesiated binary phases of Bi and Sn (Mg_3Bi_2 and Mg_2Sn respectively) have been suggested before [16] depending on the binary phase diagrams [27]. From the data of the heat of Mg_3Sb_2 alloy formation [28], the calculated potential for Mg-Sb alloy formation at room temperature is ~550 mV (vs. Mg) according to the following equations:

$$2Sb + 3Mg^{2+} + 6e^{-} \Rightarrow Mg_3Sb_2$$

$$\Delta^{o}_{f}H = -300193.56\,J/mol,$$

$$\Delta^{o}_{f}S = -52.50\,J/mol\cdot K$$

$$\Delta G = 315838.56\,J/mol$$

$$E = \Delta G \big/ zF = \frac{315838.56}{6\times 96485} = 0.54V vs. Mg$$

Therefore, the experimental positive shift in the overpotential of Mg deposition during the insertion of Mg into Sb adlayers is in agreement with the theoretical value. After the saturation of the host-layers, bulk deposition of Mg started with the corresponding decay in the cathodic current.

In the anodic going sweep, the bulk dissolution peak and the de-insertion peak overlap into a wide anodic peak (see. red curve). However, it becomes clear that the insertion and de-insertion occurr when the potential was reversed at -0.5 V, i.e. before the bulk deposition (see. blue curve). Mg de-insertion takes place at a higher overpotential

compared to that of bulk dissolution. A larger separation between the insertion and de-insertion peaks (ΔE) was found to be around 0.92 V, and it probably indicates that the electrochemical behavior is determined by the solid state diffusion step [29].

The amount of the deposited Sb and the inserted Mg in Sb (from the charge of the cathodic peak at ~-0.25 V) was calculated to be 70 and 107 nmol/cm^2 respectively according to the corresponding peak charge in the cyclic voltammograms (see. Fig. 7.11 and Fig. 7.12). By comparison, the ratio between the amount of the inserted Mg to the deposited Sb was found to be ~3:2 (Mg:Sb), which indicates the formation of Mg_3Sb_2 compound during the insertion process according to the structure module [30, 31] of Fig. 7.13.

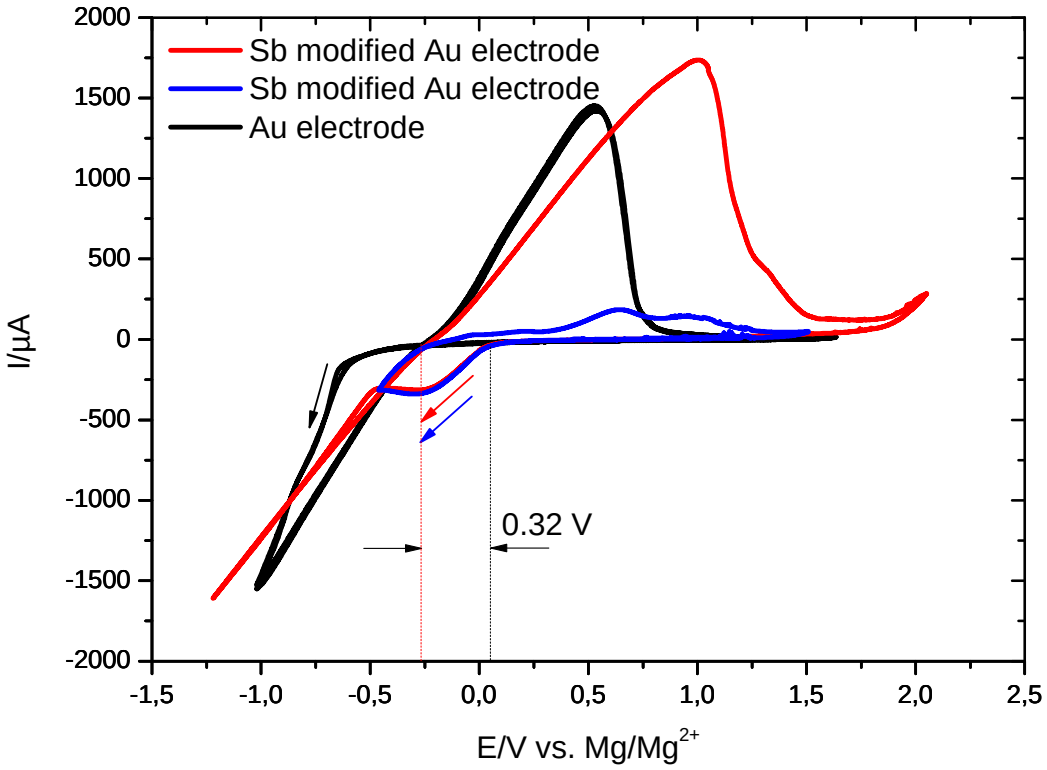

Fig. 7.12 Cyclic voltammograms of Mg deposition/dissolution at bare Au-electrode (black curve) and Sb modified Au-electrode (red and blue curves) in 0.5 M MACC/tetraglyme at the sweep rate of 17 mV s^{-1}. (Blue curve): Mg insertion/de-insertion at Sb modified electrode in the potential range of -0.5 V to 1.5 V.

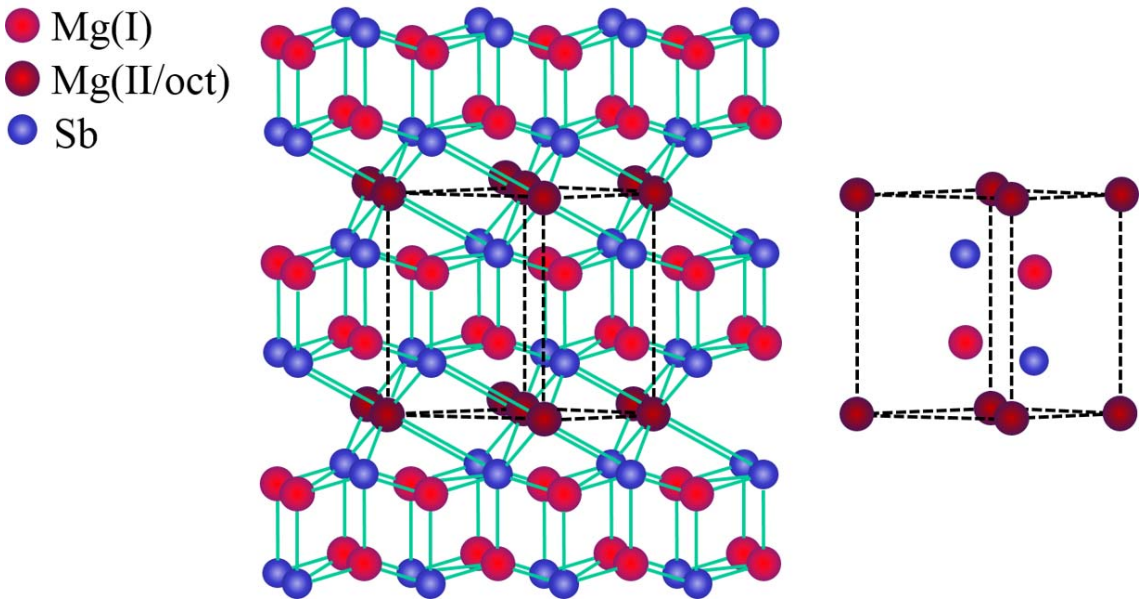

Fig. 7.13 module for the lattice structure of Mg_3Sb_2 alloy.

7.3.3.3 Determination of diffusion coefficient of Mg into Sb adlayers

One of the important evaluation parameters for fast charging and discharging metal ion battery is the diffusion coefficient of metal ions in the electrode material. For determining diffusion coefficient, the electrochemical methods such as Electrochemical Impedance Spectroscopy (EIS) [32, 33], Galvanostatic Intermittent Titration Technique [34-36] and Cyclic Voltammetry [37-39] are available. However, from cyclic voltammetry, we can easily calculate the diffusion coefficient from the change of peak current with varying sweep rates assuming simple solid state diffusion as rate limiting using the Randles-Sevcik equation (for semi-infinite diffusion) according to the following equation [29, 40]:

$$i_p = 2.69\times10^5\, n^{3/2} A D_{Mg^{2+}}^{1/2} C_0 \upsilon^{1/2}$$

where, i_p is the peak current in amps (A); n is the number of electrons transferred in the reaction ($2e^-$ for Mg^{2+}); A is the apparent surface area of the working electrode (0.785 cm^2); D_{Mg} is the diffusion coefficient of Mg ($cm^2\ s^{-1}$); υ is the sweep rate ($V\ s^{-1}$); C_0 is the concentration of Mg (theoretically, 0.038 mol cm^{-3} since the density of Mg_3Sb_2 alloy is 4.02 g/cm^3).

Due to the linear dependence of the peak current (I_p) on the √υ, the cyclic voltammograms peaks recorded at relatively high sweep rate have a semi-infinite diffusion properties [41]. So, under semi-infinite condition, the peak current is

proportional to the square root of sweep rate and the slope of this linear equation consist of a constant value and square root of the diffusion coefficient. Markovsky et al. showed a linear dependence of the CV peak currents (I_p) on the scan rate (υ) for a lithiation of a thin (10 µm) graphite electrode [42], whereas for diffusion controlled processes, I_p should depend linearly on $\sqrt{\upsilon}$.

Fig. 7.14 shows the cyclic voltammograms of Sb modified Au electrode (with the amount of ~315 nmol cm^{-2} Sb/Au) in MACC/tetraglyme at different sweep rates from 1 to 100 mV s^{-1} in the potential range of -0.3 to 1.2 V vs. Mg. The insertion and de-insertion peaks are gradually increased as the sweep rate get higher. Almost a linear relationship between the Mg insertion and de-insertion peaks current and square root of sweep rate was obtained and shown in the inset of Fig. 7.14. The slopes were calculated to be 1315 µA $V^{-1/2}$ $s^{1/2}$ and 850 µA $V^{-1/2}$ $s^{1/2}$, suggesting that the average value of diffusion coefficients is 3.37×10^{-15} cm^2 s^{-1} and 1.4×10^{-15} cm^2 s^{-1} for Mg insertion and de-insertion respectively, which is three order of magnitude lower than the value obtained for the diffusion of Li^+ ions in WO_3 [35, 40, 43] and $Li_{1-x}CoO_2$ [38, 44, 45] since the diffusion of Mg in solid host structures is more hindered than that of monovalent alkali cations such as Li^+ and Na^+ [46]. However, the diffusion coefficient of Mg in in antimony is one order of magnitude lower than the value obtained from CVs for Li^+ ions in $LiFePO_4$ [29].

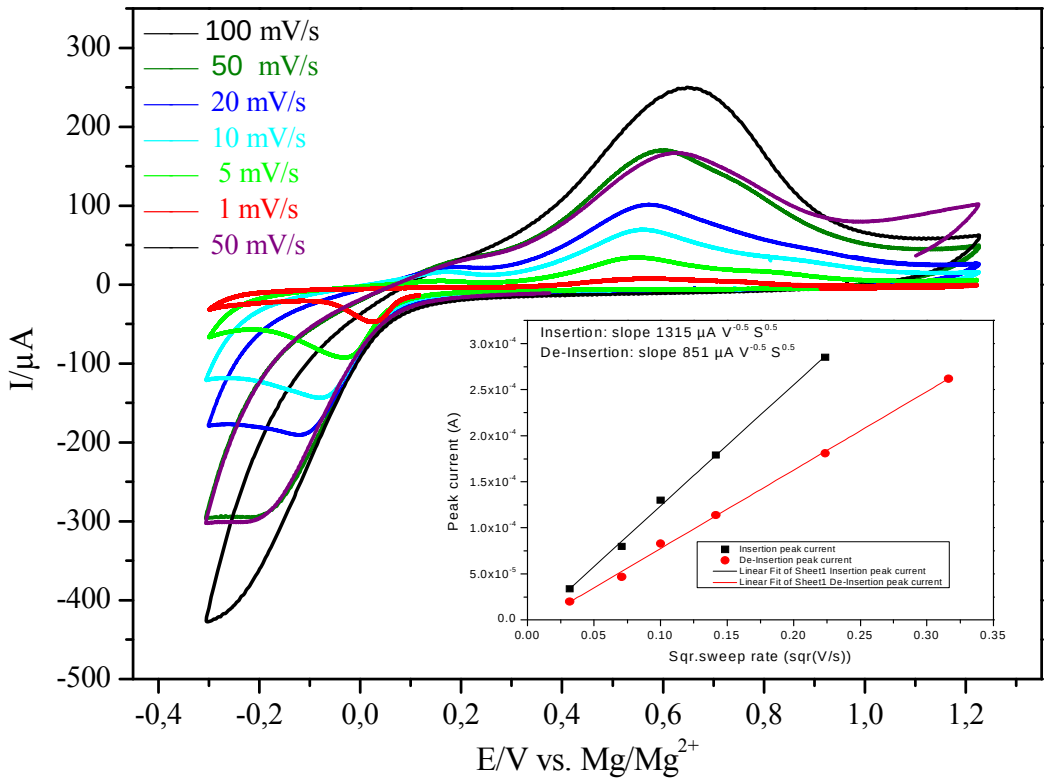

Fig. 7.14 Cyclic voltammograms of Mg insertion into Sb modified Au electrode in 0.5 M MACC/tetraglyme at different sweep rates from 1 to 100 mV s^{-1}. Inset: Plot of i_p (peaks current) vs. $\upsilon^{1/2}$ (square root of scan rate). This work was done by Da and the results were presented in his Master thesis [47].

Table 1: Dependence of Mg insertion/de-insertion integrated charges on the potential sweep rate and the corresponding coulombic efficiencies.

υ (mV/s)	**Charge (µC) (cath.)**	**Charge (µC) (anod.)**	**Col. Eff. (%)**
100	1672	1542	92
50	2407	2183	91
20	3484	3032	87
10	4337	3971	91
5	5447	5000	92
1	9239	8430	91

The charge of magnesiation/demagnesiation of antimony have been integrated from the cyclic voltammograms at different potential sweep rate as shown in table 1. The amount of integrated charge increases with increasing the time of insertion as expected (decreasing the sweep rate). The ratio between the faradaic charge of anodic (de-insertion) and cathodic (insertion) gives the apparent coulombic efficiency. So, 90% of the deposited magnesium is dissolved in the subsequent anodic sweep independently of the sweep rate. As a control experiment, the CV at 50 mV/s has been recorded in the beginning and at the end of experiment. Fig. 7.14 shows no change in the insertion/deinsertion profile and of course no deactivation of the electrode surface. The residual cathodic charge (10%) may be results from parasitic reactions [48] such as hydrogen evolution or reduction of organic solvent.

7.4 Conclusions

The electrochemical deposition of antimony on Au(111) was investigated in 0.5 M H_2SO_4 containing 0.25 mM Sb_2O_3 by cyclic voltammetry and electrochemical scanning

tunneling microscopy (EC-STM). Two peaks were observed in the UPD region, one at 0.26 V due to the reduction of the irreversibly adsorbed oxygenous Sb(III) species and the other one at 0.24 V due to the reduction of oxygenous Sb(III) species from bulk electrolyte. The coverage of Sb monolayer was calculated to be 0.44 whereas the irreversible adsorption accounted for 0.30.

By observation with STM, Sb nucleation prefers to start at the active sites on the terrace, and then epitaxial 2D growth to form the double row structure with the width of ~2.4 or ~3.2 nm, the height of 0.35 nm. The angle between two different oriented domains is around 120°, which suggests that they are probably aligned along the (111) plane. Some vacancies appeared between two parallel rows. The corrected distances between two Sb neighboring atoms were calculated be 1.076 nm and 0.821 nm, respectively. The coverage of Sb UPD adlayer obtained from STM result is in a good agreement with the CV result. The Volmer-Weber growth was observed during the bulk deposition. Furthermore, the bulk adlayer structure is depending on the roughness of the surface, which increased with the continuous deposition and dissolution of antimony in this case. Therefore, a structure change of the bulk adlayer from the double row to particle-like structure was observed during the continuous potential cycles.

Magnesium deposition/dissolution on Au and Sb modified Au electrodes were investigated in 0.5 M $MgCl_2$ + 0.5 M $AlCl_3$ in tetraglyme electrolyte. Interestingly, at the Sb modified Au electrode, a pre-cathodic peak started at around 0 V (vs. Mg/Mg^{2+}), where is 320 mV more positive than the onset potential of bulk deposition at Au electrode. It was suggested that this pre-cathodic peak is related to the insertion of Mg into Sb adlayers to form Mg_3Sb_2 alloy by the ratio of the amount of the inserted Mg to that of the deposited Sb calculated from the corresponding peak charge close to the theoretical value of 3:2 for Mg_3Sb_2 formation. High coulombic efficiencies of Mg stripping/insertion have been observed. Furthermore, the diffusion coefficient of Mg into Sb multilayers was estimated to be 4.7×10^{-14} cm^2 s^{-1}, which is two order of magnitude lower than the value for Li^+ ions [35, 38].

References

[1] G. Jung and C. K. Rhee, Journal of Electroanalytical Chemistry 436:277 (1997).
[2] M. Hara, J. Inukai, S. Yoshimoto, and K. Itaya, Journal of Physical Chemistry B 108:17441 (2004).
[3] J. W. Yan, Q. Wu, W. H. Shang, and B. W. Mao, Electrochemistry Communications 6:843 (2004).
[4] C. H. Jung and C. K. Rhee, Journal of Electroanalytical Chemistry 566:1 (2004).
[5] Q. Wu, W. H. Shang, J. W. Yan, and B. W. Mao, Journal of Molecular Catalysis a-Chemical 199:49 (2003).
[6] W. C. Butterman and J. J. F. Carlin, Mineral Commodity Profiles: Antimony, Unites States Geological Survey, 2003.
[7] J. Y. Xu, D. Aili, Q. F. Li, C. Pan, E. Christensen, J. O. Jensen, W. Zhang, G. Y. Liu, X. D. Wang, and N. J. Bjerrum, Journal of Materials Chemistry A 1:9737 (2013).
[8] H. Ipser, H. Flandorfer, C. Luef, C. Schmetterer, and U. Saeed, Journal of Materials Science-Materials in Electronics 18:3 (2007).
[9] A. Bhardwaj, A. Rajput, A. K. Shukla, J. J. Pulikkotil, A. K. Srivastava, A. Dhar, G. Gupta, S. Auluck, D. K. Misra, and R. C. Budhani, Rsc Advances 3:8504 (2013).
[10] K. Jüttner, Electrochimica Acta 31:917 (1986).
[11] G. Kokkinidis, Journal of Electroanalytical Chemistry and Interfacial Electrochemistry 201:217 (1986).
[12] C. A. Jeffrey, D. A. Harrington, and S. Morin, Surface Science 512:L367 (2002).
[13] T. S. Arthur, N. Singh, and M. Matsui, Electrochemistry Communications 16:103 (2012).
[14] Y. W. Cheng, Y. Y. Shao, L. R. Parent, M. L. Sushko, G. S. Li, P. V. Sushko, N. D. Browning, C. M. Wang, and J. Liu, Advanced Materials 27:6598 (2015).
[15] M. S. Park, J. G. Kim, Y. J. Kim, N. S. Choi, and J. S. Kim, Israel Journal of Chemistry 55:570 (2015).
[16] N. Singh, T. S. Arthur, C. Ling, M. Matsui, and F. Mizuno, Chem. Commun. 49:149 (2013).
[17] Y. Shao, M. Gu, X. Li, Z. Nie, P. Zuo, G. Li, T. Liu, J. Xiao, Y. Cheng, C. Wang, J.-G. Zhang, and J. Liu, Nano Letters 14:255 (2014).
[18] R. A. DiLeo, Q. Zhang, A. C. Marschilok, K. J. Takeuchi, and E. S. Takeuchi, ECS Electrochemistry Letters 4:A10 (2015).
[19] O. I. Malyi, T. L. Tan, and S. Manzhos, J. Power Sources 233:341 (2013).
[20] F. Hernandez, J. Sanabria-Chinchilla, M. P. Soriaga, and H. Baltruschat, in Electrode Processes VII, Vol. 18 (V.I. Birss, M. Josowicz, D. Evans, and M. Osawa, eds.), Electrochemical Society Proceedings, Pennington, 2004, p. 15.
[21] E. Bunge, R. J. Nichols, B. Roelfs, H. Meyer, and H. Baumgartel, Langmuir 12:3060 (1996).
[22] S. Yasuda, R. Kumagai, K. Nakashima, and K. Murakoshi, Journal of Physical Chemistry Letters 6:3403 (2015).
[23] H. Angerstein-Kozlowska, B. E. Conway, A. Hamelin, and L. Stoicoviciu, Journal of Electroanalytical Chemistry 228:429 (1987).
[24] J. M. Feliu, A. Fernandez-Vega, A. Aldaz, and J. Clavilier, Journal of Electroanalytical Chemistry 256:149 (1988).
[25] B. Stegemann, T. M. Bernhardt, B. Kaiser, and K. Rademann, Surface Science 511:153 (2002).
[26] A. R. Graham and S. Kaiman, American Mineralogist 37:461 (1952).
[27] T. B. Massalski, H. Okamoto, P. R. Subramanian, and L. Kacprzak, Binary Alloy

Phase Diagrams, 2nd Edition, WILEY-VCH Verlag GmbH, Weinheim, 1991.
[28] A. A. Nayeb-Hashemi and J. B. Clark, Bulletin of Alloy Phase Diagrams 5:579 (1984).
[29] A. Kumar, R. Thomas, N. K. Karan, J. J. Saavedra-Arias, M. K. Singh, S. B.Majumder, M. S. Tomar, and R. S. Katiyar, Journal of Nanotechnology 2009:10 (2009).
[30] J.-i. Tani, M. Takahashi, and H. Kido, Physica B: Condensed Matter 405:4219 (2010).
[31] S. Gupta, A. K. Ganguli, and J. D. Corbett, Inorg. Chem. 45:8175 (2006).
[32] C. O. Avellaneda and L. O. S. Bulhoes, Solid State Ionics 165:59 (2003).
[33] J. Q. Wang and J. M. Bell, Solar Energy Materials and Solar Cells 58:411 (1999).
[34] F. S. Gittleson, R. C. Sekol, G. Doubek, M. Linardi, and A. D. Taylor, Physical Chemistry Chemical Physics 16:3230 (2014).
[35] M. S. Mattsson, Solid State Ionics 131:261 (2000).
[36] J. X. Wang, X. H. Li, Z. X. Wang, H. J. Guo, B. Huang, Z. G. Wang, and G. C. Yan, Journal of Solid State Electrochemistry 19:153 (2015).
[37] S. Prato, L. Floreano, D. Cvetko, V. De Renzi, A. Morgante, S. Modesti, F. Biscarini, R. Zamboni, and C. Taliani, Journal of Physical Chemistry B 103:7788 (1999).
[38] M. D. Levi, G. Salitra, B. Markovsky, H. Teller, D. Aurbach, U. Heider, and L. Heider, Journal of the Electrochemical Society 146:1279 (1999).
[39] G. O. Kim, J. E. Hong, and K. S. Ryu, Materials Research Innovations 19:244 (2015).
[40] M. Deepa, T. K. Saxena, D. P. Singh, K. N. Sood, and S. A. Agnihotry, Electrochimica Acta 51:1974 (2006).
[41] M. D. Levi and D. Aurbach, Journal of Electroanalytical Chemistry 421:79 (1997).
[42] B. Markovsky, M. D. Levi, and D. Aurbach, Electrochimica Acta 43:2287 (1998).
[43] G. Leftheriotis, S. Papaefthimiou, and P. Yianoulis, Solid State Ionics 178:259 (2007).
[44] Y. I. Jang, B. J. Neudecker, and N. J. Dudney, Electrochemical and Solid State Letters 4:A74 (2001).
[45] H. Xia, L. Lu, and G. Ceder, Journal of Power Sources 159:1422 (2006).
[46] G. G. Amatucci, F. Badway, A. Singhal, B. Beaudoin, G. Skandan, T. Bowmer, I. Plitza, N. Pereira, T. Chapman, and R. Jaworski, Journal of the Electrochemical Society 148:A940 (2001).
[47] X. Da, in Mathematisch-Naturwissenschaftlichen Fakultät, Vol. Master, Rheinischen Friedrich-Wilhelms-Universität Bonn, Bonn, 2016, p. 97.
[48] F. M. Michalak and J. R. Owen, Solid State Ionics 86-88:965 (1996).

Chapter 8: Investigation of magnesium deposition and dissolution on Au electrode

One of the important issues in magnesium battery is to achieve high reversibility of magnesium deposition and dissolution. Therefore, in this chapter I focus on the electrochemical behaviour of Mg deposition and dissolution at Au electrode in Grignard-based and magnesium aluminum chloride complex (MACC)/tetraglyme electrolytes and the morphology observation of Mg deposited on Au(111) surface.

8.1 Introduction:

Rechargeable batteries have attracted much attention as essential energy storage devices, which are widely used for portable electronic devices and hybrid electric vehicles. Magnesium secondary batteries have been regarded as a viable 'environmental friendly, non-toxic, high safety, two-electron charge' alternative compared to the immensely popular Li-ion batteries owing to its high volumetric capacity of 3832 mAh/mL [1]. One of the main targets in the development of Mg-ion batteries is the achievement of high reversibility of Mg deposition and dissolution in a suitable electrolyte (a large electrochemical window, high conductivity and compatible with a Mg anode) without any decomposition [2].

In past few years, in order to rapidly develop the magnesium battery, some fundamental researches have been launched based on understanding the deposition mechanism of magnesium, the property of deposits, the performance of electrolytes, etc. The electrochemical behavior of Mg deposition/stripping at Au-electrode in the relevant electrolytes has been studied by different electrochemical techniques such as cyclic voltammetry (CV) [3, 4], electrochemical impedance spectroscopy (EIS) [5], electrochemical quartz crystal microbalance (EQCM) [6-8], X-ray photoelectron spectroscopy (XPS) [9], et al. For the study on the morphology of deposited Mg, to my knowledge, most of the studies have been done by scanning electron microscope (SEM) [10-12], yet, only one has been done by scanning tunneling microscope (STM) [13].

In previous studies, the reversibility of magnesium deposition (so called coulombic efficiency) has become a focal topic [14-16]. As we know, magnesium has some limitations that it is not stable in water and protic solvents and the solubility of its salts is very poor in anhydrous solvent. In addition, some external factors, such as solvent

[17, 18], salt [18, 19], electrode [5, 20, 21], electrolytic conditioning [12, 20], etc. are influence the reversibility of magnesium deposition/dissolution. Grignard reagents based electrolytes were firstly considered to be a suitable electrolyte [22], which supports magnesium deposition/dissolution. Further studies revealed that the high reversibility of magnesium deposition can be obtained from the Grignard/THF electrolyte [21, 23]. Benmayza et al. demonstrated that the complex magnesium organohaloaluminate electrolytes (C_2H_5MgCl-$((C_2H_5)_2AlCl)_2$/THF) supported nearly 100% coulombic efficiency of Mg deposition/dissolution on Pt electrode [4]. Lv et al. found that in $Mg(AlCl_2EtBu)_2$/THF electrolyte Ni electrode also allowed high reversibility of magnesium deposition/dissolution [3]. Yagi et al. suggested that water has to be eliminated in Grignard reagent-based electrolytes because it can immediately cause the decomposition of Grignard reagents leading to low coulombic efficiency of Mg deposition/dissolution [24]. Afterwards, Barile et al. pointed out that the coulombic efficiency is also dependent on the cycle number and co-deposition of Mg and Al was determined by energy-dispersive X-ray spectroscopy (EDS) in Mg organohaloaluminate/THF electrolyte systems, which have been considered not suitable for magnesium-ion batteries because of the instabilities of coulombic efficiency and electrolyte (THF decomposed into GBL) and irreversibility of the Mg deposition/dissolution process [15].

Magnesium chloride based electrolytes were also explored to achieve the reversible magnesium deposition and dissolution. Liao et al. reported that high magnesium deposition reversibility of 99% can be achieved in Lewis acid free $Mg(HMDS)_2$-$MgCl_2$/THF (HMDS = hexamethyldisilazide) electrolyte via an increase in the ratio of $MgCl_2$, which can combine with $Mg(HMDS)_2$-$MgCl_2$ to form $[(HMDS)MgCl_2]^-[Mg_2Cl_3]^-$, a stable and active species [25]. Another Lewis acid free electrolyte system consisted of only (DTBP)MgCl/THF or (DTBP)MgCl–$MgCl_2$/THF (DTBP = 2,6-di-tert-butylphenolate) for reversible magnesium deposition was reported by Pan et al. [26]. Kim et al. reported that the coulombic efficiency in HMDSMgCl-$AlCl_3$/THF electrolyte increased with the crystallization of the electrolyte, which was clarified as the result of the reaction between HMDSMgCl and $AlCl_3$ to form $[Mg_2(\mu\text{-}Cl)_3 \cdot 6THF][HMDSAlCl_3]$ with a crystal structure [27]. A similar study has also been done by Cheng et al. [28]. Inorganic salts based electrolytes, such as, $MgCl_2$-$AlCl_3$ (MACC) [29-31], $MgCl_2$-BCl_3, $MgCl_2$-$InCl_3$, $MgCl_2$-$SnCl_2$ [18] in THF/DME were also

found to support magnesium deposition and dissolution. Moreover, it was also found that the reversibility of Mg deposition/dissolution largely depends on the cycle number [32] and electrolyte conditioning [12, 18]. However, the irreversible process, co-deposition and instability of electrolyte were also observed. In our group, we ascertained that water could be reduced to hydrogen during the deposition process and the electrolyte was decomposed to ethylene during the dissolution process in MACC/tetraglyme electrolyte, resulting in the imprecise estimates for reversibility from the charge ratio. Recently, a novel MaCC electrolyte system which can achieve 100% reversibility of Mg deposition/dissolution at the first cycle without any electrolytic conditioning was explored [33].

$Mg(BH_4)_2$ [9, 34], another inorganic magnesium salt was also proposed for using in Mg battery. The reversibility of magnesium deposition/dissolution on Pt electrode can be enhanced by adding $LiBH_4$ as an additive into magnesium containing ether solvents (such as, THF, DME, diglyme and tetraglyme) electrolyte [10, 17, 35]. A handful of studies also suggested that the electrolytes based on Magnesium(II) Bis(trifluoromethane sulfonyl) Imide ($Mg(TFSI)_2$) [36, 37] and Magneisum Dialkoxides [19, 38] may be promising. Actually, we did not observe Mg deposition and dissolution from $Mg(TFSI)_2$ based electrolyte.

However, the processes of magnesium deposition and dissolution are still poorly understood and the instabilities of electrolyte and reversibility of magnesium deposition are still present in all these electrolytes. Moreover, almost all these electrolytes are not stable, air/moisture sensitive and also suffering from water.

In this work, we investigated the electrochemical behaviour of Mg deposition and dissolution at Au electrode in Grignard-based ($Mg(AlCl_2EtBu)_2$/tetraglyme) and magnesium aluminum chloride complex (MACC)/tetraglyme electrolytes by cyclic voltammetry and the morphology of the deposited Mg on Au(111) surface in MACC/tetraglyme electrolyte by EC-STM. The reversibility of magnesium deposition/dissolution increased with the cycle number in both electrolytes. The reversibility were calculated to be around 51% and 84% for $Mg(AlCl_2EtBu)_2$/tetraglyme and MACC/tetraglyme, respectively. However, once these electrolytes were exposed to air, the gel formation started immediately and deposition was unavailable, indicating

that these electrolytes are very sensitive to air/moisture. The structure and morphology of Mg bulk adlayers on Au(111) surface were observed to have a large particle-like multi-ball structure. After dissolution, some residues were observed, suggesting that it is not completely reversible. In addition, a completely irreversible surface process was observed in the presence of air and the products ($MgO/MgO_2/Mg(OH)_2$) morphology was characterized.

8.2 Experimental:

Magnesium electrochemical deposition measurements

Extra dry tetraglyme(G4) (99%, over 0.3 nm molecular sieve, Acros organics), $MgCl_2$ (98%, anhydrous, Sigma), and $AlCl_3$ (99%, anhydrous, Fluka) were used for preparing the 0.5 M MACC electrolyte (0.5 M $MgCl_2$ + 0.5 M $AlCl_3$ in G4). $Mg(AlCl_2EtBu)_2$ was synthesized from $MgBu_2$ (1 M in heptane, Aldrich) and $AlCl_2Et$ (1 M in hexane, Aldrich) according to the literature [3] and then dissolved in tetraglyme for preparing the 0.1 M $Mg(AlCl_2EtBu)_2$/G4 electrolyte. All the electrolytes were prepared in a MBraun glove box (H_2O < 0.5 ppm, O_2 < 0.5 ppm) and the water content has been determined by Karl Fischer titration (~320 ppm). All the electrochemical measurements have been done by a bi-potentiostat purchased from Pine Instruments Inc. model AFBPC1 in combination with LabVIEW software (National Instruments GmbH, Munich, Germany) for recording cyclic voltammograms (CV) in a three-electrode STM/AFM cell in the argon-filled MBraun glove box at the room temperature. A polycrystalline Au electrode (Mateck, Germany) with the diameter of 10 mm and thickness of 3 mm was employed as the working electrode. Au and Pt wires were used as the counter and reference electrodes, respectively. All the relevant material (counter and reference electrodes, STM cell and a glass pipette for transferring electrolyte, etc.) were kept in 5 M KOH bath for over night to remove organic solvents, washed and put into boiling 0.1 M H_2SO_4 and water for 5 min in turn to remove the residues salts, and then dried them in an oven at the temperature below 80 °C before each use.

EC-STM measurements

The Au(111) single crystals electrode (10 mm diameter and 3 mm thickness, Mateck, Germany) was employed for STM measurements. A gold wire was attached to its rear for handling. First, the Au(111) electrode was cleaned in 0.1 M H_2SO_4, which was prepared with Milli-Q water (18.2 MΩ cm, TOC of 5 ppm) and deaerated by purging

ultra-high pure argon (99.999%, Air Liquide). Then, it was prepared by cooling down after annealing for ~5 min in ultra-high pure argon atmosphere as described elsewhere [39].

All EC-STM measurements were performed with a Nanoscope III E controller (Digital Instruments, Santa Barbara, CA) connected with a separated potentiostat and a commercially available STM scanner (Molecular Imaging/Agilent Technologies) fitted with a homemade electrochemical cell so called AFM/STM cell as described before. Similarly, Pt and Au wires were used as the quasi reference and counter electrodes, respectively. The Pt/Ir (90:10) STM tips with a diameter of 0.25 cm were prepared by etching in a 2 M KOH + 4 M KSCN bath and coated with hot-melt glue to minimize faradaic current. The electrolytes were transferred by a well-sealed syringe and injected into the STM cell, which was placed in a glass chamber filled with argon and a continuous purge.

8.3 Results and discussion

8.3.1 Electrochemical deposition of Mg at Au in 0.1 M $Mg(AlCl_2EtBu)_2$/G4 electrolyte

The cyclic voltammograms of Mg deposition and dissolution at Au electrode recorded in 0.1 M $Mg(AlCl_2EtBu)_2$/G4 electrolyte are shown in Fig. 8.1. It shows that the electrochemical behavior of Mg deposition and dissolution is not stable at the initial several or even dozen cycles (see. Fig. 8.1a). Specifically, the initial potential of the Mg deposition increased from -2.89 V to -2.69 V with the increase of the cycle number and then became constant (see. Fig. 8.1b), meaning 200 mV positive shift; this is in good consistence with the value in the literature [3]. Furthermore, the charge transferred increased with the increase of the cycle number. It was found that the increase of charge is coincident with the increase in the surface roughness during cycling [6]. As a result, the coulombic efficiency (or reversibility) of Mg deposition/dissolution was improved from 10% at the first cycle to over 48% after around ten cycles (see. inset of Fig. 8.1a), and then increased slowly to 51% at the sixteenth cycle(see. Fig. 8.1b), but still below 100%, which probably can be achieved after several dozens or even hundred cycles. The increase in the coulombic efficiency with the cycle number was also available in the literature [15]. The lower coulombic efficiency implied that some irreversible electrochemical processes took place during the cycles, especially during initial cycles [15]. Recently, Yagi et al. [24] investigated the influence of water content on the

electrochemical deposition/dissolution of Mg in a Grignard reagent-based electrolyte and suggested that higher water content will cause the higher overpotential and lower coulombic efficiency of Mg deposition/dissolution because water may coordinate with Mg^{2+} ions and retard the formation of $[Mg_2(\mu\text{-}Cl_3)\cdot 6THF]^+$, which was considered as an electroactive species for Mg deposition [27, 40]. Of course, the co-deposition and electrolyte decomposition should be also taken into account. Moreover, we also observed that the electrochemical behavior of Mg deposition and dissolution was varied with cycle in MACC electrolyte, which was also observed by Shterenberg and Barile [12, 32]. A detailed description and explanation of Mg deposition and dissolution in MACC electrolyte will be presented later.

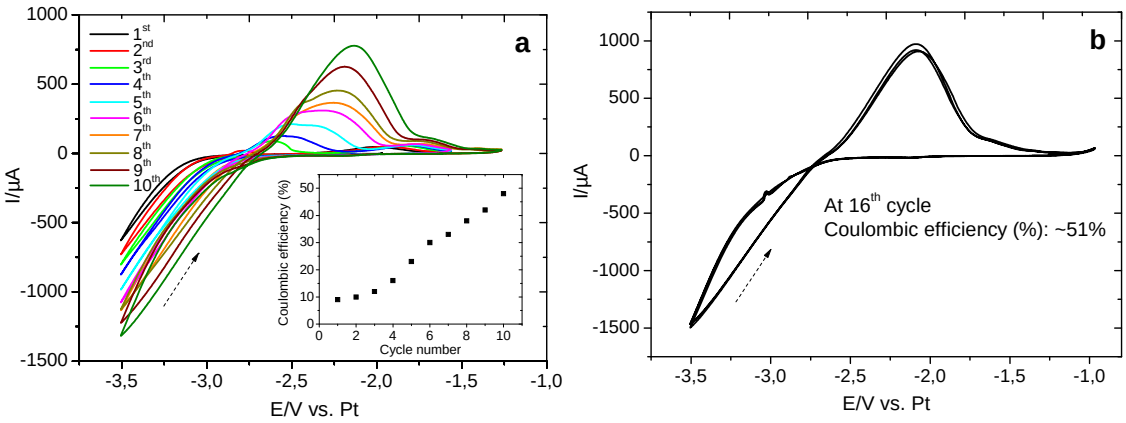

Fig. 8.1 Cyclic voltammograms of Mg deposition and dissolution at Au electrode in 0.1 M $Mg(AlCl_2EtBu)_2$/G4 electrolyte at 100 mV s^{-1} in the STM cell in the glove box. (a) The first 10 cycles, (b) after 10 cycles. Inset: Plots of the coulombic efficiencies as a function of cycle numbers. Arrow: scan direction.

Fig. 8.2b shows the current-time transient curve obtained at the potential of ~-3.4 V during Mg deposition and the corresponding cyclic voltammogram (see. Fig. 8.2a) recorded continuously after the CVs in Fig. 8.1 in 0.1 M $Mg(AlCl_2EtBu)_2$/G4 electrolyte at 100 mV s^{-1} in the STM cell in the glove box. Interestingly, the current increased with time when the potential was held at -3.4 V. Nevertheless, after dissolution the coulombic efficiency was calculated to be 45%, which is slightly less compared to 51% obtained at the sixteen cycle (see. Fig. 8.1b). This is not clear for us, whether these changes in the current and coulombic efficiency are due to the change in the interface property or electrolyte components, or some side reactions, etc. Certainly, this process is very complicated, so, more investigations are needed into its causes.

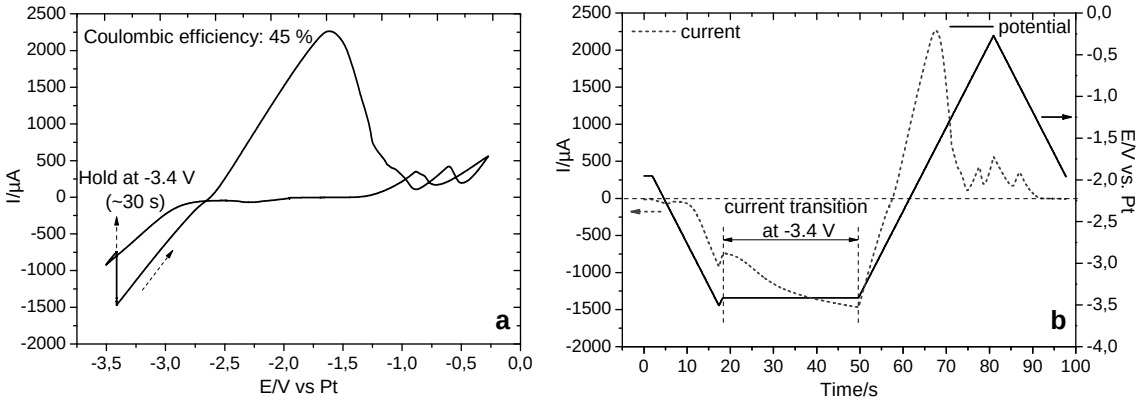

Fig. 8.2 Cyclic voltammogram of Mg deposition and dissolution at Au electrode in 0.1 M $Mg(AlCl_2EtBu)_2$/G4 electrolyte at 100 mV s^{-1} in the STM cell in the glove box (a) and the corresponding plots of current-time transient curve at -3.4 V (short dash curve) and the potential vs. time (black solid curve) (b).

However, once a small amount of air was introduced into experimental setup, the cyclic voltammogram would be distorted seriously and the gel-like film would be formed widely as shown in Fig. 8.3. Furthermore, the coulombic efficiency of Mg deposition/dissolution became worse than that obtained under carefully controlled conditions. Obviously, this electrolyte is very sensitive to air or moisture, which may cause some specific adsorptions and side reactions during or even before Mg deposition.

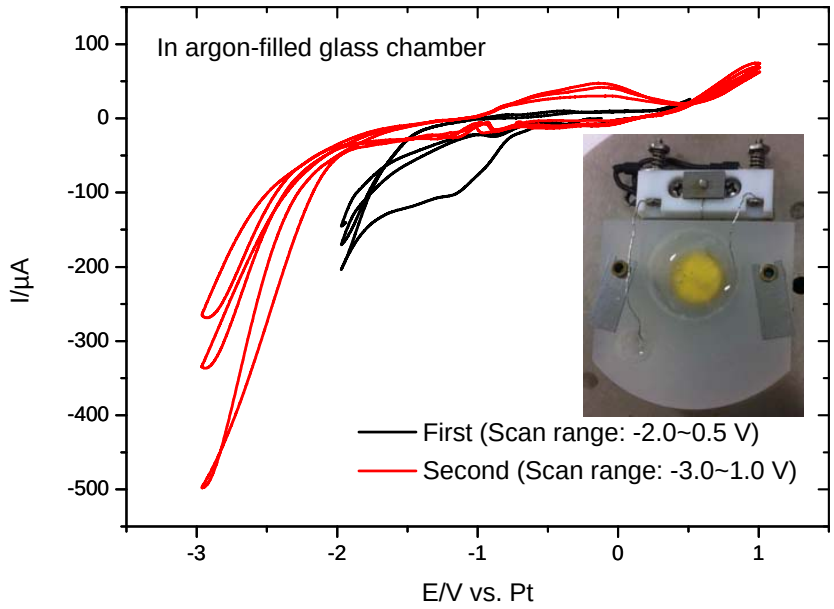

Fig. 8.3 Cyclic voltammograms of Au electrode in 0.1 M $Mg(AlCl_2EtBu)_2$/G4 electrolyte at 100 mV s^{-1} in the STM cell in an argon-filled glass chamber. Inset: The image of gel formation.

8.3.2 Electrochemical deposition of Mg at Au in MACC/G4 electrolyte

0.25 M $MgCl_2AlCl_3$/G4 electrolyte

The cyclic voltammograms of Mg deposition and dissolution at Au electrode in 0.25 M $MgCl_2AlCl_3$/G4 electrolyte were shown in Fig. 8.4. On the anodic going sweep at the initial cycles in the potential range of -2.0 to 0.2 V, the current started flowing at the electrode surface at -1.0 V, which is positive of the Mg deposition potential and probably is in the potential range of oxygen reduction [18]. With the further decrease of potential to -2.5 V, probably water reduction takes place, where the potential is slightly more positive than that of Mg deposition (confirmed by our DEMS measurement). The cathodic current in this potential range decreased along with the increase of cycle number because residual oxygen and water content were reduced by consumption. Mg deposition started at -2.8 V and its coulombic efficiency reached to 55% at the fifteenth cycle. As mentioned before, the side reactions (such as co-deposition, water reduction, etc.) may contribute only to the cathodic current, resulting in a lower coulombic efficiency. Nevertheless, it increased with the cycle number as shown below in 0.5 M $MgCl_2AlCl_3$/G4 electrolyte. This probably is owing to the contribution from side reaction becoming smaller and smaller, or simply, so called electrolytic conditioning in the literature [41].

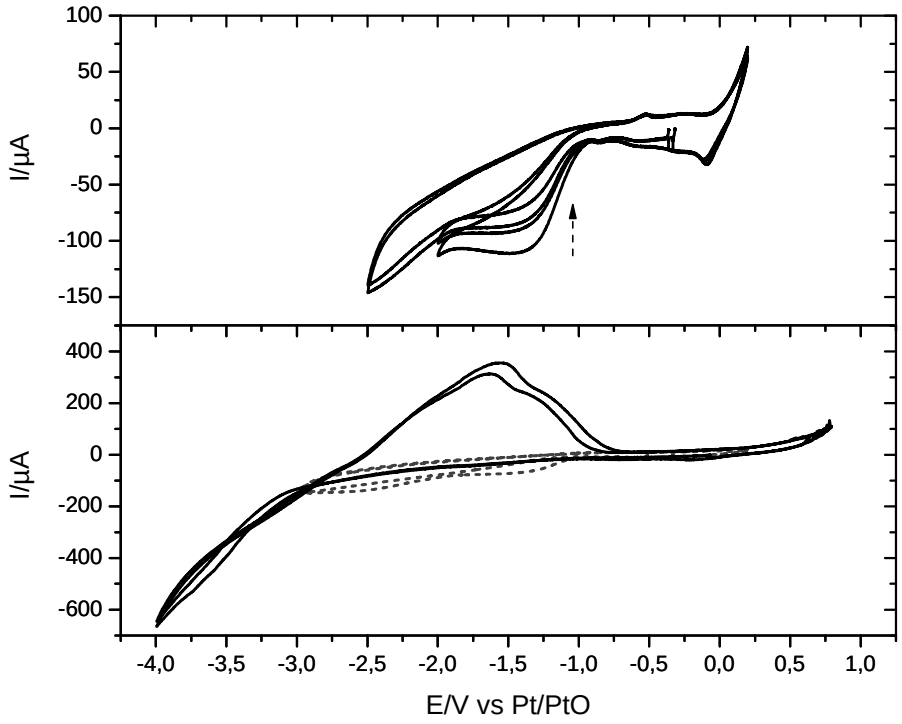

Fig. 8.4 Cyclic voltammograms of Au electrode in 0.25 M $MgCl_2AlCl_3$/G4 electrolyte at 100 mV s^{-1} in the STM cell in the glove box.

The current-time transient at the potential of ~-3.9 V for 30 s and the corresponding cyclic voltammogram recorded continuously in 0.25 M $MgCl_2AlCl_3$/G4 electrolyte (see. Fig. 8.5a) were shown in Fig. 8.5b. Once the potential was held at -3.9 V, the current initially decreased slightly, and then increased slightly again. The coulombic efficiency was found that it was decreased to 44% comparing to 55% obtained at the fifteenth cycle. It is similar to that observed in the case of 0.1 M $Mg(AlCl_2EtBu)_2$/G4 electrolyte.

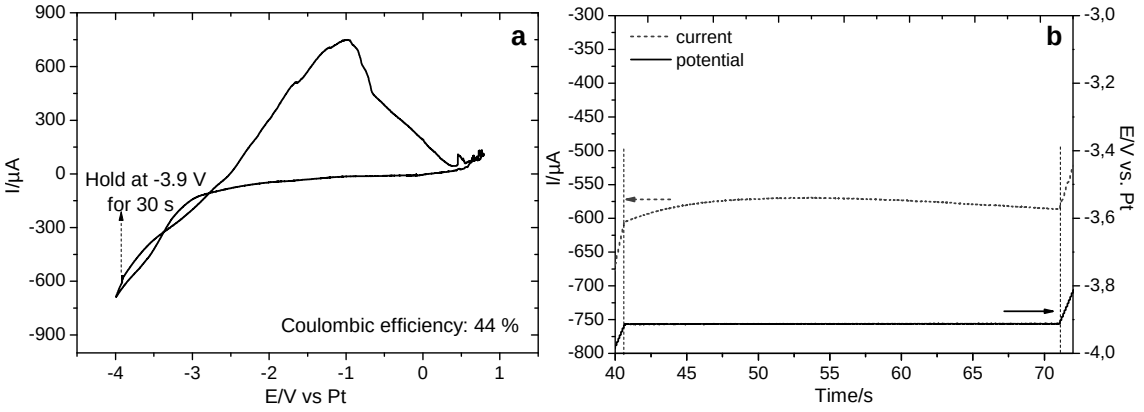

Fig. 8.5 Cyclic voltammogram of Mg deposition and dissolution at Au electrode in 0.25 M $MgCl_2AlCl_3$/G4 electrolyte at 100 mV s^{-1} in the STM cell in the glove box (a) and the corresponding plots of current-time transient curve at -3.9 V (short dash curve) and the potential vs. time (black solid curve) (b).

0.5 M $MgCl_2AlCl_3$/G4 electrolyte

Fig. 8.6 shows that the cyclic voltammograms of Mg deposition and stripping at Au electrode in 0.5 M $MgCl_2AlCl_3$/G4 electrolyte at 100 mV s^{-1}. A cycle number-dependent coulombic efficiency of Mg deposition/dissolution at the initial cycles was also performed. Specifically, the coulombic efficiency of Mg deposition increased from 4% to 12.1% in the initial 4 cycles. The increase of the coulombic efficiency with the increase of cycle number in MACC based electrolyte was also observed by Barile [12], who also found such low coulombic efficiency at the initial cycles in MACC/THF system and the irreversible deposition of Mg and Al taking place during early cycles. Furthermore, he even did not observe Mg deposition in both MACC/tetraglyme and MACC/triglyme systems since he thought that the formation of six-coordinate $Mg_2Cl_3^+$ species which are considered to be the active species for facilitating reversible Mg deposition are not entropically favorable in triglyme and tetraglyme based electrolyte [18]. To significantly improve the coulombic efficiency of Mg deposition/dissolution in this kind of electrolytes, the electrochemical conditioning process seems to be an effective and essential approach. But, this conditioning process is not fully understood

so far. Recently, Ha et al. suggested a novel approach to prepare the new named MaCC electrolyte by dissolution of magnesium metal in $AlCl_3$/THF electrolyte based on employing $CrCl_3$ as a "promoter", which exhibited 100% coulombic efficiency of Mg deposition and dissolution at the first cycle [33]. Esbenshade et al. suggested that giving a pause at open circuit potential (OCP) following Mg deposition will enhance the kinetics of Mg deposition and dissolution and improve the coulombic efficiency in both PhMgCl/$AlCl_3$ (APC) and EtMgCl electrolytes because an "enhancement layer" which consists of Mg and Cl was formed on the electrode and lends to more facile deposition and dissolution [42]. However, in Grignard based electrolyte, Yagi suggested that decreasing the water content can also improve the coulombic efficiency [24].

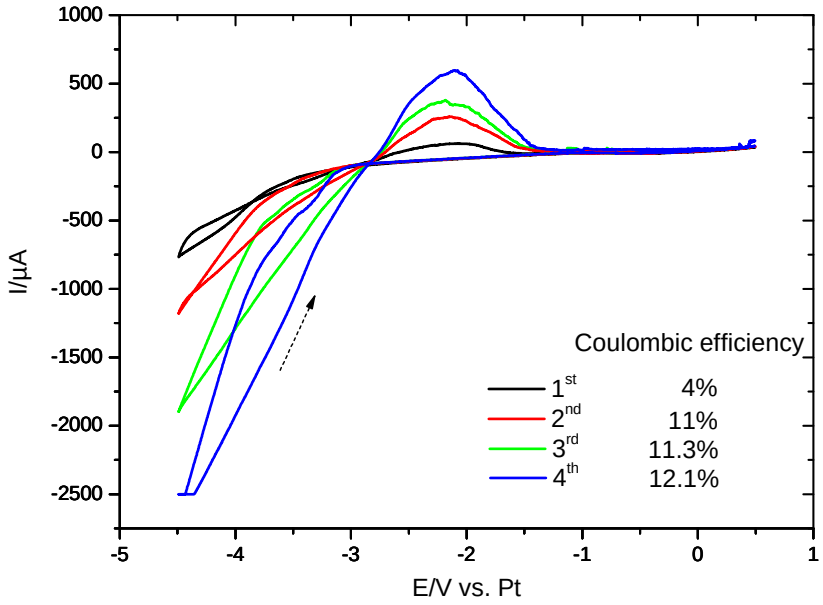

Fig. 8.6 Cyclic voltammograms of Mg deposition and dissolution at Au electrode in 0.5 M $MgCl_2AlCl_3$/G4 electrolyte at 100 mV s^{-1} in the STM cell in the glove box at the initial cycles. Inset: the coulombic efficiency at different cycles. Arrow: scan direction.

The cyclic voltammograms of Mg deposition and dissolution at Au electrode in 0.5 M $MgCl_2AlCl_3$/G4 electrolyte were recorded successively at the sweep rate from 100 mV s^{-1} to 50 mV s^{-1} to 10 mV s^{-1} and shown in Fig. 8.7. It exhibited that the cathodic current at -4 V slightly increased as the sweep rate decreased, whereas the anodic peak current decreased as the sweep rate decreased. It seems that the whole reaction process is dominated by sluggish kinetics rather than by mass transport, probably because some inert species with lower conductivity formed at electrode surface, such as oligomers, which was considered as an inhibitor for Mg deposition and dissolution in MACC/THF electrolyte [12, 18]. Furthermore, the coulombic efficiency was found to decrease with

the decrease of the sweep rate in this case.

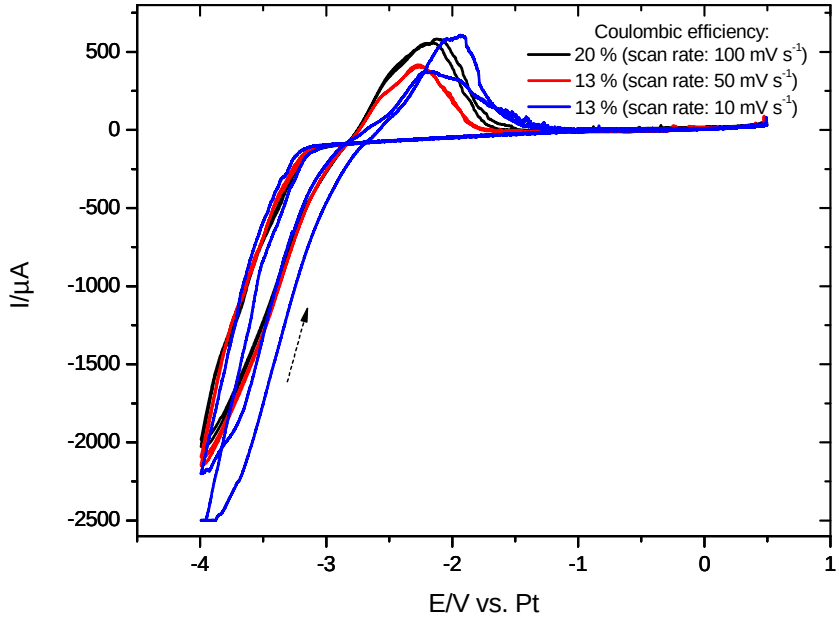

Fig. 8.7 Cyclic voltammograms of Mg deposition and dissolution at Au electrode in 0.5 M $MgCl_2AlCl_3$/G4 electrolyte at different sweep rates of 100, 50 and 10 mV s^{-1} in the STM cell in the glove box. Arrow: scan direction.

Fig. 8.8 shows the cyclic voltammograms of Mg deposition and dissolution at Au electrode recorded in 0.5 M $MgCl_2AlCl_3$/G4 electrolyte in the potential range from -4 V to three different upper limiting potentials of 0.5, 1.0 and 1.5 V. Once the upper limiting potential was increased to a more positive value, the electrolyte decomposition was observed and it started at ~0.7 V. However, it is worth to mention that ethylene formation (at ~-1 V vs. Pt) detected by DEMS in our group is much earlier than electrolyte decomposition. Moreover, the deposition current at -4 V increased slightly with cycle number whereas the dissolution peak current increased rapidly, resulting in that the coulombic efficiency also increased rapidly from 36% in the potential range of -4 to 0.5 V to reach a higher value of 84% in the potential range of -4 to 1.5 V. Probably, the potential-current curve in Mg deposition region is related to the resistance of the electrolyte. The results suggest that the appropriate increase in the upper limiting potential to the electrolyte decomposition region will improve the coulombic efficiency. It could be attributed to the depassivation process at the electrode surface or electrolytic conditioning process. As mentioned before, it is still a puzzle that the electrolytic conditioning can improve the reversibility of Mg deposition and dissolution. Nevertheless, recent discoveries suggest that the conditioning process in MACC/THF

electrolyte system promotes the formation of active Mg complex ($[Mg_2(\mu\text{-}Cl)_3 \cdot 6THF]^+$) for reversible Mg deposition/dissolution and creates free Cl^- anions, which are adsorbed at the electrode surface enhancing the Mg deposition [41]. However, no relevant reports come out for MACC/G4 electrolyte system.

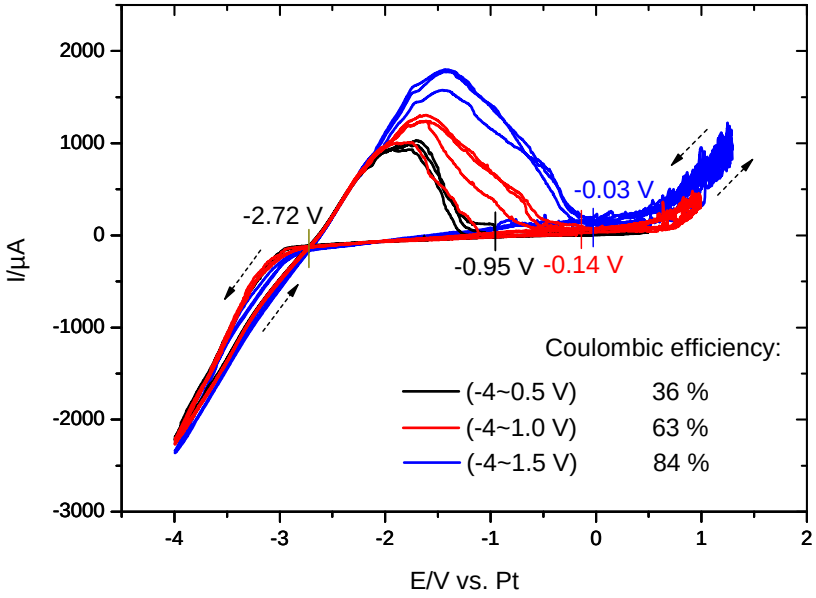

Fig. 8.8 Cyclic voltammograms of Mg deposition and dissolution at Au electrode in 0.5 M $MgCl_2AlCl_3$/G4 electrolyte at 100 mV s^{-1} in the STM cell in the glove box. Arrows: scan directions. The charges of Mg deposition (from -2.72 V at cathodic sweep to -2.72 V at anodic sweep) and dissolution (from -2.72 V to -0.95 V, -0.14 V and -0.03 V, respectively) were obtained after background subtraction.

8.3.3 STM investigation of Mg deposition at Au(111) in 0.5 M $MgCl_2AlCl_3$/G4 electrolyte

During the STM measurement, the cyclic voltammogram of Magnesium deposition and dissolution at Au(111) electrode in 0.5 M $MgCl_2AlCl_3$/G4 electrolyte was recorded in an argon-filled glass chamber (while continuously purging with a large amount of argon) is shown in Fig. 8.9. Slightly distorted CV observed in this case could be due to a small amount of air introduced into electrolyte during the transport from the glove box to the glass chamber. It was found that the water and oxygen reductions start at least 1 V earlier than Li deposition [43], so they could be also earlier than Mg deposition. However, it also seems to be common that the distorted CV appears at the initial cycles even in well-controlled experimental environment [12]. In order to avoid the effect of large faradic current flowing at electrode surface on the tunneling current and obtain a better stability of the tip, the potential was held at a suitable potential point (see. Fig.

8.9) before dissolution (nearly no faradic current flowing) starts for imaging the morphology of the deposits. In this CV, Mg deposition starts at ~-2.5 V. However, the peaks before -2.5 V are probably due to water and oxygen reduction.

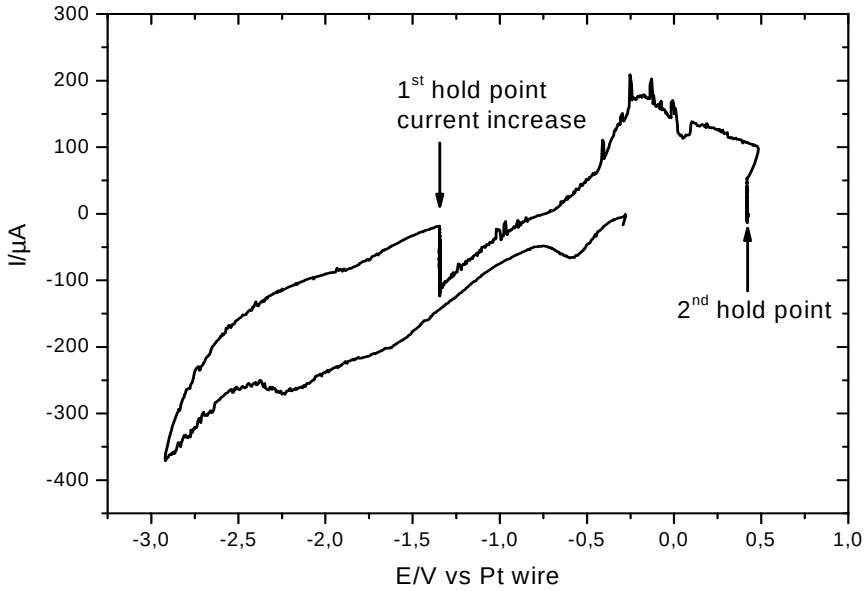

Fig. 8.9 Cyclic voltammogram of Mg deposition and dissolution at Au(111) electrode in 0.5 M $MgCl_2AlCl_3$/G4 electrolyte in the STM cell in an argon-filled glass chamber and with continuous purging a large amount of argon into during the STM measurement. Scan rate: 50 mV s^{-1}.

Mg deposition and dissolution processes at Au(111) surface in 0.5 M $MgCl_2AlCl_3$/G4 electrolyte are demonstrated in Fig. 8.10. A freshly prepared Au(111) surface with steps and terraces at the open circuit potential of -0.05 V is shown in Fig. 8.10a. As mentioned before, due to the instability of the tip when a large faradic current flows at the electrode surface, the tip was retracted during the potential cycling and approached to the surface at the potential of -1.35 V after deposition and before dissolution for probing the deposited Mg morphology. Fig. 8.10b, c and d show the surface morphology of the deposited Mg at the potential of -1.35 V. A huge amount of the particle-like Mg with a diameter of 20~100 nm and a height of ~3 nm and a few flaky structure Mg were observed on the Au(111) surface. Further deposition of magnesium on its larger particles prefers to start at the grain boundary as seen in Fig. 8.10d. Magnesium dissolution process was shown in Fig. 8.10e. When the potential was scanned positively, Mg dissolution started at ~ 0.3 V and almost completely dissolved at ~ 0 V. It shows that ~12 nm Mg was deposited on Au(111) surface as seen in Fig. 8.10e′. After dissolution Au(111) surface appeared again, but some residual particles with a

diameter of ~10 nm and a height of 1.0~1.6 nm and tiny particles remained on the terraces and at the steps (see. Fig. 8.10f and g). These particles are probably the irreversible deposited Al or Mg at initial cycles as mentioned before and in the literature [12] or some oxides.

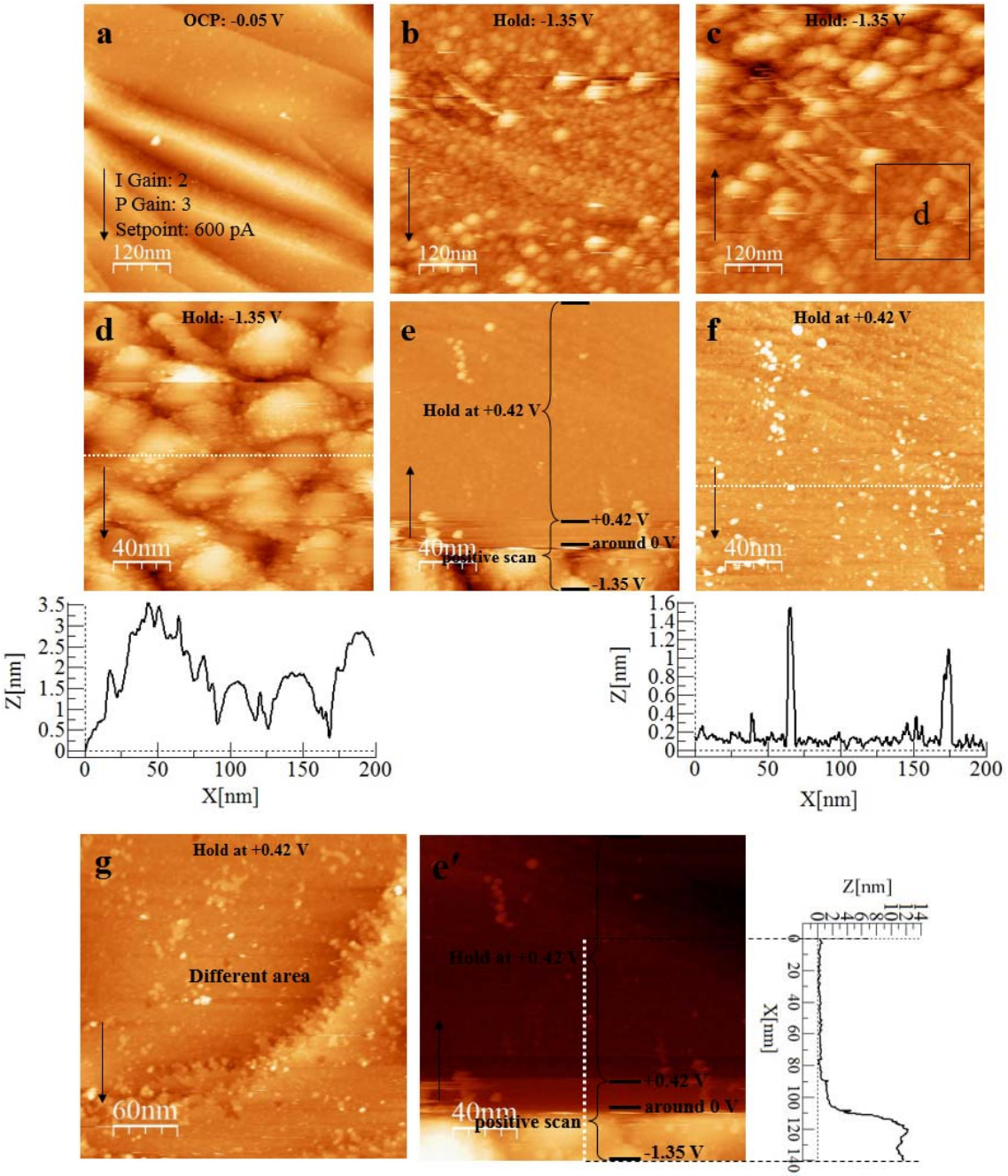

Fig. 8.10 STM images of Mg deposition/dissolution at Au(111) surface in 0.5 M $MgCl_2AlCl_3$/G4 electrolyte. (a) at open circuit potential of -0.05 V, (b) and (c) at -1.35 V at the anodic scan direction, (d) zoom-in area in black box in image c, (e and e′) potential scanning from -1.35 V to +0.42 V and then hold at +0.42 V, (f) at +0.42 V, (g) different area at +0.42 V. Sample bias of 50 mV, set point = 0.6 nA & scan rate of 5 Hz. The cross sections on images d, e′, and f (white dot line) are given near the images. Tip

potential = -0.23 V, set point = 0.5 nA & scan rate of 1.97 Hz. Integral gain: 2 and proportional gain: 3. Arrows indicate scan direction. Line by line correction is used for above image a, b, c, d, e, f and g. Plane correction is used for the image e′.

It is well known that the MACC/G4-based electrolyte is very sensitive to air (O_2 or H_2O or both). When a small amount of air was introduced into the electrolyte, a distorted CV and an irreversible surface process were observed. The cyclic voltammogram recorded for this case is shown in Fig. 8.11. It is similar to the CV which was recorded in O_2 saturated MACC/THF electrolyte and attributed to oxygen reduction reaction in place of Mg deposition/dissolution in the literature [18]. No bulk Mg dissolution peak was observed. However, gel formation at the liquid/gas phase interface was observed. It might be due to the introduced water, which probably facilitates the gel formation chemically, and the gel is probably consisting of $Mg(OH)_2$. A similar approach was adopted to probe the surface morphology of the deposits in this case. Fig. 8.12a shows the surface morphology of the deposits was probed at the potential of -1.35 V in anodic scan direction. A larger number of plate-like particles with smooth surface and an average width of ~16 nm, which is smaller than that of Mg particles observed before in a strictly controlled argon atmosphere system. However, once the potential was held at -0.05 V after the potential reversal at +0.5 V, the particle sizes became smaller than those observed under potential control of -1.35 V (see. the cross sections on Fig. 8.12a and Fig. 8.12b). It seems that the deposits were partially dissolved but some of them remained on the surface as seen in Fig. 8.12b and the inset of Fig. 8.11, which shows the photo of the electrode surface after this STM measurement. These deposits strongly adhered to the electrode surface and can not be removed electrochemically easily. The results suggest that once some impurities (such as oxygen, water, etc.) were introduced into electrolyte, the reversible deposition/dissolution processes would be seriously affected and some irreversible deposited products (such as oxides, hydroxides, etc.) would be formed on the electrode surface, leading to passivation layer formation or other issues.

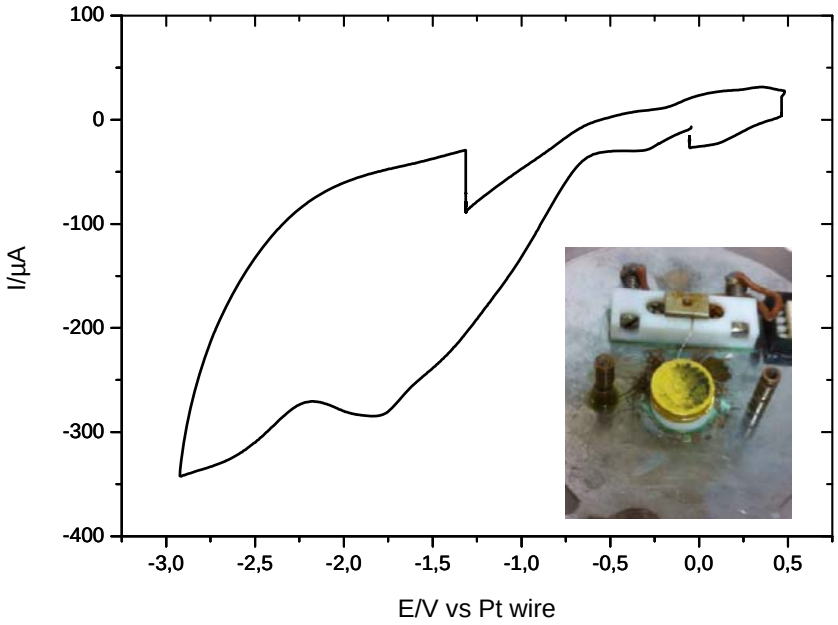

Fig. 8.11 Cyclic voltammogram of Au(111) electrode in 0.5 M $MgCl_2AlCl_3$/G4 electrolyte in the STM cell in an argon-filled glass chamber during the STM measurement. Scan rate: 50 mV s^{-1}. Inset: An actual photo of the electrode surface after this STM measurement.

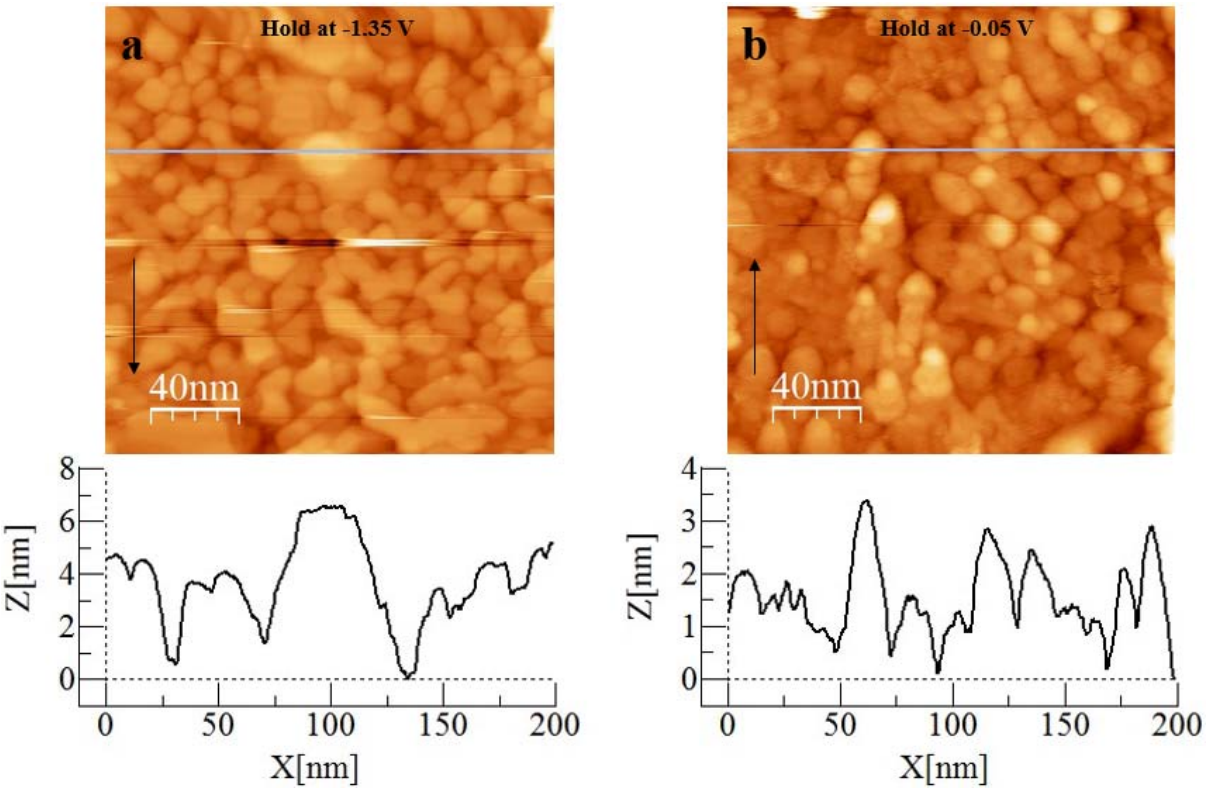

Fig. 8.12 STM images of Mg deposition/dissolution at Au(111) surface in 0.5 M $MgCl_2AlCl_3$/G4 electrolyte. (a) at -1.35 V at anodic scan direction, (b) at -0.05 V. Sample bias of 50 mV, set point = 0.6 nA & scan rate of 5 Hz. The cross sections are shown below the images. Tip potential = -0.23 V, set point = 0.5 nA & scan rate of 1.97

Hz. Integral gain: 2 and proportional gain: 3. Arrows indicate scan direction. Line by line correction is used for above images.

8.4 Conclusions

The electrochemical deposition/dissolution of magnesium at Au electrode was investigated in the Grignard-based tetraglyme electrolyte and magnesium aluminum chloride complex (MACC)/tetraglyme electrolytes by cyclic voltammetry and the morphologies of Mg and some irreversible deposited products formed on Au(111) in MACC/tetraglyme electrolyte in different conditions respectively were observed by EC-STM.

In 0.1 M $Mg(AlCl_2EtBu)_2$/tetraglyme electrolyte, Mg deposition and dissolution at Au electrode was achieved, but the electrochemical behavior is not stable and the coulombic efficiency (or reversibility) of Mg deposition/dissolution could be only increased to 51% with the increase of the cycle number. These are probably attributed to the side reactions such as water reduction, Al co-deposition and electrolyte decomposition, etc. Similar instabilities of electrochemical behavior and poor coulombic efficiency of Mg deposition and dissolution to that observed in $Mg(AlCl_2EtBu)_2$/tetraglyme electrolyte were also observed in MACC/tetraglyme electrolyte. However, we found that the coulombic efficiency can be improved significantly by increasing the upper limiting potential to the electrolyte decomposition region.

By the observation of STM in MACC/tetraglyme electrolyte, the particle-like deposits were observed on Au(111) electrode surface and almost all of these deposits could be dissolved reversibly in a strictly controlled argon atmosphere system. These deposits are probably Mg particles. However, it also exhibited that an irreversible deposition phenomenon when some impurities such as water, oxygen, etc. from air were introduced into electrolyte. This irreversible phenomenon could be due to the presence of these impurities, which could be reduced before or during Mg deposition to form the products (such as magnesium/aluminum oxide and hydroxide, etc.), which could not be oxidized at the positive potential. Furthermore, a small amount of air (probably, water) would lead to gel-like film formation in these two types of electrolytes.

References

[1] J. Muldoon, C. B. Bucur, and T. Gregory, Chemical Reviews 114:11683 (2014).
[2] D. Aurbach, Y. Gofer, A. Schechter, O. Chusid, H. Gizbar, Y. Cohen, M. Moshkovich, and R. Turgeman, Journal of Power Sources 97-8:269 (2001).
[3] D. P. Lv, T. Xu, P. Saha, M. K. Datta, M. L. Gordin, A. Manivannan, P. N. Kumta, and D. H. Wang, Journal of the Electrochemical Society 160:A351 (2013).
[4] A. Benmayza, M. Ramanathan, T. S. Arthur, M. Matsui, F. Mizuno, J. Guo, P.-A. Glans, and J. Prakash, Journal of Physical Chemistry C 117:26881 (2013).
[5] Z. Z. Feng, Y. Nuli, J. L. Wang, and J. Yang, Journal of the Electrochemical Society 153:C689 (2006).
[6] D. Aurbach, A. Schechter, M. Moshkovich, and Y. Cohen, Journal of the Electrochemical Society 148:A1004 (2001).
[7] D. Aurbach, Z. Lu, A. Schechter, Y. Gofer, H. Gizbar, R. Turgeman, Y. Cohen, M. Moshkovich, and E. Levi, Nature 407:724 (2000).
[8] D. Aurbach, M. Moshkovich, A. Schechter, and R. Turgeman, Electrochemical and Solid State Letters 3:31 (2000).
[9] J. Chang, R. T. Haasch, J. Kim, T. Spila, P. V. Braun, A. A. Gewirth, and R. G. Nuzzo, Acs Applied Materials & Interfaces 7:2494 (2015).
[10] F. Tuerxun, Y. Abulizi, Y. NuLi, S. Su, J. Yang, and J. Wang, Journal of Power Sources 276:255 (2015).
[11] I.-T. Kim, K. Yamabuki, M. Morita, H. Tsutsumi, and N. Yoshimoto, Journal of Power Sources 278:340 (2015).
[12] C. J. Barile, E. C. Barile, K. R. Zavadil, R. G. Nuzzo, and A. A. Gewirth, Journal of Physical Chemistry C 118:27623 (2014).
[13] D. Aurbach, Y. Cohen, and M. Moshkovich, Electrochemical and Solid State Letters 4:A113 (2001).
[14] Y. N. NuLi, J. Yang, and R. Wu, Electrochemistry Communications 7:1105 (2005).
[15] C. J. Barile, R. Spatney, K. R. Zavadil, and A. A. Gewirth, Journal of Physical Chemistry C 118:10694 (2014).
[16] P. Canepa, G. S. Gautam, R. Malik, S. Jayaraman, Z. Q. Rong, K. R. Zavadil, K. Persson, and G. Ceder, Chemistry of Materials 27:3317 (2015).
[17] Y. Shao, T. Liu, G. Li, M. Gu, Z. Nie, M. Engelhard, J. Xiao, D. Lv, C. Wang, J.-G. Zhang, and J. Liu, Scientific Reports 3 (2013).
[18] C. J. Barile, R. G. Nuzzo, and A. A. Gewirth, Journal of Physical Chemistry C 119:13524 (2015).
[19] C. Liao, B. Guo, D.-e. Jiang, R. Custelcean, S. M. Mahurin, X.-G. Sun, and S. Dai, Journal of Materials Chemistry A 2:581 (2014).
[20] S. Yagi, A. Tanaka, T. Ichitsubo, and E. Matsubara, Ecs Electrochemistry Letters 1:D11 (2012).
[21] C. Liebenow, Journal of Applied Electrochemistry 27:221 (1997).
[22] D. M. Overcash and F. C. Mathers, Trans. Electrochem. Soc. 64:305 (1933).
[23] J. D. Genders and D. Pletcher, Journal of Electroanalytical Chemistry 199:93 (1986).
[24] S. Yagi, A. Tanaka, Y. Ichikawa, T. Ichitsubo, and E. Matsubara, Research on Chemical Intermediates 40:3 (2014).
[25] C. Liao, N. Sa, B. Key, A. K. Burrell, L. Cheng, L. A. Curtiss, J. T. Vaughey, J.-J. Woo, L. Hu, B. Pan, and Z. Zhang, Journal of Materials Chemistry A 3:6082 (2015).
[26] B. Pan, J. Zhang, J. Huang, J. T. Vaughey, L. Zhang, S.-D. Han, A. K. Burrell, Z. Zhang, and C. Liao, Chemical Communications 51:6214 (2015).
[27] H. S. Kim, T. S. Arthur, G. D. Allred, J. Zajicek, J. G. Newman, A. E. Rodnyansky,

A. G. Oliver, W. C. Boggess, and J. Muldoon, Nature Communications 2:427 (2011).
[28] Y. W. Cheng, R. M. Stolley, K. S. Han, Y. Y. Shao, B. W. Arey, N. M. Washton, K. T. Mueller, M. L. Helm, V. L. Sprenkle, J. Liu, and G. S. Li, Physical Chemistry Chemical Physics 17:13307 (2015).
[29] R. Yasui, K. Asaka, K. Miyazaki, T. Fukutsuka, T. Abe, K. Nishio, and Y. Uchimoto, Meeting Abstracts MA2013-02:463 (2013).
[30] R. E. Doe, R. Han, J. Hwang, A. J. Gmitter, I. Shterenberg, H. D. Yoo, N. Pour, and D. Aurbach, Chemical Communications 50:243 (2014).
[31] T. Liu, Y. Shao, G. Li, M. Gu, J. Hu, S. Xu, Z. Nie, X. Chen, C. Wang, and J. Liu, Journal of Materials Chemistry A 2:3430 (2014).
[32] I. Shterenberg, M. Salama, Y. Gofer, E. Levi, and D. Aurbach, Mrs Bulletin 39:453 (2014).
[33] J. H. Ha, B. Adams, J.-H. Cho, V. Duffort, J. H. Kim, K. Y. Chung, B. W. Cho, L. F. Nazar, and S. H. Oh, Journal of Materials Chemistry A 4:7160 (2016).
[34] Y. Y. Shao, N. N. Rajput, J. Z. Hu, M. Hu, T. B. Liu, Z. H. Wei, M. Gu, X. C. Deng, S. C. Xu, K. S. Han, J. L. Wang, Z. M. Nie, G. S. Li, K. R. Zavadil, J. Xiao, C. M. Wang, W. A. Henderson, J. G. Zhang, Y. Wang, K. T. Mueller, K. Persson, and J. Liu, Nano Energy 12:750 (2015).
[35] R. Mohtadi, M. Matsui, T. S. Arthur, and S.-J. Hwang, Angewandte Chemie-International Edition 51:9780 (2012).
[36] Y. Orikasa, T. Masese, Y. Koyama, T. Mori, M. Hattori, K. Yamamoto, T. Okado, Z.-D. Huang, T. Minato, C. Tassel, J. Kim, Y. Kobayashi, T. Abe, H. Kageyama, and Y. Uchimoto, Scientific Reports 4:5622 (2014).
[37] S.-Y. Ha, Y.-W. Lee, S. W. Woo, B. Koo, J.-S. Kim, J. Cho, K. T. Lee, and N.-S. Choi, Acs Applied Materials & Interfaces 6:4063 (2014).
[38] J. T. Herb, C. Nist-Lund, J. Schwartz, and C. B. Arnold, ECS Electrochemistry Letters 4:A49 (2015).
[39] F. Hernandez, J. Sanabria-Chinchilla, M. P. Soriaga, and H. Baltruschat, in Electrode Processes VII, Vol. 18 (V.I. Birss, M. Josowicz, D. Evans, and M. Osawa, eds.), Electrochemical Society Proceedings, Pennington, 2004, p. 15.
[40] J. Muldoon, C. B. Bucur, A. G. Oliver, T. Sugimoto, M. Matsui, H. S. Kim, G. D. Allred, J. Zajicek, and Y. Kotani, Energy & Environmental Science 5:5941 (2012).
[41] K. A. See, K. W. Chapman, L. Zhu, K. M. Wiaderek, O. J. Borkiewicz, C. J. Barile, P. J. Chupas, and A. A. Gewirth, Journal of the American Chemical Society 138:328 (2016).
[42] J. L. Esbenshade, C. J. Barile, T. T. Fister, K. L. Bassett, P. Fenter, R. G. Nuzzo, and A. A. Gewirth, Journal of Physical Chemistry C 119:23366 (2015).
[43] D. Aurbach, M. Daroux, P. Faguy, and E. Yeager, Journal of Electroanalytical Chemistry and Interfacial Electrochemistry 297:225 (1991).

Summary

Metal air batteries are the energy storage devices, which possess the advantages of low cost, non-toxic, non-polluting, high theoretical specific energy, etc. Consequently, they received extensive attention and are considered as a special kind of fuel cell (FC) and one of the representatives of a new generation of the green secondary batteries. In this field, most of the works are focused on the study of oxygen reduction reaction and oxygen evolution reaction at the cathode and the selection and optimization of electrolyte composition. However, it is still far from satisfactory for commercialization, because the most efficient catalysts still consist of noble metals, such as platinum, gold, palladium, etc. and there are still many problems in nonaqueous electrolyte, such as the instability of the electrolytes, uncontrollable side reactions, poor reversibility of the ORR/OER, etc. Therefore, it is necessary and vital to make a further study and exploration to promote their development.

In aqueous electrolyte, Co_3O_4 nanoparticles modified Ag electrode was prepared as a bimetallic and bifunctional catalyst for oxygen reduction and evolution reactions in alkaline solution. By comparison with pure Ag and Co_3O_4 nanoparticles respectively, the Co_3O_4/Ag catalyst demonstrated a synergistic effect that the catalytic activity of Ag and Co_3O_4 for ORR and OER, respectively, is enhanced by each other. By the optimal experiments, it is also found that the 800 μg cm^{-2} Co_3O_4/Ag possesses the best catalytic activity and stability for both ORR and OER. The mechanisms of both reactions were examed by RRDE technique. The yield of peroxide species (H_2O_2) were found to be less than 2%, suggesting that this catalyst promoted the ORR via $4e^-$ transfer process, which is comparable to the commercial Pt/C catalyst. Moreover, only one Tafel slope of 60 mV dec^{-1} for OER was observed, suggesting that the mechanism of OER was not changed.

In addition, the Co/Ag bimetallic catalyst prepared by the electrochemical modification also showed the high catalytic activity and stability for both ORR and OER. The Co deposited on Ag electrode with a coverage of 0.7 showed the highest catalytic activity for both ORR and OER comparing to other coverages. In this case, the onset potential of ORR is 0.91 V vs. RHE more positive than pure silver and the ORR process follows the $4e^-$ pathway. And also the onset potential of OER is more negative than that observed on Co_3O_4 which is one of the most active catalysts for OER. Interestingly,

SEM results showed that these Co/Ag catalysts possess a flower-like structure. Furthermore, the growth mechanism of Co on Ag was investigated by EC-STM. All these results suggest that the Co/Ag bimetallic catalyst possesses a bifunctional catalytic activity and higher stability for both ORR and OER in alkaline electrolyte and it could be an excellent catalyst for ORR and OER in metal-air batteries.

In order to understand the effect of the solvents (acetonitrile, tetrahydrofuran, propylene carbonate and tetraglyme) which were used for batteries on the electrochemical reactions, the electrochemical deposition behavior of metals (Cu, Pb and Ag) on Au electrode in the electrolytes based on these solvents was examed. First, copper deposition on Au electrode in acetonitrile based electrolyte was carried out. A redox peak appeared at ~1.1 V (vs. Cu/Cu^{2+}) which probably is related to Cu^{2+}/Cu^{+} redox couple, two gentle peaks appeared in UPD region and the bulk deposition starts below 0 V. The UPD peaks are not as sharp as the peaks observed in aqueous solution, suggesting that the process of Cu deposition in this case is probably sluggish. Moreover, when the electrolyte was exposed to air, the characteristic polarization curve of copper deposition was distorted seriously or even disappeared. This probably is due to the effect of ORR taking place at more positive potential. Second, the lead deposition behavior was examed in tetrahydrofuran and its mixture with propylene carbonate or tetraglyme based electrolytes. The highly distorted polarization curve of Pb UPD was observed in tetrahydrofuran, which has a low dielectric constant and high donor number. However, by adding propylene carbonate into tetrahydrofuran based electrolyte, the UPD peaks would become sharper. This is probably due to the extensive ion pairing formation both at the interface and in the bulk electrolyte in the solvent with low dielectric constant. Furthermore, the unfeatured polarization curves of Pb deposition was observed when these electrolytes were exposed to air. Third, Ag deposition was carried out in acetonitrile, tetraglyme and tetrahydrofuran based electrolyte, respectively. Similar results were found that the highly distorted polarization curve of Ag deposition was observed in the solvent, which possesses low dielectric constant and high donor number. However, the difference is that the stable polarization curve of Ag deposition can be obtained as well in the case of exposing the electrolyte to air. Based on this point, an in situ STM observation of Ag deposition process on Au(111) was performed. It is observed that the first Ag layer was formed with some pre-adsorbed or co-adsorbed species in the UPD region. Furthermore, a layer by layer growth up to only

two monolayers and then starting 3D growth was observed.

ORR and OER were also investigated in nonaqueous electrolyte. The mechanism of these reactions and the morphology of their products on Au and Pt electrodes in Li or Mg-DMSO based electrolyte were studied by cycle voltammetry technique including RRDE and EC-SPM technique, respectively.

For ORR and OER on Pt(pc) electrode in Mg^{2+}-containing DMSO electrolyte with water content of 55 ppm, the results showed that ORR is via a total two electron transfer to form peroxide species. Part of the ORR products was detected at ring electrode at the potential of +0.3 V. However, the collection efficiency was not constant when the rotation rate was varied and it increased with the increase in rotation rate. The maximum relative amount of detected product was 51%. Furthermore, the deactivation of electrode was observed during ORR. It is probably due to the formation of some insoluble products at the electrode. This deactivation layer may effect on the migration of charge or the charged species. A Tafel slope of 123 mV dec^{-1} was obtained for ORR, indicating that the first electron transfer could be the rate determining step. The effect of water on ORR in this electrolyte was also investigated. The results showed that water has a large effect on the diffusion limiting current, collection efficency, and it may promote the electrolyte decompsotion. Specifically, the limiting current initially increased and then decreased but finally increased with the increase of the amount of water. The collection efficency decreased with the increase of the amount of water. The increase in Tafel slope was also observed, suggesting that the mechanism of ORR might be changed by adding a certain amount of water in this electrolyte. Unfortunately, no OER was observed in all cases.

The morphology of ORR products on Au(111) and Pt(111) was observed by EC-STM. On Au(111) electrode, it seems that a thin film was formed on the electrode surface during ORR. This kind of film may consist of gold (gold dissolution and re-deposition was observed), ORR products, some species produced by electrolyte decomposition and solvent and it can be decomposed at the positive potenial into fragments, which would take part in the new film formation when the potential was scanned back to ORR region again. The similar phenomen was observed on Pt(111) electrode, but the difference is that the decomposition of this film was not clearly observed on Pt(111).

ORR and OER on Au electrode were also studied in Li^+-containing DMSO electrolyte. Two peaks were observed only in initial two cycles and then overlapped into one peak in ORR region. OER peak was also observed in this electrolyte. The charge densities of ORR peaks (2575 μC cm^{-2}) and OER peak (685 μC cm^{-2}) suggest that the reversibility of ORR/OER is around 26.6% and only two monolayers of Li_2O_2 are formed on the electrode surface (according to the charge density of OER peak). However, in air saturated electrolyte, two ORR peaks were also observed at the initial two cycles, but the peaks current were smaller and decreased rapidly compared to that in oxygen saturated electrolyte, probably because of the low oxygen concentration or other factors. Furthermore, the OER peak current decreased rapidly as well. The reversibility of ORR/OER was calculated to be around 10% according to their charge densities. By observation of AFM and STM, no trace of toroid-like Li_2O_2 was observed, but it seems that a thin film was formed on the electrode surface during ORR. In addition, Au dissolution and re-deposition probably were taken place in this potential range.

Insertion of Mg into Sb in 0.5 M $MgCl_2$ + 0.5 M $AlCl_3$ was studied in tetraglyme based electrolyte. It was found that the insertion of Mg into Sb starts 320 mV earlier than Mg deposition. The formed component was determined to be Mg_3Sb_2 according to the mole ratio of the Sb pre-deposited on Au electrode and the inserted Mg (~3:2). The diffusion coefficient of Mg in Sb layer was calculated to be 4.7×10^{-14} cm^2 s^{-1}, which is two orders of magnitude lower than the value for Li^+ ions. Furthermore, the electrochemical deposition behavior of Sb on Au(111) was studied by cyclic voltammetry and EC-STM. Two UPD peaks were observed at 0.26 V and 0.24 V, where are related to the reduction of the irreversible adsorbed oxygenous Sb(III) species and the reduction of the oxygenous Sb(III) species from bulk solution, respectively. The total charge of UPD peaks suggests that the coverage of the deposited Sb in UPD region is around 0.48 monolayer, whereas 66.7% are from the reduction of the irreversible adsorption species. The STM results showed that the initial deposition of Sb starts preferentially at the active sites on the terrace, and then epitaxial growth in two-dimensional to form some regularly ordered rectangular arrays with the widths of ~2.4 and ~3.2 nm, a height of 0.35 nm and an angle of ~120° two different oriented arrays which are probably aligned along the (111) plane. Meanwhile, some vacancies appeared between two parallel arrays. A local certain structure (0.48 ML) of Sb was observed. The coverage of Sb UPD adlayer obtained from STM results is in a good agreement with that from the CV

results. Three-dimensional growth started immediately at the overpotential. A double row structure was observed on the Sb bulk adlayers formed on the smooth Au(111) surface. However, this bulk adlayer structure is dependent on the roughness of the surface and it will tend to particle-like structure formation on the rough surface.

In Mg batteries, a lot of work was focused on the Mg deposition and dissolution in nonaqueous electrolyte. In this work, we are also focused on this topic. The results show that the Mg deposition and dissolution at Au electrode can be obtained successfully in a Grignard-based and magnesium aluminum chloride complex (MACC)/tetraglyme electrolytes. However, the electrochemical behavior of Mg deposition and dissolution is not stable and the Coulombic efficiency is very poor at initial cycles in both electrolytes. The increase of Coulombic efficiency with the cycle number was also observed and attributed to the electrolyte conditioning process, in which water reduction, Al co-deposition and electrolyte decomposition should also be taken into account. In addition, in MACC/tetraglyme the particle-like deposits on Au(111) surface was observed by EC-STM and these deposits could be dissolved almost completely under a strictly controlled argon atmosphere condition. These deposits are probably Mg particles. However, once a small amount of air was introduced into the electrolyte, the deposits can not be dissolved again. These deposits are probably magnesium/aluminum oxide or hydroxide. Furthermore, gel-like film was formed on the electrolyte surface in the presence of air. All these results suggest that to get better electrochemical behavior of Mg deposition and dissolution, very strict conditions (absence of water and oxygen) are necessary.

Appendix A: Determination of thermal drift and calibration for atomic resolution images

Thermal drift is a common phenomenon in SPM techniques and it is especially visible in the atomically resolved images which are acquired in liquid and under potential control. To obtain accurate parameters, it is necessary to determine the thermal drift. Determination is based on the assumptions as seen below.

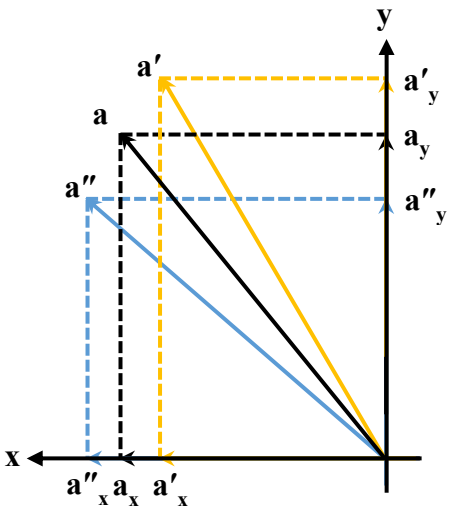

a is actual vector, however, due to drift a' (up scan) and a" (down scan) are visualised and the distances vary in x and y directions in consecutive scans.

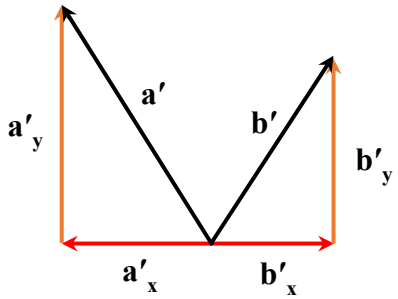

Simple trigonometric principles were used to determine drift.

a', b' and a", b" are the lattice vectors appeared on the images along scan 'up' and scan 'down', respectively.

Drift velocity $\vec{\upsilon} = (\upsilon_x, \upsilon_y)$

Scan velocity, C'_y = (Scan size × Scan rate)/No. of lines of the scan image along Y-direction

For Vector a':

$$\vec{a} + \vec{\upsilon} \cdot a'_y / C'_y = \vec{a'}$$

For Vector b':

$$\vec{b} + \vec{\upsilon} \cdot b'_y / C'_y = \vec{b'} \qquad \text{A.1}$$

After rearrangement

$$\vec{a} = \vec{a'} - \vec{\upsilon} \cdot a'_y / C'_y \qquad \vec{b} = \vec{b'} - \vec{\upsilon} \cdot b'_y / C'_y \qquad \text{A.2}$$

For Vector a'': **For Vector b'':**

$$\vec{a} - \vec{\upsilon} \cdot a''_y / C'_y = \vec{a''} \qquad \vec{b} - \vec{\upsilon} \cdot b''_y / C'_y = \vec{b''} \qquad \text{A.3}$$

After rearrangement

$$\vec{a} = \vec{a''} + \vec{\upsilon} \cdot a''_y / C'_y \qquad \vec{b} = \vec{b''} + \vec{\upsilon} \cdot b''_y / C'_y \qquad \text{A.4}$$

Combining A.2 with A.4 gives the drift velocity.

$$\vec{a'} - \vec{\upsilon} \cdot a'_y / C'_y = \vec{a''} + \vec{\upsilon} \cdot a'_y / C'_y \qquad \vec{b'} - \vec{\upsilon} \cdot b''_y / C'_y = \vec{b''} + \vec{\upsilon} \cdot b''_y / C'_y \qquad \text{A.5}$$

$$\vec{\upsilon} \cdot (a'_y + a''_y) / C'_y = (\vec{a'} - \vec{a''}) \qquad \vec{\upsilon} \cdot (b'_y + b''_y) / C'_y = (\vec{b'} - \vec{b''}) \qquad \text{A.6}$$

$$\vec{\upsilon} = (\vec{a'} - \vec{a''}) \cdot C'_y / (a'_y + a''_y) \qquad \vec{\upsilon} = (\vec{b'} - \vec{b''}) \cdot C'_y / (b'_y + b''_y) \qquad \text{A.7}$$

Atomic Vector calculations for SO_4^{2-} on Au(111)

Cyclic voltammogram of Au(111) in 0.1 M H_2SO_4 in STM cell (see. below)

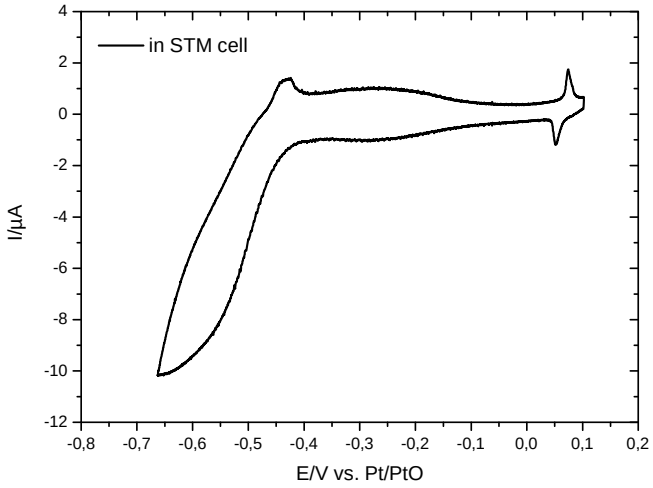

Calculations for Image 35 (scan down, zan100216x_00035) for SO_4^{2-} adsorption on Au(111) surface at the potential of 0.1 V vs. Pt/PtO.

Atomic distance Vector a' = 0.445 nm,

Atomic distance Vector b' = 0.673 nm

Two atoms taken along Vector a' 0.890 Vector a'

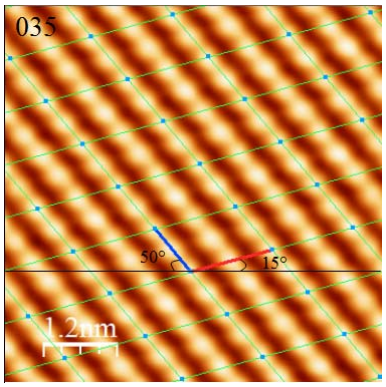

Two atoms taken along Vector b' 1.345 Vector b'

Calculation for a'$_x$ & a'$_y$ using Phythagorus theorem

Angle for Vector a along Perpendicular = 50°

a'$_y$ = Sin50° x magnitude of Vector a' = 0.682 nm,

a'$_x$ = Cos50° x magnitude Vector a' = -0.572 nm

Vector a' = (a'$_x$, a'$_y$) = (-0.572, 0.682)

Calculation for b'$_x$ & b'$_y$ using Phythagorus theorem

Angle for Vector a along Perpendicular = 15°

b'$_y$ = Sin15° · magnitude Vector b' = 0.348 nm,

b'$_x$ = Cos15° · magnitude Vector b' = 1.299 nm

Vector b' = (b'$_x$, b'$_y$) = (1.299, 0.348)

Calculations for Image 36 (scan up, zan100216x_00036) for SO_4^{2-} adsorption on Au(111) surface at the potential of 0.1 V vs. Pt/PtO.

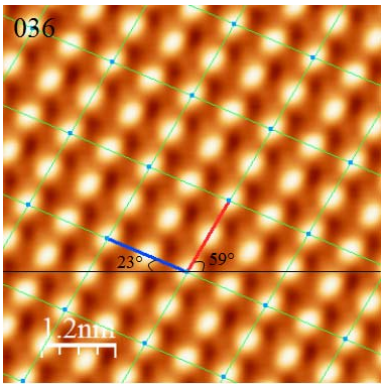

Atom distance Vector a" = 0.688 nm,

Atom distance Vector b" = 0.660 nm

Two atoms taken along Vector a" = 1.375 Vector a"

Two atoms taken along Vector b" = 1.319 Vector b"

Calculation for a"x & a"y using Phythagorus theorem

Angle determined for Vector a along Perpendicular = 23°

a"$_y$ = Sin23° · magnitude Vector a" = 0.537 nm,

a"$_x$ = Cos23° · magnitude Vector a" = -1.266 nm

Vector a" = (a"$_x$, a"$_y$) = (-1.266, 0.537)

Calculation for b"x & b"y using Phythagorus theorem

Angle determined for Vector a along Perpendicular = 59°

b"$_y$ = Sin59° · magnitude Vector b" = 1.131 nm,

b"$_x$ = Cos59° · magnitude Vector b" = 0.679 nm

Vector b" = (b"$_x$, b"$_y$) = (0.679, 1.131)

Drift velocity $\vec{\upsilon} = (\upsilon_x, \upsilon_y)$

Scan velocity, C'_y = (Scan Size × Scan Rate)/No. of lines of the scan image along Y-dir.

C'_y=0.705 (nm/s)

Thus, the drift velocities were calculated by eq. A.7

For Vector a': **For Vector b':**

$\vec{\upsilon} = (0.401,\ 0.083)$ $\vec{\upsilon} = (0.295,\ -0.373)$

The components of vector a & b can be obtained by using eq. A.2 and A.4

$$\vec{a} = \vec{a'} - \vec{\upsilon} \cdot a'_y / C'_y \qquad \vec{b} = \vec{b'} - \vec{\upsilon} \cdot b'_y / C'_y \qquad \text{A.2}$$

$$\vec{a} = \vec{a''} + \vec{\upsilon} \cdot a''_y / C'_y \qquad \vec{b} = \vec{b''} + \vec{\upsilon} \cdot b''_y / C'_y \qquad \text{A.4}$$

Vector a = (a_x, a_y) = (-0.960, 0.601) & Vector b = (b_x, b_y) = (1.154, 0.533)

Calculations of the Vector a and vector b from its components vectors

$|\mathbf{a}| = \text{Sqrt}(a_x^2 + a_y^2)$ $|\mathbf{b}| = \text{Sqrt}(b_x^2 + b_y^2)$

$|\mathbf{a}|$ = 1.13 **$|\mathbf{b}|$ = 1.27**

As both vectors compose of two lattice vectors, one lattice would be

$\left|\vec{a}\right| = 0.565$ $\left|\vec{b}\right| = 0.635$

$\theta_a = \tan^{-1}(a_y / a_x) = 32^\circ$ $\theta_b = \tan^{-1}(b_y / b_x) = 24.8^\circ$

Therefore, the angle between vector a & b is 123.2°.

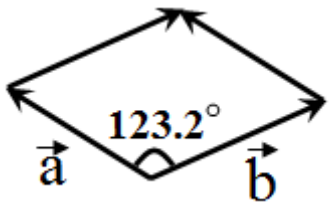

Calibration of the scanner by the SO_4^{2-} adlayer structure

Drift Corrected Vectors a & b

$$\left|\vec{a}\right| = 0.565 \qquad \left|\vec{b}\right| = 0.635$$

Actual (theoretical) sulfate adlayer vectors are

$$\left|\vec{A}\right| = 0.50 \qquad \left|\vec{B}\right| = 0.76$$

Vector components of a, A and b, B can be written as

$$A = \begin{pmatrix} A_x & B_x \\ A_y & B_y \end{pmatrix} \qquad a = \begin{pmatrix} a_x & b_x \\ a_y & b_y \end{pmatrix}$$

A calibration matrix M can be defined as following,

$$A = M \cdot a \Leftrightarrow M = A \cdot a^{-1} \qquad \text{A.8}$$

$$\text{Thus, } M = \begin{pmatrix} M_{11} & M_{12} \\ M_{21} & M_{22} \end{pmatrix} = \begin{pmatrix} A_x & B_x \\ A_y & B_y \end{pmatrix} \begin{pmatrix} b_y & -b_x \\ -a_y & a_x \end{pmatrix} \cdot 1/\left(a_x b_y - b_x a_y\right)$$

Component Vector for the theoretical sulfate adlayer (for the orientation as drawn in the figure)

Vector A

$A_y = A \cdot \text{Sin}40.1° = 0.322$

$A_x = A \cdot \text{Cos}40.1° = -0.382$

A (A_x, A_y) = **(-0.382, 0.322)**

Vector B

$B_y = B \cdot \text{Sin}30.8° = 0.389$

$B_x = B \cdot \text{Cos}30.8° = 0.653$

B (B_x, B_y) = (0.653, 0.389)

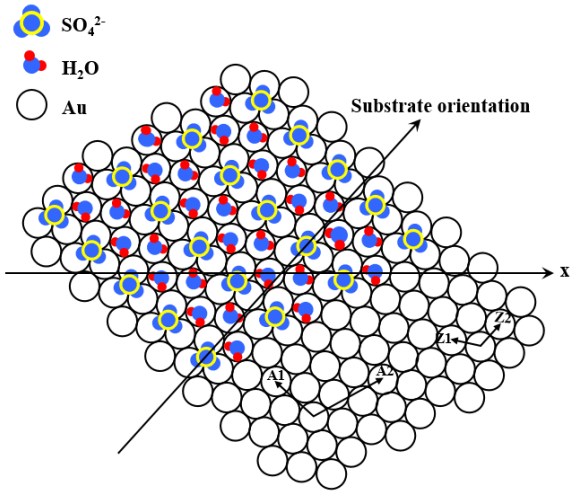

Similarly, drift corrected vectors a & b for sulfate adlayer

Vector **a** = ($\mathbf{a_x}$, $\mathbf{a_y}$) = (-0.960, 0.601) & Vector **b** = ($\mathbf{b_x}$, $\mathbf{b_y}$) = (1.154, 0.533)

a_x = -0.480 a_y = 0.301 b_x = 0.577 b_y = 0.267

By substituting these values, the vector $\mathbf{a^{-1}}$ can be calculated.

$$a^{-1} = 1/(-0.3013)\begin{pmatrix} 0.267 & -0.577 \\ -0.301 & -0.480 \end{pmatrix} = \begin{pmatrix} -0.884 & 1.915 \\ 0.997 & 1.593 \end{pmatrix}$$

Therefore, the calibration matrix can be obtained by using the eq. A.8.

$$M = A \cdot a^{-1}$$

$$\begin{pmatrix} M_{11} & M_{12} \\ M_{21} & M_{22} \end{pmatrix} = \begin{pmatrix} -0.382 & 0.653 \\ 0.322 & 0.389 \end{pmatrix} \begin{pmatrix} -0.884 & 1.915 \\ 0.997 & 1.593 \end{pmatrix}$$

$$\begin{pmatrix} M_{11} & M_{12} \\ M_{21} & M_{22} \end{pmatrix} = \begin{pmatrix} 0.989 & 0.308 \\ 0.103 & 1.237 \end{pmatrix}$$

Control of the calculation of the calibration martix M

$$A = M \cdot a$$

$$\begin{pmatrix} A_x & B_x \\ A_y & B_y \end{pmatrix} = \begin{pmatrix} 0.989 & 0.308 \\ 0.103 & 1.237 \end{pmatrix} \begin{pmatrix} -0.480 & 0.577 \\ 0.301 & 0.267 \end{pmatrix}$$

$$\begin{pmatrix} A_x & B_x \\ A_y & B_y \end{pmatrix} = \begin{pmatrix} -0.382 & 0.653 \\ 0.322 & 0.389 \end{pmatrix}$$

Finally, the matrix A is obtain again after multiplying matrix a with calibration matrix.

Drift corrected vectors for Antimony (Sb) using images 056 & 057 (files name, sb-231215x01_00056 & sb-231215x01_00057).

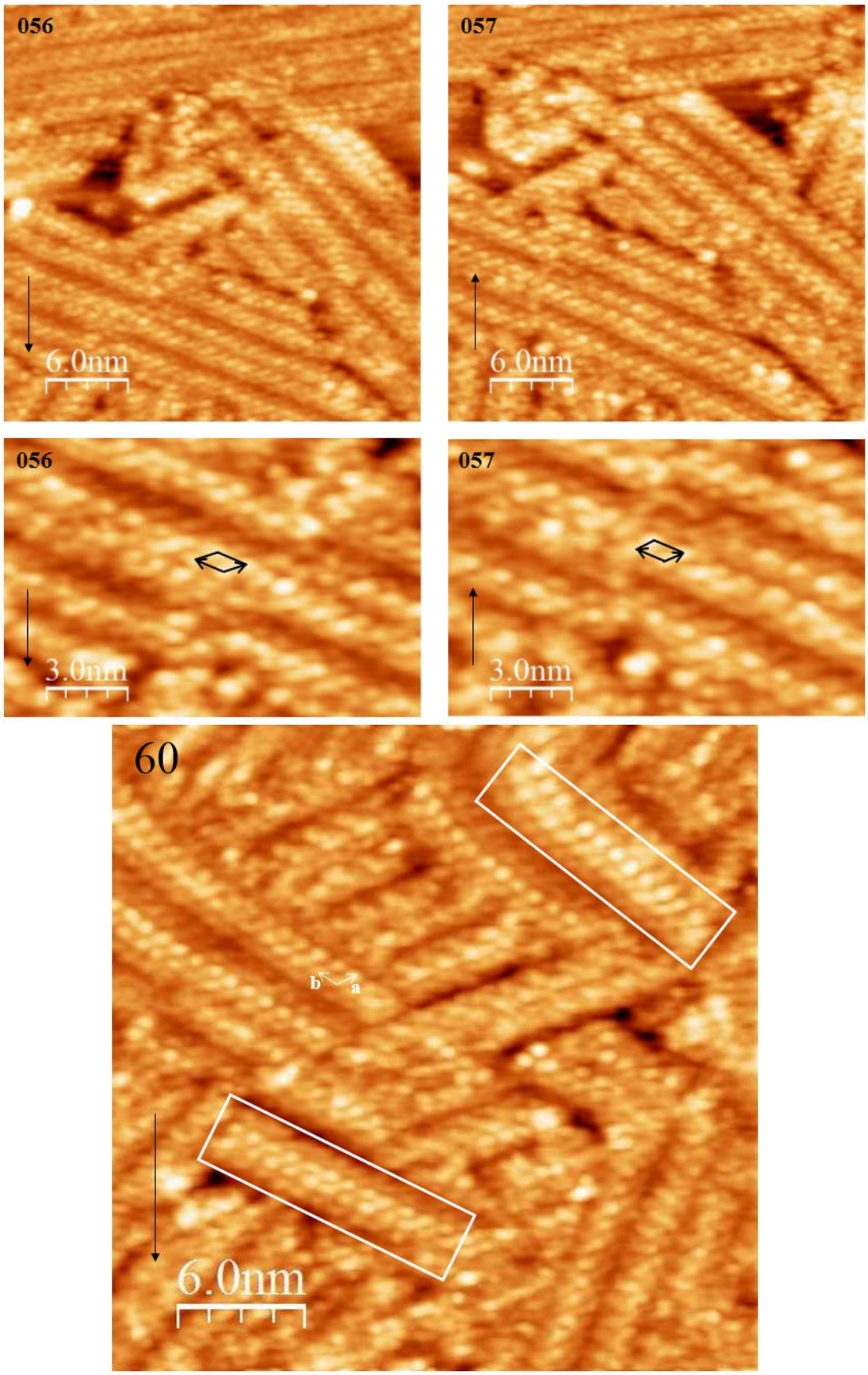

Vector $\mathbf{l_1} = (\mathbf{l_{1x}}, \mathbf{l_{1y}}) = (-2.254, 0.939)$ and vector $\mathbf{l_2} = (\mathbf{l_{2x}}, \mathbf{l_{2y}})) = (1.348, 0.467)$

Calculations of vector a and vector b from its components vectors

$|\mathbf{l_1}| = \mathrm{Sqrt}(L_{1x}^2 + L_{1y}^2)$ $\quad$ $|\mathbf{l_2}| = \mathrm{Sqrt}\ (l_{2x}^2 + l_{2y}^2)$

$|\mathbf{l_1}| = \mathbf{2.442}$ $\quad$ $|\mathbf{l_2}| = \mathbf{1.426}$

As both vectors compose of two lattice vectors, one lattice would be

$|\mathbf{l_1}| = \mathbf{1.221}$ $\quad$ $|\mathbf{l_2}| = \mathbf{0.713}$

$\theta_{l1} = \tan^{-1}(l_{1y}/l_{1x}) = 22.6^\circ$ $\quad$ $\theta_{l_2} = \tan^{-1}(l_{2y}/l_{2x}) = 19.1^\circ$

Therefore, the angle between vector $\mathbf{l_1}$ and $\mathbf{l_2}$ is **138.3°**

Similarly, drift corrected vectors $\mathbf{L_1}$ & $\mathbf{L_2}$

$\mathbf{l}_{1x} = -1.127$, $\mathbf{l}_{1y} = 0.470$, $\mathbf{l}_{2x} = 0.674$, $\mathbf{l}_{2y} = 0.233$

with, $L = M \cdot l$ A.9

$$\begin{pmatrix} L_{1x} & L_{2x} \\ L_{1y} & L_{2y} \end{pmatrix} = \begin{pmatrix} 0.989 & 0.308 \\ 0.103 & 1.237 \end{pmatrix} \begin{pmatrix} -0.127 & 0.674 \\ 0.470 & 0.233 \end{pmatrix}$$

$$\begin{pmatrix} L_{1x} & L_{2x} \\ L_{1y} & L_{2y} \end{pmatrix} = \begin{pmatrix} -0.971 & 0.738 \\ 0.464 & 0.358 \end{pmatrix}$$

$|\mathbf{L_1}| = \mathbf{1.076}$ $\quad$ $|\mathbf{L_2}| = \mathbf{0.821}$

$\theta_{L1} = \tan^{-1}(L_{1y}/L_{1x}) = 25.6^\circ$ $\quad$ $\theta_{L_2} = \tan^{-1}(L_{2y}/L_{2x}) = 25.9^\circ$

Therefore, the angle between vector L_1 and L_2 is **128.5°**

Evaluation of the adlayer structures in matrix notation

The two lattice vectors Z_1 and Z_2 are defined for the substrate (Au(111)) as a model. The relationship between matrix Z (substrate vectors) and matrix A (sulfate vectors) would be defined by the following equation.

$$A = S \cdot Z \qquad \text{A.10}$$

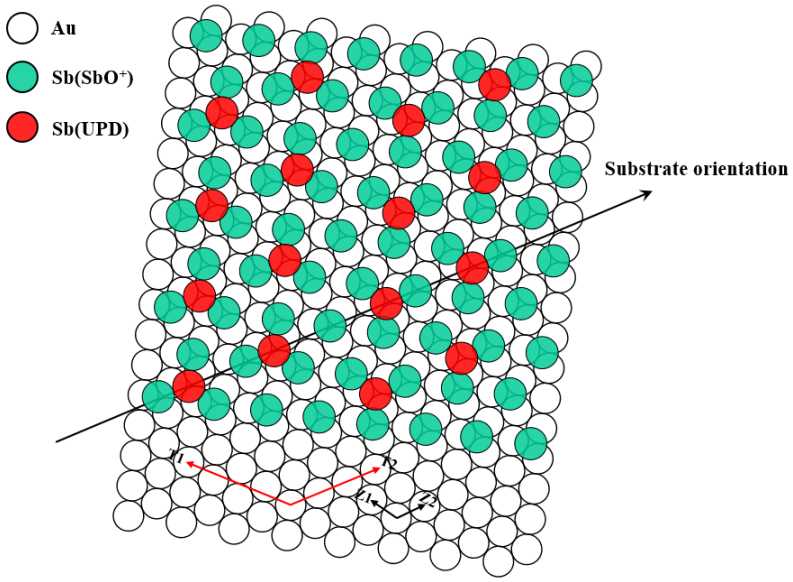

Vector $Z_1 = (Z_{1x}, Z_{1y}) = (-0.282, 0.060)$ and $Z_2 = (Z_{2x}, Z_{2y}) = (0.193, 0.214)$

So, the substrate Matrix would be

$$\begin{pmatrix} Z_{1x} & Z_{2x} \\ Z_{1y} & Z_{2y} \end{pmatrix} = \begin{pmatrix} -0.282 & 0.193 \\ 0.060 & 0.214 \end{pmatrix}$$

The sulfate adlayer matrix A was determined before.

$$\begin{pmatrix} A_x & B_x \\ A_y & B_y \end{pmatrix} = \begin{pmatrix} -0.382 & 0.653 \\ 0.322 & 0.389 \end{pmatrix}$$

By using eq. A.10 gives

$$S = Z^{-1} \cdot A \qquad \text{A.11}$$

$$S = \begin{pmatrix} 2.00 & -0.901 \\ 0.944 & 2.070 \end{pmatrix} \approx \begin{pmatrix} 2 & -1 \\ 1 & 2 \end{pmatrix}$$

Similarly, matrix is determined for Sb adlayer

$$L = T \cdot Z \Leftrightarrow T = Z^{-1} \cdot L \qquad \text{A.12}$$

$$T = \begin{pmatrix} 3.51 & 0.29 \\ -1.09 & 2.65 \end{pmatrix} \approx \begin{pmatrix} 3 & 0 \\ -1 & 3 \end{pmatrix}$$

This structure is not the superlattice. The information of Sb structure on the images is not sufficent because there is a regular arrangement of Sb atoms along the direction of vector b but there is no regular arrangment along the direction of vector a (see. the image number 60). The model shown above is just a suggested struture.

Appendix B: Description of SPM images

Chapter 4: The STM images obtained from the new setup with the 1 µm scanner

Chapter 5: The STM images obtained from the new setup with the 1 µm scanner

Chapter 6:

The STM images shown in Fig. 6.9-6.11 obtained from the old setup with the 1 µm scanner

The STM images shown in Fig. 6.13-6.16 obtained from the new setup with the 1 µm scanner

The AFM images shown in Fig. 6.18-6.21 obtained from the old setup with the old AFM scanner

The STM images shown in Fig. 6.23-6.27 obtained from the new setup with the 1 µm scanner

Chapter 7: The STM images obtained from the new setup with the 1 µm scanner

Chapter 8: The STM images obtained from the old setup with the 1 µm scanner

Appendix A: The STM images obtained from the new setup with the 1 µm scanner

Acknowledgement

I would like to express the deepest gratitude and appreciation to my research advisor, **Prof. Dr. Helmut Baltruschat**. I am very appreciative of his support and constant guidance and assistance during the entire period of my work. His unwavering enthusiasm for electrochemistry kept me constantly engaged with my research, and his kindness and generous help make my time at Bonn University enjoyable.

Besides my advisor, I would like to give my sincere appreciation to the rest of my thesis committee: Prof. Dr. Thomas Bredow, Prof. Dr. Werner Mader, Prof. Dr. Peter Koepke, for their availability and eagerness to evaluate my thesis.

My sincere thanks also goes to my colleagues Ali and Shahid for their great help in my work, and to the former and present members of our group, Christoph B., Christoph M., Ehab, Mehdi, Hatem, Philip. R., Philipp H., Sevda, Soltani, Dilek, Martina, Jan, Akos, Ana, Pawol, Da, Sergi, Ahmed, Annchristin, Frau Rossignol and Frau Thome for their help and support. In particular, I am grateful to Dr. Ernst for his valuable discussions and knowledge, Frau Rossignol for her help in administration and Frau Thome for her help in the lab.

I thank the members of mechanical, electronic and glass blowing workshops, especially Mr. Königshoven, Mr. Paulig, and Mr. Koll for their help in designing and constructing the fine cells and repairing devices.

I am thankful to KAAD for providing the Ph.D. scholarship for three and a half years. I extend my sincere thanks to the staffs of the KAAD in Bonn, especially, Dr. Geiger, Frau Wend and Frau Bialas for support and assistance.

I would like to thank my family: my parents and my two sisters for love, support, and encouragement to me throughout my educational career. Special thanks to my beloved wife, for what she has done for me, love and concern and constant support and encouragement. I would also like to express my sincere thanks to all my teachers, relatives and friends.

Zan, Lingxing